

Investigation of a medium-sized floating offshore wind turbine with stall regulation

Dissertation

zur

Erlangung des akademischen Grades

Doktor-Ingenieur (Dr.-Ing.)

der Fakultät für Maschinenbau und Schiffstechnik

der Universität Rostock

vorgelegt von

Moe Moe Aye

aus Rostock

Rostock, 2021

https://doi.org/10.18453/rosdok_id00003896

Gutachter:

Prof. Dr. rer. nat. habil. Uwe Ritschel, Universität Rostock, Fakultät für Maschinenbau und Schiffstechnik, Lehrstuhl für Windenergietechnik

Prof. Dr.-Ing. habil. Nikolai Kornev, Universität Rostock, Fakultät für Maschinenbau und Schiffstechnik, Lehrstuhl für Modellierung und Simulation

Jahr der Einreichung: 2021

Jahr der Verteidigung: 2022

ACKNOWLEDGEMENTS

The present thesis was conducted during my work as a research assistant at the Chair of Wind Energy Technology. First and foremost, I would like to express my sincere gratitude to my supervisor Prof. Dr. rer. nat. habil. Uwe Ritschel for his continuous support of my Ph.D study, heated discussions, and constant feedback. Without his guidance and patience, I would not have completed this thesis. Secondly, I also would like to express my special thanks to Prof. Dr.-Ing. habil. Nikolai Kornev for being co-supervisor and taking the time to read my thesis. My sincere thanks also go to Dr.-Ing Frank Adam for giving me the opportunity to do my doctoral research, for his prompt and great advice during the research. I also would like to express my deep appreciation to each and every employee at the Chair of Wind Energy Technology for sharing their expertise, valuable comments, and being good friends throughout the course of my research. It has been a privilege to have worked with all of you.

Finally, I would like to give my most sincere thanks to my family and friends for their unconditional love, generous support, and for being a longtime source of great advice throughout these years. Without their dedicated encouragement, I would not have made it this far.

TABLE OF CONTENTS

| | |
|---|----|
| Table of Contents | 4 |
| Abbreviations and Symbols | 7 |
| Abstract | 12 |
| 1 Introduction | 13 |
| 1.1 Motivation | 13 |
| 1.2 Research Objective | 15 |
| 2 State of the art..... | 17 |
| 2.1 Different control strategies for stall-regulated wind turbines..... | 17 |
| 2.1.1 Fixed-speed control strategy with stall regulation | 18 |
| 2.1.2 Variable-speed control strategy on stall regulation | 19 |
| 2.2 Floating substructure concepts, modelling, standards and guidelines | 24 |
| 2.2.1 Spar..... | 26 |
| 2.2.2 Tension Leg Platform | 27 |
| 2.2.3 Semi-submersible | 27 |
| 2.3 Previous research on semisubmersible floating offshore wind turbines..... | 29 |
| 2.4 Coupled simulation methods and tools for floating offshore wind turbines..... | 31 |
| 2.5 Standards and guidelines for load simulation..... | 34 |
| 3 Basic design of CART | 36 |
| 3.1 CART WT tower properties | 36 |
| 3.2 Rotor-nacelle assembly design | 38 |
| 3.3 Substructure design | 39 |
| 3.4 Model implementation in OpenFAST..... | 42 |
| 4 Development of control concept..... | 45 |
| 4.1 Aerodynamic properties of the blade..... | 45 |
| 4.2 Partial load regions..... | 49 |
| 4.3 Full load region..... | 51 |
| 4.4 Protection system..... | 53 |
| 4.5 Implementation of control concept | 53 |
| 4.5.1 Tuning generator torque control parameters..... | 53 |
| 4.5.2 Grid loss and shut down..... | 59 |
| 4.5.3 Eigenanalysis | 60 |

| | | |
|-------|--|-----|
| 4.5.4 | Hydrostatic restoring stiffness calculation | 61 |
| 4.5.5 | Free-decay tests | 62 |
| 4.5.6 | Platform motion and Response of controller as a function of wind speed | 65 |
| 5 | Loads acting on a typical floating offshore wind turbine..... | 69 |
| 5.1 | Gravity and Buoyancy | 69 |
| 5.2 | Wind loads..... | 70 |
| 5.3 | Wave loads..... | 73 |
| 5.3.1 | Sea state | 73 |
| 5.3.2 | Water levels, tide and storm surges..... | 74 |
| 5.3.3 | Calculation of wave loads | 75 |
| 5.4 | Current loads..... | 79 |
| 5.5 | Mooring line design loads..... | 79 |
| 5.6 | Reference site and its metocean data | 81 |
| 6 | Load Analysis..... | 83 |
| 6.1 | Load components and Reference coordinate systems | 83 |
| 6.2 | Design load cases | 85 |
| 6.3 | Normal operating conditions..... | 88 |
| 6.3.1 | Dynamic response of CART System during normal operation..... | 89 |
| 6.3.2 | Design driving load cases in normal operating conditions | 94 |
| 6.3.3 | Platform Yaw Motion in wind gusts | 100 |
| 6.3.4 | Comparison of offshore and onshore wind turbine loads..... | 103 |
| 6.3.5 | Fatigue loads..... | 108 |
| 6.4 | Extreme conditions with faults | 114 |
| 6.4.1 | Design driving load cases | 115 |
| 6.4.2 | Comparison of offshore and onshore CART system..... | 115 |
| 6.4.3 | Tower top side-to-side displacement for onshore wind turbine..... | 117 |
| 6.4.4 | Extreme Surge Motion in extreme wind and wave conditions..... | 120 |
| 6.4.5 | Extreme Pitch Motion in extreme wind and wave conditions | 123 |
| 6.5 | Extreme conditions with faults and worst consequences | 126 |
| 6.5.1 | Comparison of offshore and onshore wind turbine | 127 |
| 6.5.2 | Responses in normal operation, extreme events with faults, and faults events with worst consequences for offshore CART system..... | 129 |
| 6.5.3 | Influence of wind-wave misalignment on platform motions..... | 131 |

| | | |
|-------|---|-----|
| 6.5.4 | Influence of current loads on platform motions | 132 |
| 6.5.5 | Extreme Edgewise bending moment at the blade root for the onshore CART system | 133 |
| 7 | Discussion, Conclusions and Outlook..... | 136 |
| 7.1 | Discussion and Conclusions..... | 136 |
| 7.2 | Outlook..... | 140 |
| 8 | References..... | 141 |
| | List of figures..... | 148 |
| | List of tables | 152 |
| | Declaration | 153 |

ABBREVIATIONS AND SYMBOLS

This section lists the abbreviations and symbols which have been used in this study. Some abbreviations that appear only once have been explained directly where they appear.

Abbreviations

| | |
|----------|--|
| BEM | Blade element momentum |
| CART | Compact and Robust Medium-sized Wind Turbine |
| COB | Centre of buoyancy |
| COG | Centre of gravity |
| COM | Centre of mass |
| DLC | Design load case |
| DLL | Dynamic link library |
| DOF | Degree of freedom |
| ECD | Extreme coherent gust with direction change |
| EESG | Electrically excited synchronous generator |
| ETM | Extreme turbulence model |
| EWM | Extreme wind model |
| FAST | Fatigue aerodynamic structure turbulence |
| FEM | Finite element method |
| FFT | Fast Fourier Transform |
| FLS | Fatigue limit state |
| FOWT | Floating offshore wind turbine |
| HAWT | Horizontal axis wind turbine |
| IEC | International Electro technical Commission |
| JONSWAP | Joint North Sea Wave Project |
| KC | Keulegan-Carpenter number |
| LCOE | Levelized cost of energy |
| LPV | Linear Parameter Varying |
| LQ | Linear Quadratic |
| LQG | Linear Quadratic Gaussian |
| LTI | Linear time invariant |
| MBS | Multi body simulation |
| metocean | Meteorological and oceanographic |
| NREL | National Renewable Energy Laboratory |
| NSS | Normal Sea State |
| NTM | Normal turbulence model |
| NWLR | Normal water level range |

| | |
|----------|-----------------------------|
| OpenFAST | An improved version of FAST |
| P | Proportional |
| PI | Proportional-integral |
| PMSG | Permanent magnet generator |
| PSF | Partial safety factor |
| Re | The Reynolds number |
| RNA | Rotor Nacelle Assembly |
| SSS | Severe sea state |
| TLP | Tension leg platform |
| TSR | Tip speed ratio |
| ULF | Ultimate load factor |
| ULS | Ultimate limit state |

Latin large symbols

| | |
|------------------------------|--|
| A | cross sectional area [m ²] |
| A _r | 1- 0.287 ln(γ) is a normalizing factor [-] |
| A _{wp} | water plane area of the platform when it is not displaced [m ²] |
| C _B | coefficient of static friction of stretched portion of mooring line resting on the seabed [-] |
| C _D | viscous-drag coefficient in Morison's equation [m] |
| C _{ij} | (i,j) component of restoring matrix [kg/s ² , kg-m/s ² , kg-m ² /s ²] |
| C _M | added mass coefficient in Morison's equation [-] |
| C _{p,max} | maximum power coefficient [-] |
| DEL _{eq} | damage equivalent loads [kN-m] |
| EA | extensional stiffness of a mooring line [N] |
| F _D | design current load [N] |
| $F_i^{Hydrostatic}$ | (i) component of the hydrostatic load on the floating platform [N, N-m] |
| H | wave height [m] |
| H _A | effective tension in the mooring line at the anchor [N] |
| H _F | horizontal component of the effective tension in the mooring line at the fairlead [N] |
| H _s | significant wave height [m] |
| I | turbulence intensity [-] |
| L | length of the mooring line [m] |
| L _C | coherence scale parameter [m] |
| L _i ^{RF} | the cycle's load range about a fixed load-mean value at time series i [kN-m] |

| | |
|---------------------|--|
| L_K | an integral length scale for IEC Kaimal model where K equals the spectra for the three wind components [m] |
| M_{thrust} | wind heeling moment [kN-m] |
| P_a | aerodynamic power [kW] |
| R | rotor radius [m] |
| S_{kaimal} | power spectral density for Kaimal model [m^2/s^2] |
| T_a | aerodynamic torque [kN-m] |
| U_D | design current velocity [m/s] |
| V | effective wind speed [m/s] |
| V_0 | Displaced volume of fluid when the platform is not displaced [m^3] |
| V_A | vertical component of the effective tension in the mooring line at the anchor [N] |
| V_F | vertical component of the effective tension in the mooring line at the fairlead [N] |

Latin small symbols

| | |
|--|---|
| d | water depth to still water level [m] |
| f | cyclic frequency [s^{-1}] |
| g | acceleration due to gravity [m/s^2] |
| k | for generator torque, torque curve coefficient [-] |
| k | wave number [-] |
| m | Wöhler's exponent [-] |
| n_{eq} | equivalent count for the time series [-] |
| n_i | cycle count [-] |
| q_D | design current pressure [Pa] |
| q_j | (j^{th}) system degree of freedom [m, rad] |
| t | Simulation time step [s] |
| V_{mean} | mean wind speed [m/s] |
| V_{ref} | reference wind velocity at z_{ref} [m/s] |
| w | weight [kN] |
| $x_{\text{cob}}, y_{\text{cob}}, z_{\text{cob}}$ | set of orthogonal axes of a body-fixed location of centre of buoyancy of the support platform [m] |
| $x_{\text{cog}}, y_{\text{cog}}, z_{\text{cog}}$ | set of orthogonal axes of a body-fixed location of centre of gravity of the support platform [m] |
| x_F | horizontal distance between the anchor and fairlead of a mooring line [m] |
| z | for wind loads, height above ground or still water level [m] |

| | |
|--------------------|---|
| z | for wave loads, vertical co-ordinate positive upward, origin at still water level [m] |
| z_0 | roughness length in the current wind direction [m] |
| z_F | vertical distance between the anchor and fairlead of a mooring line [m] |
| z_{ref} | reference height in wind shear equation [m] |
| z_s | stretched vertical coordinate [m] |
| u, \dot{u} | wave particle velocity/acceleration [m/s, m/s ²] |
| \dot{u}_{struct} | velocity of the structure [m/s] |
| u_{rel} | relative velocity [m/s] |

Greek large symbols

| | |
|------------|---|
| Ω_o | Optimum rotational speed of the rotor [rpm] |
|------------|---|

Greek small symbols

| | |
|----------------------|--|
| α | wind shear exponent [-] |
| $\alpha_{max,pitch}$ | maximum static inclination [°] |
| δ_{i3} | (i,3) component of the Kronecker-Delta function (i.e., identity matrix) [-] |
| η | wave surface elevation [m] |
| λ | tip speed ratio [-] |
| λ_o | optimum tip speed ratio [-] |
| π | Mathematical constant, pi [-] |
| ρ_a | air density [kg/m ³] |
| ρ_w | seawater density [kg/m ³] |
| σ | for wave loads, spectral width parameter [-] |
| σ | for wind loads, standard deviation [m/s] |
| σ_K | standard deviation of wind speed for IEC Kaimal model where K equals the spectra for the three wind components [m/s] |
| Y | peak enhancement parameter [-] |
| ω | wave angular frequency [rad/s] |
| ω_p | spectral peak frequency [rad/s] |

Definitions

| | |
|-------------------|--|
| Rotor | The rotor consists of two or three blades made of fibreglass-reinforced epoxy and the hub made of high-quality cast iron. It transfers all loads from the blade driving a wind generator. |
| Drivetrain | The drivetrain converts kinetic energy into electrical power via either a gearbox and generator assembly or a direct drive. |
| Direct drive | Direct drive mechanism takes the torque coming from a motor without any gearing reductions. |
| Nacelle | Nacelle houses mechanical and electrical components such as gearbox, generator, yaw system, brake, lubrication, and cooling system. It is mounted on top of the tower connecting the tower with the rotor. |
| Yaw mechanism | Yaw angle is the angle of rotation of the nacelle around its vertical axis. The yaw mechanism ensures that the wind turbine rotor always faces into the wind as the wind direction changes. |
| Support structure | Support structure of a wind turbine consists of a tower and foundation. |
| Tower | Tower supports rotor nacelle assembly. They can be tubular steel towers, concrete towers, lattice towers, and guyed-tubular towers. |
| Substructure | It provides stability and resists overturning moment due to the thrust force exerted at the hub height. |

ABSTRACT

In most low-income countries especially Southeast Asian countries, clean and sustainable energy at an affordable price is highly demanded. Furthermore, land scarcity and population growth are giving a strong impetus for developers to venture into deep waters teeming with steadier wind resources, yet additional design challenges. Motivated by the need to develop a new concept which covers all these requirements, a medium-sized stall regulated wind turbine was developed within the frame of research project CART (Compact and Robust Medium-sized Wind Turbine) in cooperation with the Chair of Wind Energy Technology the University of Rostock, several German companies, the Vietnam National University, and several companies in Vietnam. The major goal was to reduce the cost of energy through innovative solutions and ultimately develop mini-grids and off-grid solutions. The special focus was put on developing a concept in more affordable ways at lower costs with higher efficiencies and less need for maintenance which most already available wind turbines in the market do not cover.

The thesis begins with the development of a stall control concept for a variable-speed medium-sized floating wind turbine. Firstly, the control concept was developed to ensure the highest possible efficiency in normal operation. Then, the protection concept was developed to ensure safe operation during grid failure or storm conditions. The feasibility of the proposed control concept was evaluated for both land- and sea-based CART hypothetical wind turbine. The outcomes of the initial stage of the work indicate that the developed control concept can contribute to power stability quite well. Thus, it serves as a good starting point to further conduct load analyses.

As a second part of the thesis, fully integrated aero-hydro-servo-elastic simulations were performed to characterize the global dynamic response of the system, identify the design driving loads for both onshore and offshore CART systems, and highlight the impacts brought about by the floating support structure. Based on the findings from the normal operation, the load responses to be more specific mean values of most parameters increase with the increase in wind speed for both systems. This is mainly due to the nature of stall-regulated wind turbines which have no active aerodynamic control system to reduce the rotor thrust force in high winds. According to results from events with faults, the resulted extreme loads are larger for the CART atop floating support structure than that for the onshore CART system. Particularly, parking in storm conditions induces large platform motions. It is therefore recommended to integrate structural control systems like tuned mass damper to reduce the platform motions to a certain degree. Overall, the results of this study form the basic input to further assess the technical and economic feasibility of the CART system, especially for offshore deployment.

1 INTRODUCTION

This chapter sets the background for this dissertation and provides an introduction to this study. It begins with the motivations for undertaking this research, addresses the current issues facing offshore wind development projects for developing countries, and explains the objectives of this research. It also provides an overview of the subsequent chapters of the dissertation.

1.1 MOTIVATION

Global climate change has the potential for more devastating impacts on lives on our planet. More frequent natural disasters have reminded us that we need to decarbonize our economics more urgently than ever to restore the balance. At the moment, the global energy production by renewable sources is about 28 % (International Energy Agency, 2020) which was 20 % by 2010. This substantial progress in renewable energy sectors is encouraging us that we can eradicate climate change by accelerating the pace of progress on green energy transition, yet we need to take steps right now with the utmost speed to achieve this goal. When it comes to renewable energy, the last decades have shed light on us that wind energy is undoubtedly the cleanest energy source and has the least amount of impact on the environment in comparison with other energy sources. Especially offshore wind energy has gained an impressive degree of market uptake across the globe. Rising sea level and land scarcity gave a strong impetus for developers to venture into deep waters teeming with steadier wind resources, yet additional design challenges (Butterfield et al., 2007). Nevertheless, rapid development in offshore technology has blazed a path in floating offshore wind turbines (FOWT). At the same time, the increased interest in installing wind farms further offshore demands simple and robust design solutions.

Over the last three decades, we have witnessed the progress of the evolution of offshore wind turbines from small to multi-megawatt ones. The technological advances that have propelled this progress enabled the cost of offshore wind energy to continuously come down in the market. In fact, cost reduction relies not only on the advancement in technology but also on the developers who relentlessly innovate the substructure designs, generator types, new concepts, and installation methods, etc. When it comes to the economics of floating offshore wind turbines, the upfront capital is substantially influenced by the additional costs of the substructure and power distribution system (Butterfield et al., 2007).

In spite of being green and sustainable, wind energy is intermittent. The energy production is not constant throughout the day even in an open sea environment. At certain times of the day, the energy demand outstrips energy production. For this, we need an advanced storage system like power-to-x technologies which can store large amounts of surplus energy over time and release it downtime. Power-to-X technologies is a carbon-neutral storage system that

converts renewable electricity to for example hydrogen and methane gas. In the future, power-to-x fuels will undoubtedly provide a stable power grid at an affordable price for all regions of the world.

As important as innovations in renewable energy themselves, these innovations in one country should contribute equally to the other especially low-income countries through shared knowledge and technology. In most low-income countries like Southeast Asian countries where energy demands are growing day by day, clean and sustainable energy at an affordable price is a question yet to be answered. Moreover, the availability of land and resources is limited whereas the population growth is substantially high. Therefore, moving farther offshore along with technological breakthroughs, which are suitable for places far from electrical infrastructure, is a potential solution in the future. At the same time, there is also a need to develop a design concept that is suitable for tropical and subtropical climates. The frequently cited environmental conditions like extreme heat, extreme rainfall and high wind speeds are unavoidable during the typhoon season from September to December there. This kind of environment needs a dedicated concept rather than the currently available concepts which were designed for European and the US sea sites. Because they significantly drive loads acting on the structures and ultimately the material strength and fatigue life of the wind turbine.

Motivated by the need to develop a new concept which covers the above-mentioned factors, a medium-sized stall-regulated wind turbine was developed within the framework of research project CART (Compact and Robust Medium-sized Wind Turbine) in cooperation with the Chair for Wind Energy Technology the University of Rostock, several German companies, the Vietnam National University, and several companies in Vietnam. Why a medium-sized wind turbine? Because the medium-sized wind turbine has a great potential in terms of low costs, low impact on the environment, and being able to be deployed for isolated communities like remote villages or islands for decentralized supply of electrical energy. While the cost of energy may not be lower than the ones for large offshore wind turbines, it might be lower than the cost of other technologies like diesel generators or other types of generation. The major goal was to reduce the cost of energy through innovative solutions and ultimately develop mini-grids and off-grid solutions. The special focus was put on developing a concept in more affordable ways at lower costs with higher efficiencies and less need for maintenance which most already available wind turbines in the market do not cover.

Several parameters can be adjusted accordingly to achieve this goal, such as using standardized modular structures to transport, replace and maintain easily, reducing system complexity to cut down the maintenance cost, and improving the control system, or even increasing the complexity to increase the system efficiency. Considering these facts, the CART system applied a robust and modular design that can be easily transported and installed in

remote regions. From the logistics point of view, the size of the individual component of the CART system was constrained to fit in 40-foot standard containers. Furthermore, stall regulation requires no pitch system for the rotor blades, and thus reduces system complexity and brings economic benefits especially for offshore applications, where maintenance is one of the major issues. With the application of a permanent magnet generator, the CART concept also eliminates the requirement of a gearbox, which subsequently reduces the overall weight of the system while keeping the maximum efficiency. Unlike most wind turbines which are connected to national grids, CART utilizes decentralized mini-grids. The fundamental premise of generating the energy close to where it is needed is to alleviate transmission losses and simultaneously grantee lower electricity costs, high power reliability, and minimum impact on the environment. What is more remarkable about the CART concept is its advanced battery storage system that is coupled with CART WT. It holds a lot of promises: it will grantee uninterrupted energy at a really high level all the time, affordable levelized cost of energy LCOE, and can play a key role in helping the country's economics decarbonize.

1.2 RESEARCH OBJECTIVE

To design and verify a new concept efficiently, it is of paramount importance to conduct the preliminary estimates of critical design loads. The overarching goal of this thesis is to develop a control concept and carry out fully integrated load analyses of the newly developed concept designed for an off-grid solution.

Developing a new floating offshore wind turbine concept suitable for tropical climates needs a dedicated concept rather than currently available concepts which were designed for the European and the US sea sites. The major challenges are related to the dynamics behaviour of the system in response to combined wind and wave loading and the choice of power regulation. The coupling of aerodynamic forces, structural forces, and hydrodynamic forces can lead to large amplitude motions. Therefore, load analyses are necessary to characterize the global dynamic behaviour of the coupled model, identify design driving loads, and highlight the impact brought about the floating substructure.

To begin with load analyses, the wind turbine needs to have an efficient power regulation that can optimize power output, provide the highest possible efficiency in normal operation and ensure safe operation during grid loss or storm conditions. Of equal importance, power regulation must ensure that the structural loads are reduced especially when exposed to constantly changing environments like wind gusts and turbulence. Therefore, it is needed to develop a control concept that can ensure good performance of the wind turbine in a constantly changing environmental conditions. After that, series of design load cases are needed to perform both for the land-based CART system and sea-based CART system. Aiming to better

understand the dynamic effects brought about by the floating systems, the results will be compared and elaborated on the ultimate loads and fatigue loads of several load components.

2 STATE OF THE ART

The literature is sparse on the variable-speed stall regulated floating offshore horizontal axis wind turbines. Certainly, several concepts of stall regulated both horizontal-axis wind turbines and vertical-axis wind turbines have been developed and their benefits over pitch regulation have been highlighted. However, horizontal axis FOWT assisted with variable-speed stall regulation have yet to be developed and the concept needs to be verified thoroughly.

This chapter reviews research literature on different control strategies of stall-regulated wind turbines. First of all, state-of-the-art in control strategies for variable-speed stall regulation is collected and reviewed. And hence, a control strategy and protection system for CART wind turbine will be developed. Secondly, the working principle of different floater concepts is reviewed and publications and previous research on semisubmersible floaters are studied and reviewed, focusing on modelling and load simulation of semisubmersible FOWT. Thirdly, it will provide an overview of coupled simulation methods and tools for FOWT and the applicable design standards.

2.1 DIFFERENT CONTROL STRATEGIES FOR STALL-REGULATED WIND TURBINES

In the last decades, horizontal axis wind turbines (HAWT) have been deployed on a large scale. The performance of the wind turbine depends on the availability of wind resources, design characteristics, and how the turbine delivers power. Therefore, the rotor configuration and power regulation strategy should be carefully considered depending on the distribution of the wind speeds along with other factors. To begin with the working principle of a wind turbine, the rotor blades can either be fixed to the rotor hub at a fixed pitch angle or through a pitch mechanism, that can vary the pitch angle to achieve the desirable power (Burton et al., 2011). The incoming wind causes the rotor to rotate and generate an aerodynamic torque. This aerodynamic torque is transmitted to the generator either by direct coupling called direct-drive concept or via gearbox so-called geared drive concept. Finally, the generator converts rotational kinetic energy into electrical energy.

When rotor blades are fixed to the hub, the aerodynamic properties of aerofoils of rotor blades need to be designed to ensure that the blades gently stall when undergone high wind speeds. This can be done by creating flow separation on the side of the blade which is not facing the wind at a particular wind speed. Figure 1 depicts how the air flows over the different aerofoil sections along the blade span. The inner blade section goes in stall whereas the outer blade section is in attached flow. The outer blade sections tend to be thinner and are aerodynamically active meaning that they have a great impact on the thrust force and aerodynamic performance. In high winds, it is, therefore, necessary to ensure that the blades gently stall from the blade root and outwards toward the blade tip. Stall regulation is a very simple, robust,

and cost-effective power regulation because it eliminates the pitch system and subsequently reduces the maintenance and repair costs significantly. For direct-drive system, one of its shortcomings is the requirement of a large generator with a large number of pole pairs that can cope with large torque and power spike experienced above rated wind speeds.

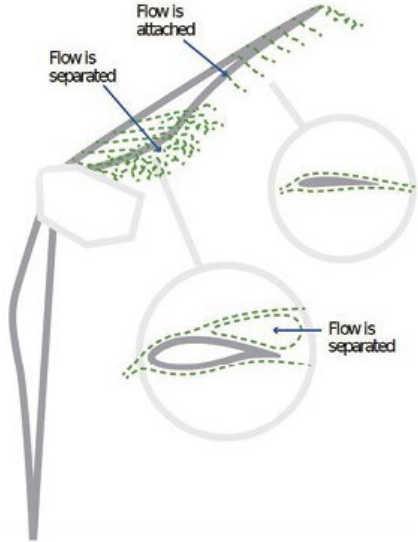


FIGURE 1: AIR FLOW PATTERN ON WIND TURBINE BLADE (WINDPOWER ENGINEERING AND DEVELOPMENTS, 2014)

When considering rotational speed, the control strategy can be classified into the constant speed and the variable speed concept (Bianchi et al., 2006). Due to constrained rotor speed, the energy capture of a constant speed stall design is generally lower than that of a variable speed stall regulation concept. On the other hand, with a variable speed operation, it is possible to adjust continuously the rotor speed with respect to the wind speed and thus the power regulation can be optimized to extract as much energy as possible. The following sections review fixed-speed control strategies on stall regulation briefly and more extensively about variable-speed control strategy on stall regulation since the latter control strategy is applied in this study and it serves as a foundation for this research.

2.1.1 FIXED-SPEED CONTROL STRATEGY WITH STALL REGULATION

Fixed-speed control strategy in combination with stall regulation has been pervasive during the past few decades due to its simplicity and low cost. Typically, an induction generator or asynchronous generator is used in this control strategy. The generator is directly connected to the power grid. Thus, the generator speed is locked to the grid frequency and varies only a few percent due to its slip. This subsequently results in large variations in shaft torque as the wind speed fluctuates. Figure 2 depicts the control strategy for fixed speed stall regulation in terms of rotational speed and torque curve. In the torque-speed curve, grey lines represent the aerodynamic performance of the blade with respect to rotor speed at different wind speeds while the solid line represents the reaction torque at a specific fixed speed at different wind speeds. The operating regions can be divided into two parts: partial load region, where V_{cut-in}

$< V_{\text{inflow}} < V_{\text{rated}}$, and full load region, where $V_{\text{rated}} < V_{\text{inflow}} < V_{\text{cut-out}}$. Apparently, the reaction torque of such a control strategy is constraint along the line FD meaning that the optimum power can be achieved only for a specific wind speed range. It is found at wind speed V_E in the figure. In the partial load region (point F and J), power is regulated using passive stall. Obviously, the generated power cannot be achieved at an optimum level because the turbine operates at a constant speed. In the full load region (point D and G), the power production drops and increases again when the wind speed gets higher before the cut-out wind speed. The speed range in which the turbine produces electricity is very narrow. This poor power quality control throughout operating regions leads to constantly active power fluctuations in the grid which is not the purpose of a control system. Clearly, a large fluctuation in torque subsequently can yield high mechanical stresses in the drivetrain and the rotor. All in all, this control strategy has many major shortcomings such as complexity of the aerodynamic design of rotor blade, noises in high winds, and difficulty to alleviate mechanical loads and improve energy captured. Therefore, it has become less popular these days.

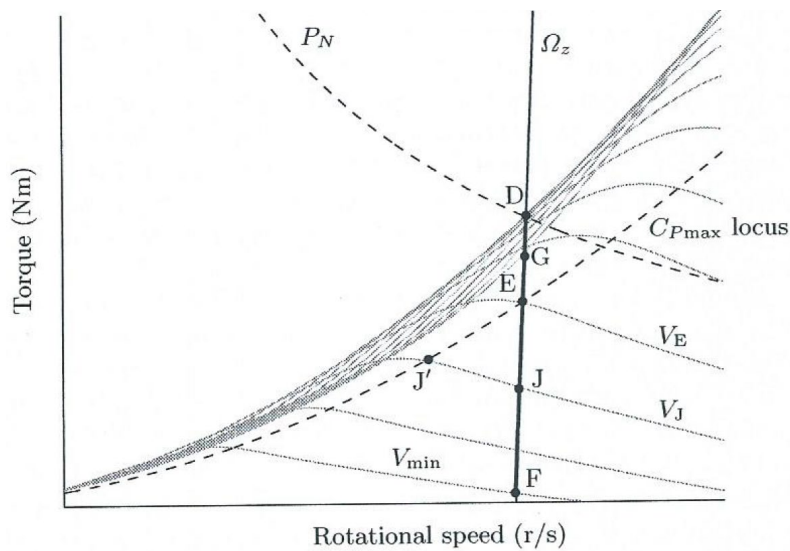


FIGURE 2: CONTROL STRATEGY OF A FIXED SPEED STALL REGULATED WIND TURBINE (BIANCHI ET AL., 2006)

2.1.2 VARIABLE-SPEED CONTROL STRATEGY ON STALL REGULATION

Much research on variable-speed control strategies has been conducted to improve wind energy conversion systems focusing on the generator modelling, control system for load alleviation, etc. (Muljadi et al., 1997, 1998a, 1998b, 2000a, 2000b; Bossanyi, 2000; Bourlis, 2011; Leith and Leithead, 1997; Leithead and Connor, 2000a, 2000b; Rosmin, 2015). This section reviews the previous study on control concepts of the variable speed stall-regulated wind turbines.

Typically, geared double fed induction generator or geared synchronous generator, gearless electrically excited synchronous generator (EESG), and gearless permanent magnet generator (PMSG) are utilized in a variable-speed control strategy. With the synchronous

of electrical power extracted from the wind to mechanical power available from the wind (Burton et al., 2011). In fact, C_p changes nonlinearly with pitch angle and TSR. Theoretically, a maximum of 59 % of wind energy can be extracted from the wind, which is also known as the Betz limit (Burton et al., 2011). In practice, this value is slightly lower, usually 50 %. Commonly, the wind turbine should achieve maximum available energy in partial load regions meaning that the turbine operates at $C_{p,max}$ for every wind speed in this region. Typically, the value of optimum TSR, λ_o corresponding to $C_{p,max}$ for a fixed-pitch machine can be expressed as:

$$\lambda_o = \frac{\Omega_o R}{V} \quad 2-2$$

Where Ω_o represents the optimum rotational speed of the rotor for a specific wind speed. Accordingly, the maximum aerodynamic torque can be computed as follow.

$$T_a = \frac{P_a}{\Omega_o} = \frac{1}{2\Omega_o} \rho_a \pi R^2 C_{p,max} V^3 \quad 2-3$$

The above equation can be represented in terms of torque-speed curve, which is sometimes called quadratic law (Leithead and Connor, 2000a). The equation becomes:

$$T_a = k \Omega_o^2 \quad 2-4$$

Where, the torque curve coefficient k can be determined according to 2-5.

$$k = \frac{1}{2\lambda_o^3} \rho_a \pi R^5 C_{p,max} \quad 2-5$$

Equation 2-3 is also known as the maximum power tracking algorithm and is widely used in commercial wind turbines. For a direct-drive concept in which the rotor is directly coupled with the generator, the rotor speed and generator speed are the same neglecting the shaft torsional flexibility. When it is assumed that the speed can be measured, the generator torque can be set directly to $k\Omega_o^2$. This method is stable in the way that the optimal power curve is automatically reached (Leithead et al., 2000b). However, it is mentioned that this approach leads to a significant deviation of C_p curve from the maximum C_p locus in turbulent winds. Especially for large wind turbines, large rotor inertia leads to large torque transients in the drivetrain (Leithead et al., 2000b).

In the full load regions, the main objective of the control system is to limit the aerodynamic power captured from the inflow wind not to exceed the maximum allowable power of the generator. This is accomplished by forcing the blades to stall and hence keeping the rotor speed or the extracted power at a constant level by improving some form of aerodynamic balance in the control strategy. According to Pierce and Migliore (2000) and Muljadi et al.,

(2000), the active control method and soft-stall method are of interest for stall-regulated wind turbines.

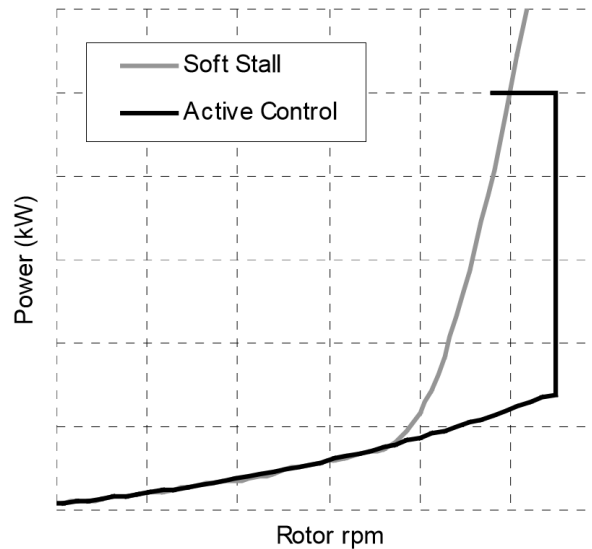


FIGURE 4: COMPARISON OF ACTIVE CONTROL AND SOFT STALL CONTROL STRATEGY ON STALL REGULATION (PIERCE AND MIGLIORE, 2000)

Figure 4 compares different control methods for a variable speed stall-regulated wind turbine. In the active control method, the turbine follows the trajectory of the maximum power curve over the widest possible range of rotor rotational speed. Thereafter, the turbine is forced to operate at constant speed until reaching the maximum power. Upon reaching the maximum power, the turbine operates at reduced rotor speed. This method is called active control, in which the rotational speed of the rotor is limited not to exceed the maximum rotor speed. The second approach is the soft-stall method. In this method, the turbine deviates from the maximum power curve a little earlier. The power and rotor speed in full load regions are controlled by adding more torque or power to the actual maximum power of the turbine (Pierce and Migliore, 2000). Muljadi et al. (2000b) investigated the feasibility of the soft stall approach and compared the results with those of fixed-speed fixed-pitch wind turbine. It was found that the drivetrain fatigue loads are apparently reduced for variable-speed operation in comparison to constant-speed operation because of the aerodynamic balance improved in the control system. In comparison with the active control method, the soft stall method seems more conservative, but its major advantage is that it needs no aerodynamically active control device like blade tip brake to limit the rotor speed and power output (Muljadi et al., 2000b). Soft stall approach is applied in this study due to its simplicity.

There are also some studies (Bossanyi, 2000; Hoffmann, 2002) in which the optimum rotor speed is tracked with the assistance of Proportional-Integral (PI) in speed loop or torque loop or power loop. Details about tuning parameters of PI controller are described in Bossanyi (2000). Hoffmann (2002) estimated the aerodynamic torque using torque observer assisted

with PI controller. The aerodynamic torques are filtered with a low-pass filter, in which turbine inertia and generator are considered. The power regulation developed in his study consists of two controllers: power controller and speed controller. The power controller provides the reference rotor speed for the speed controller and the speed controller provides the reference rotor torque. In his method, the power and rotor speed are limited not to exceed the maximum value based on wind speeds. Thereby, the operating regions are divided into three parts with predefined referenced power: below-rated region, transition regions, and above-rated regions respectively. The power deviation in the system is calculated depending on the pilot rotor power and power reference. This is fed into the power controller of the PI type. It is stated in (Hoffmann, 2002) that the integral part of the controller should be limited to prevent steady-state errors, which otherwise can cause the controller to drift away from the set point. In addition, the entire speed controller should be limited not to request very high rotor speed which otherwise can lead to system failures. The speed controller is a simple P-type in which the observed aerodynamic torque is fed back directly into the speed controller. Finally, the larger of the two torque values is selected as the actual generator torque. The actual generator torque should be limited to the allowed maximum generator torque to prevent overspeed.

Some studies (Ekelund, 1994; Bianchi et al., 2005; Bianchi et al., 2006) also applied more sophisticated methods like Linear Quadric (LQ), Linear Parameter Varying (LPV), and Linear Quadratic Gaussian (LQG) to track the optimum rotor speed. In the study by Ekelund (1994), a simple linear quadric (LQ) control design was proposed for a fixed-pitch variable-speed stall regulated wind turbine. In his study, a cascade control with an outer power controller and an inner speed controller was proposed, in which the generator power is directly fed back to the plant. According to his finding, this type of controller provides strong stability to variation in torque parameters and is significantly better than a traditional Proportional-Integral (PI)-controller at high wind speeds because it can minimize large load variations in high winds. Bianchi et al. (2005) applied LPV gain-schedule control design using linearized models. The optimal rotor speed is tracked through the torque or speed control loop algorithms in which an effective wind speed is estimated by the Kalman filter. They have also addressed the issues related to wind speed dependent controllers. Obtaining the wind speed measurement by the anemometer is inaccurate due to the delay between measured wind speed and actual wind speed experienced by the blades. Therefore, they proposed an aerodynamic torque observer in which the wind speed is estimated using the Kalman filter. This method enables to include explicitly the stochastic nature of wind speed. Bourlis (2011) proposed a feedback control system for a variable speed stall regulated wind turbine. In his study, an adaptive Kalman filter is applied to estimate the aerodynamic torque. A Newton-Raphson method is used to derive the effective wind speed from the aerodynamic torque. Hence, the referenced speed is estimated based on the effective wind speed. To take the nonlinear dynamics of the wind

turbine into account, a gain scheduled controller consisting of PI or H-Infinity was applied in his study.

2.2 FLOATING SUBSTRUCTURE CONCEPTS, MODELLING, STANDARDS AND GUIDELINES

The following sections review different configurations of floating substructure used in FOWT industries and their concepts which have been explored to date. Then, modelling and simulation tools for floating offshore wind turbines and applicable standards and guidelines for the load analyse of floating offshore wind turbines will be presented.

When exposed to combined wind and wave loads, the rotational and translational movement of a floating platform is analogue to a ship's movement as shown in Figure 5a. Thus, the rigid body motions of the floating platform can be described as surge, sway, heave, roll, pitch and yaw. The stability of a floating platform depends on the development of righting moment when the centre of gravity (COG) and centre of buoyancy (COB) are no longer aligned vertically (Journée and Pinkster, 1997). Figure 5b-d depict forces acting on the floating platform in static equilibrium conditions. Once the COB shifts from the vertical alignment due to an external load, the platform will translate about its COG, which is denoted as S_k in figures. The righting moment created by buoyancy should be able to restore to an equilibrium position from a tilted position. The location of centre of gravity with respect to the metacentre M has a significant effect on the righting arm, which is the distance between S_k and M in figures, and the ability of the platform to restore to an equilibrium position from a tilted position.

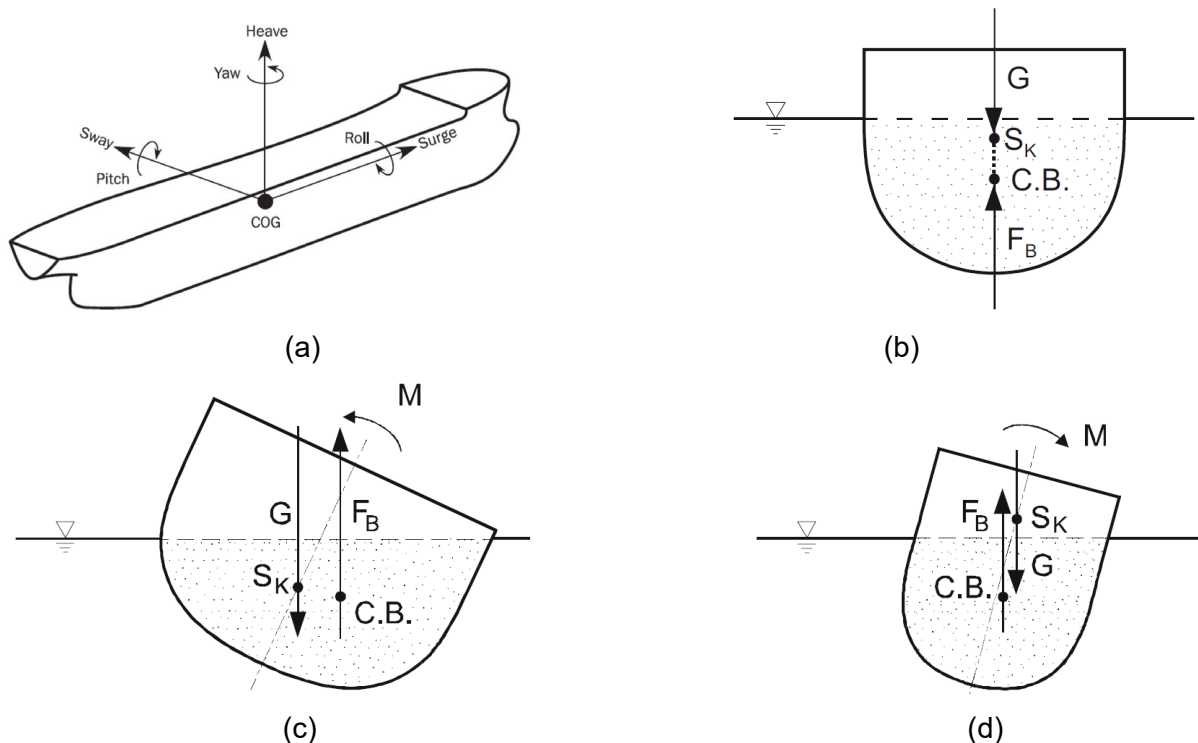


FIGURE 5: RIGID BODY MOTION OF A SHIP (A) (DNVGL-CG-0130, 2018), FLOATING BODIES IN STABLE CONDITIONS (B,C) AND UNSTABLE CONDITION (D) (JIRKA, 2007)

The substructure design of FOWT principally differs from each other depending on how the stability is achieved. When the wind turbine is in operating conditions, the rotor thrust generates an overturning moment. This overturning moment is eventually transmitted to the sea bed through the substructure, i.e., the floater and the mooring system. Therefore, the substructure needs to be designed to provide sufficient stability to counteract the overturning moment while keeping the possible floater motion within acceptable limits. To date, there are different types of floating substructure concepts at various stages of development. According to Butterfield et al. (2007), the most commonly used foundation concepts are spar buoy, tension leg platform, and semisubmersible platform. They differ from each other depending on the stabilization systems namely ballast-stabilized, buoyancy-stabilized, and mooring line-stabilized system. The suitable foundation type is chosen depending on several boundary conditions like water depth, technical viability, ecological impacts, and economical constraints. A comparative summary of the FOWT design challenges along with their advantages and disadvantages have been provided in (Butterfield et al., 2007).



FIGURE 6: FLOATING OFFSHORE WIND TURBINE SUBSTRUCTURE CONCEPTS (GRAPHIC BY JOSH BAUER, NREL)

2.2.1 SPAR

Spar floaters achieve stability through a mass-based righting moment. They are designed like spar buoys with a long cylindrical caisson and a relatively small waterplane area (Atcheson et al., 2016). Commonly, the cylinder is ballasted with water or gravels. Usually, they have a deep draft and the draft is larger or at least equal to the hub height so that the centre of gravity lies well below the centre of buoyancy. This means that the stability of the floater mainly relies on gravity and heave motion is thus minimized. Since the waterplane area contribution to stability is considerably reduced, it is more sensitive to pitch and roll motions. The floater is usually anchored to the seabed by taut or catenary mooring lines. Spar floaters are advantageous particularly for the deep-water sea, enabling access to deep-water wind resources located along the coastline like the Atlantic coast. Other advantages are simple technology with minimum requirements for welding, excellent stability of substructure, and know-how experiences in the oil and gas industry. Their shortcoming is that the assembly of the spar wind turbine in shallow water is not possible, special attention has to be paid to fatigue loads in tower and blades due to the large weight and size of the substructure. Furthermore, their nature of large draft makes towing back to the port for repairs and maintenance difficult.

An example of a spar floater support structure for offshore wind turbines is the Hywind floating wind turbine concept developed by Statoil (now Equinor). Hywind Spar was designed to be capable of supporting a 2-10 MW wind turbine in water depths from 100 m to 700 m. In 2009, Hywind Demo has put into a test operation about 10 km off the island of Karmøy in Norway (Bratland, 2009). It was the first full-scale spar floating wind turbine. In 2017, a Hywind Scotland wind farm comprised of five 6 MW wind turbines atop spar floater was commissioned. It is

located 30 kilometres off the coast of Scotland (Carbon Trust, 2015). Hywind Tampen wind farm with a capacity of 88 MW is scheduled to operate in the third quarter of 2022. Located approximately 140 km off the Norwegian coast, it will be the first floating offshore wind farm specifically designed for supplying renewable energy to offshore oil and gas platforms (Equinor, 2021).

2.2.2 TENSION LEG PLATFORM

Tension leg platforms (TLPs) achieve stability mainly from the tension in the mooring lines (Butterfield et al., 2007). Usually, TLPs consist of one or more slender cylindrical buoys and are attached to taut mooring lines that are loaded in tension (Atcheson et al., 2016). The pre-tensioned tethers are anchored to the sea bed using gravity-based foundations or suction buckets or pile-driven anchors so that sufficient tension is generated in the mooring lines. Because the mooring lines are designed to be rigid in the axial direction, the heave, roll, and pitch motion are relatively small. On the other hand, the surge, sway, and yaw motion might be significant due to the forces arising from the inclination of the mooring lines. TLPs have a relatively less dynamic response to wave in comparison with spar buoy and semi-submersible floaters. Although TLPs seem to have the minimum amount of physical footprint, they require a complex mooring system mainly for the deployment sites where the tidal variations are high. Moreover, there are also operational risks if tension loses in one or more tethers. TLPs are deployable across a wide range of water depth from 45 m to 350 m. They can be fully assembled onshore and towed to the offshore site. During the installation process, they often require special offshore vessels since they are vulnerable to inherent instability during tow-out. Like spar floaters, towing back to port for repairs and maintenance can be costly.

To date, various concepts of TLP types have been developed such as PelaStar by Glosten, Blue H TLP by Blue H Group, GICON-SOF by GICON, PivotBuoy by X1 Wind, and SBM Offshore Wind Floater by SBM Offshore. The first full-scale prototype of Blue H TLP with an 80 kW wind turbine has been installed off the coast of Italy in 2008 (Bastick, 2009). GICON-SOF has been carried out a series of tank tests to optimize the design (Carbon Trust, 2015). The PivotBuoy concept has been model tested in the lab at 1:64 and 1:50 scales. The 1:3 scale prototype of PivotBuoy with a 200 kW downwind turbine is planning to be installed at PLOCAN test site in the Canary Islands (X1 Wind, 2021). SBM Offshore Wind Floater has been issued Approval in Principle (AIP) by classification society American Bureau of Shipping (ABS). SBM Offshore Wind Floater with an 8 MW wind turbine has been planning to install off southern France (SBM Offshore, 2019).

2.2.3 SEMI-SUBMERSIBLE

Semi-submersible platforms achieve stability mainly by large waterplane area moment of inertia (Butterfield et al., 2007). The submerged part of the structure mainly provides the

necessary buoyancy for the entire system. They are typically truss-type structures consisting of three or more vertical cylindrical columns connected to each other by tubular members, see, e.g., WindFLOAT by Roddier et al. (2009, 2010) and OC4 semi-submersible platform by NREL (Robertson et al., 2014) or by pontoons, see, e.g., Karimirad and Michailides (2015). To some extent, the stability is enhanced by adding the ballast in the columns, or drag-augmenting devices like heave plates and pontoon which are typically installed at the base of the columns. This arrangement enhances the vortex shedding process due to increased sharp edges, as well as increases the effective vertical mass of the structure, consequently changes the hydrodynamic properties by introducing extra damping and added mass (Tao and Dray, 2008). In operating conditions, the hydrodynamic performance of the semi-submersible FOWT can be affected by heave, pitch and roll movements caused by wind and wave loads. With pontoons or heave plates, the heave, roll, and pitch motion can be significantly alleviated.

Generally, the semi-submersible floating wind turbine is kept in position by catenary mooring lines. Each catenary line is composed of four parts: anchor, part of catenary laying on the seabed, part of catenary suspended in the seawater, and fairlead. The fairlead is installed in the semi-submersible and the anchor holds its position on the seabed. In operating conditions, the platform drifts away from the equilibrium position until the tension forces in the mooring line rise to keep the platform in station. Thus, the restoring forces resulted from the weight of the mooring restrain the surge, sway, and yaw motions to be within the acceptable ranges.

One of the major advantages of semi-submersible platforms is the wide area resulting from the structural configuration. This ensures the shallow draft and site flexibility when it comes to water depth. Another advantage is that they can be fully assembled onshore and transported to the site by simple tug vessels (Atcheson et al., 2016). This makes the installation under rough sea conditions more adaptable in comparison with other concepts. As a result, it reduces the possible risks associated with offshore installation. The downside of this concept is the fabrication and manufacturing efforts and costs required for welded structures that are constantly exposed to cyclic loading. Joint welding can be a very complex and expensive process, and the fatigue life of joints can become a highly critical issue due to stress concentration at the joints. Another shortcoming is the requirement of mooring system design for shallow water.

One concept is the WindFloat® semisubmersible platform developed by Roddier et al. (2009). It was designed to accommodate a wind turbine of 5 MW or larger. The prototype of a 2MW WindFloat unit (WindFloat 1) was installed 5 km off the coast of Portugal in 2011 and was decommissioned in 2016. During five years of successful operation, it produced around 16 GWh of energy. WindFloat Atlantic comprised of three 8.3 MW turbine was installed 20km off the coast of Viana do Castelo, Portugal and commissioned in 2020 (Principle Power, 2020a).

WindFloat Kincardine with a capacity of 50 MW located 15 km east of Scotland in water depths of 60 m is the world's largest floating array (Principle Power, 2020b). Huijs et al. (2013) presented a concept of 5-MW GustoMSC Tri-Floater which consists of three slender, robust, and braceless columns. Experimental scale model tests were carried out in 2013 at MARIN. Another semisubmersible platform concept is OC4-DeepCWind platform which was developed for the Offshore Code Comparison Collaboration Continuation in Phase II (OC4) (Robertson et al., 2014). The platform consists of four columns a central column connected through cross braces to three offset columns. At the base of each offset column, there is a lower column with a greater diameter which technically behaves like a heave plate and increases the heave added mass and damping. The platform is moored by three catenary lines with an offset of 120° from each other. Luan et al. (2016, 2017) presented a concept design of 5-MW-CSC which is different from the former ones in that the central column is connected through pontoons, instead of braces, to three offset columns. The structural complexity especially joint welding is thus reduced in this concept. The symmetrically distributed pontoons serve to provide not only the buoyancy but also added mass and viscous damping in response to heave, roll and pitch motion. The platform is anchored to the seabed by three catenary-shaped mooring lines.

There are also multi-turbine concepts consisting of two or more turbines mounted on a single semisubmersible platform. Examples of multi-turbine concepts are SCDnezzy2 developed by Aerodyn Engineering, FLOW developed by Flowocean, and Hexicon developed by Hexicon AB (Carbon Trust, 2015).

2.3 PREVIOUS RESEARCH ON SEMISUBMERSIBLE FLOATING OFFSHORE WIND TURBINES

Many authors (Ishihara et al., 2007a, 2007b, 2009; Roddier et al., 2010; Karimirad and Michailides, 2015a, 2015b; Lemmer et al., 2020) have developed different concepts for the semisubmersible floater type and presented different methods for numerical prediction of motion responses of semisubmersible platforms. The majority of these methods is based on time-domain simulations which can predict coupled nonlinear motion responses of the floater. Some studies have validated their numerical results with experimental ones (Ishihara et al., 2009; Tao et al., 2008).

Ishihara et al. (2007a, 2007b) proposed a concept design of a semi-submersible platform that supports three wind turbines. They investigated the effect of the hydrodynamic damping and the nonlinear wave on the response of the floating structures by comparing the numerical results and experimental findings. In their numerical model, a FEM code with Morison's

equation and Srinivasan's model was developed to investigate the effects of the hydrodynamic damping and the nonlinear wave on the response of the floating structures.

Tao et al. (2008) investigated experimentally the hydrodynamic characteristics of oscillatory solid and porous disks in viscous flow at KC number range of 0.2 to 1.2 and frequencies of 0.1 Hz, 0.5 Hz, and 1.0 Hz respectively. They observed that the porosity of the disk has a significant influence on the hydrodynamic damping at low KC number whereas solid disk appeared to have the highest damping at large KC number. In contrast to hydrodynamic damping, porous disks produce a lower added mass coefficient than solid ones. The reduction of the added mass coefficient is more pronounced as porosity increases, and such a trend is more obvious at higher oscillating frequencies.

Ishihara et al. (2009) performed a series of wave tank experiments on 1:100 scale models to investigate the influence of heave plates on the dynamic response of a single wind turbine atop a semi-submersible floater. They found out that the heave plates help to shift the resonance peak to longer periods, thereby improving the heave response at rated and extreme states.

Roddier et al. (2010) performed the numerical hydrodynamic analysis of the WindFloat platform and mooring system, wave tank testing of a scale model of the platform with the simplified aerodynamic simulation of the wind turbine, and coupled simulation using FAST. Evaluations were made with a focus on the structural design of the platform in particular the coupling between the wind turbine and the platform and the interface between the hydrodynamic loading and the structural response. WindFloat platform has a movable ballast system in which water is actively pumped from one column to another to keep the axis of the wind turbine upright when wind speed and directions change significantly.

Bachynski et al. (2013) carried out coupled non-linear time-domain simulations for a semisubmersible platform for different fault cases. The results were compared with normal condition and storm conditions. They found out that the extreme wave condition has a great influence on the global platform motion and the fairlead tensions while fault conditions have an influence on the tower top and blade bending moment. More specifically, rotor imbalance loads lead to tower top bending moment, blade imbalance followed by the shutdown in near-rated conditions affects the fore-aft tower top loads and blade imbalance at higher wind speeds affects side-side tower top loads.

Karimirad and Michailides (2015a, 2015b) proposed a V-shaped braceless semisubmersible floater to support the 5-MW NREL reference wind turbine. The floater consists of three columns and the wind turbine was positioned on one of the three columns. The remaining two columns are connected to the main column by pontoons. They carried out fully integrated time-domain simulations to investigate the static and dynamic response of the system for their selected

design load cases. The response of the platform, mooring system and the controller, when subjected to wind and wave loads, are highlighted. Their findings indicated that a braceless V-shaped semisubmersible can be a feasible innovative concept for offshore wind industries.

Lemmer et al. (2020) presented a parametric design optimization procedure for a semisubmersible platform by performing coupled simulation in the Simplified Low-Order Wind Turbine (SLOW) model. They found out that the hull design of lower draft gives a significant improvement of the response of the tower-base bending and rotor fore-aft motion in harsh wind and wave conditions, thereby ultimately leading to the reduction in the fluctuation in power, rotor speed, generator torque, and blade pitch angle.

2.4 COUPLED SIMULATION METHODS AND TOOLS FOR FLOATING OFFSHORE WIND TURBINES

The evolution of offshore wind turbine design towards more flexible structures simultaneously necessitates the development of multi-physic tools and computationally efficient models that can be run quite quickly, capture the major physics in the system and compute the structural responses to derive the engineering design (Butterfield et al., 2007). Especially for floating offshore wind turbines, the loading acting on them is rather complex due to the response amplitude of a floating body, the influence of the mooring system, and wave diffraction to obtain the forces and moments of the wave and wind exciting forces on the structure. Therefore, it requires a sufficiently sophisticated tool that covers all probabilistic design situations. IEC recommended applying aeroelastic models for calculations of the effect of loads and performance in design evaluations (International Electrotechnical Commission, 2019). With aeroelastic tools, it is possible to consider all forces acting on the wind turbine namely aerodynamic forces, inertial forces, elastic forces, hydrodynamic forces, and their interaction with one another. To date, several aeroelastic tools that are capable of performing multibody simulations covering both the structural aspects and motion response of FOWT have been developed. Although the exact prediction of the response of the structure is beyond the capabilities of computer simulations, the existing software tools have managed to cope with the complexity of numerical simulation by considering a number of degrees of freedom. Some of them have been extended from existing land-based wind turbine specific tools such as OpenFAST, HAWC2, FLEX5, and Bladed while some have been adapted either from offshore structures such as SIMA or automotive, aerospace, and robotics industries such as SIMPACK, ADAMS.

OpenFAST is an improved version of FAST (fatigue, aerodynamics, structures, and turbulence) which is an open-source aeroelastic Computer-Aided Engineering (CAE) tool developed by NREL and mostly by Jonkman (2007) to simulate the nonlinear coupled dynamic

response of onshore and offshore wind turbines in the time domain. It is possible in OpenFAST to simulate wind turbines with two or three blades, pitch or stall regulation, upwind or downwind rotor, teetering or rigid hub, lattice or tabular tower, and fixed or floating substructures. OpenFAST encompasses five categories: structural dynamics (ElastoDyn, BeamDyn), aerodynamics (AeroDyn), control system (ServoDyn), hydrodynamics (HydroDyn), and mooring dynamics (MoorDyn) or mooring analysis program (MAP++). Most of them namely BeamDyn, AeroDyn, HydroDyn, MoorDyn, and MAP++ can be run as either a standalone driver or an integrated tool.

Structural representation is based on a combined modal and multibody system dynamics (MBS) formulation which considers the elasticity of the tower and rotor together with the elastic coupling between their motions and the motion of the support floater. It uses both rigid and flexible bodies. Nacelle, hub, floater, and ground are modelled as rigid bodies since they are influenced by rigid body motions whereas tower, drivetrain, and blades are modelled as flexible bodies to account for elastic deformations. ServoDyn includes the control options such as the controller logic, sensors, and actuators of the blade-pitch, generator-torque, nacelle-yaw, and other user-defined and built-in electrical drives such as the generator and power converter. AeroDyn (Jonkman et al., 2015) computes aerodynamic loads acting on the blades using quasi-steady BEM theory or a generalized dynamic wake inflow model. It is also possible to take into account tip and hub losses using Prandtl and skewed-wake corrections. Transient aerodynamics caused by the turbulent nature of wind can be taken into account using dynamic stall models like the Beddoes-Leishman model and dynamic inflow models. HydroDyn (Jonkman et al., 2014) models regular or irregular sea states and computes hydrodynamic loads acting on the submerged part of the substructure using either linear potential flow solution or Morison's equation, in which wave kinematics parameters are defined using Airy wave theory with free-surface corrections. The frequency-dependent hydrodynamic parameters such as added mass, damping, linearized hydrodynamic radiation, and diffraction are calculated using WAMIT (Wave Analysis at Massachusetts Institute of Technology).

The nonlinear restoring forces of the mooring system can be calculated using a quasi-static mooring analysis program (MAP++) by Masciola (2015) or MoorDyn by Hall (2015). MAP++ models mooring lines as multisegmented mooring lines represented by nodes and elements. The model accounts for the distributed cable mass, elasticity, geometric nonlinearities, and seabed friction. Hence, the effective forces acting on the mooring lines at static equilibrium are computed, but it ignores bending, torsion, inertial forces, and hydrodynamic forces. In contrast, it is possible to take structural dynamic and hydrodynamic forces acting on the mooring lines into account using MoorDyn which uses a simple lumped-mass formulation. The latest version of MoorDyn allows for simulating shared-mooring array between platforms (Hall, 2020) along

with considering synthetic fibre mooring lines and ballast or buoyancy bodies on the mooring line. The aero-hydro-servo-elastic capabilities of OpenFAST have been successfully verified and validated in multiples studies, for example, (Stewart et al., 2012; Robertson et al., 2017; Popko et al., 2021).

HAWC2 (Horizontal Axis Wind turbine simulation Code 2nd generation) (DTU Wind Energy 2021) developed by DTU Wind Energy is one of the most widely used aeroelastic codes in research and industries for both design and verification process of onshore and offshore wind turbines. It is the new version of HAWC which was initially developed by Riso-DTU and has been enhanced with some features related to the design and simulation of large multi-megawatt offshore wind turbines. The aerodynamic loads are calculated basically using blade element momentum theory (BEM). There are also possibilities to account for dynamic inflow, skew inflow, the shear effect on induction, the effect from large blade deflections, tip loss, and different 3D-stall. The structural representation of HWAC2 is based on multibody formulation, which enables a wide range of model capabilities and is also particularly well suited for calculations on very flexible turbines subjected to, for instance, large blade deflections.

SIMA is a time-domain commercial simulation program developed by SINTEF Ocean (formerly MARINTEK) and Equinor (SINTEF, 2021). It consists of two modules namely SIMO (Simulation of Marine Operation) and RIFLEX which can be run either independently of each other or together. SIMO is designed to compute hydrodynamic loads, motion response, and station keeping of floating structures in the time domain whereas RIFLEX is designed for static and dynamic responses of slender marine structure using nonlinear finite-element which enables modelling the nonlinearities and large deflections. SIMO uses Multibody System (MBS) for structural modeling. For computing hydrodynamic loads, it considers linear potential forces, whereby the frequency-dependent excitation, added mass, and damping contributions are solved in the frequency domain using WAMIT, and Morison formulation for slender members. Mooring forces can be calculated using the quasi-static method or fully finite element method, considering material nonlinearity and dynamic properties. The aerodynamics forces are calculated using BEM theory considering dynamic-inflow effects, dynamic stall effects.

SIMPACK Wind, a special version of SIMPACK for wind turbines developed by SIMPACK AG, is a validated commercial multi-body simulation tool that can be used to run a fully coupled wind turbine load simulation. In SIMPACK, the parts of the wind turbine model are connected by complex joints. The code models flexible bodies such as gear tooth, mooring system by a beam, or modally reduced flexible finite element approach to account for the effect of flexible deformations on the global motion of the FOWT. Aerodynamic loads can be computed by interfacing with NREL's software package AeroDyn aerodynamic module or AeroModule

developed by ECN. Hydrodynamic loads are computed by coupling to the HydroDyn hydrodynamic module developed by NREL. The nonlinear restoring forces acting on the mooring lines can be calculated using either the quasi-static approach or the MBS approach. The latter allows modeling an integrated wind turbine-floater system with high fidelity.

ADAMS (Automatic Dynamic Analysis of Mechanical Systems) is a commercial MBS code developed by MSC Software Corporation. Like SIMPACK, the code is mostly used by the automotive, aerospace, and robotics industries. Structural representation in ADAMS is based on MBS that permits many structural degrees of freedom to be taken into account. The wind turbine blades and tower are modelled based on lumped-mass formulation and the bodies are connected by flexible joints with linear stiffness and damping. Aerodynamic loads are calculated by coupling to the AeroDyn aerodynamic module by NREL. Hydrodynamic loads are calculated by coupling to HydroDyn hydrodynamic module by NREL or other user-defined external subroutines. The nonlinear restoring forces from the mooring lines can be calculated by a quasi-static approach or by a simple look-up table specifying the relationship between the restoring force and platform displacement. Similar to FAST code, it is possible in the ADAMS code to model the mooring system. This can be done by interfacing with a separate module, in which mooring line tensions are computed quasi-statically at each time step. Alternatively, it is also possible to use a look-up table which is characterized by the relationship between restoring force and platform displacement at the mooring-line interface point (Cordle and Jonkman, 2011).

All in all, each software has its own merits and shortcomings. This study applies OpenFAST simulation tool because it is open-source, user-friendly especially for researchers and designers, high-quality supports are available through documentation and NREL forum and Github, and it has been well validated against tank test data.

2.5 STANDARDS AND GUIDELINES FOR LOAD SIMULATION

In the conceptual design stage, loads analysis of a set of design load cases according to recognized standards need to be carried out to ensure that the turbine performance is favourable and the structural integrity is well maintained during its lifespan. A number of state-of-the-art design practices and recommended guidelines have been developed by national and international bodies to minimize technical risks and other factors related to costs. The International Electrotechnical Commission (IEC) 61400-3(2009) specifies the design requirements for bottom-fixed offshore wind turbines. IEC 61400-3 (2009) has been changed to IEC 61400-3-1 (2019) (International Electrotechnical Commission, 2019a) which covers bottom-fixed offshore wind turbines and extended to IEC 61400-3-2 (2019) (International Electrotechnical Commission, 2019b) to cover the design requirements for floating offshore

wind turbines. A series of load cases have been formulated, ranging from regular power production in normal environmental conditions to extreme conditions i.e., storms and failures. The design standards recommend an integrated load analysis using state-of-the-art models. Regarding site conditions, the IEC 61400-1 is applied in this study. However, it is worth mentioning that site conditions should also be considered according to standards and guidelines recommended by national bodies such as DNVGL guidelines, Maritime and Hydrographic Agency of Germany (BSH) guidelines for offshore wind turbine installation in Germany, and ABS guidelines for installations in North America.

3 BASIC DESIGN OF CART

This chapter describes the design and development of the CART wind turbine, support structure, substructure, control concept, environmental conditions at the reference site used in this study. CART model implementation in OpenFAST is also explained briefly and the simulation results of the basic design are evaluated and discussed.

CART named after the CART project (Compact And Robust Medium-Sized Wind Turbine) aims to develop a medium-sized wind turbine in the power range of around 100kW to 200kW in cooperation with several German companies, the Chair for Wind Energy Technology the University of Rostock, the Vietnam National University and several companies in Vietnam. The principle of CART concept is an integration of a horizontal axis wind turbine and stall regulation with a floating substructure solution. Figure 7 gives an impression of what CART wind turbine and its logistic concept would look like (Adam et al., 2019). The advantages brought about by the CART concept is:

- The structural design is simple and robust through the application of modular structures
- Stall regulation will reduce system complexity like pitch system
- RNA is simple and cheap due to its direct-drive unit with a permanent magnet generator
- No loss of transmission as well as grid stability is ensured by decentralized mini-grids
- Transportation and maintenance cost shall be significantly low
- Levelized cost of energy (LCOE) shall be low
- Applicable for many areas such as remote islands and villages, residential and resorts for decentralized supply of electricity, off-grid solutions, etc.

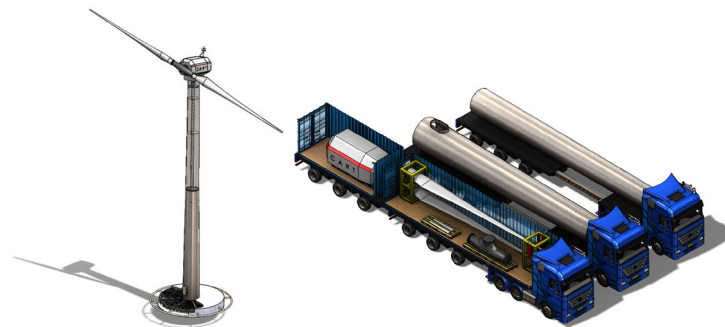


FIGURE 7: CART SYSTEM (LEFT) AND IMPRESSION OF ITS LOGISTIC CONCEPT (RIGHT) (ADAM ET AL., 2019)

3.1 CART WT TOWER PROPERTIES

The tower design was carried out within the framework of the CART project. Like most developed tower designs, the tower is a tapered unstiffened cylindrical tube with linearly increasing diameter and wall thickness from tower top to tower bottom. The tower height, which largely depends on the characteristics of the installation site, was chosen as 27.8 m and was

designed to support a 120-150 kW wind turbine with a top mass of about 3000 kg (Adam et al., 2019). For offshore deployment, it is connected to the tower column (TC) of the semisubmersible floater through bolted or welded flange connection. The base of the tower is located 2.4 m above mean sea level (MSL) and the platform level is also located at the same height of 2.4 m above MSL. By considering 1 m vertical offset of the nacelle, the tower hub height results in 31.2 m above MSL. The tower material is chosen to be steel with a minimum yield strength of 355 MPa, the Young's modulus of 210 GPa, and the shear modulus of 80.08 GPa. To take into account secondary steel parts that are not covered by tower thickness data, the density of steel was assumed to be 8500 kg/m³. The tower integrated mass is about 21853 kg. Table 1 summarizes distributed structural properties of the tower which are based on tower bottom diameter of 2 m with wall thickness 20 mm and tower top diameter of 1.32 m with wall thickness of 12 mm. Elev refers to the vertical locations along the tower centreline relative to the tower bottom. HtFract refers to the fractional height along the tower centreline from the tower bottom (0.0) to the tower top (1.0). TMassDen refers to the distributed tower section mass per unit length. TwFAStif, TwSSStif, TwGJStiff, TwEASTif, TwFAlner, TwSSIner refer to tower section fore-aft stiffness, side-to-side stiffness, torsional stiffness, fore-aft mass inertia per unit length, and side-to-side mass inertia per unit length respectively.

Table 2 briefly lists undistributed tower properties.

TABLE 1: DISTRIBUTED TOWER PROPERTIES

| Elev [m] | HtFr [-] | TMassDen [kg/m] | TwFAStif [N-m ²] | TwSSStif [N-m ²] | TwGJStiff [N-m ²] | TwEASTif [N] | TwFAlner [kg-m] | TwSSIner [kg-m] |
|-------------|-------------|--------------------|---------------------------------|---------------------------------|----------------------------------|-----------------|--------------------|--------------------|
| 2.40 | 0 | 1057.46 | 1.28E+10 | 1.28E+10 | 9.85E+09 | 5.03E+09 | 1036.5 | 1036.5 |
| 5.18 | 0.1 | 1021.14 | 1.15E+10 | 1.15E+10 | 8.87E+09 | 4.85E+09 | 933.4 | 933.4 |
| 7.96 | 0.2 | 984.83 | 1.03E+10 | 1.03E+10 | 7.96E+09 | 4.68E+09 | 837.3 | 837.3 |
| 10.74 | 0.3 | 948.51 | 9.24E+09 | 9.24E+09 | 7.11E+09 | 4.51E+09 | 748.0 | 748.0 |
| 13.52 | 0.4 | 912.19 | 8.22E+09 | 8.22E+09 | 6.32E+09 | 4.34E+09 | 665.4 | 665.4 |
| 16.30 | 0.5 | 789.25 | 6.57E+09 | 6.57E+09 | 5.06E+09 | 3.75E+09 | 532.1 | 532.1 |
| 19.08 | 0.6 | 756.56 | 5.79E+09 | 5.79E+09 | 4.45E+09 | 3.60E+09 | 468.7 | 468.7 |
| 21.86 | 0.7 | 723.88 | 5.07E+09 | 5.07E+09 | 3.90E+09 | 3.44E+09 | 410.5 | 410.5 |
| 24.64 | 0.8 | 615.25 | 3.94E+09 | 3.94E+09 | 3.03E+09 | 2.92E+09 | 319.0 | 319.0 |
| 27.42 | 0.9 | 440.93 | 2.58E+09 | 2.58E+09 | 1.98E+09 | 2.10E+09 | 208.7 | 208.7 |
| 30.20 | 1 | 419.14 | 2.22E+09 | 2.22E+09 | 1.70E+09 | 1.99E+09 | 179.3 | 179.3 |

TABLE 2: UNDRISTRIBUTED TOWER PROPERTIES

| | |
|---|------------|
| Elevation to Tower Base (Platform Top) Above SWL | 2.4 [m] |
| Elevation to Tower Top (Yaw Bearing) Above SWL | 30.2 [m] |
| Overall (Integrated) Tower Mass | 21853 [kg] |
| CM Location of Tower Above SWL Along Tower Centreline | 16.68 [m] |

3.2 ROTOR-NACELLE ASSEMBLY DESIGN

The rotor nacelle assembly was designed within the framework of the CART project. The nacelle design is based on a direct-drive concept that requires fewer components and reduces system complexity while ensuring high reliability. Especially for offshore deployment, the direct-drive solution can offer a significant advantage of reduced maintenance requirements. The direct-drive generator considered for this study is a permanent magnet generator (PMSG) with a rated generator speed of 43 rpm and rated power of 130 kW. The nacelle consists of: yaw system, main bearing, machine bed, mainframe, generator stator, generator rotor, hub, and rotor blades.

TABLE 3: DRIVETRAIN PROPERTIES

| | |
|---------------------------------|----------------------------|
| Rated Generator Speed | 43 [rpm] |
| Electrical Generator Efficiency | 97 [%] |
| Generator Inertia | 181 [kg.m ²] |
| Rotor Inertia | 44123 [kg.m ²] |

Above Table 3 summarizes the drivetrain properties of CART machine. The drivetrain has a tilt angle of 5°. This leads to the distance directed along the shaft from the hub centre to the yaw axis 2.24 m and the vertical distance along the yaw axis from the tower top to the shaft 1.15 m. Following Jonkman et al. (2009), the natural frequency of the nacelle-yaw actuator was assumed to be 11 Hz, which roughly equals the highest full-system natural frequency in the OpenFAST model. Assuming a damping ratio of 2 % critical, an equivalent nacelle-yaw-actuator linear-spring constant of 2.00E+08 N-m/rad and an equivalent nacelle-yaw-actuator linear-damping constant of 1.16E+05 N-m/(rad/s) has resulted. The nominal nacelle-yaw rate was assumed to be the same as that for the AWT-27 wind turbine FAST model. In Table 4, the properties of the nacelle and hub are summarized.

TABLE 4: NACELLE AND HUB PROPERTIES

| | |
|--|---------------------------|
| Elevation of Yaw Bearing above MSL | 30.2 [m] |
| Vertical Distance along Yaw Axis from Yaw Bearing to Shaft | 1.15 [m] |
| Distance along Shaft from Hub Center to Yaw Axis | 2.24 [m] |
| Hub Mass | 1346 [kg] |
| Hub Inertia about Low-Speed Shaft | 988 [kg.m ²] |
| Nacelle Mass | 3521 [kg] |
| Nacelle Inertia about Yaw Axis | 4275 [kg.m ²] |
| Nacelle CM Location Downwind of Yaw Axis | 0.39 [m] |
| Nacelle CM Location above Yaw Bearing | 0.76 [m] |

| | |
|---|-------------------------|
| Natural frequency of nacelle-yaw actuator | 11 [Hz] |
| Damping ratio | 2 % critical |
| Equivalent Nacelle-Yaw-Actuator Linear-Spring Constant | 2.00E+08 [N-m/rad] |
| Equivalent Nacelle-Yaw-Actuator Linear-Damping Constant | 1.16E+05 [N-m/(rad/s)] |
| Nominal Nacelle-Yaw Rate | 2 [°/s] |

3.3 SUBSTRUCTURE DESIGN

For FOWT, the substructure is one of the major cost-driving parameters. Preliminary substructure design and final design study were performed by Schröter (Schröter, 2018) within the framework of his master thesis and Adam et al. (2019). Pre-design study of the floater included the choice of suitable substructure type, pre-dimensioning of the substructure, and hydrostatic stability check in terms of righting moment and heeling moment. By taking into account the technical and economic feasibility of the system at the potential installation site, a semisubmersible floater was pre-designed for the offshore deployment of the CART system. Based on the pre-design, the final design of the substructure was refined by taking into account the dynamic wave loadings acting on the substructure in addition to wind loadings. For hydrodynamic modelling, it used ANSYS Aqua as a pre-processor to compute wave interaction effects using potential flow theory. It did not take into account the viscous forces due to vortex shedding around the substructure. The parameters of the floater such as diameter, wall thickness, and stiffeners were adjusted until the functional requirements such as the necessary floating stability and motion characteristics are achieved. Besides floating stability, structural stability analyses were carried out using ANSYS Mechanical APDL to check if the stresses are within the allowable stress range. Parameters of the floater were further adjusted to ensure that the stresses are within safe limits. In fact, the design spiral involved quite a lot of work and multiple refinements. For more information about substructure design development, the author would recommend studying (Schröter, 2018; Adam et al., 2019).

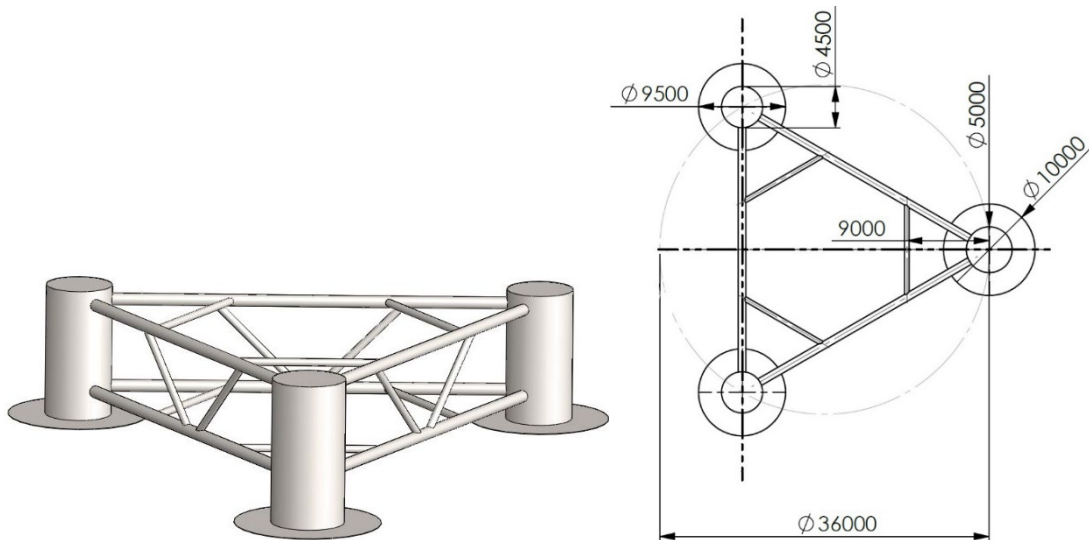


FIGURE 8: 3D IMPRESSION (LEFT) AND PLAN (RIGHT) OF THE CART FLOATER (LEFT) (SCHRÖTER, 2018)

A 3D impression of the CART floater and its plan view is provided in Figure 8. The floater consists of three columns: the largest one is the tower column, where the tower is attached, and the other two columns of the same size are offset columns. Each column is located at a radius of 18 m from the centre of the floater and arranged with an angular distance of 120° from each other. The columns are connected to each other with main horizontal braces. The vertical diagonal bracing between main horizontal braces provides vertical stiffness and horizontal diagonal bracing between main horizontal braces provides horizontal stiffness to resist the lateral loads from wind and wave. The tower column is 10 m high and the height of offset columns is 9 m. The floater has a draft of 7.6 m and this left 2.4 m of freeboard. Heave plates are installed at the bottom of each column in order to reduce heave, pitch, and roll motions. The geometric properties of the floater are summarized in Table 5 and the structural properties of the floater are summarized in Table 6.

TABLE 5: GEOMETRIC PROPERTIES OF THE FLOATER

| | |
|--|---------|
| Diameter of tower column | 5 [m] |
| Diameter of offset column | 4.5 [m] |
| Diameter of main brace | 0.8 [m] |
| Diameter of vertical diagonal brace | 0.5 [m] |
| Diameter of horizontal brace | 0.5 [m] |
| Diameter of heave plate of tower column | 10 [m] |
| Diameter of heave plate of offset column | 9.5 [m] |
| Thickness of heave plates | 40 [mm] |
| Wall thickness of tower column | 40 [mm] |
| Wall thickness of offset columns | 40 [mm] |
| Wall thickness of main brace | 35 [mm] |

| | |
|---|-----------|
| Wall thickness of vertical diagonal brace | 35 [mm] |
| Wall thickness of horizontal brace | 35 [mm] |
| Spacing between column | 21.68 [m] |

TABLE 6: STRUCTURAL PROPERTIES OF THE FLOATER

| | |
|---------------------------------|-------------------------------|
| Floater mass | 3.57E+05 [kg] |
| COM of floater below MSL | X: 0.62 [m]; Z: 2.70 [m] |
| Floater roll inertia about COM | 5.54E+07 [kg-m ²] |
| Floater pitch inertia about COM | 5.93E+07 [kg-m ²] |
| Floater yaw inertia about COM | 8.83E+07 [kg-m ²] |

The floater is moored to the seabed by three catenary mooring lines. The fairleads of the mooring lines are located at the bottom of the heave plates, the mooring lines lie horizontally on the seabed, and the anchors hold into the seabed at a radius of 150 m from the centre of the floater. The unstretched length of the mooring lines is 142 m for the tower column and 143 m for the offset columns. While designing the floater, the stiffness of the mooring system was carefully chosen to be sufficient to keep the horizontal offset of the floater within the safe range. Generally, the stiffness of a catenary mooring line is due to the tension in the mooring lines which depends on the weight and elasticity of the submerged part of the mooring lines. The properties of mooring systems are provided in Table 7.

TABLE 7: MOORING SYSTEM PROPERTIES

| | |
|---|------------------------|
| Number of mooring lines | 3 [-] |
| Unstretched length of mooring line (Tower Column) | 142 [m] |
| Unstretched length of mooring line (Offset Columns) | 143 [m] |
| Equivalent mooring line mass density | 120 [kg/m] |
| Mooring line tension force | 7.5E+03 [kN] |
| Equivalent mooring line extensional stiffness | 9.0E+05 [kN] |
| Cross-sectional area of mooring line | 0.01 [m ²] |

Based on the findings of hydrostatic stability test, it was observed that there is a small amount of surge and pitch motion even in the absence of wind, wave, and operating loads. This is primarily due to the overhanging weight of the rotor-nacelle assembly. Furthermore, the CART wind turbine is mounted on an asymmetric semi-submersible platform. The main column on which the CART turbine is mounted is greater than the other columns. This means that the platform centre of mass (CoM) has non-zero offset in the x and the y direction. The additional moment resulted from the non-zero offset might also affect coupled motions. As a result, pitch

and surge motions of the platform lead to small oscillation in heave direction and there is a cross-coupling between these motions.

3.4 MODEL IMPLEMENTATION IN OPENFAST

This study applies OpenFAST v2.2.0 aeroelastic software tool. This section explains modelling of CART atop semisubmersible floater in OpenFAST briefly. The aero-hydro-servo-elastic model of CART is implemented through 18 DOFs in OpenFAST, where OpenFAST main program is coupled with ElastoDyn, ServoDyn, AeroDyn, HydroDyn, and MAP++. Figure 9 illustrates the interaction between each module. The DOFs are related to platform motions (6 DOFs), first and second tower bending moments (4 DOFs), nacelle yaw motion (1 DOF), variation in generator speed (1 DOF), and blade flexibility (6 DOFs). In OpenFAST, time-marching analyses can be performed using one of three predictor-corrector scheme approaches: Runge-Kutta (RK), Adams-Bashforth (AB), and fourth-order Adams-Bashforth-Moulton (ABM4). This study applied ABM4 multi-step predictor-corrector integration method. For each time step t , OpenFAST solves the equation of motion by estimating displacements and velocities at time step $t + \Delta t$.

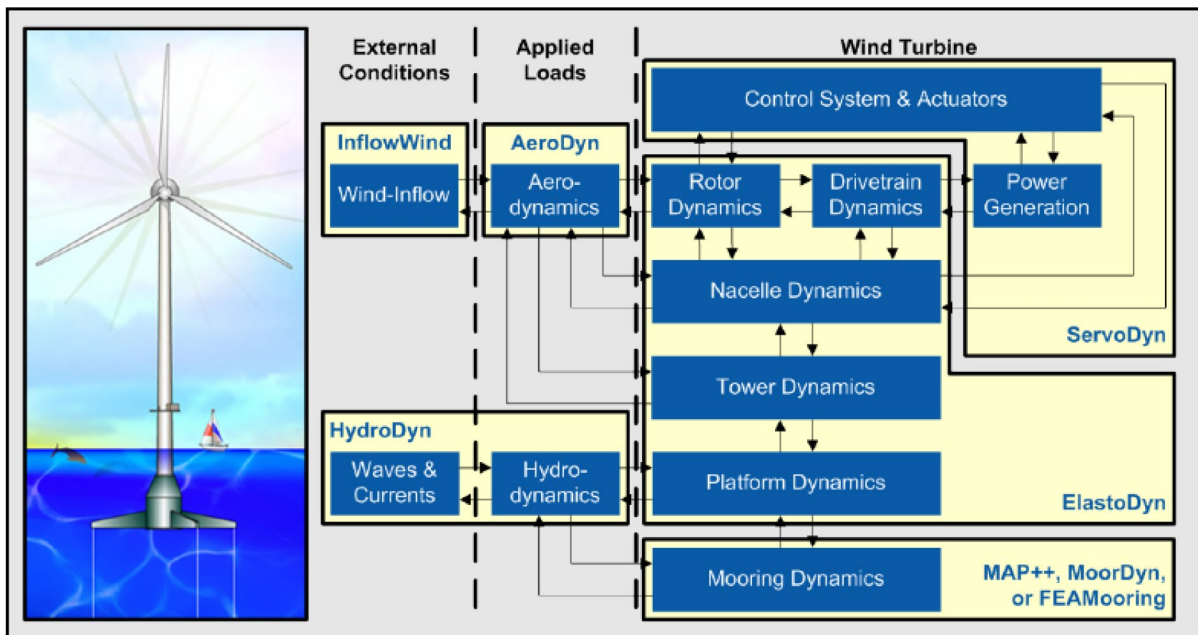


FIGURE 9: SCHEMATIC OF COUPLED AERO-HYDRO-SERVO-ELASTIC MODULES (OPENFAST, 2021)

InflowWind

InflowWind receives coordinate positions of tower and blade nodes from AeroDyn. It computes wind velocities as a function of coordinates position through interpolating wind speed time series and returns these undistributed wind velocities to AeroDyn. In this study, wind speed time series data for the stochastic wind model is generated using NREL **TurbSim** (Jonkman and Buhl, 2005) standalone pre-processor tool whereas wind speed time series data for

deterministic wind models (ECD, ECG, EOG, and EWM) are generated using NREL **IECWind** standalone pre-processor tool. In TurbSim, IEC Kaimal wind spectral model is applied to generate a full-field stochastic and turbulence wind inflows required for load simulations in this study. For this purpose, mean hub-height wind speed and turbulence intensity are specified in the TurbSim input file. CART system was designed for turbine class 1 with IEC turbulence category B indicating moderate turbulence.

AeroDyn

This study applied AeroDyn v.15 module to compute aerodynamic loads on the wind turbine blade. AeroDyn computes aerodynamic loads on the blades based on the velocities and positions provided by the ElastoDyn, ServoDyn, and InflowWind module. Then, it returns these loads to dynamic modules. In this study, a quasi-static BEM is applied to account for the influence of rotor wake via induction effect from the rotor. This model assumes that the wake reacts instantaneously to the changing flow conditions i.e the flow field around the airfoil is always in equilibrium. The Prandtl correction factors are applied to account for the hub and tip loss. Pitt/Peters skewed wake model is incorporated in this quasi-steady wake model to capture skewed inflow resulted from yaw misalignment. In reality, there is a time delay and the overrun reacts with a delay time to the change in the flow conditions. For this purpose, AeroDyn14 includes another model called the generalized dynamic wake model (GDW). However, this model applies to wind speeds above 8 m/s. If the wind speed is below 8 m/s, AeroDyn switches to the BEM method. The load analysis will be mainly based on the quasi-static BEM model. Beddoes-Leishman unsteady dynamic stall model is used to reflect the transient aerodynamics. The influence of the tower on the flow local to the blade is taken into account based on the baseline potential flow model. This model can include both a velocity deficit and a speed-up depending on where the blade is in the flow relative to the tower. The aerodynamic load on the tower is also considered by enabling TwrAero. Other options such as environmental conditions, airfoil aerodynamic properties, tower nodal properties are also assigned as defined in sections 3.1 to 3.3 and section 5.6.

ElastoDyn

ElastoDyn module computes the structural dynamics of the FOWT system. For this, ElastoDyn needs several parameters of the FOWT system such as turbine configuration (see more in Jonkman and Buhl (2005)), blade structural properties, mass and moment of inertia of the system, rotor properties, drivetrain properties, and tower structural properties. CART machine does not have teeter mechanism and also does not consider rotor furling. These structural properties of the tower and floater and turbine configuration are measured from 3D CAD models with their respective coordinate systems defined in Jonkman and Buhl (2005). The

DOFs and initial conditions of the system such as fixed pitch angle and initial displacement of the structure, if any, are also defined in ElasoDyn.

ServoDyn

ServoDyn module regulates generator torque and generator power. In this study, the torque controller is implemented by interfacing with an external dynamic-link-library (DLL), in which the variable-speed generator torque control algorithm is written and compiled as "DISCON.DLL" file. The mechanical properties of the turbine brake system and yaw system are set to the values determined in above section 3.2 and section 4.4. CART system has no yaw controller. Therefore, YCMode is set to 0. For load cases in which the turbine braking system is considered, a simple brake system is enabled by setting HSSBrMode to 1.

HydroDyn

HydroDyn receives substructure motion from the structural dynamic module (ElastoDyn) and mooring dynamic modules (MoorDyn, MAP++). It calculates hydrodynamic loads acting on the substructure and returns these loads to ElastoDyn and MAP++ or MoorDyn. Hydrodynamic loads can be computed using one of the three methods: the potential-flow theory, the strip theory, and a combination of these two methods. The hydrodynamic loads on the substructure are calculated based on Morison's equation in the present study. For Morison's approach, the geometry of strip-theory members of the floater including member properties (diameter, thickness, and drag coefficients) are specified as described in section 3.3. HydroDyn generates waves using linear wave theory. In the present study, second-order nonlinear wave loads including mean drift, slow drift, and sum-frequency terms are taken into account since they could influence the dynamic response of the semisubmersible wind turbine. JONSWAP spectrum is used to idealize the sea state for most operating conditions. Thereby, peak enhancement parameter is set to 3.3 for every sea state for simplification. Pierson-Moskowitz (PM) spectrum is used to idealize the fully developed sea state for fatigue loads calculation. For this model, peak-shape parameter is set to 1. Significant wave height and peak-spectral period of waves are assigned to the values defined in section 5.6.

MAP++

The mooring dynamic module receives hydrodynamic loads from HydroDyn and floater motions from ElastoDyn, computes the mooring line loads, and returns them to HydroDyn and ElastoDyn. This study applied NREL MAP++ module to model mooring lines. The Map++ routine is based on a multisegmented, quasi-static model to compute the mooring forces, which does not take drag and inertia forces into account, but it considers elasticity, geometric nonlinearities, and mooring line weight in the fluid. The properties of mooring lines including the position of anchors, fairleads provided in section 3.3 are assigned in the input file.

4 DEVELOPMENT OF CONTROL CONCEPT

As described in the previous section 3, the CART machine utilizes a direct-drive concept in which the rotor is directly coupled with the generator. The generator type is gearless PMSG in which the rotor speed can be varied throughout the operating regions. The following sections start with examining the aerodynamic performance of rotor blades and then explain the choice of a control concept for the CART machine and the developed control algorithm and protection system.

TABLE 8: CONTROL SYSTEM PROPERTIES

| | |
|---|-----------|
| Peak Power Coefficient | 0.44 [-] |
| Tip-Speed Ratio at Peak Power Coefficient | 9 [-] |
| Rated Mechanical Power | 144 [kW] |
| Generator efficiency | 90 [%] |
| Maximum Generator Torque | 43.2 [kN] |
| Rated rotational speed of generator | 43 [rpm] |
| Cut-in wind speed | 3.0 [m/s] |
| Rated wind speed | 15 [m/s] |
| Cut-out wind speed | 20 [m/s] |

4.1 AERODYNAMIC PROPERTIES OF THE BLADE

Rotor performance plays an important role in maximizing the power output. The aerodynamic design of blades for stall regulated wind turbine is rather complex than that for pitch regulated wind turbine. Preliminary rotor design study and choice of the blade geometry, appropriate airfoils for rotor blades were carried out within the student research work by Parlak (2017). It was concluded that the blades are made up of airfoil sections similar to those of AWT-26/27 wind turbine developed by NREL. Table 9 lists the distributed blade aerodynamic properties. Nodes refer to the node number along the blade. BISpn, BITwist, and BICHord refer to the local span of the blade node along the blade-pitch axis from the root, local aerodynamic twist angle, and local chord length respectively.

TABLE 9: DISTRIBUTED BLADE AERODYNAMIC PROPERTIES

| Nodes | BIspn [m] | BITwist [°] | BIChord [m] | Airfoil |
|-------|-----------|-------------|-------------|----------|
| 1 | 0.00 | 5.80 | 0.86 | AWT27_05 |
| 2 | 0.63 | 5.80 | 0.86 | AWT27_05 |
| 3 | 1.89 | 5.20 | 1.05 | AWT27_15 |
| 4 | 3.14 | 4.66 | 1.15 | AWT27_25 |
| 5 | 4.40 | 3.73 | 1.12 | AWT27_35 |
| 6 | 5.66 | 2.64 | 1.05 | AWT27_45 |
| 7 | 6.92 | 1.59 | 0.98 | AWT27_55 |
| 8 | 8.17 | 0.73 | 0.89 | AWT27_65 |
| 9 | 9.43 | 0.23 | 0.78 | AWT27_75 |
| 10 | 10.69 | 0.08 | 0.65 | AWT27_85 |
| 11 | 11.94 | 0.03 | 0.49 | AWT27_95 |
| 12 | 12.57 | 0.03 | 0.49 | AWT27_95 |

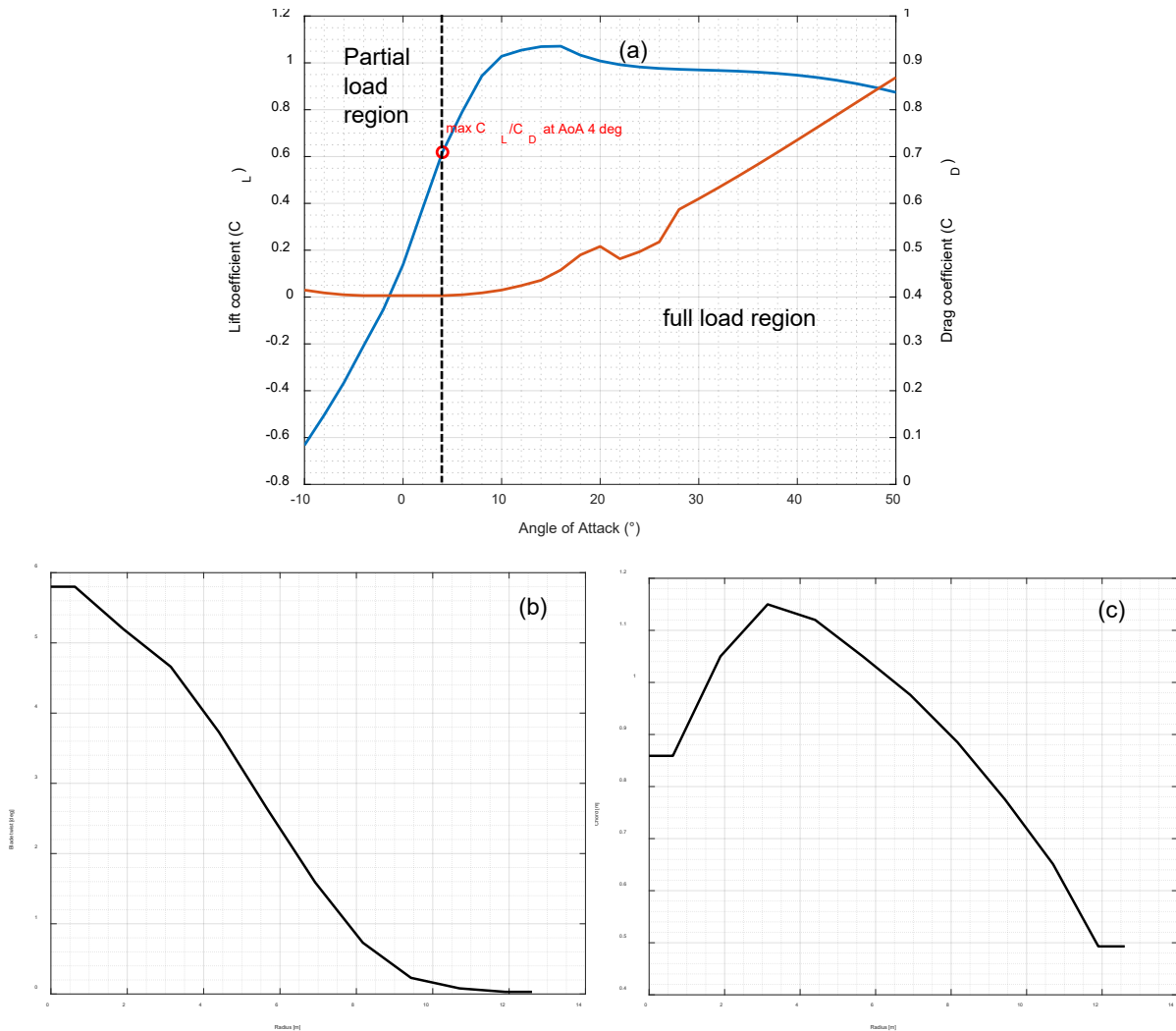


FIGURE 10: AERODYNAMIC CHARACTERISTICS OF AIRFOIL SECTION AT 75% R (A), CHORD (B) AND BLADE TWIST (C) DISTRIBUTION OF BLADE FOR CART WIND TURBINE

Figure 10a depicts the aerodynamic characteristics against variations in the angle of attack for one particular airfoil section which is at 75% of blade radius. As can be seen, the maximum lift-to-drag ratio occurs at an angle of attack of 4° . The behaviour of aerodynamic lift force is linear in the partial load region. In the full load regions where the blades are designed to stall, the drag force sharply increases as the angle of attack increases due to flow separation. In fact, the relative air velocity tends to increase from the blade root to the blade tip. For this reason, the blades are twisted in such a way that the aerofoil sections exhibit an optimal aerodynamic performance. For stall-regulated wind turbines, the blade twist angle plays a major role, especially in stall regions. The stall progression along the blade should be adjusted so that the rotational speed is kept nearly constant after stall. Figure 10b and Figure 10c illustrate the nonlinear distribution of the chord and twist angle of the blade for the CART system.

To formulate an appropriate control strategy, the aerodynamic responses of rotor blades were computed in AeroDyn standalone driver. AeroDyn is a time-domain wind turbine aerodynamic module, which can be either coupled in OpenFAST or driven as a standalone code to investigate wind turbine aerodynamic responses. The rotor power versus rotor speed curve was generated at various wind speeds as depicted Figure 11. It is evident from the power curve that the rotor speed increases continuously with the increase in wind speeds. Therefore, a control concept is necessary to ensure that the turbine operates safely under all operating modes. Figure 12 depicts the relationship between the power coefficient and tip speed ratio of the CART WT, which is often called C_p - λ curve. The maximum C_p value is achieved as 0.44 at tip speed ratio (λ) of 9.11. The rotor has a peak C_p - λ , which is why it well suits stall regulation.

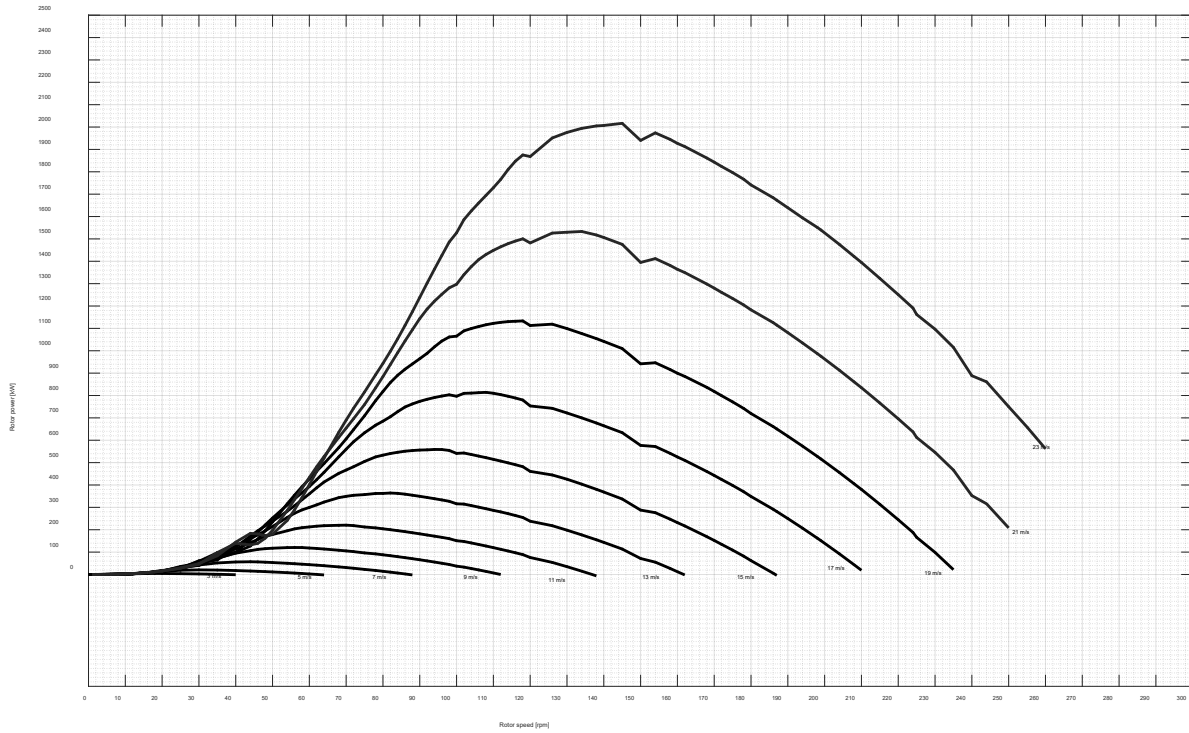


FIGURE 11: ROTOR POWER AS A FUNCTION OF ROTOR SPEED AT VARIOUS WIND SPEEDS

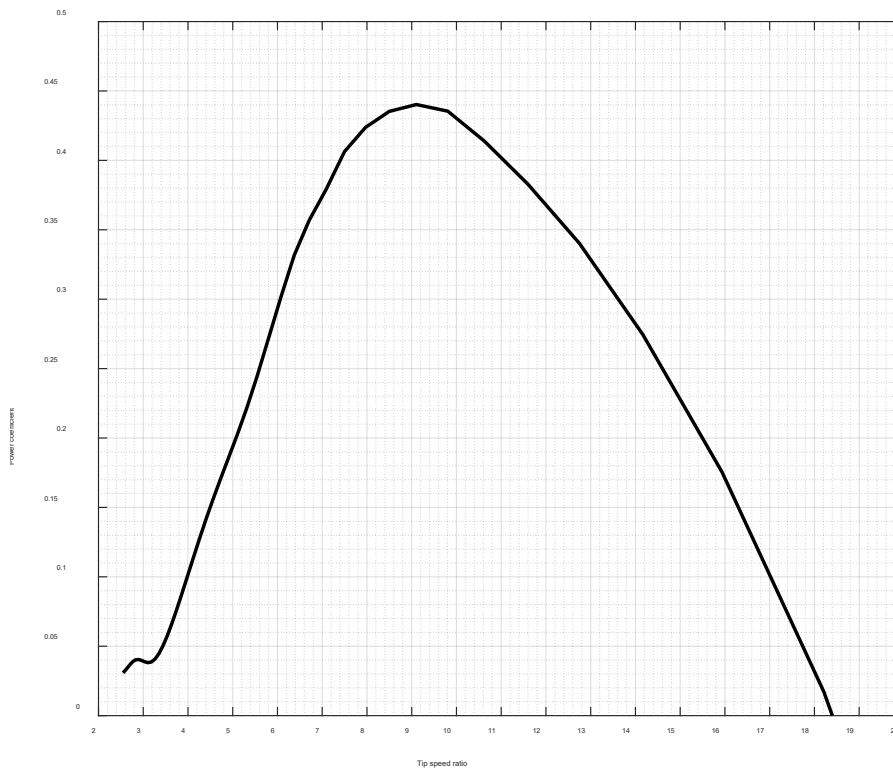


FIGURE 12: CP-λ CURVE OF CART WIND TURBINE

To implement a variable control strategy on stall regulation which is explained in section 2.1.2, it is a prerequisite to understand how the rotor torque changes with variation in rotor speed at different wind speeds. Figure 13 depicts the ideal torque-speed curve of CART. The black dotted curve represents the maximum power coefficient curve of the CART wind turbine.

Provided the generator torque control follows the $C_{p,max}$ curve in partial load region as depicted in the figure, the turbine will reach nearly its maximum allowable rotor speed of 43 rpm at the wind speed of 7 m/s. After this point, the turbine operates in the full load region and the generator torque should be deviated from the $C_{p,max}$ curve as depicted in the figure. Another generator torque control strategy is needed to ensure that the turbine operates safely in high wind speeds. In practice, it is difficult to implement a torque controller which is dependent on the wind speed. Therefore, this study considers a torque controller which will operate depending on the rotor speed. Thus, the operating regions of the CART wind turbine can be divided into partial load regions, where the rotor speed is lower than 40.85 rpm, and full load regions, where the rotor speed is equal to or higher than 40.85 rpm.

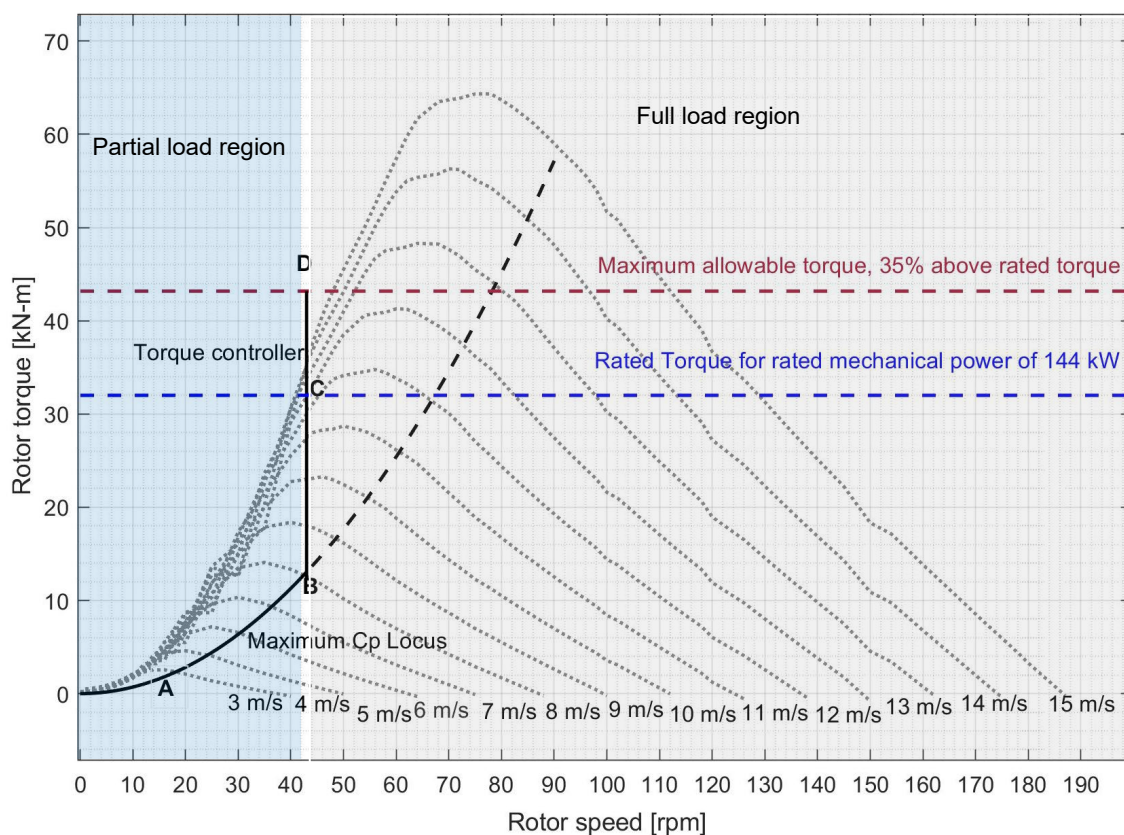


FIGURE 13: ROTOR TORQUE AS A FUNCTION OF ROTOR SPEED AT VARIOUS WIND SPEED

4.2 PARTIAL LOAD REGIONS

As explained in the torque-speed curve of Figure 13 in section 4.1, the objective of the generator torque control is to maximize power output in the partial load region. On this account, the generator torque as a function of rotor speed is implemented.

Additionally, it is also worth mentioning again that the CART machine utilizes a direct-drive generator system, in which the rotor is directly coupled with the generator. Thus, neglecting the shaft torsional flexibility, rotor speed and generator speed are the same. The torque

controller attempts to keep TSR at optimum level by changing the rotor speed using torque-speed curve defined by Leithead and Connor (2000). Assuming that the dynamics of the wind turbine response are fast enough with the change in wind speeds, the generator torque is set directly to $K\Omega^2$ according to equation 2-4 of section 2.1.2. The torque curve follows the trajectory of the maximum power curve in the partial load region until the maximum speed for this region is reached, which is 95% of Ω in our case, as schematically shown in Figure 13. To alleviate high-frequency excitations of the control systems (Jonkman et al., 2009), the measured generator speed is filtered before it is fed back. For this, a first-order recursive low pass filter is implemented which is based on the filter used in the NREL 5 MW wind turbine baseline controller. The cutoff frequency of the filter is set to approximately one-fourth of the blade's first edgewise natural frequency.

As explained in earlier section 2.1.2, this approach can lead to constantly deviation of C_p curve from the maximum C_p locus in turbulent winds. This is true especially for large wind turbines since large rotor inertia leads to the presence of large torque transients in the drivetrain. Since CART is a medium-sized wind turbine, it is assumed it should not be the case. Nevertheless, different efficiency curves are compared as depicted in Figure 14 to examine the power loss due to slow tracking of the $C_{p,max}$ curve of CART WT.

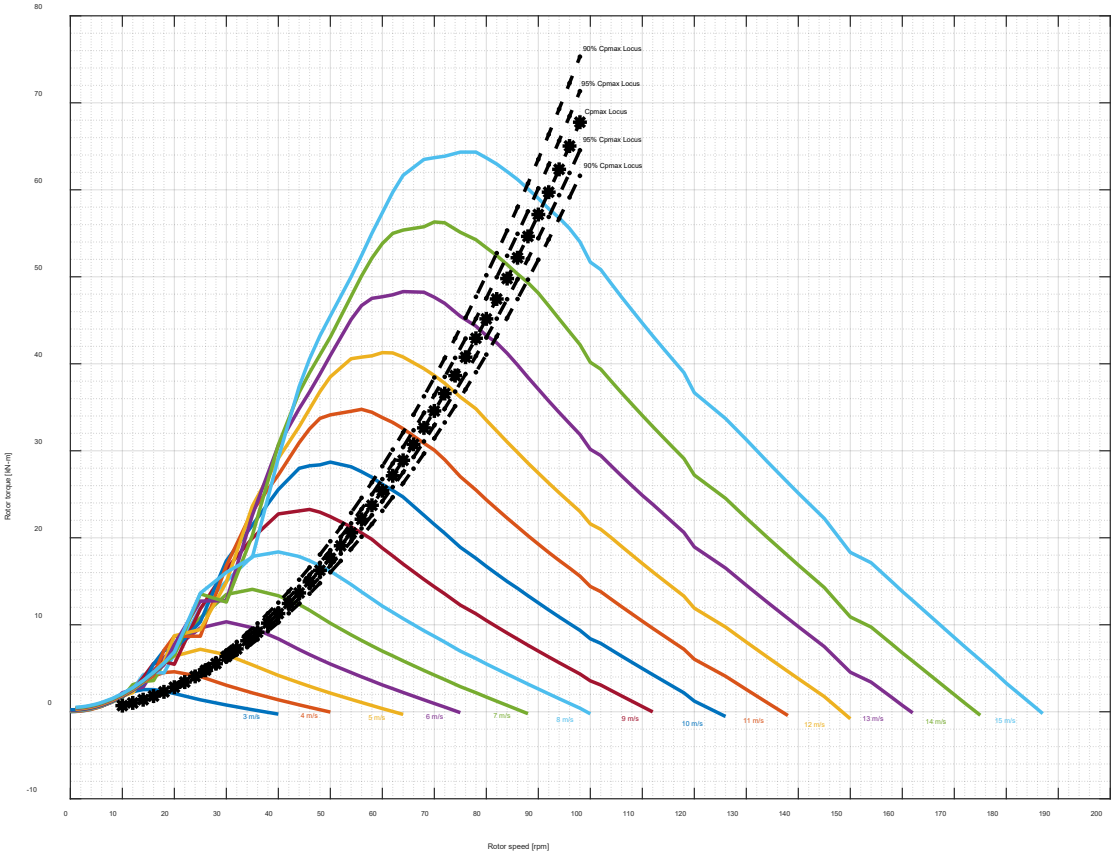


FIGURE 14: TORQUE SPEED CURVE WITH DIFFERENT EFFICIENCY RATIOS AT VARIOUS WIND SPEEDS

Based on the findings, the curves above the $C_{p,max}$ curve are symmetric about $C_{p,max}$ curve with those below the $C_{p,max}$ curve. This can be translated that the rotor performance is not much sensitive to the tracking error in the aerodynamic torque and falling on either side of $C_{p,max}$ curve does not cause considerable power loss. Therefore, the generator reaction torque in partial load region for the CART wind turbine is estimated by the maximum power point tracking algorithm using quadratic law for generator torque which is stated in equation 2-4.

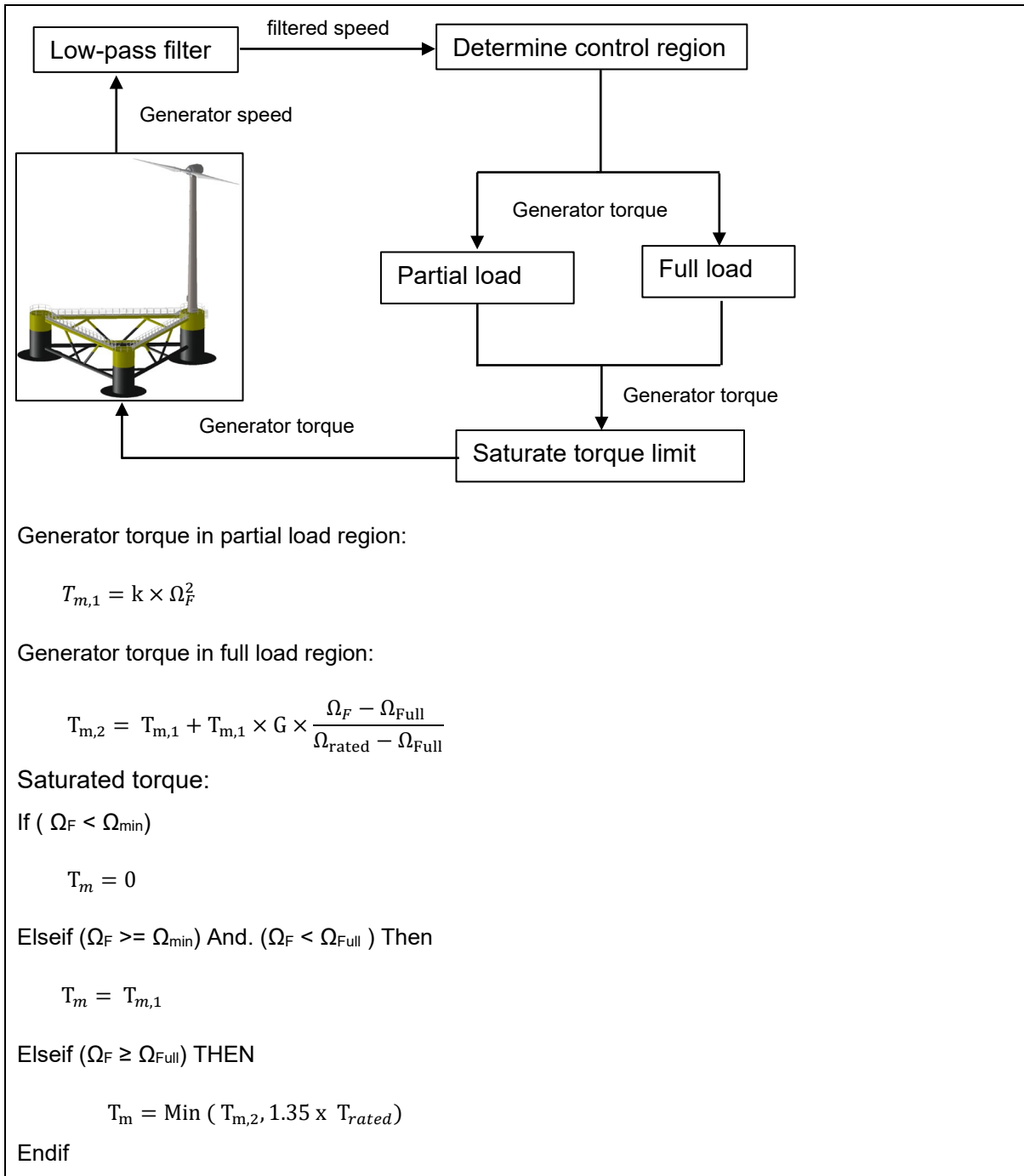
4.3 FULL LOAD REGION

Again, as explained in the ideal torque-speed curve of Figure 13 in section 4.1, another different torque control algorithm was proposed to limit the rotor speed not to exceed its maximum allowable speed in the full load region. Similar to the partial load region, the generator torque was implemented as a function of rotor speed in the full load region. The measured speed is fed back as input directly into the torque controller. To alleviate high-frequency excitations of the control systems (Jonkman et al., 2009), the same first-order recursive low pass filter is implemented similar to the partial load region.

The implemented generator torque control algorithm is described in Table 10. Whenever the generator speed exceeds the predefined generator speed setpoint in the full load region, which is denoted by Ω_{Full} , the turbine requests a higher generator torque than the current value. The current generator torque is estimated by tracking $C_{p,max}$ curve continuously and adding part of the torque found at maximum $C_{p,max}$ to it. The amount of additional torque is obtained by multiplying part of the torque found at maximum $C_{p,max}$ by a variable slope G . The value of the slope G and Ω_{Full} can be varied depending on the size of the generator and the converter rating. Tuning these variables will be explained in section 4.5.1 broadly. Furthermore, the generator torque is limited not to exceed 35% above the value of the rated torque in order to prevent requesting high torque, which can otherwise cause overheating and ultimately lead to system failure. In this way, the rotor speed is limited not to exceed the allowed maximum rotational speed of the rotor in above-rated regions.

The complete algorithm for this control strategy follows:

TABLE 10: FLOW CHART AND CONTROL ALGORITHM OF CART MACHINE



where,

Ω_F = filtered generator speed

Ω_{min} = minimum generator speed at which the torque controller should start working

Ω_{Full} = rotational speed of the generator in full load regions

Ω_{rated} = rated rotational speed of the generator

- $T_{m,1}$ = generator torque in partial load regions
- $T_{m,2}$ = generator torque in full load regions
- T_{rated} = nominal torque at rated power

4.4 PROTECTION SYSTEM

Bringing the wind turbine to a stop is one of the most critical operations because it can cause high stresses on the components of the wind turbine. CART machine utilizes no active control system like blade tip brake to reduce the rotor speed in very high winds. Instead, it uses a mechanical brake to bring the turbine to a standstill at any time. The mechanical brake consists of a brake disc that rotates with the shaft and brake callipers that apply friction on the disc when activated. The braking torque of the brake system needs to be large enough to overcome the aerodynamic torque, additionally dissipate the kinetic rotational energy of the rotor, and ultimately bring the rotor to a halt quickly. In the torque control algorithm, it is assumed that the turbine will allow 35% above the nominal values of rotor speed, generator torque, and the power output for a short period. Once the rotor continuously accelerates and exceeds its maximum permissible limit, the mechanical brake will be activated and it forces the rotor to slow down.

It is assumed that a brake torque of 55 kN-m is achieved in its fully deployed state for an emergency or a fault condition, parking in storm conditions, and overspeed protection and it takes 0.5 s of time lag for the mechanical brake to reach its maximum brake torque. For this, a simple linear ramp from zero to fully deployed shaft brake torque over a period of 0.5 s is implemented in OpenFAST.

TABLE 11: PROPERTIES OF MECHANICAL BRAKE

| | |
|-----------------------------------|-----------|
| Fully-deployed shaft brake torque | 55 [kN-m] |
| Decay time constant | 0.5 [s] |

4.5 IMPLEMENTATION OF CONTROL CONCEPT

This section covers the development of power regulation for the CART wind turbine. It includes tuning of generator torque control parameters, examining the stability of the control system and studying the fundamental structural dynamic response of the CART system.

4.5.1 TUNING GENERATOR TORQUE CONTROL PARAMETERS

As discussed in section 4.3, the implemented torque control algorithm contains two variable parameters which can be adjusted depending on the size of the generator. To begin with tuning torque control parameters, the allowed maximum generator torque is limited to 35% above the nominal value of rotor torque at the rated power of 144 kW. It is needed to mention that the power output of 144 kW refers to the mechanical power of the generator and this value needs

to be multiplied by conversion efficiency to obtain the generated power. In the control algorithm, Ω_{Full} is set to 5% below the rated rotational speed of 43 rpm, and the maximum generator speed is set to the nominal generator speed. This means that the turbine operates in partial load mode if the generator speed is lower than 40.85 rpm. The value of the slope G is varied between 0.5 -2 until the desirable captured power for the given wind speed is achieved. The minimum generator speed at which the turbine should start operating is set to 4 rpm.

In order to find an appropriate value of the slope for all operating regions, time-domain simulations were carried out in OpenFAST coupled with AeroDyn, ServoDyn, and ElastoDyn for cases in which the turbine is subjected to single steady wind velocity ranging from 3 m/s to 20 m/s. As recommend by Jonkman and Buhl (2005), an initial ramp-up in wind velocity for about 1 second was introduced at each wind speed to examine the response and stability of the control system. The time series results were post-processed using the in-house software developed by Windrad Engineering GmbH, which is compatible with FAST output files and can convert the time history results to the Fast Fourier Transform (FFT) spectrum. The best performance was found at $G = 1.86$.

Figure 15 to Figure 18 show the simulation results at $G = 1.86$ for rotor speed, generator torque, and generator power at wind velocity 8 m/s, 9 m/s, 13 m/s, 14 m/s, 15 m/s, 16 m/s, 19 m/s and 20 m/s respectively. In figures, the x-axis represents time and the y-axis represents the quantity of each parameter. It is observed in the first case under moderate wind speed of 8 m/s and 9 m/s (see Figure 15) that the rotor speed overshoots at the beginning for 2 seconds and thereafter the oscillation died out. Nevertheless, the value of overshoot does not exceed the rated rotor speed. For cases under wind velocity 13 m/s and 15 m/s and 19 m/s, the rotor speed overshoots approximately 0.05 %, 0.44% of rated generator speed respectively (see Figure 16 -Figure 18). It takes about 2 seconds for rotor speed to come into a stable state for all cases. The small fluctuation in the rotor speed and the generator torque in high wind velocity of 19 m/s and 20 m/s (see Figure 18) reflects rotor harmonic oscillations. The target rated power of 144 kW is achieved at a wind velocity of 15 m/s and generator torque of 38.58 kN-m (see Figure 17). Upon taking a closer look at the mean, standard deviation, and maximum values of each parameter in all cases, the torque controller seems to be stable for the given control parameters. Figure 19 shows the performance of the control system under linearly varying wind conditions from wind speed of 3 m/s to 20 m/s with step of 1 m/s. It is observed that the rated power is achieved only one wind speed. Thereafter, the turbine enters into the stall region and the generator power decreases gradually. All in all, the response and performance of the turbine for the given wind conditions were found to be resemble with that of the typical variable speed stall-regulated wind turbine and stable for the proposed torque control concept.

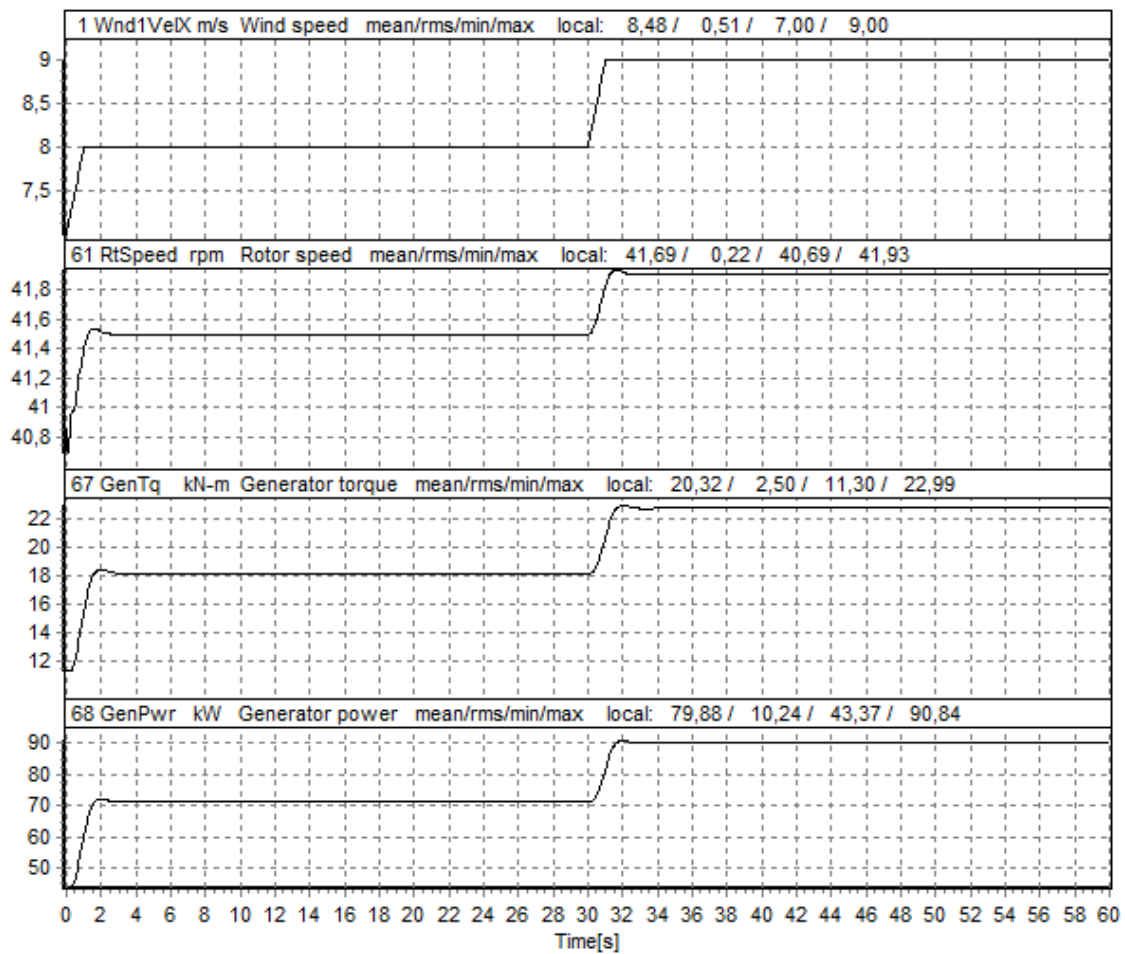


FIGURE 15: TIME HISTORY OF ROTOR SPEED, GENERATOR TORQUE AND GENERATOR POWER UNDER STEADY WIND 8 M/S AND 9 M/S

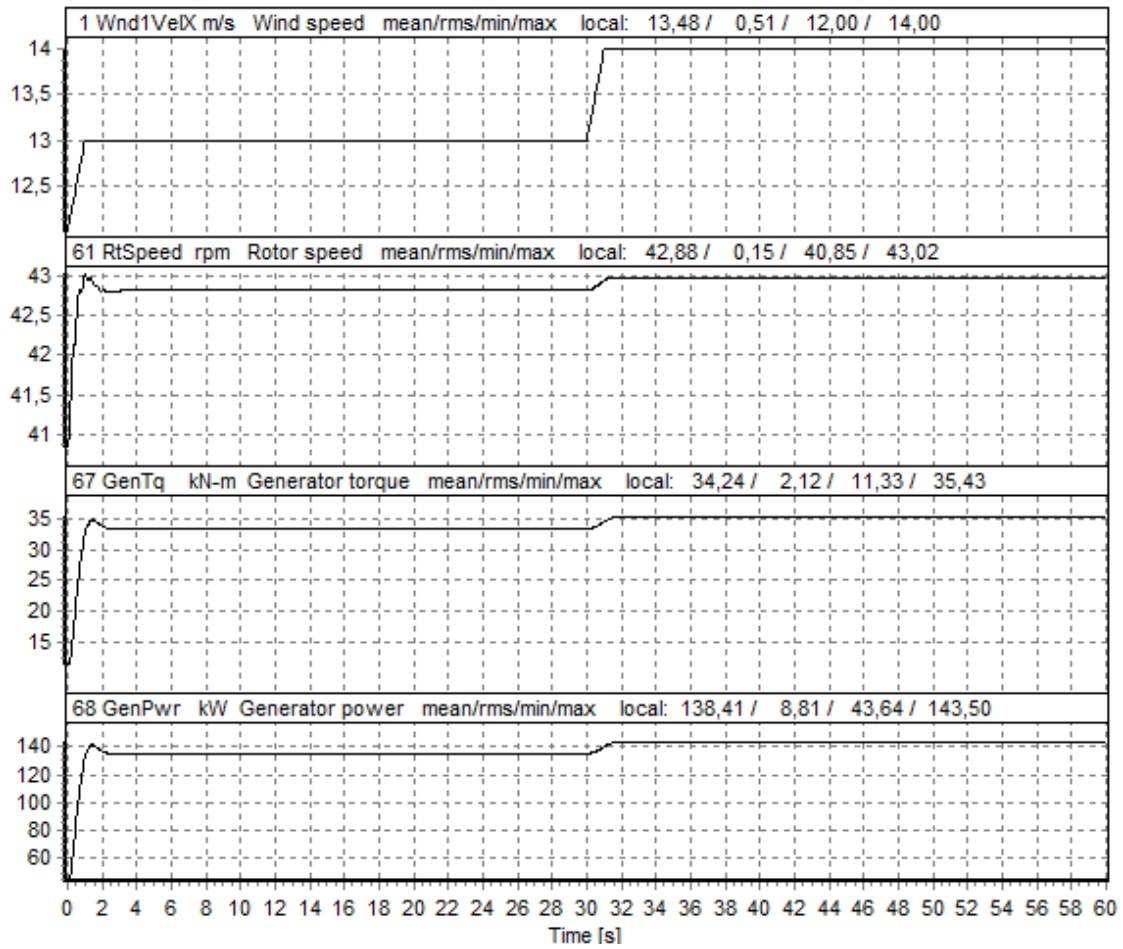


FIGURE 16: TIME HISTORY OF ROTOR SPEED, GENERATOR TORQUE AND GENERATOR POWER UNDER STEADY WIND 13 M/S AND 14 M/S

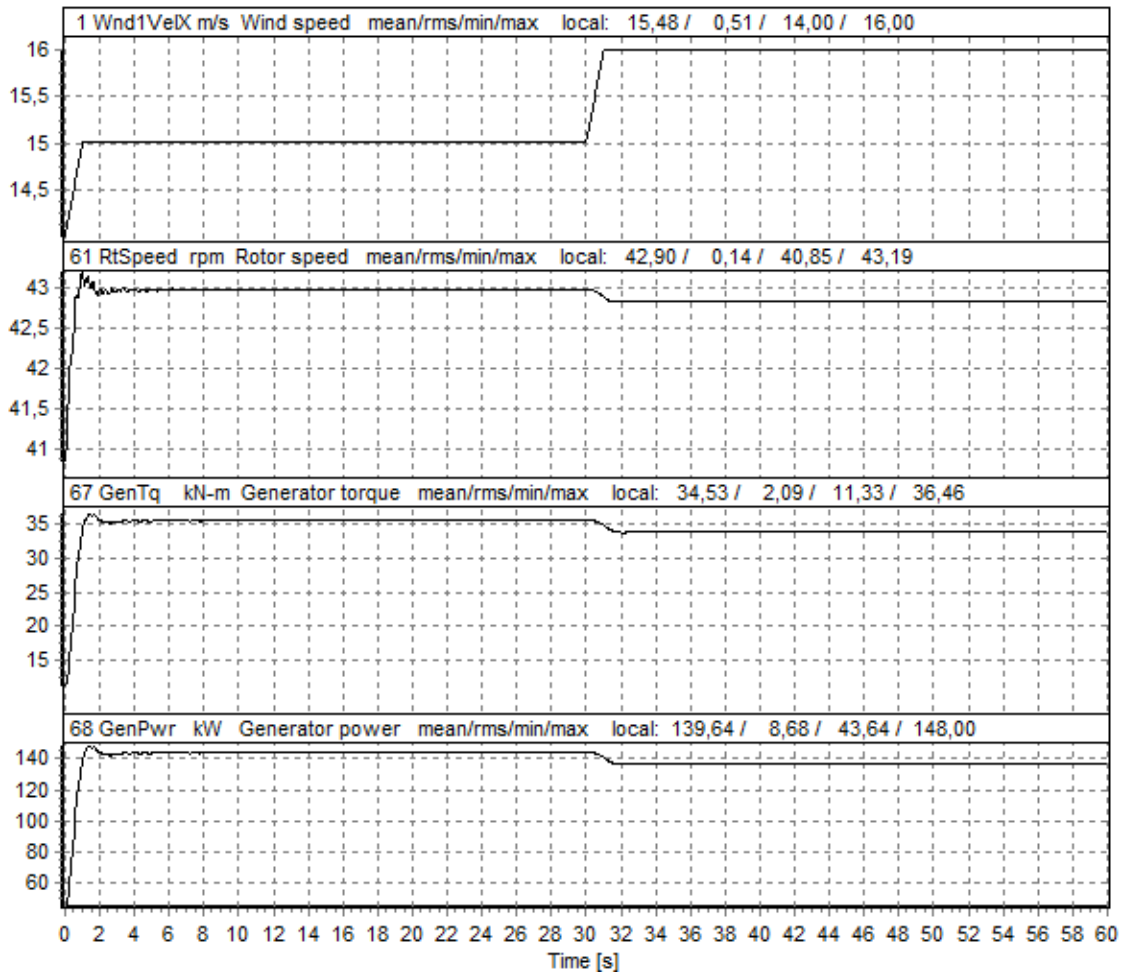


FIGURE 17: TIME HISTORY OF ROTOR SPEED, GENERATOR TORQUE AND GENERATOR POWER UNDER STEADY WIND 15 M/S AND 16 M/S

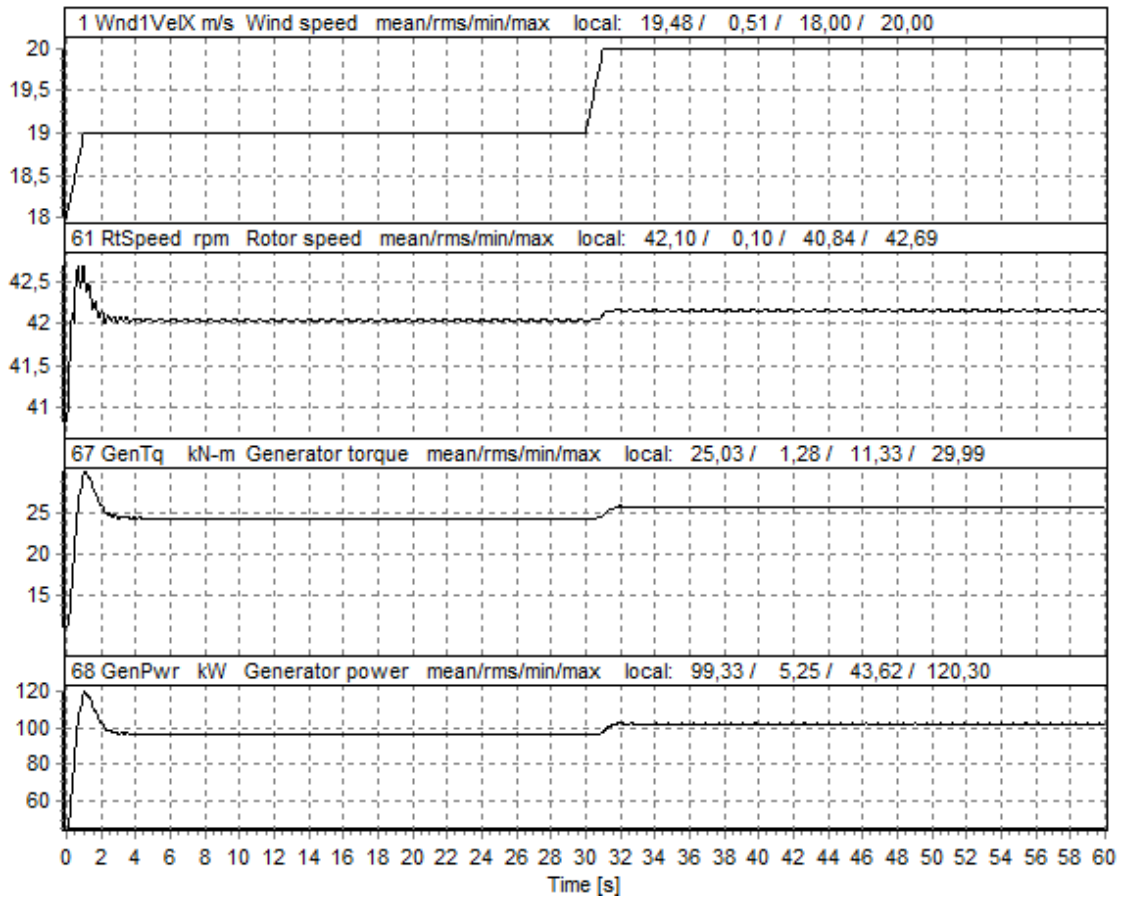


FIGURE 18: TIME HISTORY OF ROTOR SPEED, GENERATOR TORQUE AND GENERATOR POWER UNDER STEADY WIND 19 M/S AND 20 M/S

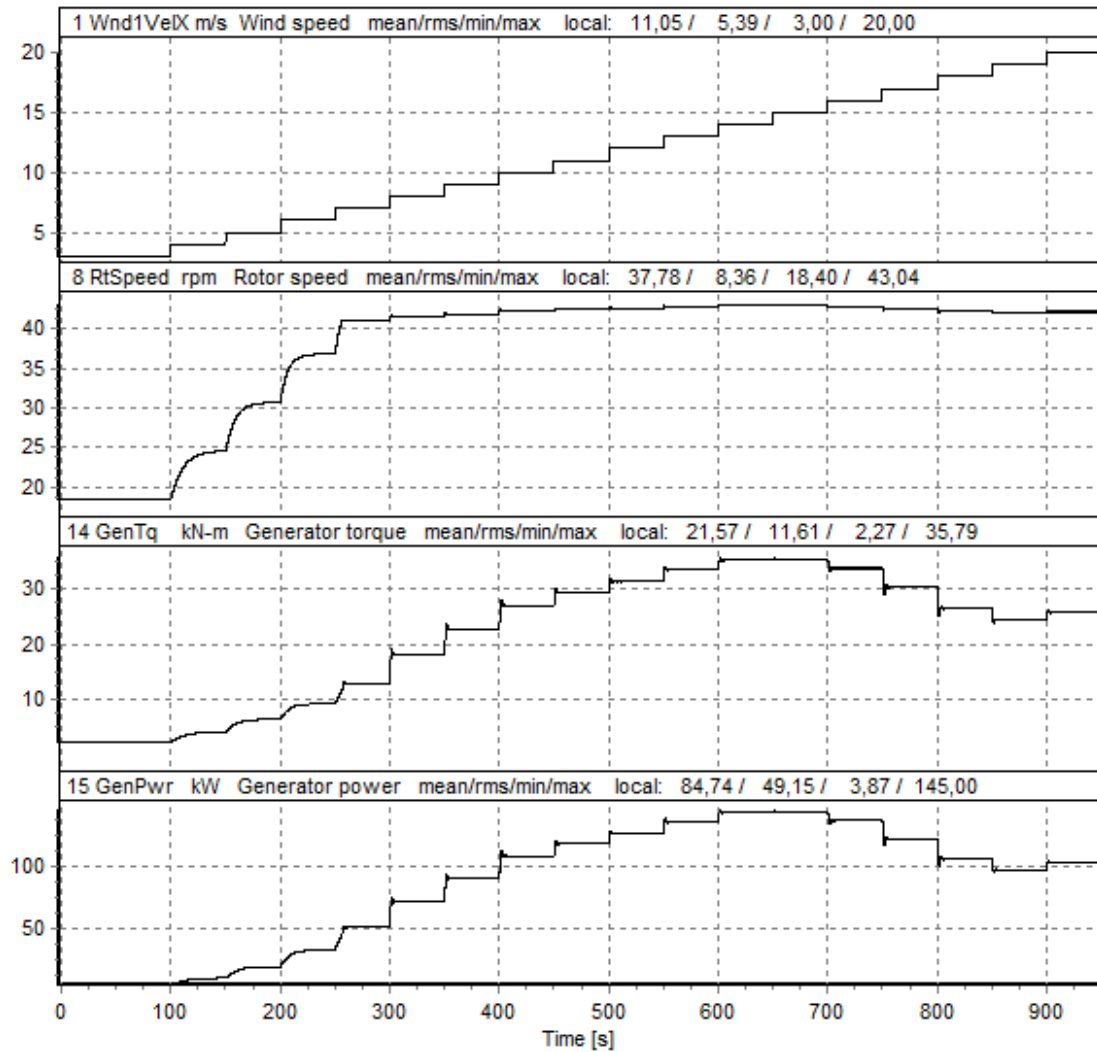


FIGURE 19: TIME HISTORY OF ROTOR SPEED, GENERATOR TORQUE AND GENERATOR POWER UNDER UNIFORM STEP WINDS

4.5.2 GRID LOSS AND SHUT DOWN

The control algorithm does not contain startup and shutdown logic. Therefore, some parameters in the ServoDyn module need to be defined in order to perform a time history simulation for startup and shutdown mode. As an example, grid loss followed by shutdown was simulated at a wind speed of 15 m/s. The generator was disconnected at time 30 s and the mechanical brake was engaged to stop the turbine at 30.5 s. The amount of brake torque was assigned as discussed in section 4.4. The time history of the controller and rotor thrust force is depicted in Figure 20. It is observed that the rotor speed increases continuously until the shaft brake reaches its fully deployed torque. After that, the rotor speed decelerates to zero within a reasonable time. The transient response in thrust force is visible where the grid is lost, and then the thrust force is decreased to nearly zero quite quickly due to the shaft brake. Based on this result, the implemented protection concept seems reasonable as it has managed to bring the rotor to a standstill quite quickly.

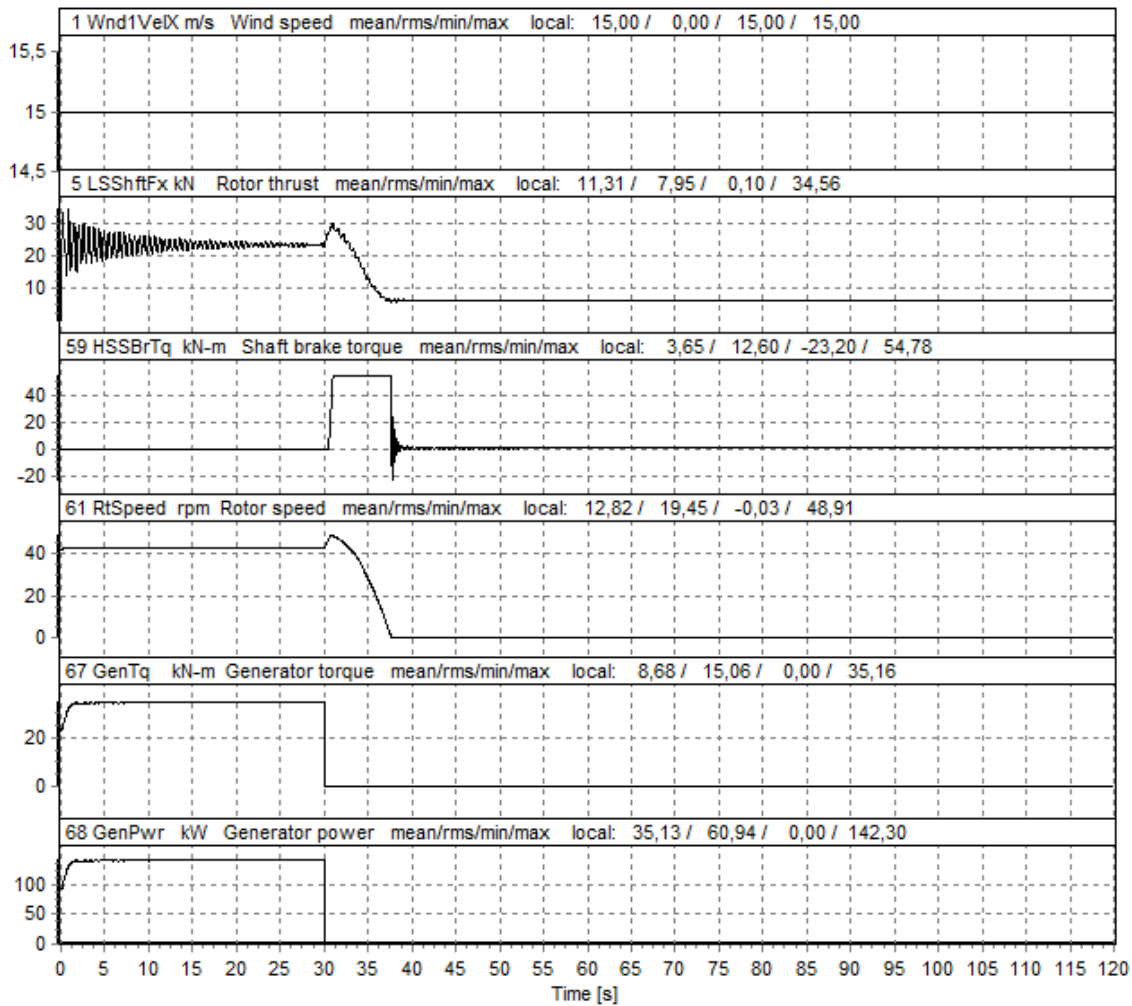


FIGURE 20: GRID LOSS AND SHUTDOWN CASE

4.5.3 EIGENANALYSIS

Wind turbine towers are usually long slender columns with a rotating mass at the top. These structures are prone to vibration when exposed to forces arises from the rotation of the rotor and other environmental forces which are varying with time. Therefore, it is of paramount importance to understand the basic structural dynamic behaviour of such a system at the initial stage before carrying out a number of load cases. Modal analysis helps to identify the natural frequency and natural mode shape of a structure. Thus, potential instabilities like structural resonant oscillations and critical rotor speeds, which can potentially lead to large fatigue loads, can be avoided by tuning the lowest natural frequency of the tower. Using NREL Bmodes (Bir, 2005), modal analyses were carried out to identify eigenfrequencies and eigenmodes of the land- and sea-based CART tower. Figure 21 compares the tower modes displayed in the Campbell diagram for the land-based CART system and CART atop semisubmersible floater. In the figure, the black lines indicate harmonic frequencies of the rotor, where 1P represents the primary excitation frequency of the rotor and 2P and multiple of 2P represents the blade passing frequency of the rotor, which is equal to harmonic frequencies of the rotor. Harmonic frequencies of the rotor are simply obtained by multiplying rotor rotational frequency by the

number of blades on the rotor. According to the results, it is clear that the rotational frequency of the rotor (1P) is far away from the lowest natural frequencies of the tower. In addition to this, the lowest natural frequencies of the tower are greater than 2P meaning that the tower is very stiff with a high natural frequency. It is interesting to note that the natural frequencies of the first tower bending modes both in fore-aft and side-to-side directions are greater for the offshore CART system than the land-based one. This can be attributed to the stiffness of the platform and the mooring system. On the other hand, natural frequencies of the second tower bending modes in fore-aft and side-to-side directions are larger for the land-based tower than the sea-based one.

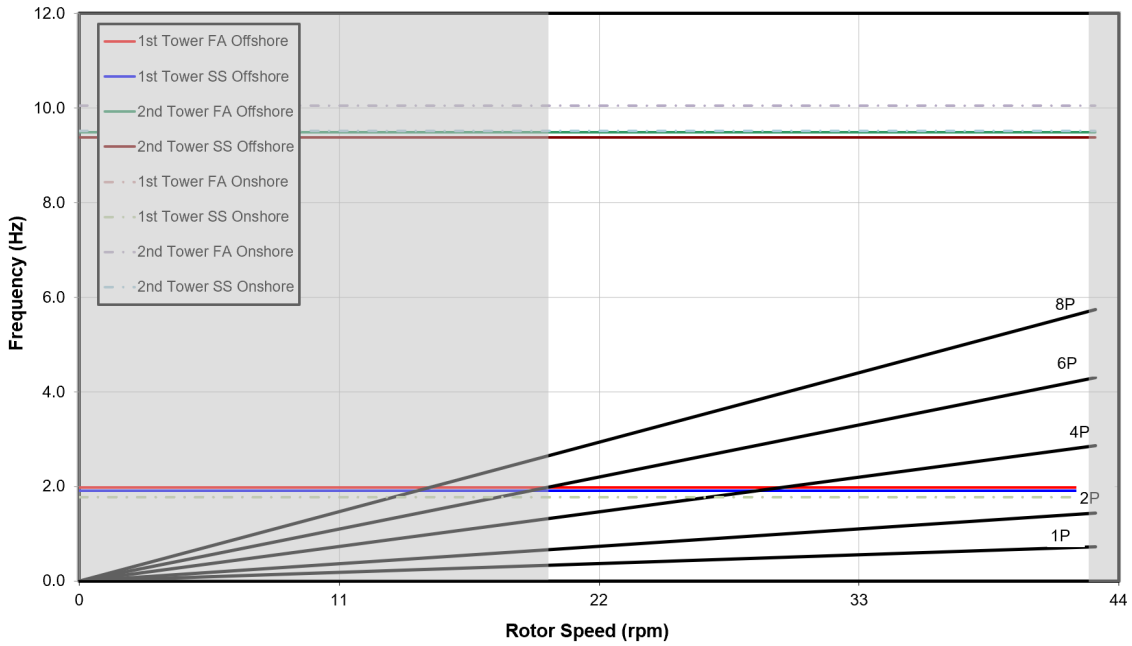


FIGURE 21: TOWER MODE CAMPBELL DIAGRAM OF LAND-BASED CART SYSTEM AND SEA-BASED CART SYSTEM

4.5.4 HYDROSTATIC RESTORING STIFFNESS CALCULATION

The hydrostatic restoring forces are both gravitational and buoyancy forces. The way they achieve hydrostatic restoring forces is different depending on the type of floater. The hydrostatic restoring forces are typically represented as the spring forces in a mass-damper-spring system. Thus, the change in hydrostatic forces with respect to the substructure displacement is estimated using a linear hydrostatic approach which assumes a small platform inclination as the following equation 4-1 (Jonkman et al., 2014).

$$F_i^{Hydrostatic} = \rho_{water} g V_0 \delta_{i3} - C_{ij}^{Hydrostatic} q_j \quad 4-1$$

The term $\rho g V_0 \delta_{i3}$ represents the buoyancy force which is calculated using Archimedes' principle. Thus, this buoyancy force equals to the weight of the fluid displaced by the body. The restoring stiffness matrix of the platform resulting from the change in COB upon heave, roll, and pitch are estimated using the following equations taken from (Jonkman et al., 2014).

$$C_{ij} = \begin{bmatrix} 0 & 0 & 0 & 0 & 0 \\ 0 & 0 & 0 & 0 & 0 \\ 0 & \rho g A_{wp} & 0 & -\rho g \iint x_{cog} dA_{wp} & 0 \\ 0 & 0 & \rho g \iint y_{cog}^2 dA_{wp} + \rho g V_0 z_{cob} & 0 & -\rho g V_0 x_{cob} \\ 0 & -\rho g \iint x_{cog} dA_{wp} & 0 & \rho g \iint y_{cog}^2 dA_{wp} + \rho g V_0 z_{cob} & -\rho g V_0 y_{cob} \\ 0 & 0 & 0 & 0 & 0 \end{bmatrix}$$

Using the above equation, the hydrostatic restoring stiffness matrix for CART system becomes

$$C_{ij} = \begin{bmatrix} 0 & 0 & 0 & 0 & 0 \\ 0 & 0 & 0 & 0 & 0 \\ 0 & 5.30E + 05 & 0 & 3.15E + 05 & 0 \\ 0 & 0 & 6.81E + 07 & 0 & -2.65E + 05 \\ 0 & 3.15E + 05 & 0 & 7.96E + 07 & 3.74E + 03 \\ 0 & 0 & 0 & 0 & 0 \end{bmatrix}$$

C33, C44, and C55 correspond to the hydrostatic restoring stiffness in heave, roll, and pitch direction respectively. Since the CART floater is asymmetric, the hydrostatic stiffness in pitch and roll direction is not identical. The hydrostatic restoring stiffness C33 is related to the change in upward buoyancy force when the platform is displaced from its initial position. The hydrostatic restoring stiffness C44 and C55 are related to the moment of the waterplane area. The hydrostatic restoring stiffness in pitch direction has a substantial influence on the mean pitch angle of the turbine when subjected to wind loads. Change in platform pitch angle causes the rotor plane to deviate from the wind direction. Ultimately, this can lead to a reduction in performance. The thrust force acting on the rotor creates an overturning moment and the substructure must counteract this overturning moment. In an initial stage, the maximum static inclination can be verified by dividing the maximum rotor thrust moment by hydrostatic pitch stiffness as follows:

$$\alpha_{max,pitch} = \frac{M_{thrust}}{C55} \cdot \left(\frac{180}{\pi}\right) \quad 4-2$$

By multiplying the maximum thrust force at a wind speed of 50 m/s by the moment arm which is the distance between the centre of hub and the centre of buoyancy, the wind heeling moment of 1.68E+06 Nm is obtained. Thus, the maximum static inclination becomes

$$\alpha_{max,pitch} = \frac{1.68E + 06}{7.96E + 07} \cdot \left(\frac{180}{\pi}\right) = 1.21 \text{ deg} < 12 \text{ deg} \quad 4-3$$

As recommended by (DNV-GL-OS-C301, 2020), the static inclination angle should not be greater than 6° for normal condition and 12° for survival conditions.

4.5.5 FREE-DECAY TESTS

The goal of free decay simulations is to understand the restoring characteristics of the platform in a freely floating condition and hence to identify the natural frequencies and periods of the

platform motion. To perform free-decay tests, the response of the system in a non-equilibrium condition was examined under no wind, wave, and the control system. An initial offset of the floater is given and the system is released to freely oscillate. The total simulation duration was 500 s. Figures on the left side of Figure 22 - Figure 27 show how the platform restores to its equilibrium condition in a freely floating condition in the time domain. The floater motions die out with time due to the presence of damping in the system. The FFT spectrum is used to identify the natural frequency of the floater motions. As can be clearly seen in the figure, the structural natural frequency of the platform corresponds to the frequency containing the most energy in the FFT spectrum. The natural period is determined as the period corresponding to the natural frequency.

It is evident in figures that the natural period of surge, sway, and yaw are almost the same whereas the natural period of heave, pitch, and roll are close to each other. Motions in surge, sway and yaw direction are mainly influenced by the mooring system whereas motions in heave, pitch, and roll direction are influenced by the hydrostatic restoring stiffness of the floater. Surge, sway, and yaw motions have longer periods than heave, pitch, and roll motions. This means that the damping in heave, roll and pitch motion are much larger than the rest motions. This is primarily related to the presence of the heave plates, which increase the drag force and this ultimately leads an increase in system damping. Furthermore, natural frequencies of surge, sway, and yaw motion are as low as about 0.06 Hz. The calculated natural frequencies and periods of platform motion are listed in Table 12.

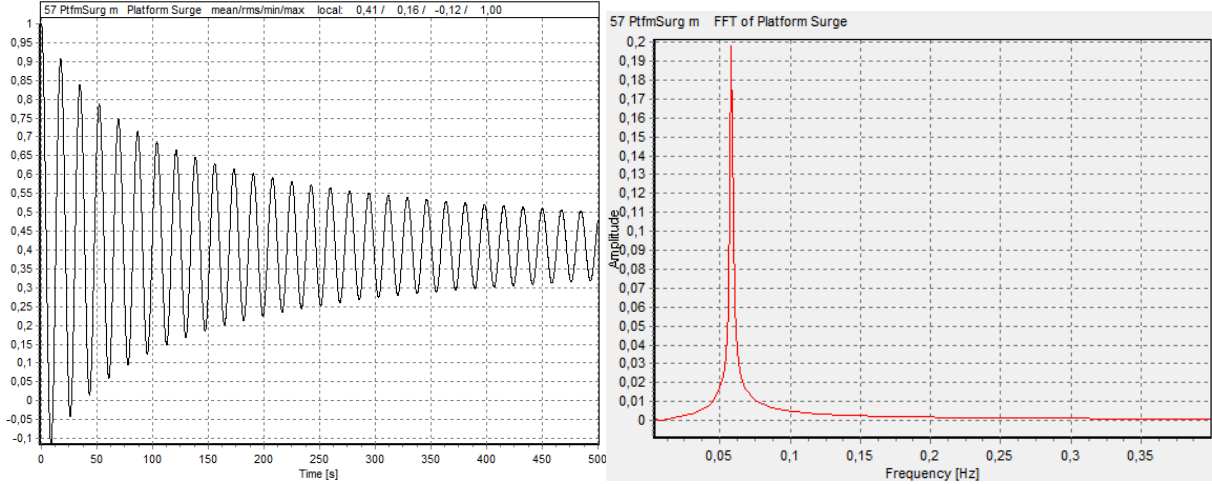


FIGURE 22: TIME HISTORY (LEFT) AND FFT DIAGRAM (RIGHT) OF SURGE MOTION

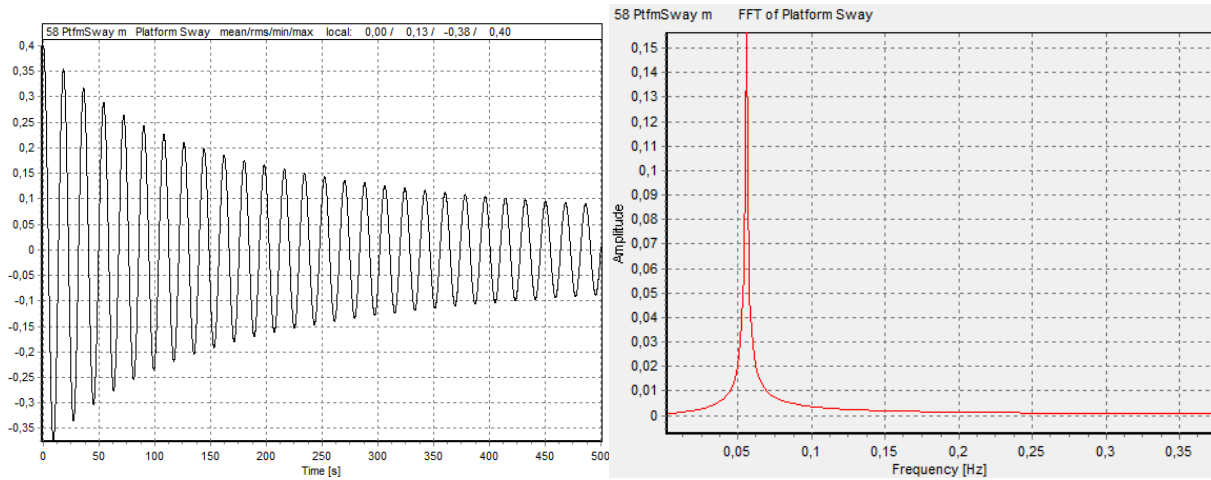


FIGURE 23: TIME HISTORY (LEFT) AND FFT DIAGRAM (RIGHT) OF SWAY MOTION

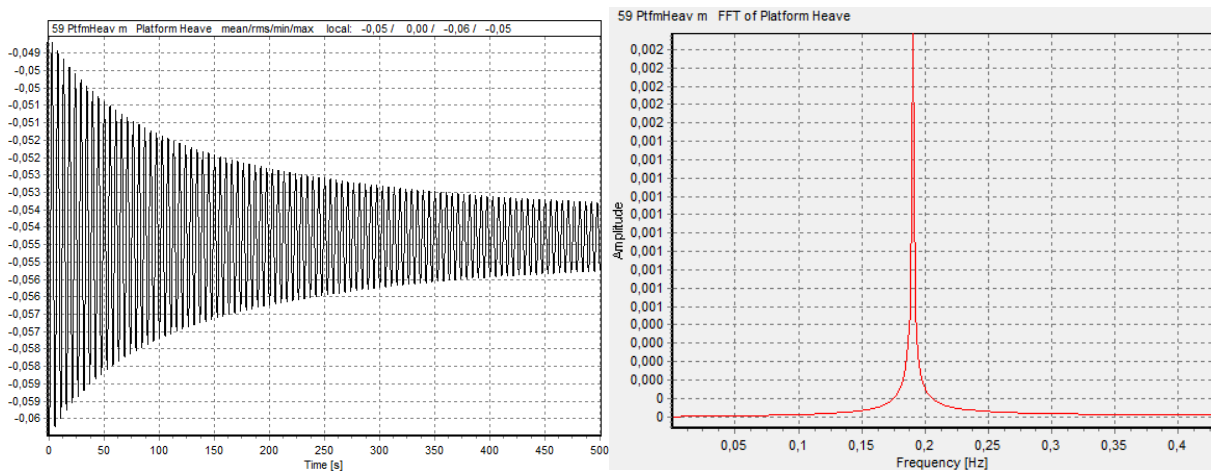


FIGURE 24: TIME HISTORY (LEFT) AND FFT DIAGRAM (RIGHT) OF HEAVE MOTION

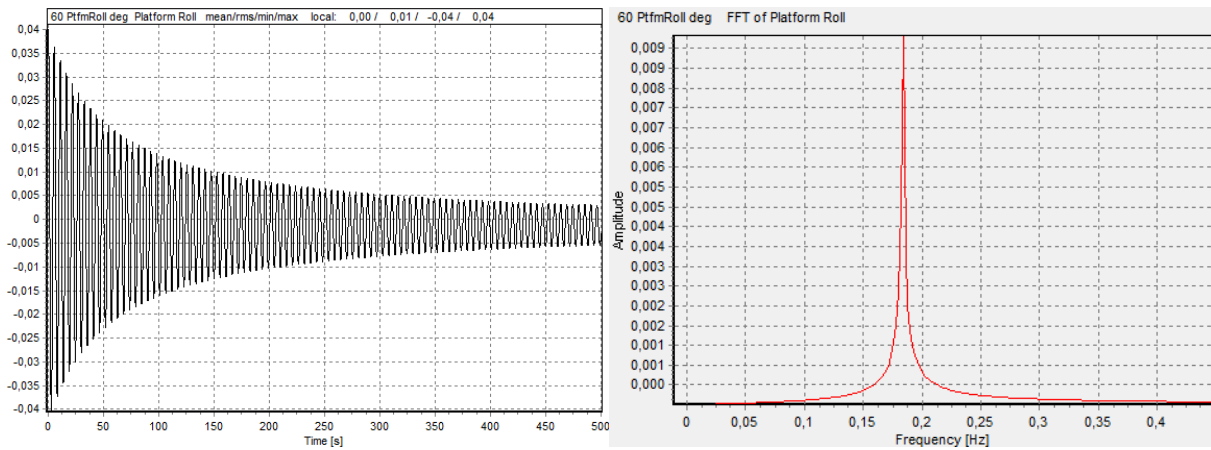


FIGURE 25: TIME HISTORY (LEFT) AND FFT DIAGRAM (RIGHT) OF ROLL MOTION

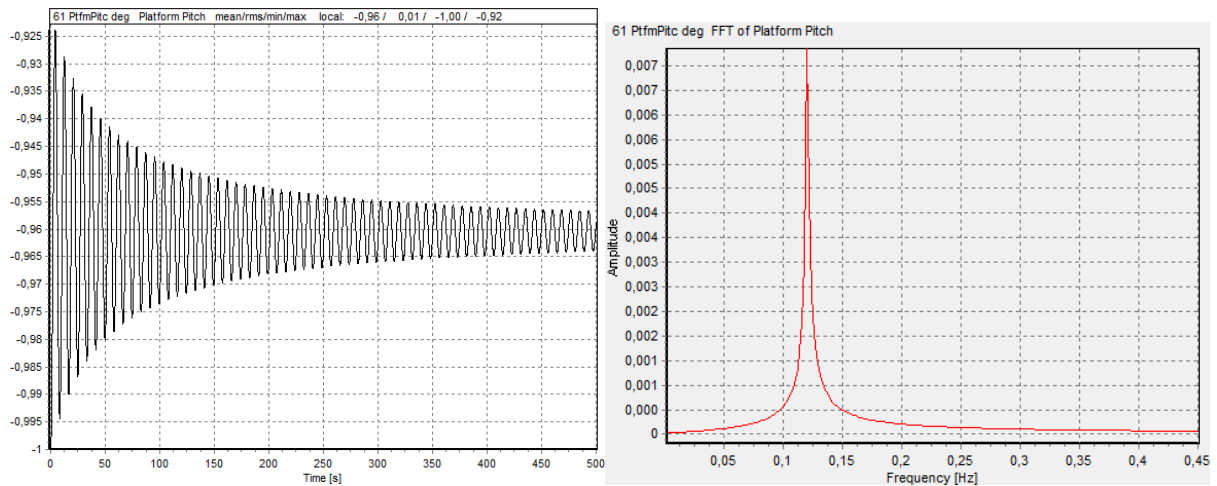


FIGURE 26: TIME HISTORY (LEFT) AND FFT DIAGRAM (RIGHT) OF PITCH MOTION

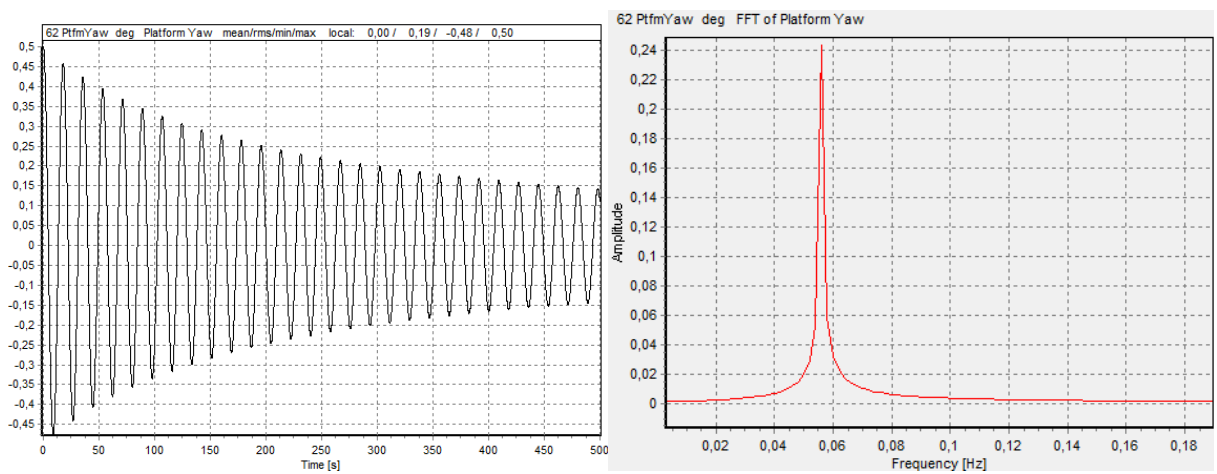


FIGURE 27: TIME HISTORY (LEFT) AND FFT DIAGRAM (RIGHT) OF YAW MOTION

TABLE 12: NATURAL FREQUENCY AND NATURAL PERIOD OF PLATFORM MOTIONS

| Platform motion | Natural frequency [Hz] | Natural period [s] |
|-----------------|------------------------|--------------------|
| Surge | 0.06 | 17.24 |
| Sway | 0.06 | 17.86 |
| Heave | 0.19 | 5.26 |
| Roll | 0.18 | 5.43 |
| Pitch | 0.12 | 8.3 |
| Yaw | 0.06 | 17.86 |

4.5.6 PLATFORM MOTION AND RESPONSE OF CONTROLLER AS A FUNCTION OF WIND SPEED

It is also important to understand the performance of the system and motion responses under steady-state conditions before conducting a series of load cases. The goal is to examine the mean offset of floater motions and the response of controller, which helps to enhance the controller design to keep the platform motion within a safe range. This also helps to tune the stiffness of the floater as well as the mooring system if necessary. During steady wind

simulations, a constant uniform wind inflow is applied perpendicular to the rotor plane for 400 s and no wave and current loads are considered. The turbine was operating with a generator torque controller to optimize the power in the partial load region and limit the power in the full load region.

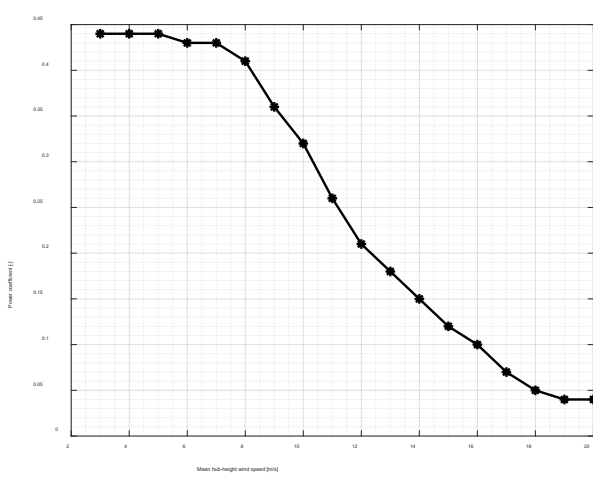
Table 13 and Figure 28 show the mean values of the response of controller and platform motion as a function of wind speeds. In partial load regions, the turbine managed to operate with constant C_p whereas the mean value of C_p decreases with the increase in wind speed as expected (see Figure 28a). Since the turbine uses stall regulation, the mean rotor thrust force increases with the increase in wind speeds (see Figure 28b). Special attention needs to be paid in extreme conditions since there is no active aerodynamic control to reduce the thrust force and hence this can affect the dynamic response of the substructure. In Figure 28c, the mean mechanical power of onshore and offshore CART systems is compared. It was found that mechanical power of the offshore CART system is slightly lower than the land-based one. This is due to the pitch motion of the floater, which consequently causes the rotor plane deviate from the inflow wind direction.

It is worth mentioning that the start-up transient can be minimized by setting proper initial conditions for the rotor speed, platform surge, and platform pitch offset based on their expected value for the given mean hub-height wind speed while performing load simulations.

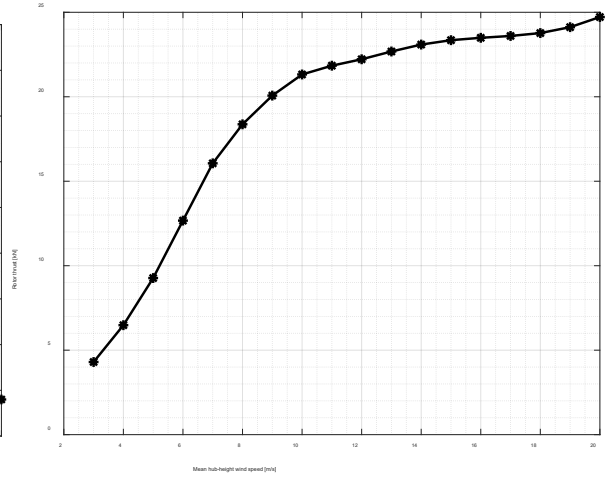
TABLE 13: PLATFORM MOTION AND RESPONSE OF CONTROLLER AS A FUNCTION OF WIND SPEED

| Wind speed [m/s] | Rotor speed [rpm] | Surge [m] | Heave [m] | Pitch [°] | Rotor Thrust [kN] | Torque [kNm] | Power [kW] |
|---------------------|----------------------|--------------|--------------|--------------|----------------------|-----------------|---------------|
| 3 | 18.44 | 0.45 | -0.04 | -0.88 | 4.32 | 2.3 | 3.98 |
| 4 | 24.55 | 0.49 | -0.04 | -0.84 | 6.49 | 4.1 | 9.47 |
| 5 | 30.7 | 0.55 | -0.04 | -0.79 | 9.28 | 6.4 | 18.51 |
| 6 | 36.82 | 0.62 | -0.04 | -0.72 | 12.68 | 9.21 | 31.98 |
| 7 | 41 | 0.69 | -0.04 | -0.66 | 16.07 | 13.03 | 50.35 |
| 8 | 41.5 | 0.74 | -0.04 | -0.65 | 18.38 | 18.23 | 71.28 |
| 9 | 41.91 | 0.78 | -0.04 | -0.62 | 20.08 | 22.81 | 90.10 |
| 10 | 42.28 | 0.80 | -0.05 | -0.56 | 21.33 | 27.12 | 108.06 |
| 11 | 42.48 | 0.81 | -0.05 | -0.55 | 21.85 | 29.48 | 118.04 |
| 12 | 42.64 | 0.82 | -0.05 | -0.54 | 22.23 | 31.40 | 126.16 |
| 13 | 42.82 | 0.83 | -0.05 | -0.54 | 22.69 | 33.60 | 135.61 |
| 14 | 42.96 | 0.84 | -0.05 | -0.53 | 22.75 | 35.33 | 143.05 |
| 15 | 42.98 | 0.84 | -0.05 | -0.52 | 23.36 | 35.58 | 144.11 |
| 16 | 42.84 | 0.85 | -0.05 | -0.52 | 23.5 | 33.84 | 136.63 |

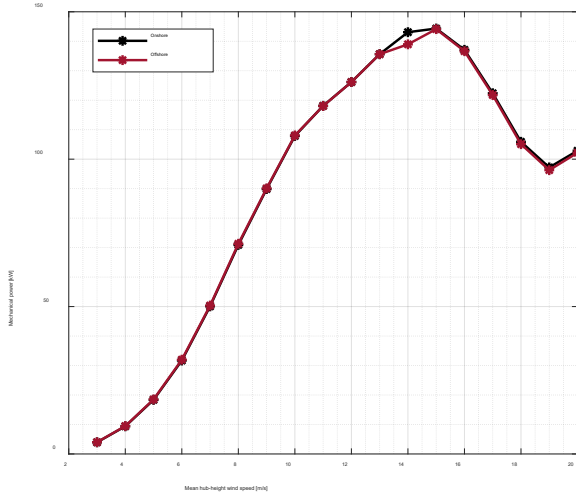
| Wind speed [m/s] | Rotor speed [rpm] | Surge [m] | Heave [m] | Pitch [°] | Rotor Thrust [kN] | Torque [kNm] | Power [kW] |
|---------------------|----------------------|--------------|--------------|--------------|----------------------|-----------------|---------------|
| 17 | 42.55 | 0.85 | -0.05 | -0.52 | 23.61 | 30.36 | 121.75 |
| 18 | 42.22 | 0.85 | -0.05 | -0.52 | 23.78 | 26.41 | 105.09 |
| 19 | 42.04 | 0.86 | -0.05 | -0.51 | 24.13 | 24.30 | 96.28 |
| 20 | 42.16 | 0.87 | -0.05 | -0.50 | 24.73 | 25.71 | 102.17 |



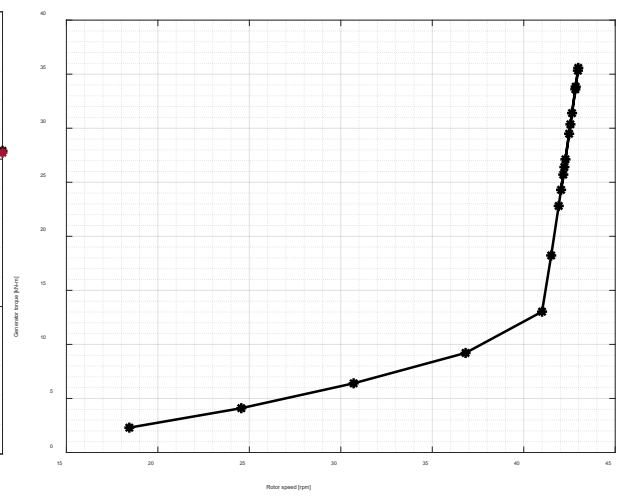
(a)



(b)



(c)



(d)

FIGURE 28: RESPONSE OF POWER COEFFICIENT (A), ROTOR THRUST (B), GENERATOR POWER (C) AS A FUNCTION OF WIND SPEED, AND TORQUE-SPEED CURVE OF CART SYSTEM (D)

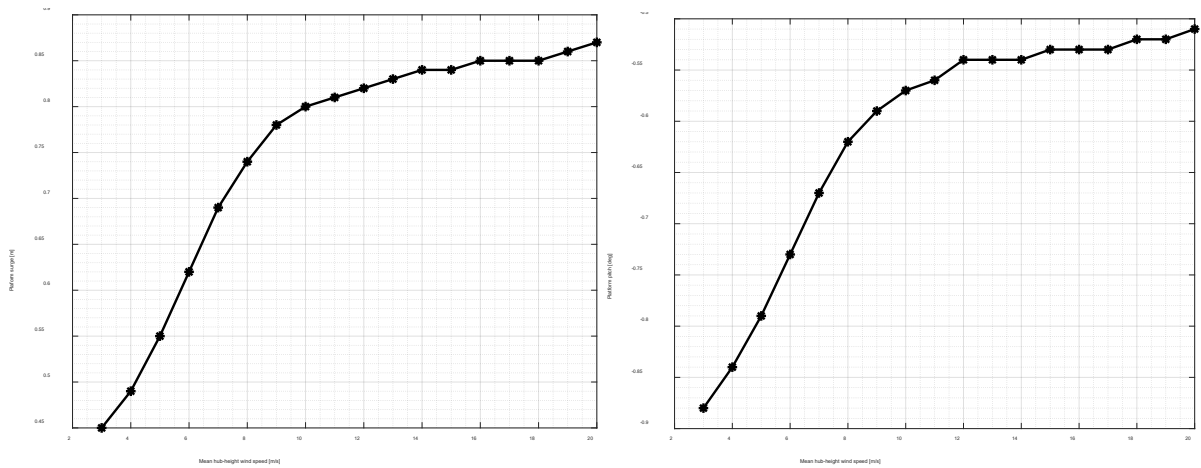


FIGURE 29: MEAN OFFSET OF SURGE (LEFT) AND PITCH (RIGHT) MOTION AS A FUNCTION OF WIND SPEEDS

Figure 29 shows how the mean offset of the platform motion changes with the increase in wind speeds. Comparing Figure 29 with Figure 28b, it was found that the surge and pitch motions increase with the increase in aerodynamic thrust force on the rotor. Especially in high winds, the large platform motion causes the rotor plane to deviate from the incoming wind. As a result, the rotational speed is decreased and there is a change in power output. This can also imply that the CART system is more likely to be affected by cut-out load cases since the rotor blades are forced to stall at high winds.

5 LOADS ACTING ON A TYPICAL FLOATING OFFSHORE WIND TURBINE

The loads acting on a typical floating offshore wind turbine can be divided into static and dynamic loads. Static loads are mainly due to gravity, hydrostatic load, loads from pay-load or equipment, whereas the dynamic loads represent the inertial loads resulted from rotation, vibration, and seismic activities which are time-varying loads from waves or wind, environmental conditions, and the operational behaviours over the lifetime. Both aerodynamic and hydrodynamic loads acting on the FOWT cause elastic deformation of the structure. The aerodynamic loads are transferred to the platform through the tower. In this section, methods to estimate environmental loads such as wind, wave, and currents loads will be explained. Figure 30 depicts environmental loads acting on a floating offshore wind turbine.

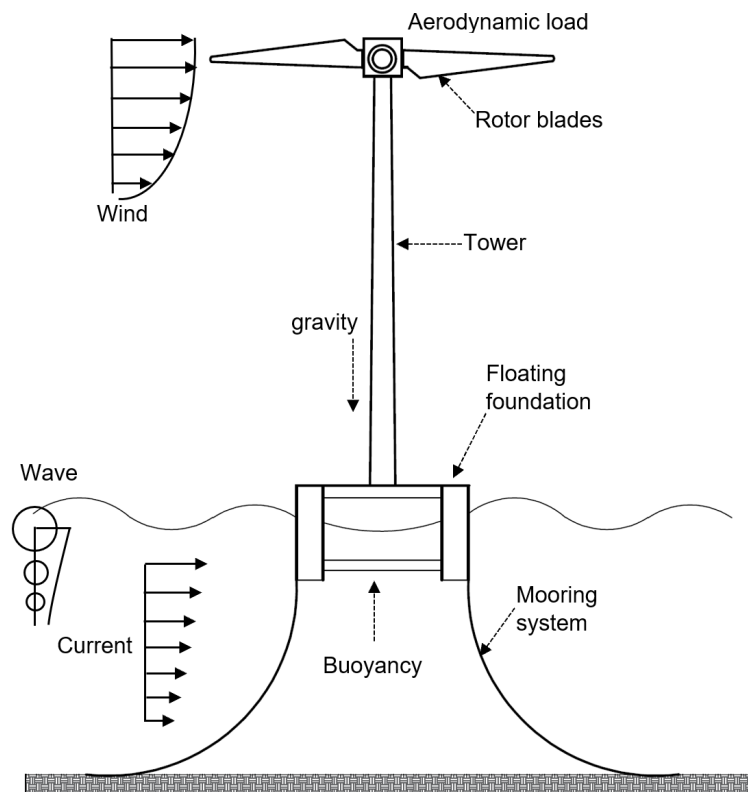


FIGURE 30: TYPICAL ENVIRONMENTAL LOADS ACTING ON A FLOATING OFFSHORE WIND TURBINE

5.1 GRAVITY AND BUOYANCY

For floating offshore wind turbines, a substructure means the floater and the mooring system both together. The substructure has to provide enough buoyancy and restoring forces so that the entire system remains stable, the rotor tilt angle and the platform motions are within the acceptable limits when the wind turbine undergoes wind-wave excitation forces. Usually, the centre of gravity should be kept as low as possible and the centre of buoyancy should be kept as high as possible. The buoyancy is mainly provided by the submerged part of the floating

substructure. The distribution of floater weight defines the centre of mass and thus influences the overall dynamic behaviour of the floater, and hence the floater stability.

5.2 WIND LOADS

Wind is the motion of air in the atmospheric boundary layer and turbulent in nature. Wind speed and direction are evolving with time and space. According to assumptions made by Van der Hoven, time variation of wind speed can be described by two peaks within the wind energy spectrum (Burton et al., 2011) as shown in Figure 31. To investigate the response of wind turbines, wind speed variations at high-frequency range are of interest, which is also known as short-term distribution of wind speeds within a period of 10 minutes to 1 hour. These fluctuations in wind speed are caused by turbulence and contribute to stochastic aerodynamic loads which can significantly affect the fatigue life and the performance of the wind turbine (Burton et al., 2011). Usually, wind can be described as mean wind speed and turbulence intensity.

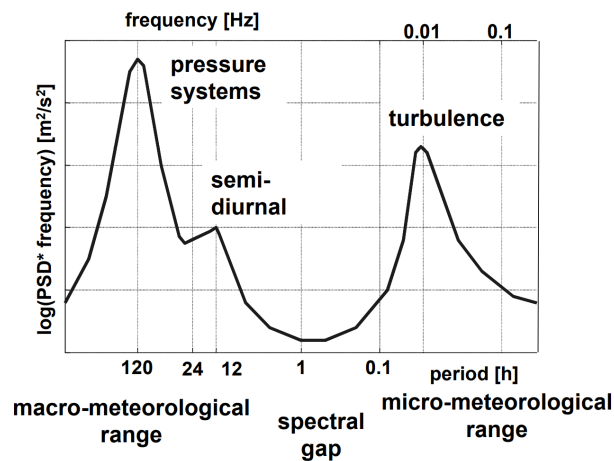


FIGURE 31: WIND ENERGY SPECTRUM ACCORDING TO VAN DER HOVEN (KÜHN, 2001).

Mean wind speed is an important parameter to study the economic feasibility of a wind energy project. It varies vertically with the height above the ground or still water level and can be described by the logarithmic wind shear as in equation 5-1 or power law as in equation 5-2. In this study, power law was used to represent vertical wind profile and a shear exponent of $\alpha = 0.14$ for all normal wind conditions and $\alpha = 0.11$ in extreme 1- and 50-year wind conditions were considered according to IEC 61400-3. Wind shear contributes periodic cyclic loads on the blades and turbine.

$$v_{\text{mean}}(z) = v_{\text{ref}} \left(\frac{\ln(z/z_0)}{\ln(z_{\text{ref}}/z_0)} \right) \quad 5-1$$

$$v_{\text{mean}}(z) = v_{\text{ref}} \left(\frac{z}{z_{\text{ref}}} \right)^\alpha \quad 5-2$$

Turbulence is mainly caused by topographical features and decreases with the increase in wind speed. Turbulence intensity is the most important statistical property of turbulent inflow. It can be described by standard deviation σ and mean wind speed v_{mean} as the following equation.

$$I = \frac{\sigma}{v_{mean}} \quad 5-3$$

A number of wind spectrum models have been developed to describe the short-term stationary wind condition. Some commonly used models include the Mann uniform shear model, von Karman spectral model, the Kaimal spectrum, etc. This study applied IEC Kaimal wind spectral model to generate a full-field stochastic and turbulence wind inflows required for load simulations. IEC Kaimal spectrum is based on the following equation:

$$S_{Kaimal}(f) = \frac{4\sigma_K^2 L_K / v_{mean}}{\left(1 + \frac{6fL_K}{v_{mean}}\right)^{5/3}} \quad 5-4$$

where f is the cyclic frequency and L_K is an integral length scale. Stochastic wind fields required for wind turbine load simulations are generated in the time-domain by applying the wind spectra model combined with the coherence functions. The coherence function for the IEC spectral models is:

$$Coh_{i,jK} = \exp \left[-12 \left(\left(f \cdot \frac{r}{v_{mean}} \right)^2 + \left(\frac{0.12r}{L_C} \right)^2 \right)^{0.5} \right] \quad 5-5$$

where r is the distance between i and j on the grid and L_C is the coherence scale parameter. An exemplary turbulent wind field generated by NREL TurbSim is depicted in Figure 32. It shows how the wind speed varies with time and space.

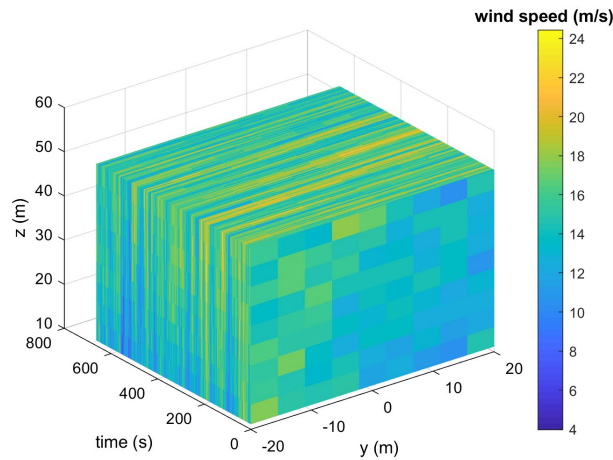


FIGURE 32: EXAMPLE OF 3D TURBULENT WIND FIELD GENERATED BY NREL TURBSIM

In addition to stochastic, steady, and cyclic loads contributed by wind turbulence and wind shear, transient loads caused by wind gust can impose extreme peak load on the wind turbine

within a short duration. Wind gust is caused by a sudden increase in wind speed. The duration of the gust lasts 20 sec or less. It is very short on timescales of the FOWT and can cause horizontal slow drift oscillation of the floater. To capture the extreme response of the wind turbine in these conditions, NREL IECWind module is used in the present study. It is possible to generate different discrete models recommended by IEC such as ECD, ECG, EDC, EOG, NWP, and EWM. These models cover a 50-year extreme gust profile, shear, direction change, and several other wind conditions.

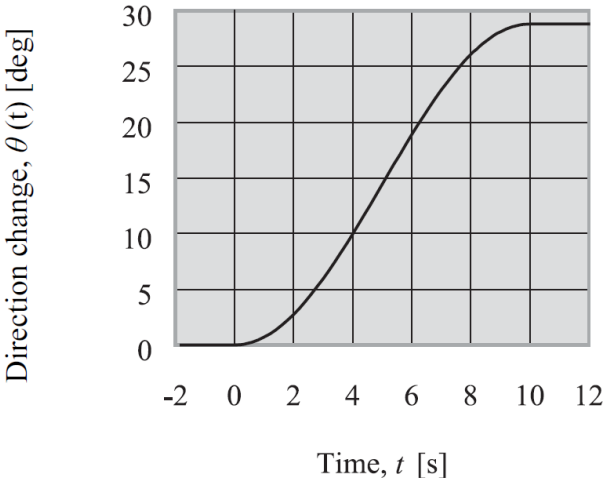


FIGURE 33: EXAMPLE OF AN EXTREME COHERENT GUST WITH DIRECTION CHANGE (AG, 2012).

In addition to the short-term distribution of wind speed, the long-term distribution of mean wind speed is also essential in wind energy projects to predict the energy yield at a specific site over a certain period. This long-term metrological data can be collected from weather stations, metrological buoys, etc. Hourly or seasonal distribution of mean wind speed can be approximated by their frequency distribution. The Weibull distribution as shown in Figure 34 is widely used at most sites and can be characterized by two parameters: the shape k and the scale c . The shape parameter describes how the wind speeds are distributed and the scale parameter is related to how spread the distribution of mean wind speeds. Moreover, the distribution of mean wind direction is also important for wind farm siting and load calculations. It is usually described by a wind rose.

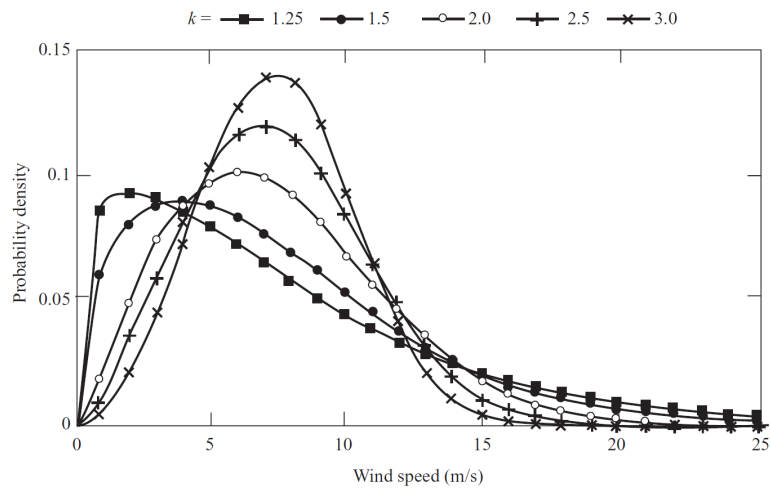


FIGURE 34: EXAMPLE OF WEIBULL'S DISTRIBUTION FOR DIFFERENT K AT CONSTANT MEAN WIND SPEED (BURTON ET AL., 2011)

5.3 WAVE LOADS

5.3.1 SEA STATE

In order to compute the wave loads on the structure, the sea state should be defined which is representative of the specific site. Sea state is generally characterized by surface waves driven by local wind and swell waves driven by a storm some distance away (Journée and Pinkster, 1997). Waves can be categorized into regular and irregular waves. Regular waves are characterized to be periodic and symmetric in space and time whereas irregular waves are characterized by randomness. However, the real state is formed by irregular waves. It is common to model irregular waves by superimposing sine waves with different heights, different periods, and partly also different directions. Indeed, a detailed description of sea climate is impossible and therefore some simplifications must be made to be able to describe the larger changes in characteristics of the wave pattern.

In offshore structural designs, it is generally assumed that the sea climate is stationary and homogeneous within periods of three hours (Journée and Pinkster, 1997) meaning that the significant wave height and peak period are constant. Sea states within such periods are known as short-term responses and can be described by either the probability of individual waves or stochastic wave spectra characterized by the significant wave height and period for each wave direction. Meanwhile, several wave spectrums had been developed to idealize the real sea state. The most common two spectrums are Pierson-Moskowitz (PM) spectrum developed by Pierson and Moskowitz (1964) and JONSWAP spectrum developed by Hasselmann et al. (1973). The former describes the fully developed sea state e.g in the Atlantic Ocean whereas the latter refers to sea states developed over a limited stretch of ocean, e.g in the North Sea.

The PM spectrum formulation described in equation 5-6 is based on the significant wave height (H_s) and a period, which is either the zero mean crossing period (T_z) or the peak spectral period (T_p). The two parameters H_s and T_p depend on the duration and strength of the acting wind and can be determined from other equations or from fitting to measured met-ocean data like 2D or 3D long-term statistics wave-scatter diagrams.

$$S_{PM}(\omega) = \frac{5}{16} \cdot H_s^2 \omega_p^4 \cdot \omega^{-5} \exp\left(-\frac{5}{4} \left(\frac{\omega}{\omega_p}\right)^{-4}\right) \quad 5-6$$

- ω = wave frequency in rad/s
- ω_p = spectral peak frequency in rad/s
- γ = peak enhancement parameter
- σ = spectral width parameter
- A_r = $1 - 0.287 \ln(\gamma)$ is a normalizing factor

JONSWAP spectrum is a modification of PM spectrum and uses a peak enhancement parameter derived from the significant wave height (H_s) and the peak spectral period (T_p). Since the sea state is not fully developed, the wave energy spectrum has more peaked. For simplification, $\gamma = 3.3$ is mostly considered for every sea state. Sometimes, the peak enhancement parameter for the JONSWAP-spectrum is chosen as $\gamma = 1$ for fatigue loads calculation. By taking $\gamma = 1$, JONSWAP spectrum also becomes equal to the PM-spectrum.

$$S_j(\omega) = A_\gamma S_{PM}(\omega) \gamma^{\exp\left(-0.5 \left(\frac{\omega - \omega_p}{\sigma \omega_p}\right)^2\right)} \quad 5-7$$

5.3.2 WATER LEVELS, TIDE AND STORM SURGES

In modelling hydrodynamic loads on offshore wind turbines, sea-level variations at a specific site should be taken into account since they can change wave and current loads. The variation of the sea surface level is characterized by storm surges and astronomical tides. Storm surges are generated by the combined action of wind and the ocean's water surface. Astronomical tides are generated by the gravitational pull of the moon. Figure 35 explains the definition of water levels.

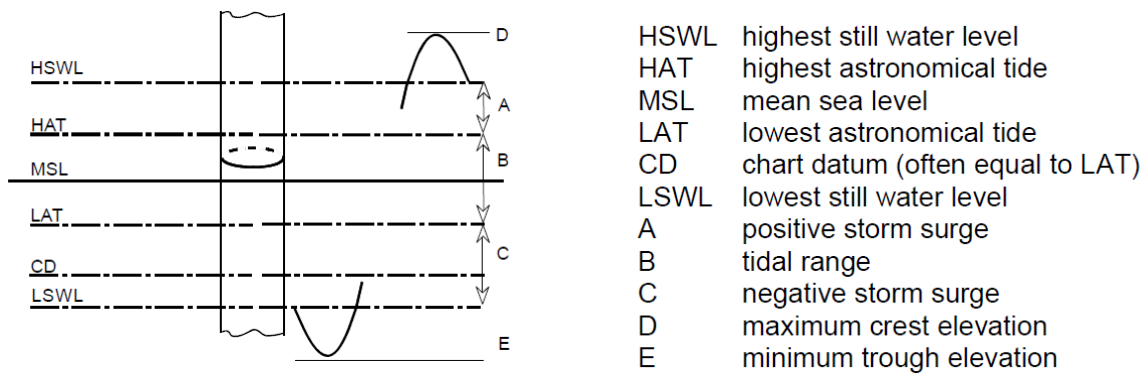


FIGURE 35: SEA LEVELS (DNVGL-RP-C205, 2017)

5.3.3 CALCULATION OF WAVE LOADS

Wave-induced loads on offshore structures are usually estimated by the wave particles kinematics of wave, i.e., wave velocities and accelerations. Wave particles kinematics can be grouped into regular and irregular waves. Regular waves can further be subdivided into linear and nonlinear waves.

Figure 36 illustrates the wave particles movement in different water depths. In deep water, the particles move in an orbital path and the motion decreases exponentially with increasing depth below the surface. In shallow water, the particles move in an elliptical orbit, but the motion remains almost the same over the entire depth. In General, the wave particles kinematics can be described by different wave theories. In intermediate water, which is the transition between deep and shallow water, the particles move in an elliptical path. IEC recommended selecting the appropriate models of wave kinematics depending on the relationship between the relative water depth and the relative wave height.

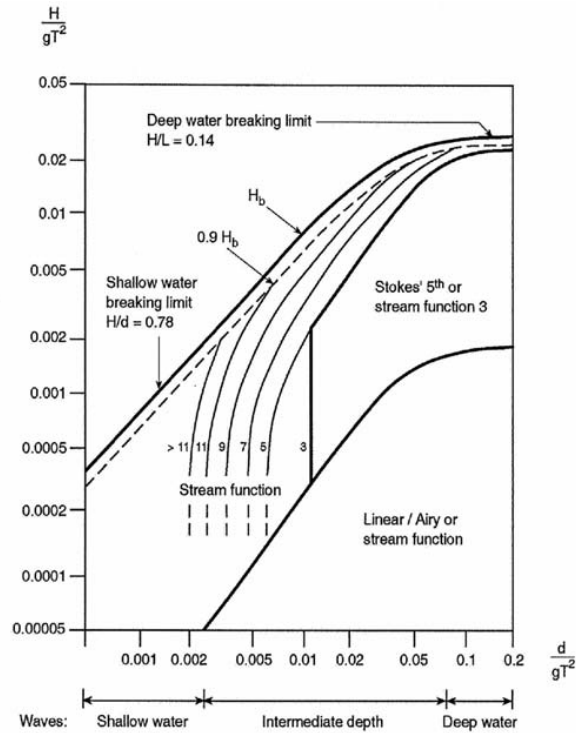


FIGURE 36: WAVE PARTICLES MOVEMENT IN DIFFERENT WATER DEPTH (DNVGL-RP-C205, 2017)

Airy wave theory also known as linear wave theory or Stokes 1st order theory is generally applicable for non-breaking waves with small amplitude, i.e. when the amplitude is smaller than the wave length and the water depth, in other words, for deep water and intermediate water waves, if the limitations for $H/(gT^2)$ and $d/(gT^2)$ as shown in Figure 36 are fulfilled. The wave profile is described as a sine function. According to linear wave theory, the horizontal wave velocity and horizontal wave acceleration for regular sinusoidal waves propagating on finite water depths can be determined using the following equations.

$$u = \frac{\pi H \cosh[k(z + d)]}{T \sinh(kd)} \cos\theta \quad 5-8$$

$$\dot{u} = \frac{2\pi^2 H \cosh[k(z + d)]}{T^2 \sinh(kd)} \sin\theta \quad 5-9$$

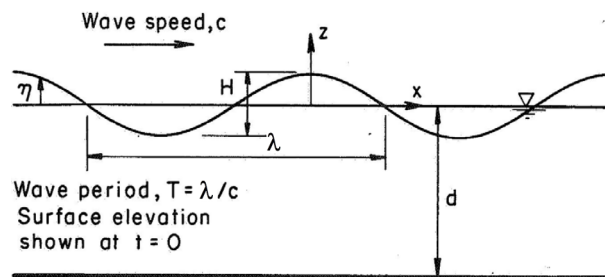


FIGURE 37: DEFINITION OF WAVE PROPAGATION (DNVGL-RP-C205, 2017)

Nevertheless, the wave kinematics for linear Airy's wave theory is only applicable up to still water level. This necessitates the extension of wave kinematics up to the free surface to include the hydrodynamic forces due to wave elevation. For this purpose, Wheeler's stretching method is widely used. The vertical coordinate z in equation 5-8 and 5-9 is stretched to z_s , as depicted in Figure 38 and z becomes:

$$z = \frac{z_s - \eta}{1 + \frac{\eta}{d}} \quad ; \quad -d < z < 0; \quad -d < z_s < \eta \tag{5-10}$$

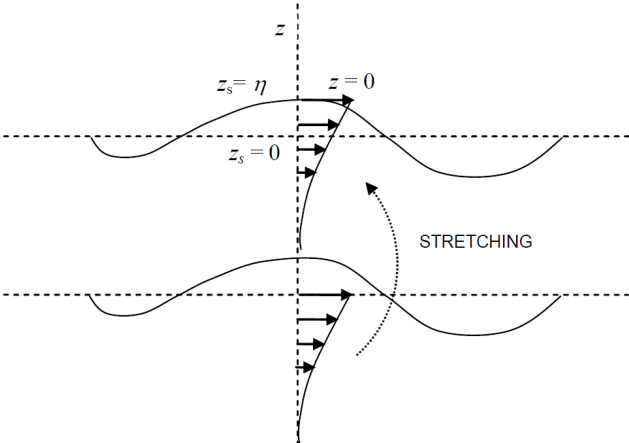


FIGURE 38: WHEELER'S STRETCHING METHOD (DNVGL-RP-C205, 2017)

By far, Stokes 1st order theory is applicable for many situations, but this theory is only valid for low steepness waves in relatively deep water. To simulate surface wave elevation with steeper wave crests and broader wave troughs, Stokes wave theory is extended to higher orders namely Stokes 2nd, 3rd and 5th order theory. According to the guideline prescribed by DNVGL (DNVGL-RP-C205, 2017), Stokes 5th order wave theory is applicable for higher waves having Ursell number (UR) up to 30.

Generally, there are two approaches to calculate wave loads such as diffraction analysis and Morison's method. A non-dimensional number which is the ratio of the structural member diameter to the wavelength of the incident indicates how the structure and waves interact and hence assists in the selection of the appropriate approach. Morison's method is applicable only for hydrodynamically transparent structures, in other words, for small structural members with ($D/\lambda < 0.2$). Morison's equation assumes that the wave loads on a fixed cylindrical strip can be described as the sum of the drag forces and inertia forces of the wave particle kinematics of incident waves:

$$F_{Morison} = C_M \cdot \rho_w \cdot A \cdot \dot{u} + \frac{1}{2} \cdot C_D \cdot \rho_w \cdot D \cdot |u|u \tag{5-11}$$

For a moving structure like the floating substructure, the velocity of the structure should also be taken into account. the Morison's equation becomes:

$$F_{Morison} = C_M \cdot \rho_w \cdot A \cdot \dot{u} - (C_M - 1) \cdot \rho_w \cdot A \cdot \dot{u}_{struct} + \frac{1}{2} \cdot C_D \cdot \rho_w \cdot D \cdot |u_{rel}| u_{rel}$$

Where,

C_M = coefficient of inertial force

C_D = coefficient of drag force

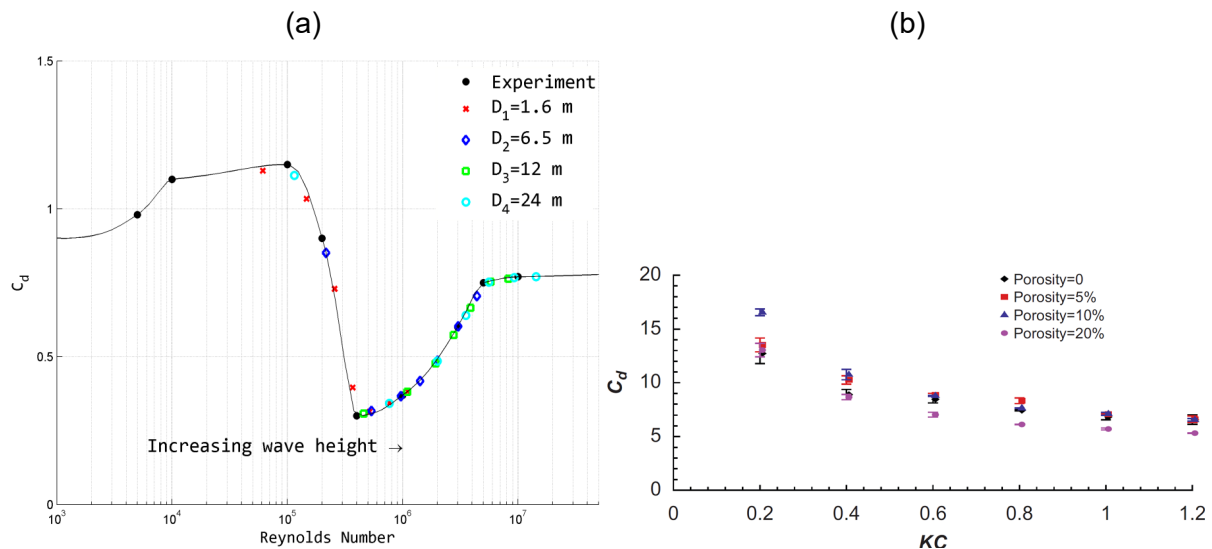


FIGURE 39: LATERAL DRAG COEFFICIENT AS A FUNCTION OF RE NUMBER (A) (ROBERTSON ET AL., 2014) AND AXIAL DRAG COEFFICIENT AS A FUNCTION OF KC (B) (TAO AND DRAY, 2008)

The hydrodynamic drag and mass coefficients C_D and C_M depend on the shape of the structure, state of flow around the structure, and roughness of the structure. Commonly, these values can be obtained from experimental results and their dependencies are described in terms of the Reynolds-number Re or Keulegan-Carpenter-number KC and the roughness of the structure. Extensive experiments have been done by Sarpkaya (1981) to obtain values for C_D and C_M . In the present study, the drag coefficients of Morison's members are determined according to Figure 39a and Figure 39b respectively. As can be seen clearly, both the transverse and axial drag coefficients change in fact with different sea states. Nonetheless, it was assumed that the drag coefficients are constant for all sea states in the present study.

In contrast, if the diameter of the structural member is considerably larger than the wavelength, the effect of reflection and radiation from the substructure on the wave field becomes important. Forces arising from radiated and diffracted waves can be estimated using diffraction theory also called potential flow theory. Radiation forces are generated by the oscillation of the structure whereas diffraction forces are caused by the excitation of incoming waves. Potential flow theory does not take viscous drag forces into account. On the other hand, radiation damping caused by waves generated at the motion of the body in or close to the free surface is included, which lacks in the Morison approach. In the present study, ANSYS AQWA is used to compute the frequency-dependent values such as the hydrodynamic added-mass and the

additional damping from the radiation problem as well as the frequency and direction-dependent first order wave-excitation force from the linear diffraction problem.

In addition to first-order wave kinematics, second-order wave kinematic can contribute to the dynamic response and extreme loads of semisubmersible platforms as highlighted by some studies. Therefore, second-order wave loads including difference- and sum frequencies are taken into account in the present study.

5.4 CURRENT LOADS

The presence of currents can affect the mean wave loads and hence the platform motions especially surge, sway, and yaw motions which are greatly influenced by the mooring system. In conditions where current and wave travel in the opposite direction, the wave height increases because the waves are refracted by the current, whereas the following currents reduce the wave height (Peregrine and Jonsson, 1983). Therefore, current velocity and direction should be taken into account in load simulations of FOWT except for fatigue design. Because fatigue loads are influenced by cyclic loads and current loads can increase the hydrodynamic damping of the floater, reducing cyclic loads. Several models exist to model current-induced hydrodynamic loads. In the present study, a simple Morison's equation is applied in which the design current load F_D is estimated through the viscous drag terms C_D of the strip-theory members as in equation 5-13, where $D(z)$ is the diameter of the member at elevation z . The design current pressure q_D at elevation z is determined according to equation 5-14 where U_D is the design current velocity at elevation z and ρ_w is the density of sea water.

$$F_D(z) = C_D \cdot q_D(z) \cdot D(z) \quad 5-13$$

$$q_D(z) = \frac{\rho_w}{2} U_D^2(z) \quad 5-14$$

5.5 MOORING LINE DESIGN LOADS

Mooring line design loads are computed using nonlinear quasi-static mooring module MAP++ developed by NREL. The analytical formulation of the mooring system is based on the elastic cables freely suspended between two points as depicted in Figure 40. For semisubmersible platforms with slack catenary mooring lines, either a portion or no portion of the mooring lines lie on the seabed depending on the state of operations. The mooring system module decides which state is relevant and applies relevant equation of motion accordingly. For instance, when a portion of mooring lines rest on the seabed, the nonlinear equation for effective fairlead tensions H_F and V_F can be expressed as in equation 5-15. Given the properties of mooring line such as length L , weight w , stiffness of mooring line EA and coefficient of static friction C_B ,

nonlinear equations 5-15 and 5-16 are solved using a Newton-Raphson method. In equations, x_F and z_F refer to the position of the fairlead relative to the anchor of the mooring line.

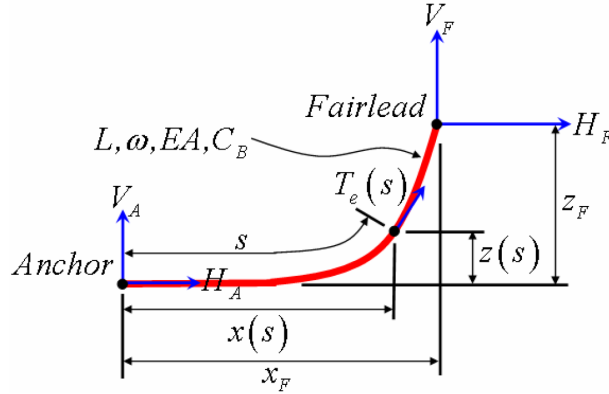


FIGURE 40: GEOMETRY OF MOORING LINE (JONKMAN, 2007)

$$x_F(H_F, V_F) = L - \frac{V_F}{w} + \frac{H_F}{w} \ln \left[\frac{V_F}{H_F} + \sqrt{1 + \left(\frac{V_F}{H_F} \right)^2} \right] + \frac{H_F L}{EA} \quad 5-15$$

$$+ \frac{C_B w}{2EA} \left[- \left(L - \frac{V_F}{w} \right)^2 + \left(L - \frac{V_F}{w} - \frac{H_F}{C_B w} \right) \text{Max} \left(L - \frac{V_F}{w} - \frac{H_F}{C_B w}, 0 \right) \right]$$

$$z_F(H_F, V_F) = \frac{H_F}{w} \left[\sqrt{1 + \left(\frac{V_F}{H_F} \right)^2} - \sqrt{1 + \left(\frac{V_F - wL}{H_F} \right)^2} \right] + \frac{1}{EA} \left(V_F L - \frac{wL^2}{2} \right) \quad 5-16$$

$$T_e = \sqrt{H_F^2 + V_F^2} \quad 5-17$$

$$H_A = \text{Max} \left(H_F - C_B w \left(L - \frac{V_F}{w} \right), 0 \right) \quad 5-18$$

The first two terms of equation 5-15 characterize a portion of the mooring line resting on the sea bed and projected base length. The third term characterizes rope elongation and the last two terms characterize the stretched portion of the mooring lines through static friction with the seabed. 5-17 and 5-18 correspond to the effective tension in the mooring line at point e and effective tension in the mooring line at the anchor. The vertical tension in the mooring line at the anchor is zero, $V_A = 0$, when a portion of the mooring line lie horizontally on the seabed meaning $L - \frac{V_F}{w} > 0$. Otherwise, $V_A = V_F - wL$. For more information, the author would recommend studying Masciola (2016).

5.6 REFERENCE SITE AND ITS METOCEAN DATA

CART wind turbine is envisioned to be located 20 km offshore to mitigate the visual impacts from the coastline. The water depth is assumed to be 50 m. Although CART wind turbine is envisioned to be deployed off Vietnam coastline in the South China Sea, no met-ocean data were publicly available for this site to date. Therefore, Biscay Marine Energy Platform (BIMEP) Area was selected after examining the following criteria: data availability, and suitability of meteorological and oceanographic (metocean) conditions to obtain representative environmental conditions for floating offshore wind turbines. Nevertheless, the met-ocean data are set to a scale of 1:2 in the present work due to the fact that the environmental conditions in the South China Sea are very benign and the CART wind turbine itself is a medium-sized one.

With the above assumption, a brief description of the met-ocean conditions characterized at the referenced site is given in the following Table 14.

TABLE 14: SEA STATES

| Wind speed V_{hub} [m/s] | Normal Sea State | | Severe Sea State | |
|-------------------------------|--------------------------|------------------------|--------------------------|------------------------|
| | Wave height H_s [m] | Wave Period T [s] | Wave height H_s [m] | Wave Period T [s] |
| 3 | 0.20 | 1.58 | 3.15 | 4.45 |
| 4 | 0.20 | 1.58 | 3.15 | 4.45 |
| 5 | 0.20 | 1.58 | 3.15 | 4.45 |
| 6 | 0.40 | 2.24 | 3.15 | 4.45 |
| 7 | 0.60 | 2.75 | 3.15 | 4.45 |
| 8 | 0.90 | 3.36 | 3.20 | 4.48 |
| 9 | 1.10 | 3.72 | 3.25 | 4.52 |
| 10 | 1.40 | 4.19 | 3.50 | 4.69 |
| 11 | 1.40 | 4.19 | 3.60 | 4.75 |
| 12 | 1.60 | 4.48 | 3.60 | 4.75 |
| 13 | 1.80 | 4.75 | 3.65 | 4.79 |
| 14 | 1.90 | 4.89 | 3.65 | 4.79 |
| 15 | 2.10 | 5.14 | 3.70 | 4.82 |
| 16 | 2.40 | 5.49 | 3.70 | 4.82 |
| 17 | 2.60 | 5.71 | 3.75 | 4.85 |
| 18 | 2.60 | 5.71 | 3.75 | 4.85 |
| 19 | 2.90 | 6.04 | 3.75 | 4.85 |
| 20 | 3.00 | 6.14 | 3.80 | 4.89 |

The variation in sea level for normal conditions is set to 0.875 m. For extreme sea conditions, sea level variation for a return period of 10 years was set to 1.25 m and for a return period of 50 years was set to 1.275 m respectively.

The current speed is assumed to have no vertical gradient close to the free water surface. The mean current velocity is set to 0.18 m/s for normal conditions and 0.65 for extreme conditions. The current direction is taken to be 90°.

6 LOAD ANALYSIS

The following sections cover load analyses of onshore and offshore CART systems. Fully integrated aero-hydro-servo-elastic simulations are carried out in order to characterize the dynamic response of the system, identify critical loads of each component for both systems, and highlight the impacts brought about by the floating support structure.

6.1 LOAD COMPONENTS AND REFERENCE COORDINATE SYSTEMS

The load components which shall be examined in this study are listed in Table 15. The second and third column list the symbol of parameters which will be evaluated and their corresponding units. The first column presents a short description of the parameters. They are measured from their corresponding reference coordinate system defined in OpenFAST simulation tool. Thereby, the last letter n refers to the nacelle coordinate system, s refers to the shaft coordinate system, c refers to the chord coordinate system, b refers to blade coordinate system, p refers to the tower-top coordinate system, and t refers to the tower bottom coordinate system respectively. For instance, TwrBsMxt means tower base side-to-side moment measured from tower bottom coordinate system. More information can be found in Jonkman and Buhl (2005) and Jonkman et al., (2014) respectively.

TABLE 15: MEASURED LOAD COMPONENTS

| Description | Symbol | Entity |
|--|-----------|--------------------|
| Angular speed of the rotor | RotSpeed | rpm |
| Angular speed of the generator | GenSpeed | rpm |
| Electrical generator torque | GenTq | kN-m |
| Electrical generator power | GenPwr | kW |
| Rotor thrust force | LSShftFxa | kN |
| Non-rotating shaft shear force directed along the y-axis | LSShftFys | kN |
| Non-rotating shaft shear force directed along the z-axis | LSShftFzs | kN |
| Rotor azimuth angle (position) | LSSTipPxa | deg |
| Nacelle yaw angle (position) | YawPzn | deg |
| Nacelle yaw angular velocity | NacYawV | deg/s |
| Nacelle yaw angular acceleration | NacYawA | deg/s ² |
| Angle of attack at Blade 1, Node 1 | B1N1Alph | deg |
| Angle of attack at Blade 1, Node 2 | B1N1Alph | deg |
| Angle of attack at Blade 1, Node 3 | B1N1Alph | deg |
| Nacelle acceleration directed along x-axis | NcIMUTAxS | m/s ² |
| Nacelle acceleration directed along y-axis | NcIMUTAyS | m/s ² |

| Description | Symbol | Entity |
|--|-----------|------------------|
| Nacelle acceleration directed along z-axis | NcIMUTAys | m/s ² |
| Non-rotating shaft bending moment about y-axis | LSSGagMys | kN-m |
| Non-rotating shaft bending moment about z-axis | LSSGagMzs | kN-m |
| Rotor torque | LSShftMxa | kN-m |
| Shaft brake torque | HSSBrTq | kN-m |
| Blade 1 out-of-plane tip deflection | TipDxc1 | m |
| Blade 1 in-plane tip deflection | TipDyc1 | m |
| Blade 1 axial tip deflection | TipRDzc1 | m |
| Blade 2 out-of-plane tip deflection | TipDxc2 | m |
| Blade 2 in-plane tip deflection | TipDyc2 | m |
| Blade 2 axial tip deflection | TipRDzc2 | m |
| Blade 1 tip-to-tower clearance | TipClrnc1 | m |
| Blade 2 tip-to-tower clearance | TipClrnc2 | m |
| Blade 1 out-of-plane shear force at the blade root | RootFxc1 | kN |
| Blade 1 in-plane shear force at the blade root | RootFyc1 | kN |
| Blade 1 axial force at the blade root | RootFzc1 | kN |
| Blade 1 in-plane moment at the blade root | RootMxc1 | kN-m |
| Blade 1 out-of-plane moment at the blade root | RootMyc1 | kN-m |
| Blade 1 pitching moment at the blade root | RootMzc1 | kN-m |
| Blade 1 edgewise moment at the blade root | RootMxb1 | kN-m |
| Blade 1 flapwise moment at the blade root | RootMyb1 | kN-m |
| Blade 2 out-of-plane shear force at the blade root | RootFxc2 | kN |
| Blade 2 in-plane shear force at the blade root | RootFyc2 | kN |
| Blade 2 axial force at the blade root | RootFzc2 | kN |
| Blade 2 in-plane moment at the blade root | RootMxc2 | kN-m |
| Blade 2 out-of-plane moment at the blade root | RootMyc2 | kN-m |
| Blade 2 pitching moment at the blade root | RootMzc2 | kN-m |
| Blade 2 edgewise moment at the blade root | RootMxb2 | kN-m |
| Blade 2 flapwise moment at the blade root | RootMyb2 | kN-m |
| Tower-top / yaw bearing fore-aft (nonrotating) shear force | YawBrFxp | kN |
| Tower-top / yaw bearing side-to-side (nonrotating) shear force | YawBrFyp | kN |
| Tower-top / yaw bearing axial force | YawBrFzp | kN |
| Nonrotating tower-top / yaw bearing roll moment | YawBrMxp | kN-m |
| Nonrotating tower-top / yaw bearing pitch moment | YawBrMyp | kN-m |

| Description | Symbol | Entity |
|--|-----------|--------|
| Tower-top / yaw bearing yaw moment | YawBrMzp | kN-m |
| Tower-top / yaw bearing fore-aft displacement | YawBrTDxt | m |
| Tower-top / yaw bearing side-side displacement | YawBrTDyt | m |
| Tower base fore-aft shear force | TwrBsFxt | kN |
| Tower base side-to-side shear force | TwrBsFyt | kN |
| Tower base axial force | TwrBsFzt | kN |
| Tower base side-to-side moment | TwrBsMxt | kN-m |
| Tower base fore-aft moment | TwrBsMyt | kN-m |
| Tower base torsional moment | TwrBsMzt | kN-m |
| Platform horizontal surge (translational) displacement | PtfmSurge | m |
| Platform horizontal sway (translational) displacement | PtfmSway | m |
| Platform vertical heave (translational) displacement | PtfmHeave | m |
| Platform roll rotational displacement | PtfmRoll | deg |
| Platform pitch rotational displacement | PtfmPitch | deg |
| Platform yaw rotational displacement | PtfmYaw | deg |
| Tension at fairlead in mooring line 1 | T[1] | N |
| Tension at fairlead in mooring line 2 | T[2] | N |
| Tension at fairlead in mooring line 3 | T[3] | N |
| Tension at anchor in mooring line 1 | T_a[1] | N |
| Tension at anchor in mooring line 2 | T_a[2] | N |
| Tension at anchor in mooring line 3 | T_a[3] | N |

6.2 DESIGN LOAD CASES

The DLCs as specified in the design requirements for offshore wind turbines by IEC can be categorized into ultimate and fatigue load cases. The ultimate load analyses are performed to verify the ultimate strength resistance of a component due to very rare events. These events mainly include power production in extreme turbulence, power production in severe sea states, the turbine being parked during a 50-year storm event, and during a transient event triggered by a grid loss. Usually, extreme loads are quite difficult to predict and statistical extrapolation of the load distribution is applied to compute the extreme loads. On the other hand, fatigue load analyses are performed to verify the damage tolerance of the system due to cyclic loadings, which needs to consider environmental conditions over a long period. Fatigue loads are extremely smaller than static loads acting on the structure. However, the accumulation of these repetitive loads results in a progressive crack in the material and this can finally lead to the collapse of the structure.

IEC guidelines prescribed a number of load cases to verify a concept. Nevertheless, it could result in more than 10^3 load cases if all environmental states were considered. It is time-consuming and also computationally demanding to run all DLCs. For these reasons, design load cases which reflect the most significant operational conditions that the CART system might experience during its design life were considered in this study. In addition to this, the reduced set of load cases were investigated following the recommended practice DNVGL-RP-0286 (2019) and the work of GL (2015) and Jonkman (2007) in order to reduce the bandwidth of the design process, focusing only on a subset of critical design load cases. As mentioned in section 4.5.2, the control algorithm does not include logic for start-up and shutdown events. On that account, load cases related to start-up and shutdown events are not carried out. Moreover, load cases namely DLCs 8.x defining transport, installation, and maintenance, DLCs 9.x defining drifting sea ice events, DLCs 10.x defining temperature effects, DLCs 11.x defining earthquake, DLC 12.x defining wind farm influence, are not carried out in this study. This leaves the following set of environmental states:

- Power production: 1.1, 1.2, 1.3, 1.4, 1.6
- Power production with faults: 2.1, 2.2, 2.3
- Parked: 6.1, 6.2
- Parked and fault: 7.1, 7.2

These load cases are divided into normal operating conditions, extreme conditions with faults, and severe conditions with the worst consequences. For normal conditions, load cases defining power production namely DLC 1.1, DLC 1.2, DLC 1.3, DLC 1.4 were considered. For extreme conditions with faults, load cases defining extreme sea states and power production in faults namely DLC 1.6, DLC 2.3, and DLC 6.1 were considered. For survival conditions, load cases defining faults events with the worst consequences namely DLC 2.1, DLC 2.2, DLC 6.2, DLC6.3, DLC7.1a, and DLC 7.2 were considered. Table 16 lists the summary of selected design loads cases along with their wind models, wave models, and partial safety factor (PSF). Considering each environmental condition for each load case, a total of 1623 simulations were run for onshore wind turbine and 2352 simulations for offshore wind turbine. It is worth mentioning here again that all wind models both deterministic and turbulent wind are kept the same for both onshore and offshore CART system in order to compare the responses of both systems fairly. This means that wind shear component of 0.14 is used for the onshore CART wind turbine instead of the value of 0.2 prescribed by IEC 61400-1. Both systems also use the same torque control concept.

In all load cases, rotor imbalances, in other words, aerodynamic and mass imbalance are taken into account. According to the Germanischer Lloyd (AG, 2012), an aerodynamic imbalance in terms of a pitch angle deviation of $\pm 0.3^\circ$ can be assumed if a verified tolerance is not available.

Therefore, in the present study, a pitch angle deviation of 0.3° was applied to blade two whereas no deviation in pitch angle was considered for blade one. Similar to aerodynamic imbalance, no production tolerance is available for the investigated rotor blades. Therefore, as a rule of thumb, a mass imbalance was taken into account by setting blade two as much as 0.05% heavier than blade one in the present study.

TABLE 16: SELECTED DESIGN LOAD CASES

| DLC | Wind condition | Wave conditions | Events | PSF | No. load case |
|--|--|--|--------------------------------------|------|---------------|
| (1) Power Production | | | | | |
| 1.1 | NTM, $V_{in} < V_{hub} < V_{out}$ | NSS, $H_s = E [H_s V_{hub}]$, $\beta = 0^\circ$ | Normal | 1.25 | 180 |
| 1.2 | NTM, $V_{in} < V_{hub} < V_{out}$ | NSS, $H_s = E [H_s V_{hub}]$, $\beta = 0^\circ$ | Normal | 1.0 | 180 |
| 1.3 | ETM, $V_{in} < V_{hub} < V_{out}$ | NSS, $H_s = E [H_s V_{hub}]$, $\beta = 0^\circ$ | Normal | 1.35 | 180 |
| 1.4 | ECD, $V_{hub} = V_r - 2m/s, V_r, V_r + 2m/s$ | NSS, $H_s = E [H_s V_{hub}]$, $\beta = 0^\circ$ | Normal | 1.35 | 486 |
| 1.6 | NTM, $V_{in} < V_{hub} < V_{out}$ | SSS, $H_s = H_{s50}$, $\beta = 0^\circ$ | Normal | 1.35 | 180 |
| (2) Power production plus occurrence of fault | | | | | |
| 2.1 | NTM, $V_{in} < V_{hub} < V_{out}$ | NSS, $H_s = E [H_s V_{hub}]$, $\beta = 0^\circ$ | Grid loss | 1.35 | 12 |
| 2.2 | NTM, $V_{in} < V_{hub} < V_{out}$ | NSS, $H_s = E [H_s V_{hub}]$, $\beta = 0^\circ$ | Faults in yaw system | 1.10 | 54 |
| 2.3 | EOG, $V_{hub} = V_r \pm 2m/s, V_{out}$ | NSS, $H_s = E [H_s V_{hub}]$, $\beta = 0^\circ$ | Grid loss | 1.10 | 60 |
| (6) Parked | | | | | |
| 6.1 | EWM, $V_{hub} = V_{ref}$ | ESS, $H_s = H_{s,50}$, $\beta = 0^\circ, \pm 30^\circ$ | Yaw = 0, $\pm 8^\circ$ | 1.35 | 370 |
| 6.2a | EWM, $V_{hub} = V_{ref}$ | ESS, $H_s = H_{s,50}$, $\beta = 0^\circ, \pm 30^\circ$ | $180^\circ < \text{Yaw} < 180^\circ$ | 1.10 | 108 |
| 6.3 | EWM, $V_{hub} = V_{ref}$ | ESS, $H_s = H_{s,1}$, $\beta = 0^\circ, \pm 30^\circ$ | $-20^\circ < \text{Yaw} < 20^\circ$ | 1.35 | 54 |
| (7) Parked and fault | | | | | |
| 7.1a | EWM, $V_{hub} = V_{ref}$ | ESS, $H_s = H_{s,1}$, $\beta = 0^\circ, \pm 30^\circ$ | Yaw = 0, $\pm 8^\circ$ | 1.10 | 108 |
| 7.2 | NTM, $V_{in} < V_{hub} < V_{out}$ | NSS, $H_s = E [H_s V_{hub}]$, $\beta = 0^\circ, \pm 30^\circ$ | Yaw = 0, $\pm 8^\circ$ | 1.35 | 380 |

The time-series results are post-processed using either MCrunch (Buhl, 2008) or MExtremes (Hayman, 2015) developed by NREL. It is possible in MCrunch to generate each load component in terms of statistical value: minimum, mean, maximum, standard deviation, skewness, and range. When evaluating the results, the first 60 s of the simulation are discarded to get rid of transient effects. For each mean wind speed, the mean of maximum loads resulting from different time series of turbulent wind is determined. Hence, the maximum value among the averaged mean of maximum loads of all wind velocities is chosen as a representative for the maximum characteristic design load of each component.

6.3 NORMAL OPERATING CONDITIONS

As mentioned in the previous section, load cases defining power production namely DLC 1.1, DLC 1.2, DLC 1.3, DLC 1.4 were considered for normal operations. DLC 1.1 relates to power production in normal turbulence wind and normal sea state. Simulations are performed with a yaw misalignment of $\pm 8^\circ$ as prescribed by IEC guidelines in order to take possible delay in the yaw control system into account. A wind speed interval of 2 m/s was considered. For each environmental condition, simulations were performed with 10 min mean wind speed containing six different wind seeds and a stochastic irregular wave model containing six different wave seeds. This results in a 1-hr simulation length for each environmental condition.

DLC 1.2 deals with power production in normal turbulence wind and normal sea state. This particular load case is carried out to analyse fatigue loads of wind turbine over a period of time during normal operating conditions. A joint probability distribution of the significant wave height H_s , the peak spectral period T_p , and hub-height wind speed V_{hub} was considered in modelling the sea state. Currents are ignored and the wind-wave directionality was assumed to be unidirectional. A misaligned yaw between the direction of average inflow wind and the direction of rotor axis was taken to be $\pm 8^\circ$. Similar to DLC 1.1, a wind speed interval of 2 m/s was considered. For each environmental condition, simulations were performed with six different wind and wave seeds.

Simulated environmental conditions for DLC 1.3 are the same as DLC 1.1 except for the wind models, which use the Extreme Turbulence Model (ETM). Yaw misalignment of $\pm 8^\circ$ was taken into account. Similar to DLC 1.1, turbulence wind field and stochastic waves were generated with six different wind and wave seeds at each mean wind speed. Wind and wave propagate in the same direction. A simple normal current model is simulated assigning the current velocity given in section 5.6.

DLC 1.4 deals with power production in an extreme coherent gust with a simultaneous change of the wind direction. The wind speed close to rated wind speed is considered. The magnitude of the wind speed increases along with the change in wind direction. The ECD event starts at

60 s and the duration of wind gust is 10 s. The extreme coherent gust has a magnitude of 15 m/s. Yaw misalignment of $\pm 8^\circ$ was taken into account. Different from the above load cases, the change in initial rotor azimuth angle of 0° to 360° with an interval of 45° was simulated. According to IEC 61400-3, the vertical inflow was considered to be inclined 0° and $\pm 8^\circ$.

The following subsections discuss the dynamic response of onshore and offshore CART system during normal operating conditions and identify the design driving load cases for normal conditions. It also highlights the impact on structural loads brought about by the floating substructure.

6.3.1 RESDYNAMIC RESPONSE OF CART SYSTEM DURING NORMAL OPERATION

In order to gain insight into the dynamic response of the CART system in normal operating conditions, several load components resulted from each simulation in DLC 1.1 are analysed in terms of their statistical values: minimum, mean, maximum. Statistical variation of loads plays an important role to assess the structural safety of a wind turbine. Figure 41 shows how the statistical values of several load components change with the wind speed. The mean values are indicated by star, the minimum values are indicated by circle and the maximum values are indicated by square respectively. These values were already weighted with PSF described in section 6.2.

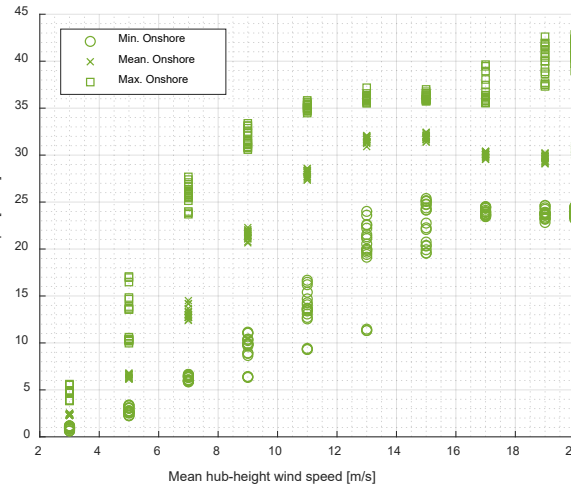
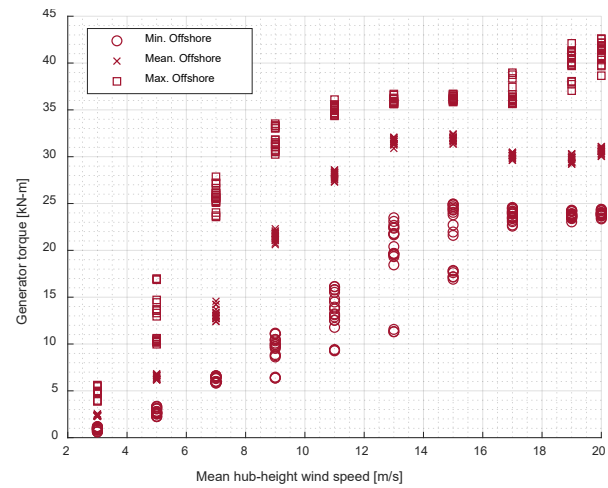
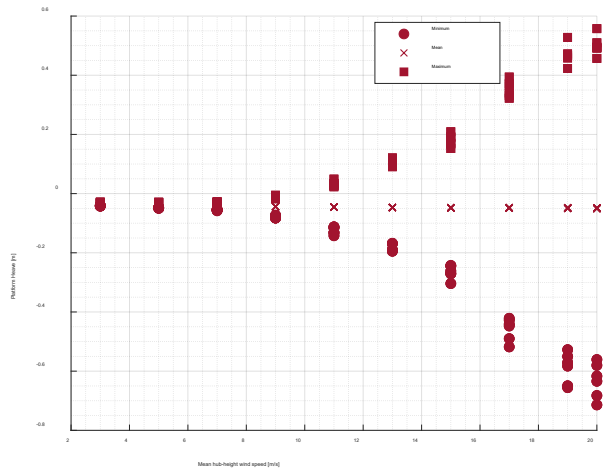
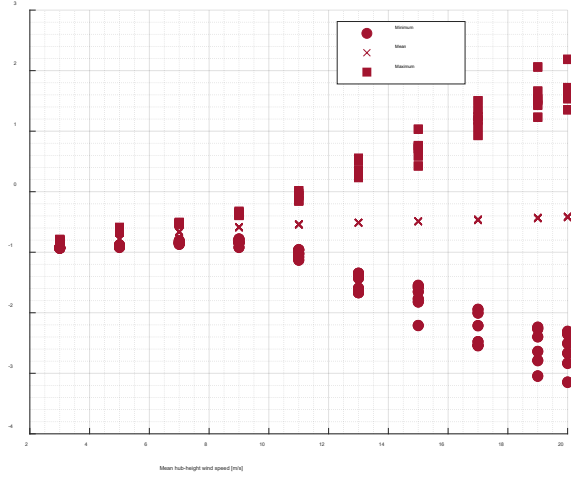
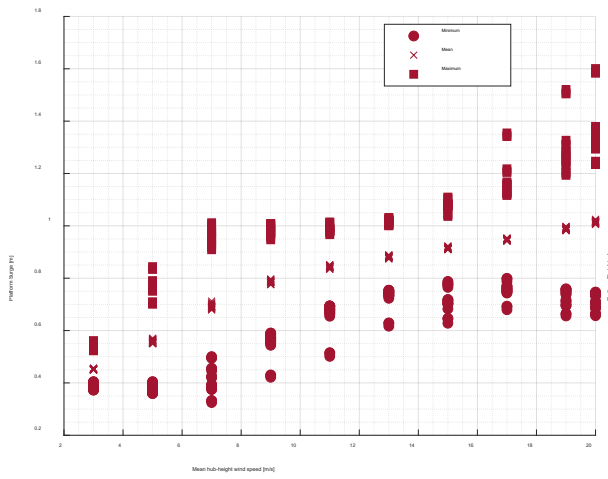
From the statistical values in the figures, we can observe that the mean values of rotor speed, generator torque, generator power, and blade 1 out of plane deflection are similar between offshore and onshore CART system. However, there is a small difference in mean values of tower-top fore-aft deflection and tower-top bending moment between offshore and onshore CART system. Mean values of the rotor speed increase linearly with mean hub-height wind speed in partial load regions, which is between cut-in wind speed of 3.0 m/s and wind speed of 7 m/s. This is because the system operates with a constant tip-speed ratio and optimal power coefficient to extract the maximum available power from the wind. After that the rotor speed approaches its rated value. Thus, it needs to be slow down by the torque controller not to exceed its rated rotor speed. In the full load region, the rotor operates with almost constant speed. Similarly, the generator torque increases quadratically with the mean wind speed and the generator power increases cubically with the mean wind speed in partial load regions. In the full load region, the generator torque increases until the rated generator power is reached and decreased after that when it enters into the stall region.

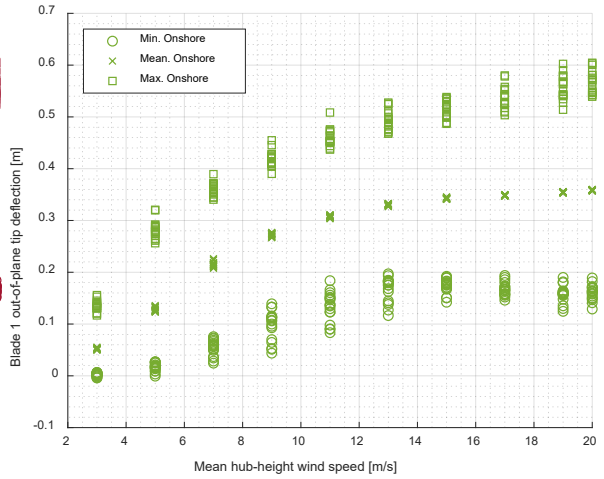
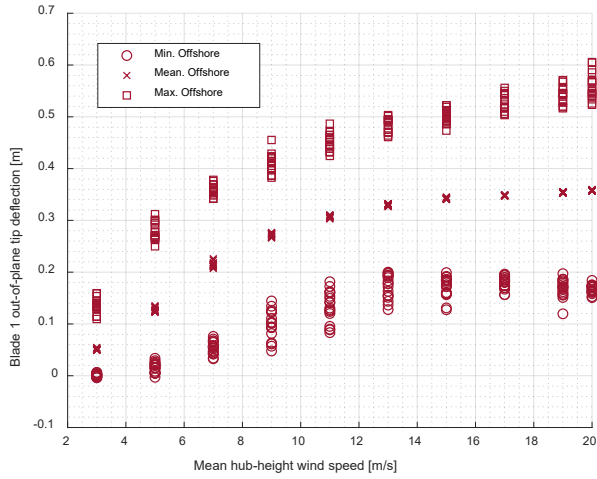
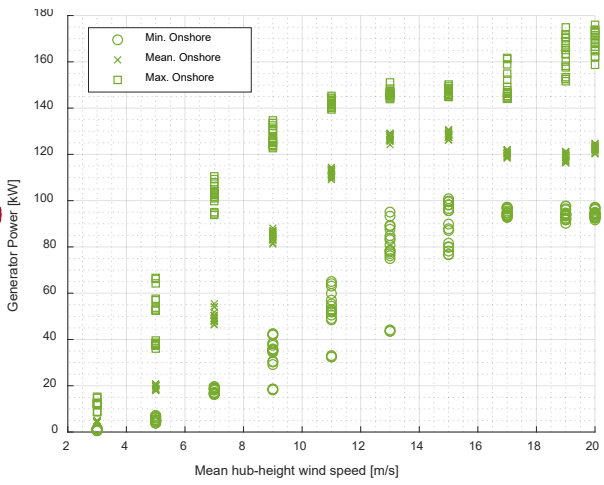
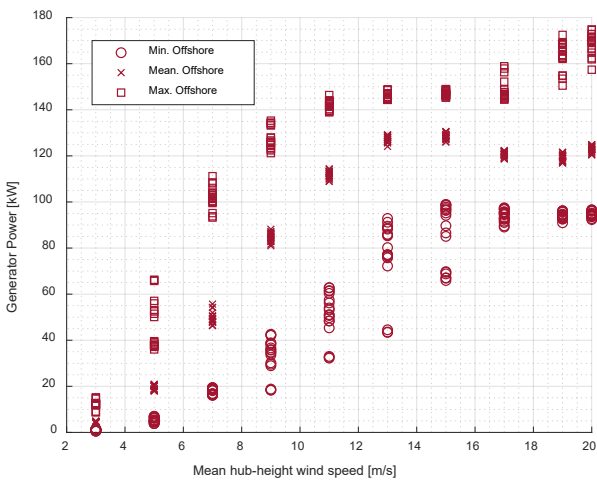
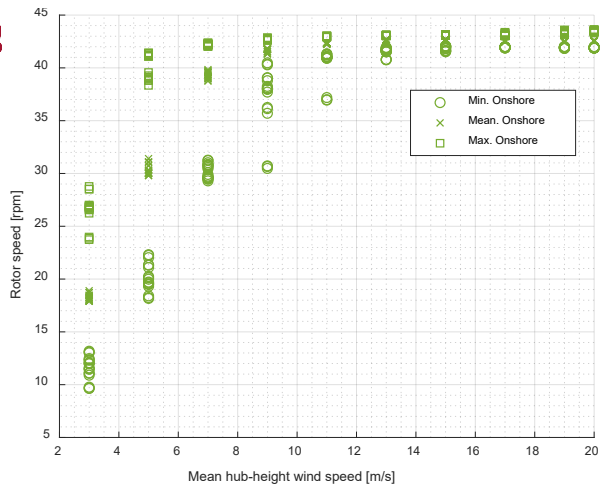
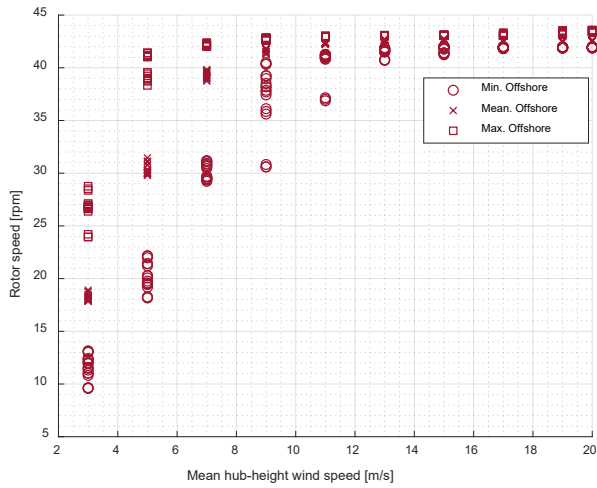
Based on the findings, the mean value of out-of-plane tip deflection and out-of-plane blade bending moment increase with the increase in wind speed. This can be explained by the variation of mean values of steady-state response of the rotor thrust discussed in section 4.5.6. This behaviour can be observed in any stall-regulated wind turbine because it has no active aerodynamic control system to reduce the rotor thrust in high winds. As a result, the rotor thrust

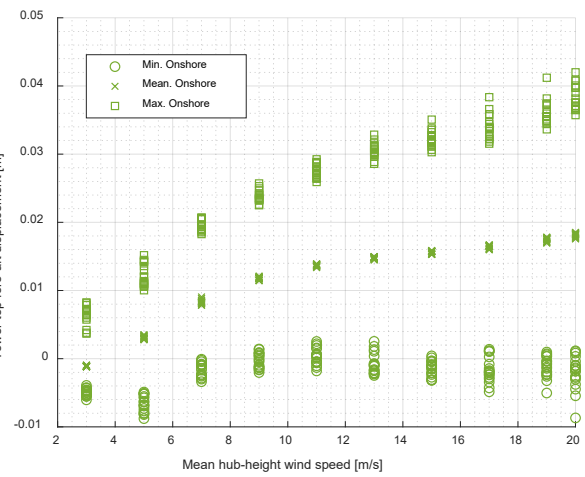
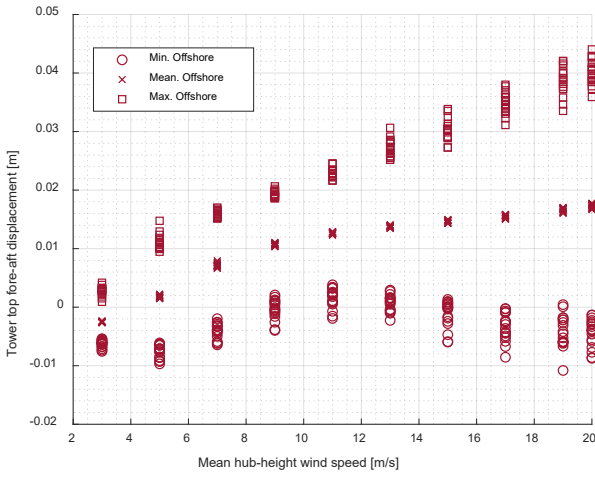
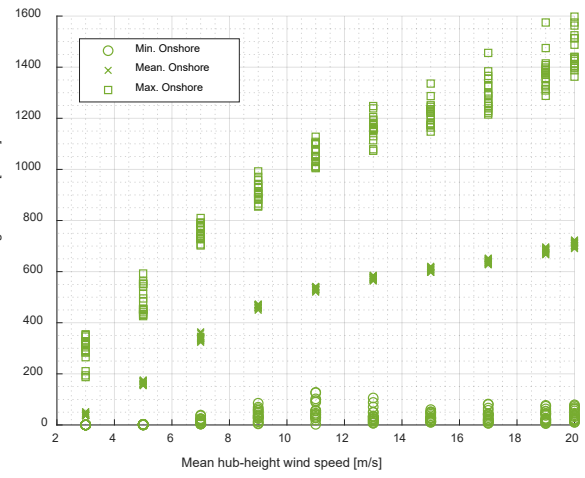
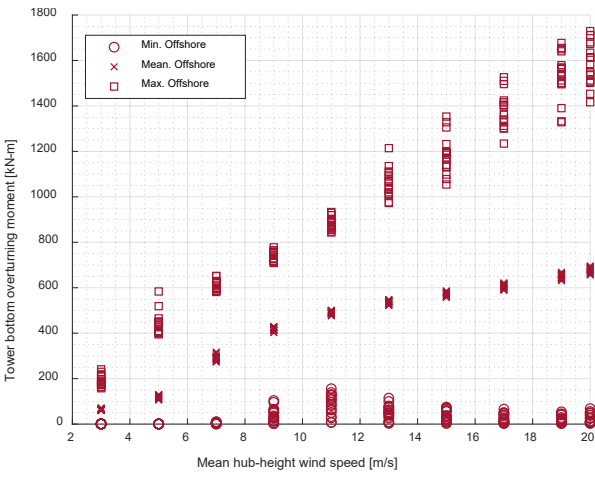
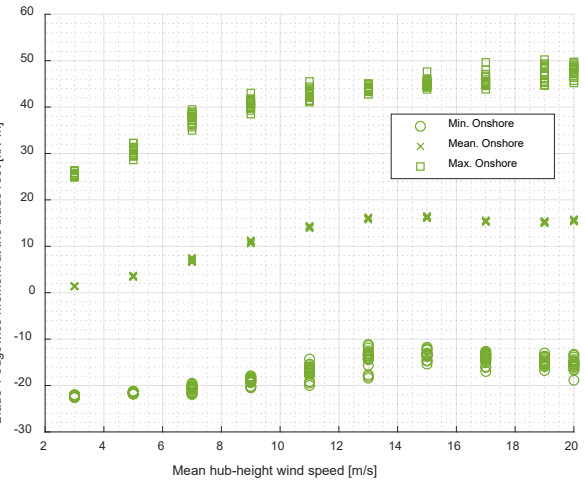
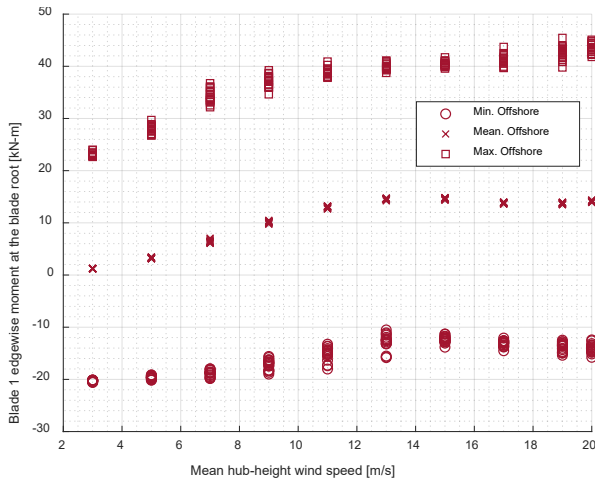
continuously increases with the increase in wind speed. This response is also noticeable in the platform surge motions. By the same token, the pitch motion follows a similar pattern of the thrust curve. The mean value of heave motion is nearly zero which reflects oscillation in still water level. Unlike other load components, the difference in the mean value of tower-top fore-aft displacement and tower-bottom bending moment is sensitive to the floater motions due to an inverted pendulum effect which causes coupled response of wind turbine with the floater, leading to large structural loads. In addition to inertia forces due to tower deflection and floater motions, moment arms due to tower deflection or platform motion also contribute to the tower-bottom bending moments.

Although the mean values of most parameters are similar between the offshore and onshore CART system, the excursions of the minimum and maximum values for the offshore CART system are larger. The variability of the minimum and maximum values for floater motions increases significantly with the increase in mean wind speed due to the presence of high wave amplitudes. Thus, the widest spread of the excursions was observed in floater pitch and heave motions. This reflects the nature of the semisubmersible floater, which moves with the surface waves. Floater pitch motion causes large fluctuations in power and generator torque in high winds. Similarly, large excursions are observed in tower-top fore-aft displacement and tower bottom fore-aft moment of the offshore CART system due to an inverted pendulum effect as mentioned above, which is mainly contributed from inertial forces due to tower deflection or platform motions. The narrowest excursion was observed in rotor speed especially in high winds for both the offshore and onshore CART system.

Taken altogether, the difference between the offshore and onshore CART system was moderate. The dynamic response of the system resulted from DLC 1.3 and DLC 1.4 are not further discussed here. Obviously, the responses become larger for these load cases since they greatly influence the extreme loads in normal operations.







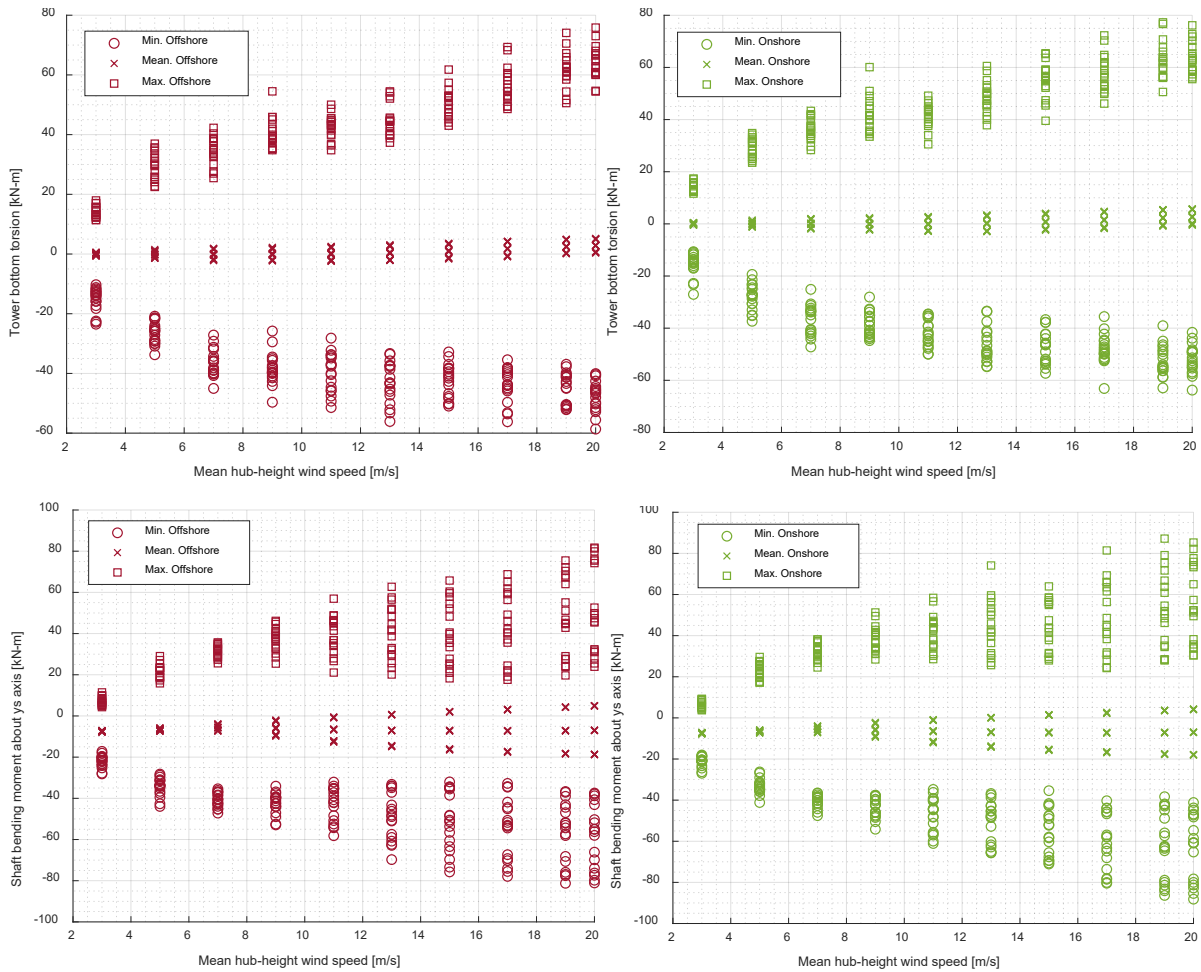


FIGURE 41: STATISTICS VALUES OF RESPONSE OF CART SYSTEM AS A FUNCTION OF WIND SPEED FOR EACH SIMULATION IN DLC 1.1

6.3.2 DESIGN DRIVING LOAD CASES IN NORMAL OPERATING CONDITIONS

The time-series results from all simulations in normal operating conditions are post-processed using NREL MExtremes to identify the design driving load cases and quantify the characteristic design loads. Table 17- Table 20 shows exemplary extreme event tables for blade 1 bending moments and tower bottom bending moment for both the onshore and offshore CART system respectively. Extreme event tables are generated for each load component described in Table 15. The shaded values refer to the minimum and maximum ultimate loads. In the third column, the specific simulation which causes the extreme loads can be found. All extreme loads are already weighted with their corresponding PSFs described in Table 16. Regarding the blade root bending moment in blade 1, DLC 1.4 triggers most of the extreme loads for both onshore and offshore CART system. Similarly, DLC 1.4 drives the most extreme loads for both onshore and offshore CART system regarding tower bottom bending moment.

TABLE 17: EXTREME EVENTS FOR THE BLADE 1 ROOT MOMENTS- ONSHORE

| Parameter | Type | File | RootMxb1 [kN-m] | RootMyb1 [kN-m] |
|-----------|------|----------------------------------|--------------------|--------------------|
| RootMxb1 | Min | .\DLC1.3_08\CART_SpaceatSea.out | -3.28E+01 | 4.18E+01 |
| RootMxb1 | Max | .\DLC1.4_233\CART_SpaceatSea.out | 7.40E+01 | 1.57E+02 |
| RootMyb1 | Min | .\DLC1.3_65\CART_SpaceatSea.out | -2.04E+01 | -1.02E+01 |
| RootMyb1 | Max | .\DLC1.4_214\CART_SpaceatSea.out | 6.23E+01 | 3.03E+02 |

TABLE 18: EXTREME EVENTS FOR THE BLADE 2 ROOT MOMENTS- OFFSHORE

| Parameter | Type | File | RootMxb1 [kN-m] | RootMyb1 [kN-m] |
|-----------|------|----------------------------------|--------------------|--------------------|
| RootMxb1 | Min | .\DLC1.3_68\CART_SpaceatSea.out | - 2.98E+01 | 1.52E+01 |
| RootMxb1 | Max | .\DLC1.4_456\CART_SpaceatSea.out | 6.73E+01 | 1.20E+02 |
| RootMyb1 | Min | .\DLC1.3_05\CART_SpaceatSea.out | - 6.79E+00 | - 1.40E+01 |
| RootMyb1 | Max | .\DLC1.4_06\CART_SpaceatSea.out | 3.76E+01 | 2.90E+02 |

TABLE 19: EXTREME EVENTS FOR TOWER BOTTOM BENDING MOMENT – ONSHORE

| Parameter | Type | File | TwrBsMxt [kN-m] | TwrBsMyt [kN-m] | TwrBsMzt [kN-m] |
|-----------|------|----------------------------------|--------------------|--------------------|--------------------|
| TwrBsMxt | Min | .\DLC1.4_233\CART_SpaceatSea.out | -5.17E+02 | 4.85E+01 | 5.35E+00 |
| TwrBsMxt | Max | .\DLC1.4_160\CART_SpaceatSea.out | 7.44E+02 | 3.17E+03 | 2.71E+01 |
| TwrBsMyt | Min | .\DLC1.3_38\CART_SpaceatSea.out | -1.42E+02 | -6.95E+02 | -7.67E+00 |
| TwrBsMyt | Max | .\DLC1.4_89\CART_SpaceatSea.out | 2.63E+02 | 2.85E+03 | 1.34E+01 |
| TwrBsMzt | Min | .\DLC1.4_110\CART_SpaceatSea.out | 2.49E+02 | 1.01E+03 | -1.61E+02 |
| TwrBsMzt | Max | .\DLC1.4_321\CART_SpaceatSea.out | -1.63E+02 | 2.05E+03 | 1.79E+02 |

TABLE 20: EXTREME EVENTS FOR TOWER BOTTOM BENDING MOMENT - OFFSHORE

| Parameter | Type | File | TwrBsMxt [kN-m] | TwrBsMyt [kN-m] | TwrBsMzt [kN-m] |
|-----------|------|----------------------------------|--------------------|--------------------|--------------------|
| TwrBsMxt | Min | .\DLC1.4_359\CART_SpaceatSea.out | - 3.08E+02 | 2.54E+02 | -8.64E+00 |
| TwrBsMxt | Max | .\DLC1.4_58\CART_SpaceatSea.out | 4.75E+02 | 1.37E+03 | 4.07E+00 |
| TwrBsMyt | Min | .\DLC1.3_155\CART_SpaceatSea.out | -5.88E+01 | - 7.58E+02 | -2.27E+01 |
| TwrBsMyt | Max | .\DLC1.4_89\CART_SpaceatSea.out | 1.47E+02 | 2.90E+03 | 3.65E+01 |
| TwrBsMzt | Min | .\DLC1.4_236\CART_SpaceatSea.out | 4.97E+01 | 8.36E+02 | - 1.56E+02 |
| TwrBsMzt | Max | .\DLC1.4_447\CART_SpaceatSea.out | 6.76E+01 | 1.59E+03 | 1.84E+02 |

By examining the extreme loads generated by all DLCs during normal operations, it was interesting to note that the out-of-plane blade deflection and blade root moments were driven by DLC 1.4 in both onshore and offshore CART system. The discussion made in the present section will mainly focus on the offshore CART system. Figure 43 compares the time history of a particular event which triggers the most extreme loads in blade root bending moment at blade 2 denoted by RootMyc2 and out-of-plane blade deflection denoted by TipDxc1 for

offshore CART system. In figure, the red line represents simulation number 6 and the blue one represents simulation number 431. In addition to Figure 43, close-ups of these two particular events are depicted in Figure 44 and Figure 45. In figures, the x-axis represents time and the y-axis represents the quantity of each load parameter. These results were generated directly from OpenFAST output file. Therefore, they are not weighted by PSFs.

Simulation number 431 was run with an IEC discrete wind model ECD-r+2 considering no yaw misalignment, slope of vertical inflow of 8° , and an initial azimuth angle of 90° whereas simulation number 6 with ECD+r+2, a yaw misalignment of 8° , slope of vertical inflow of -8° , and an initial azimuth angle of 0° . The change in wind direction is 42.35° to the right for simulation number 431 and the same magnitude to the left for simulation number 6. The maximum out-of-plane deflection was found at blade two in simulation number 431 at a time of 142.59 s, wind speed of 23.42 m/s, and azimuth angle of 202° (see Figure 44). The maximum blade root deflection occurs at blade two in simulation number 6 at a time 144.27 s, wind speed of 23.42 m/s and azimuth angle of 1.73° (see Figure 45). In this case, blade two is pointing almost vertically down into the wind and the blade experiences the tensile force. By observing both cases, it seems that the blade deflection and blade root bending moment are sensitive to the wind speed close to the turbine cut-out wind speed. This is because the rotor thrust increases with the increase in wind speed. Furthermore, it is obvious from Figure 43 that the floater pitch motion is influenced by wave elevation as it moves with the surface wave which is common for semisubmersible platforms. Rotor speed, generator torque and generator power go up with the rise in wind speed as ECD event starts. Eventually, transient behaviour was observed in rotor speed, generator torque, generator power, blade tip deflection, and blade root bending moment. Although it shows that the wind gust does not influence on pitch motion, it does influence on floater yaw motion. It is visible as a perturbing in floater yaw angle during wind gust, followed by a gentle yaw to the wind direction when the event is over. Negative yaw angle indicates the reverse movement of the platform. The difference in power production between these two load cases reflect that the power production is higher when the platform moves in the wind direction whereas the production is lower when the platform move from the wind direction (see Figure 43B). It is obvious that DLC 1.4 is a particular event which is primarily influenced by wind gust and extreme change in wind direction. The influence of wave-induced loads on structural loads seems insignificant.

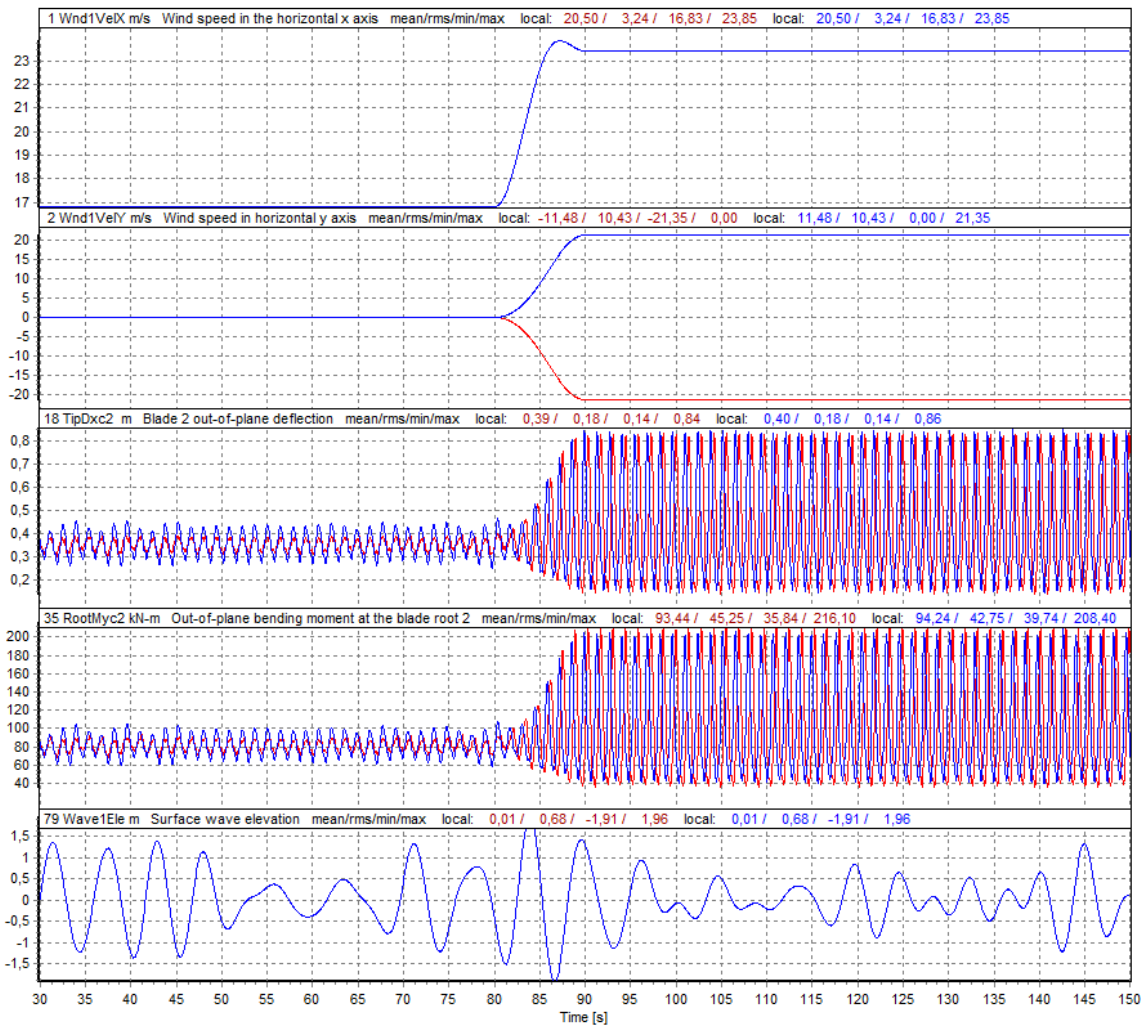


FIGURE 42: TIME HISTORIES FROM DLC 1.4 SIMULATION NUMBER 6 SHOWN IN RED AND 431 SHOWN IN BLUE FOR OFFSHORE CART SYSTEM (A)

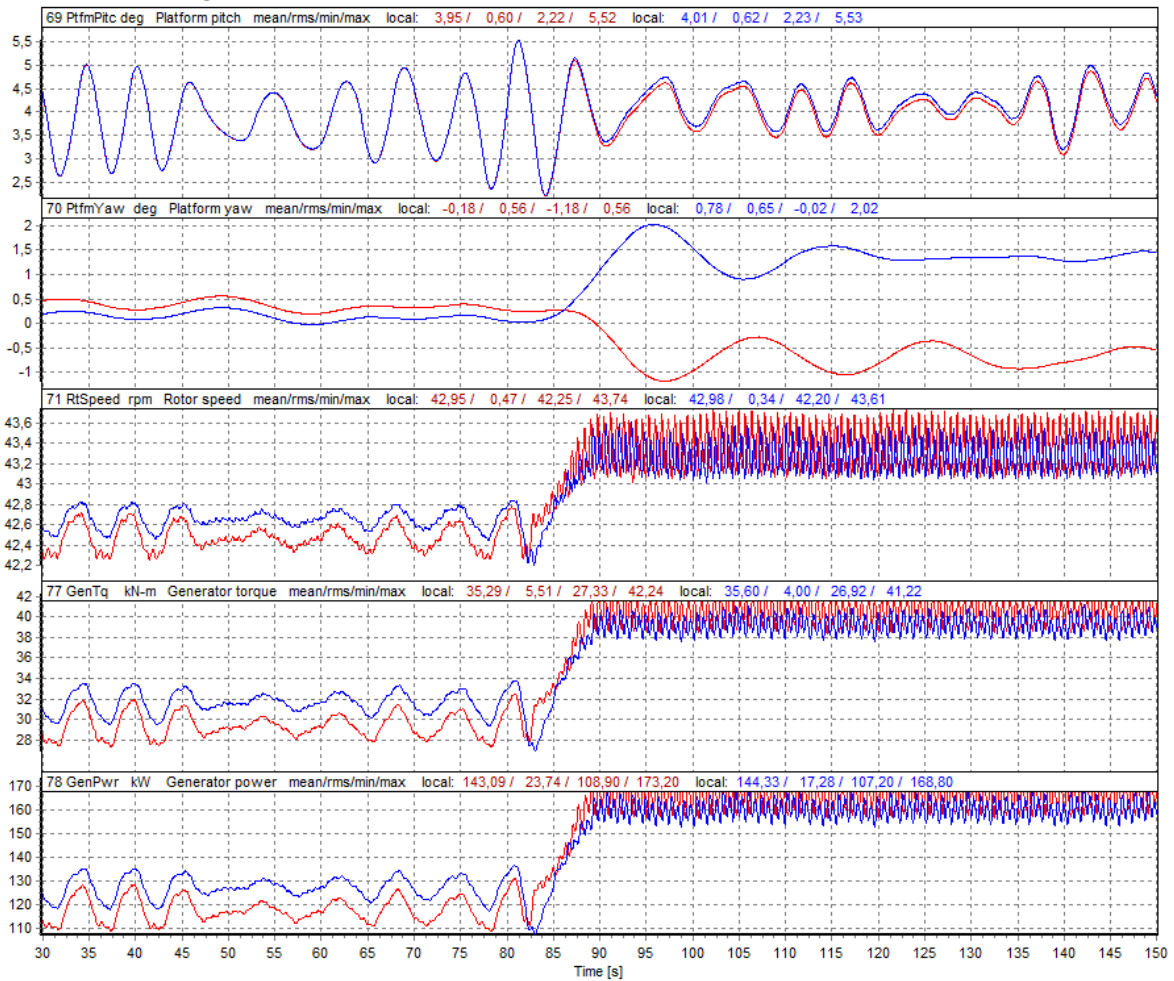


FIGURE 43: TIME HISTORIES FROM DLC 1.4 SIMULATION NUMBER 6 SHOWN IN RED AND 431 SHOWN IN BLUE FOR OFFSHORE CART SYSTEM (B)

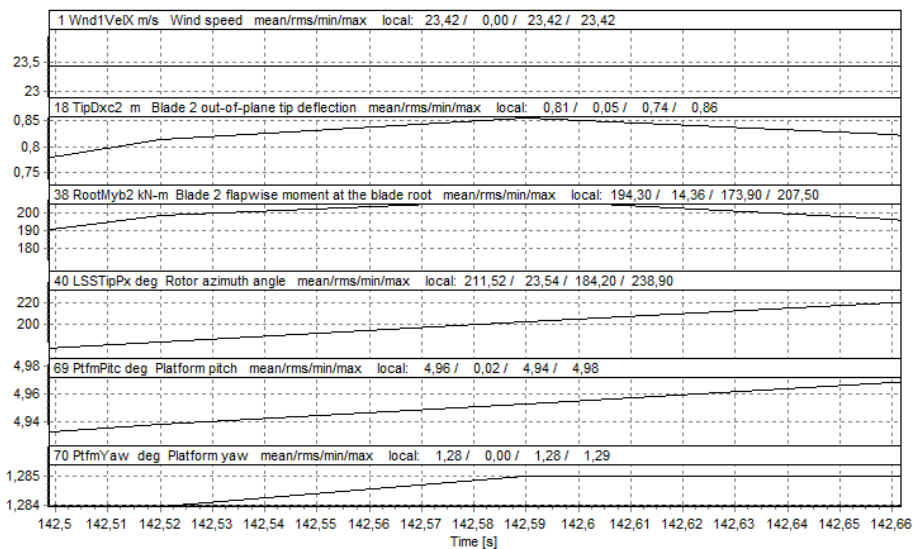


FIGURE 44: CLOSE-UP TIME HISTORY FROM SIMULATION NUMBER 431

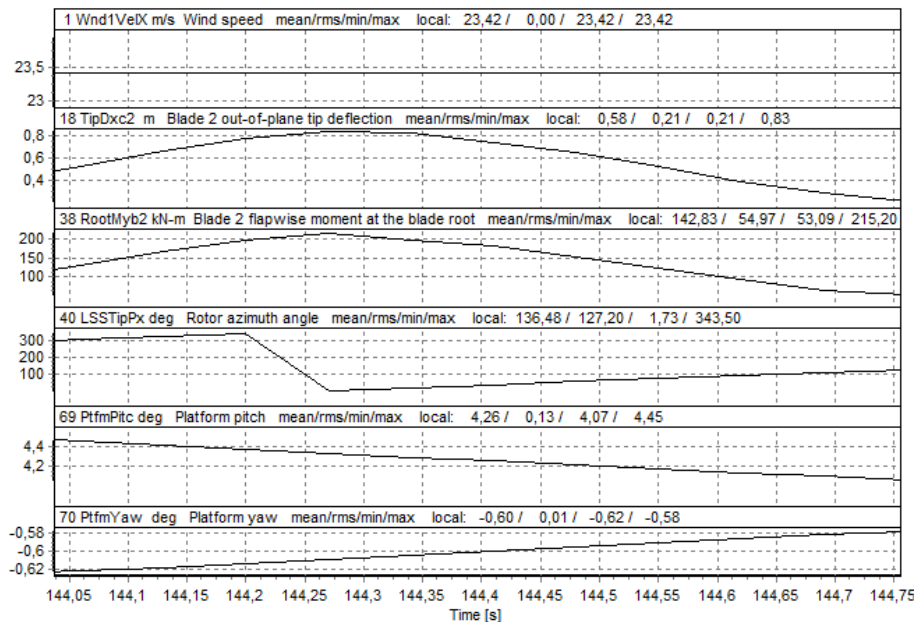


FIGURE 45: CLOSE-UP OF TIME HISTORY FROM SIMULATION NUMBER 6

Regarding platform motions in normal operating conditions, the extreme sway, heave, roll, pitch, and yaw motions appear at simulations in DLC 1.4. However, the extreme turbulence in DLC 1.3 triggers the extreme surge motion. This can be correlated to the fact that the tensions in the mooring lines are more influenced by wind turbulence. Figure 46 shows how the tensions in mooring lines response to the extreme turbulence wind for simulation number 180 in DLC 1.3. Again, it is worth mentioning that the first 60 s of simulation was discarded to get rid of start-up transients. In figure, T1 and T3 represent tensions at fairleads of the mooring line 1 and mooring line 3 and T1[a] and T3[a] represent tensions at their corresponding anchors. It is obvious that the tensions in the upwind mooring lines denoted by T3 were driven by high sustained winds greater than the rated wind speed. This is particularly due to the nature of stall regulated wind turbines, whose sustained rotor thrust tends to increase with the wind speed. As a result, the platform is being pushed downward (in the axial direction) and the mooring line in the upwind side is being pulled upwards. The bar charts in Figure 47 show the extreme platform motions, whereby the left figure shows the extreme maximum motions and the left figure shows the extreme minimum motions.

According to the findings, the structural loads in normal operating conditions were driven by DLC 1.3 and DLC 1.4 for both onshore and offshore CART system.

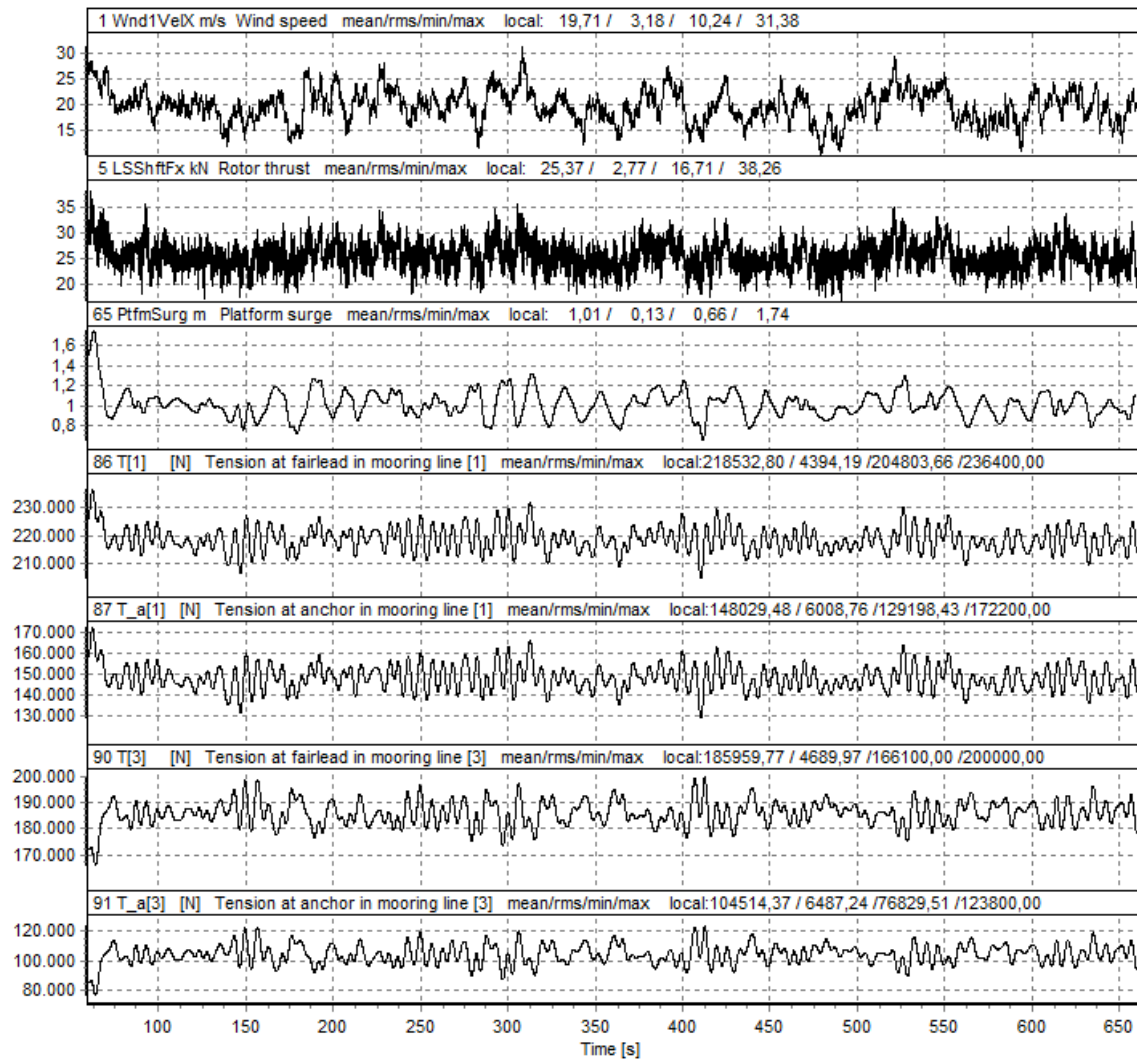


FIGURE 46: TIME HISTORY FROM SIMULATION WHICH YIELDS EXTREME SURGE MOTION

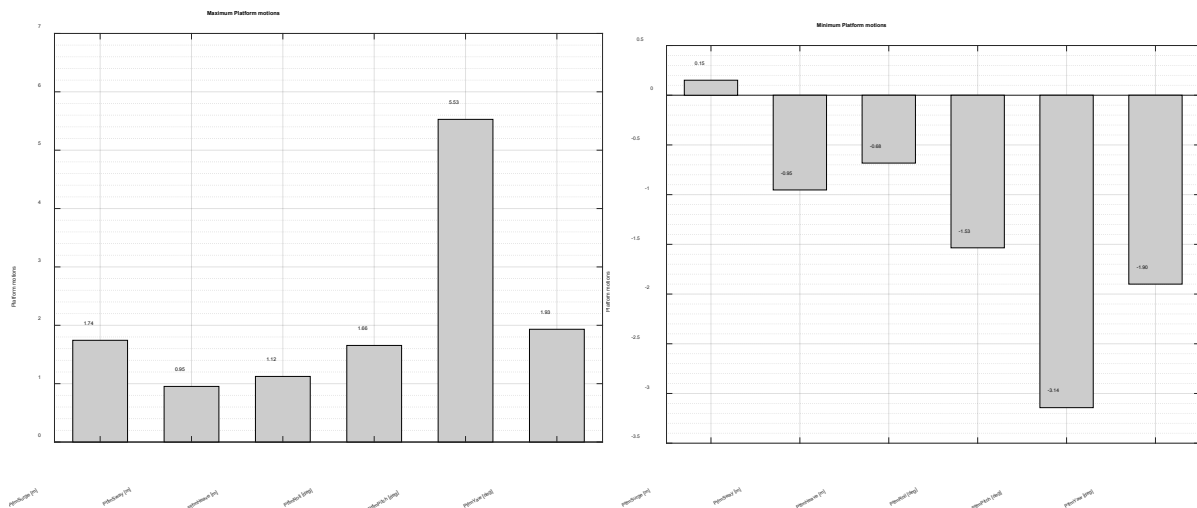


FIGURE 47: EXTREME PLATFORM MOTIONS FROM NORMAL OPERATING CONDITION: MAXIMUM (LEFT) AND MINIMUM (RIGHT)

6.3.3 PLATFORM YAW MOTION IN WIND GUSTS

The extreme yaw motion of 1.93° appears in simulation 269 of DLC 1.4 which simulates power production during extreme coherent gusts with a simultaneous change of the wind direction.

Simulation 269 was run with IEC discrete wind model ECD-r+2 considering a vertical inflow slope of 8° , an initial azimuth angle of 90° , but no yaw misalignment. Figure 48 and Figure 49 depict time history and close up of this particular case respectively. The maximum wind gust speed is 15 m/s and occurs at a time of 70 s. The extreme yaw motion was identified at a wind speed of 15.75 m/s and a time of 75.6 s which is just after the peak wind gust. In this situation, the azimuth angle is 5.52° , which is to say the blades are almost symmetrical. There is a small shift which reflects yawing resulted from the rotor aerodynamic and mass imbalance. On top of that, there are also flow variations across the rotor due to both vertical and horizontal wind shear. This causes the nacelle yaw angle to operate with a mean angle of 0.01° and a standard deviation of 0.02° . This yaw error is exacerbated by the large motion of the platform since the platform, tower, and RNA assembly are rigidly connected. Hence, the yaw error can alter the transfer of tension in mooring lines through the change in rotor thrust. By taking a closer look at yaw motion in time history, it was observed that the platform gently yaws with the change in wind direction, which is 42.35° to the right, and finally to the wind direction when the gust event is over. Although the time history of sway and roll motions is not shown here, it was observed that they exhibit the same response like yaw motions. It is therefore relevant to highlight that sway, roll, and yaw motions are related to each other as well. A discussion on extreme yaw motion would be more complete with some discourse on dominant frequencies on platform yaw motion. FFT diagrams of Figure 50 helps us understand better which frequency excites with the platform yaw motion. As can be seen clearly in figure, the wave energy exists in 0.15 to 0.25 Hz. The observed largest peak of 0.041 Hz in FFT of yaw motion corresponds to the structural natural frequency of the platform in yaw direction. This confirms that yaw motion is not influenced by wave-induced loads. In fact, it is greatly influenced by the restoring stiffness of the mooring system. To attenuate yaw motion of the platform, one way is to increase the yaw stiffness by modifying the geometrical and material stiffness of the mooring lines. The other way to increase the yaw stiffness can be done by augmenting clump weight and buoyancy to lower and upper end of the mooring lines, or augmenting crowfoot at the connection between each mooring line and the platform as recommended by Jonkman (2007).

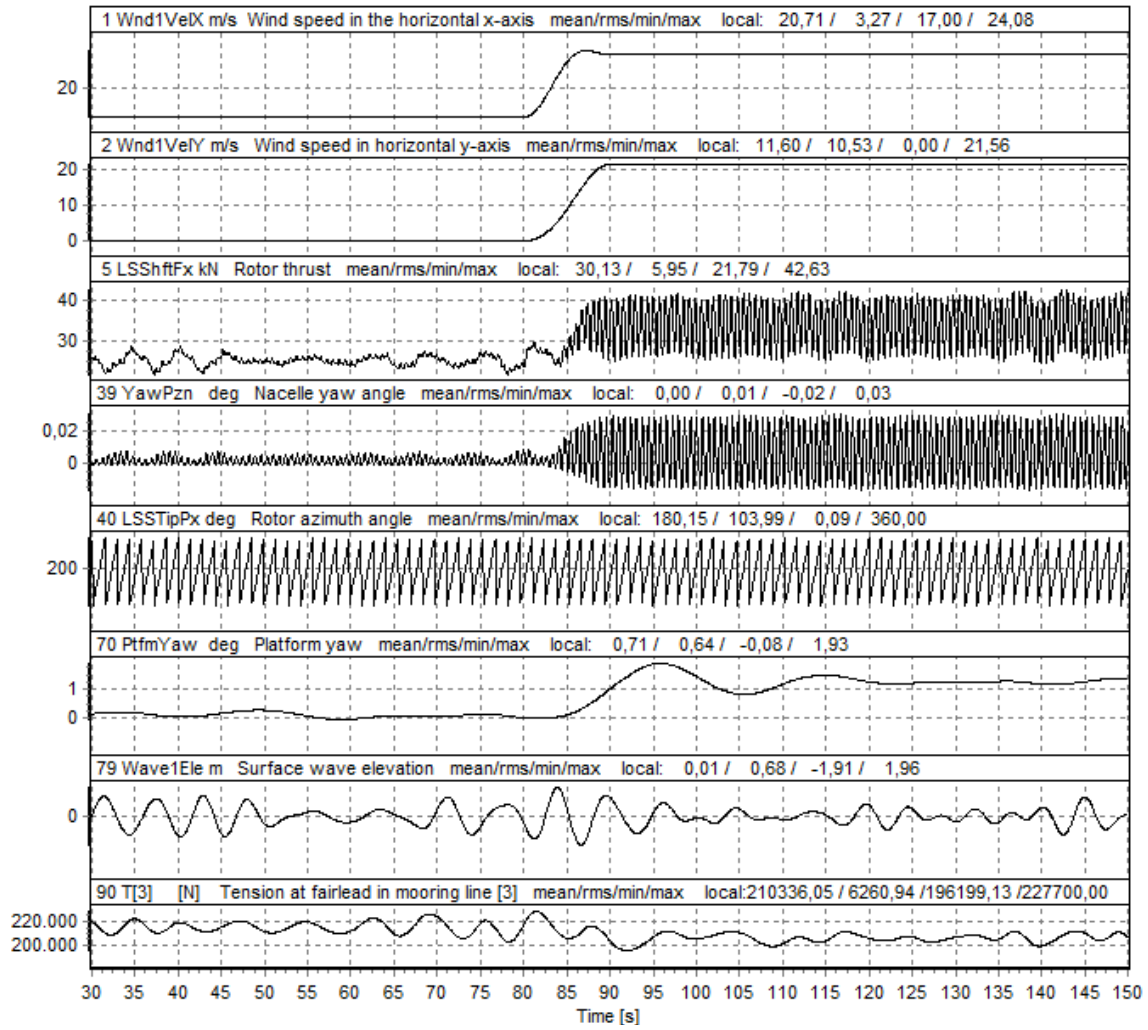


FIGURE 48: TIME HISTORY OF SIMULATION 269 IN DLC 1.4

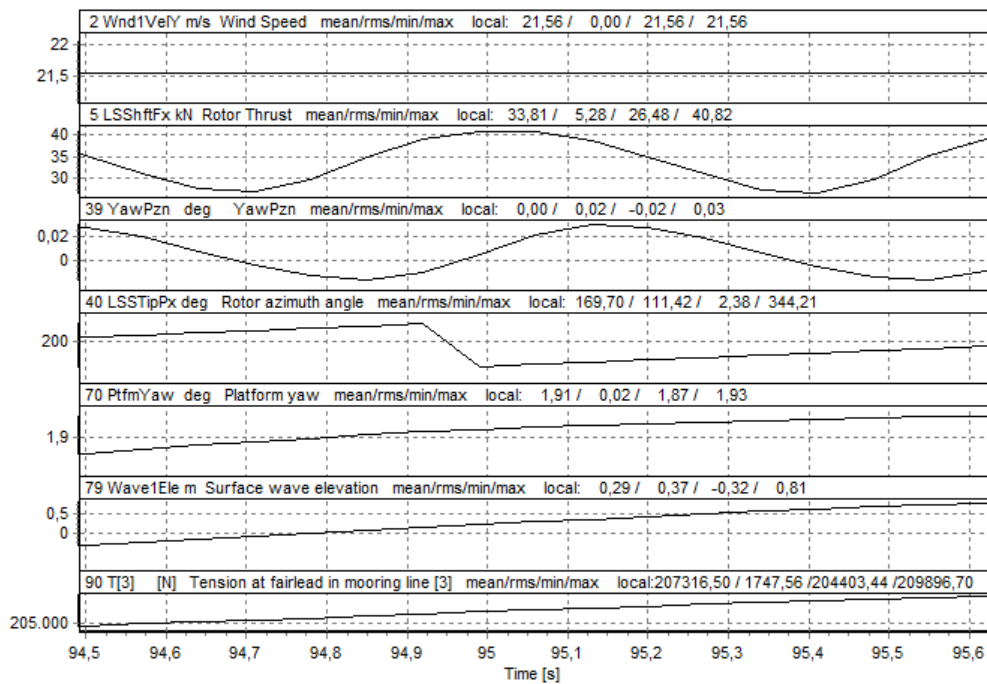


FIGURE 49: CLOSE-UP OF TIME HISTORY FROM SIMULATION NUMBER 269

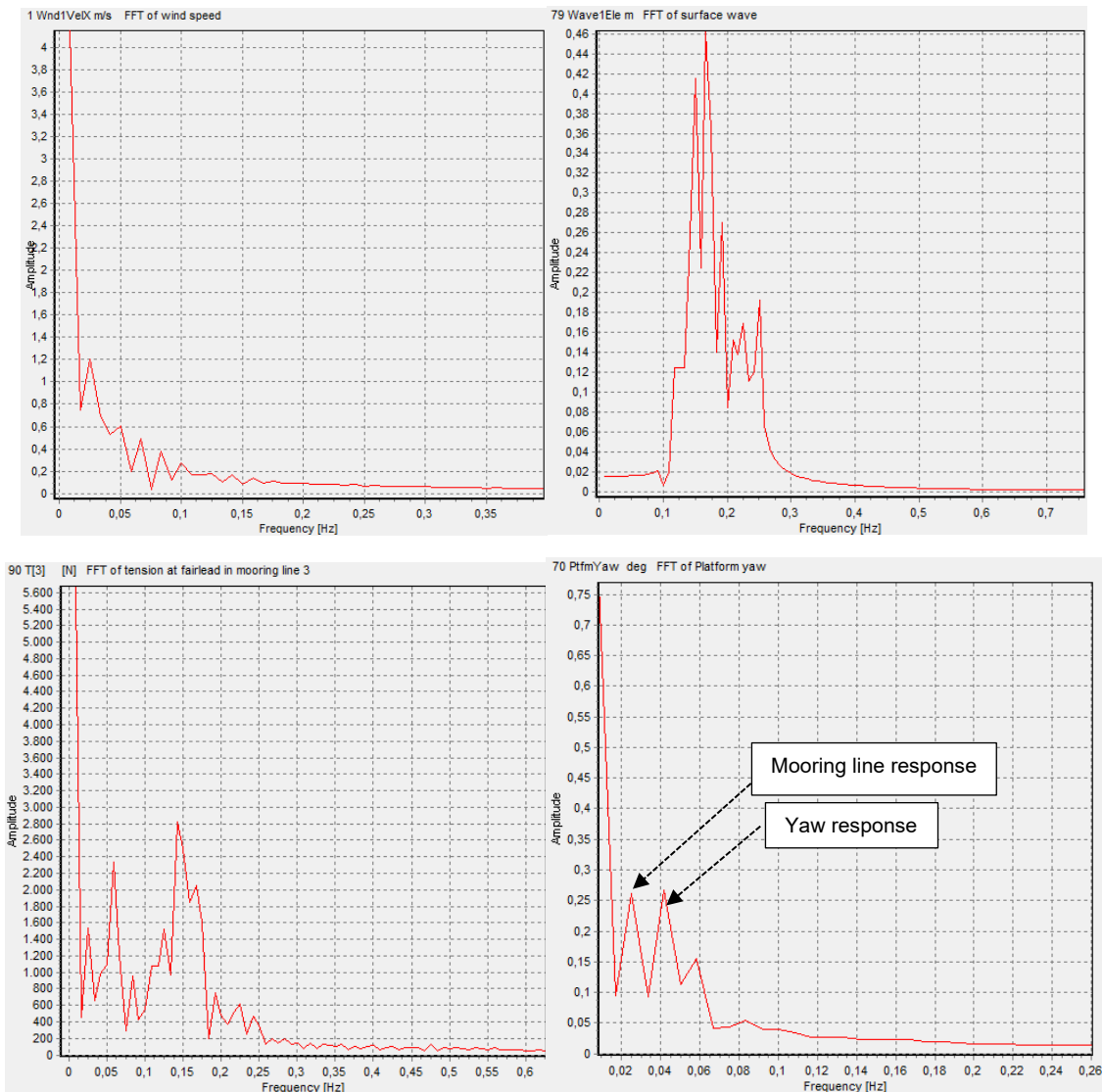


FIGURE 50: FFT OF WIND SPEED (UPPER LEFT), SURFACE WAVE ELEVATION (UPPER RIGHT), TENSION AT FAIRLEAD OF MOORING LINE (LOWER LEFT), AND PLATFORM YAW MOTION (LOWER RIGHT)

6.3.4 COMPARISON OF OFFSHORE AND ONSHORE WIND TURBINE LOADS

Aiming to identify the impact brought about by the floating support structure, the extreme loads of several parameters described in section 6.1 were compared between the onshore and offshore CART system. This is done by evaluating the ratio of absolute maximum extreme loads resulted from the offshore CART system to that of the onshore CART system. The bar charts in Figure 51 give information about the ratio of the extreme loads resulted from offshore to onshore CART system. The ratio of 1 implies that there is no difference in loads between the two systems. When the ratio becomes greater or less than 1, it means that the structural loads on the offshore wind turbine have increased or decreased due to the presence of the floating substructure. All measured parameters are already explained with their respective short description in Table 15 in the previous section 6.1.

By examining the response of the control system, it was found that the absolute maximum extreme loads in generator torque, generator power, rotor speed, rotor thrust, and rotor torque

are almost the same between the offshore and onshore wind turbine. This is because both systems use the same torque control algorithms. This can be explained by examining the steady-state response of torque controller as discussed in section 4.5.6 (see Figure 28c).

It is interesting to note that the tower top side-to-side displacement has reduced by 41% for the offshore CART system. By examining the load cases which trigger this extreme displacement, it was found that the tower-top side-to-side displacement is only dominated by wind-induced forces for onshore CART system whereas the tower-top side-to-side displacement is more dominated by wave excitations for offshore CART system. To be more precise, the extreme maximum tower-top side-to-side displacement of the onshore CART system is driven by wind gust at wind speed above rated wind speed when the rotor blades are facing to the wind at an azimuth angle of 180° . For the offshore CART system, it was affected by the excitation of platform yaw motion with low frequencies wave and wind forces at cut-in wind speed. Again, out-of-plane blade tip deflection has been slightly decreased by the presence of the floating substructure. It is also noticeable that in-plane blade tip deflection has been increased by as much as 2 % for offshore CART system. Similarly, tower top fore-aft and side-to-side shear forces and tower-top axial force have decreased by about 3 %, 17 % and 4 % respectively. The tower top roll moment and pitch moment have been decreased by approximately 7 % whereas tower top yaw moment was increased by only 1%. The tower top pitching moment is related to the difference in aerodynamic loads in the upper and lower parts of the rotor plane.

Similarly, the blade root out-of-plane shear force, the blade root bending moments, and blade flapwise and edgewise bending moment have been reduced by a small percent. Blade edgewise bending moment has reduced by 8 %. It was also obvious that the tower bottom fore-aft shear force has increased by 15 % whereas the tower bottom side-to-side shear force has reduced by 36%. This is contributed by the inverted pendulum effect. As a result, the tower bottom fore-aft bending moment has reduced by as much as 27% whereas the tower bottom side-to-side bending moment and the tower bottom torsion moment have been increased by 2 % and 1 % respectively. Shaft shear forces directed along the y-axis and z-axis and shaft bending moment about y-axis have significantly reduced in the presence of floating substructure.

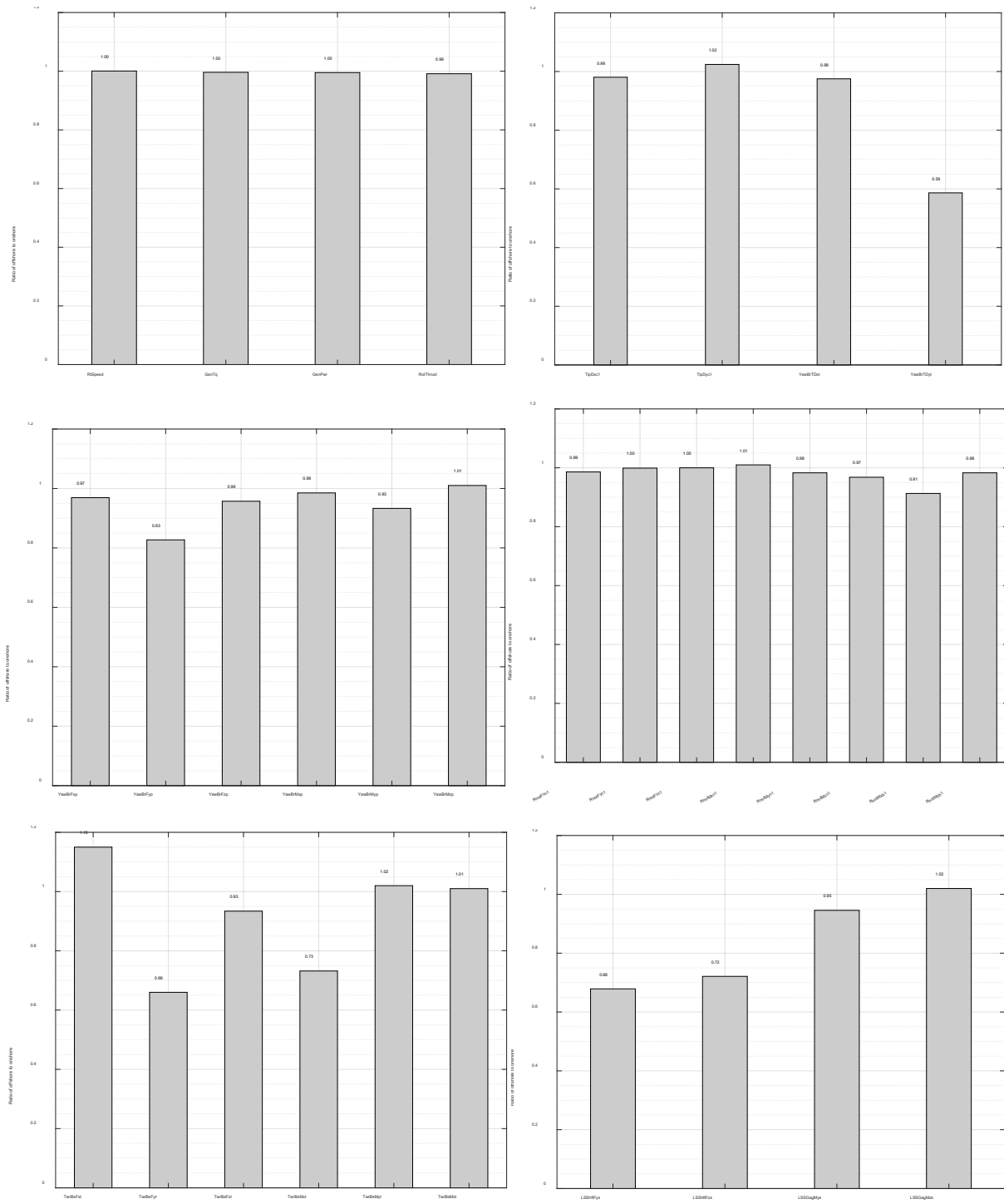


FIGURE 51: RATIO OF OFFSHORE TO ONSHORE CART SYSTEM FOR NORMAL OPERATIONS

In order to gain more insights into the differences in dynamic response of offshore and onshore CART system, Figure 52 compares the time history of wind speed, tower bottom side-to-side bending moment, tower bottom fore-aft moment, tower bottom torsional moment, tower top side-to-side displacement and nacelle acceleration between offshore- and onshore based system. The red line represents onshore CART system and the blue line represent offshore CART system. The results were based on the simulation at mean hub-height wind speed of 20 m/s from DLC 1.1 which corresponds to the cut-out wind speed of the turbine. Due to the

difference in hub-height, the time series of wind speed is not exactly identical between them. It is evident that the acceleration of the nacelle in the y-direction has significantly decreased for offshore CART system. However, the acceleration of the nacelle in the z-direction was found to be significantly larger for offshore system. This might be related to the coupling between platform pitch and heave motion. As a result, tower bottom fore-aft and torsional moment has increased for offshore system. In order to get a better understanding of the correlation among wave loads, the tower vibration and the nacelle acceleration, Figure 53 compares FFT diagrams of nacelle acceleration along the y axis and z axis between onshore and offshore CART system. Regarding the nacelle acceleration along the y axis for the onshore CART system, the peak energy was found to be mainly due to tower vibration for onshore system as represented by the red line and 1P rotor frequency and 2P rotor blade passing frequency are also visible. In contrast, the nacelle acceleration along y axis seems be excited by wave loads, 2P and 4P rotor harmonic frequencies, and the tower vibration for offshore system. However, the response amplitude of tower eigenfrequency was observed to be somewhat smaller than that of the onshore system and the tower vibration and nacelle acceleration have obviously reduced. As a result, tower bottom side-to-side moment has reduced for offshore CART system. Regarding the nacelle acceleration along the z axis, the largest amount of energy was found to be the wave energy range for offshore system, whereby the response amplitude is quite large. Apart from wave excitation forces, the nacelle acceleration was found to be dominated by the platform heave motion, rotor harmonic frequencies. This might be related to the coupling between platform pitch and heave motion. As a result, tower bottom fore-aft moment and tower bottom torsional moment have increased for offshore CART system.

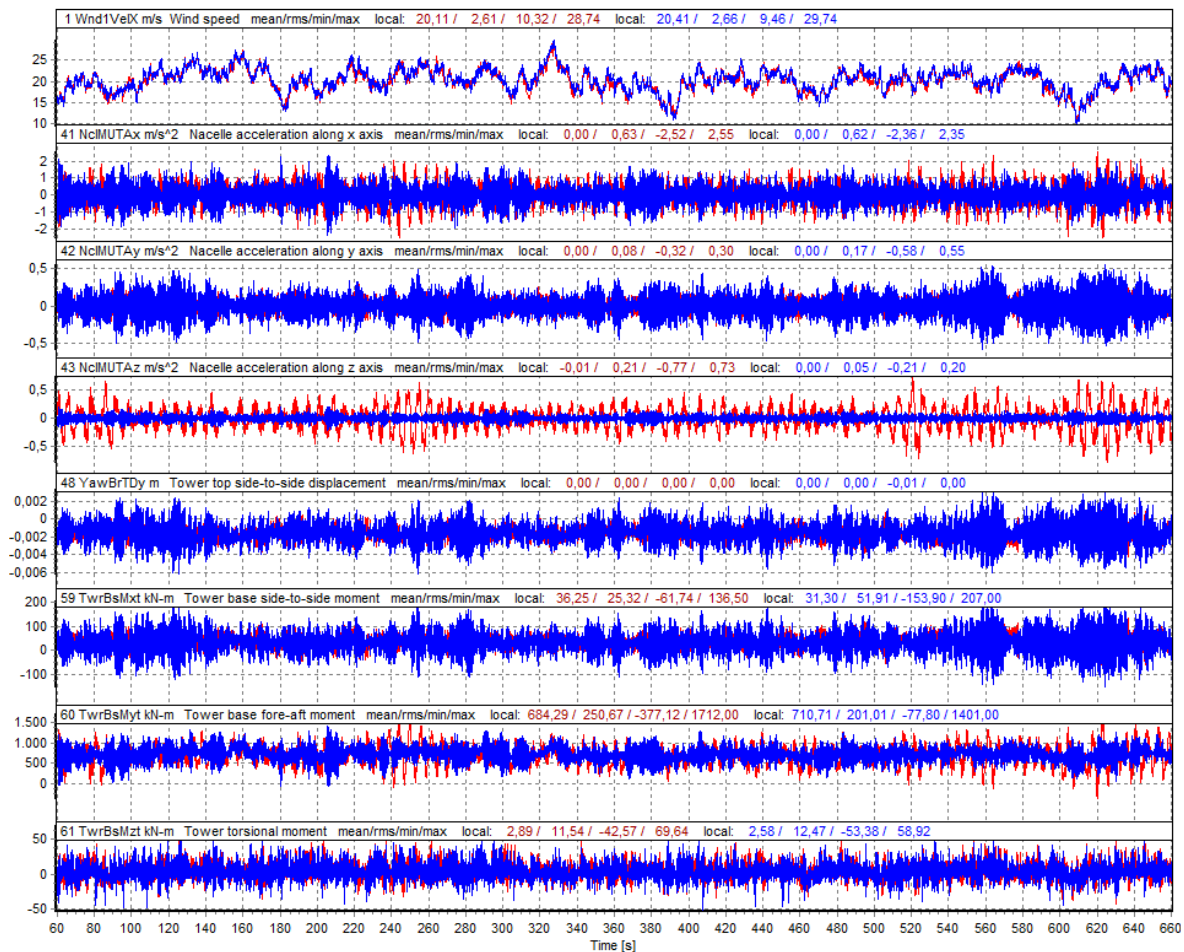


FIGURE 52: COMPARISON OF TIME HISTORIES FROM DLC 1.1 SIMULATION NUMBER 29 BETWEEN OFFSHORE (SHOWN IN BLUE) AND ONSHORE (SHOWN IN RED) WIND TURBINE

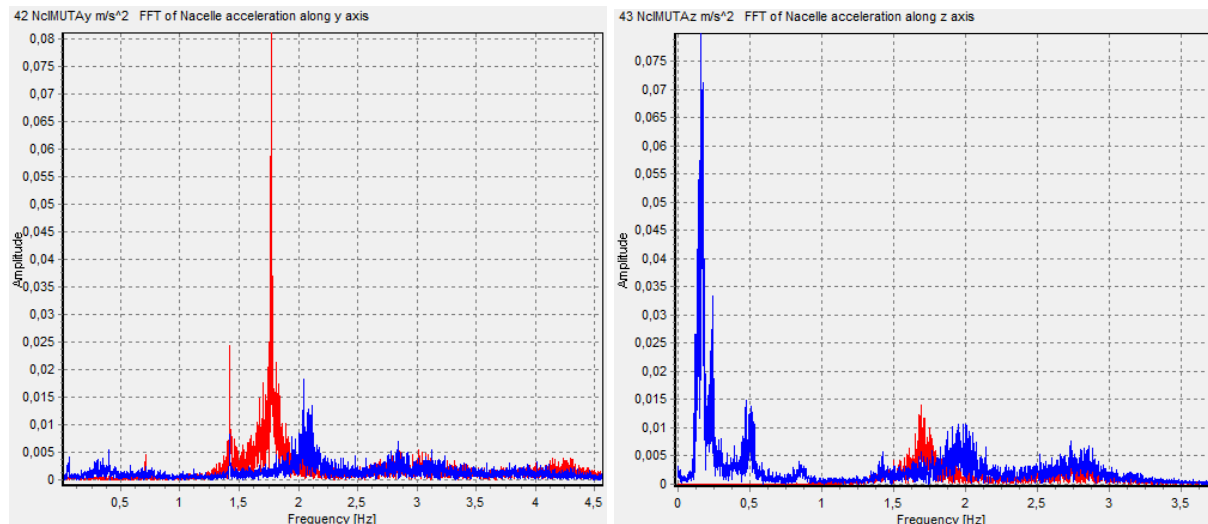


FIGURE 53: COMPARISON OF FFT OF NACELLE ACCELERATION ALONG Y AXIS AND Z AXIS BETWEEN ONSHORE (SHOWN IN RED) AND OFFSHORE (SHOWN IN BLUE) CART SYSTEM

Upon comparison of the response between the onshore and offshore system, the change in structural loads due to the presence of floating substructure seems moderate. The response of the control system shows not much significant difference between both systems in terms of

load excursion of rotor speed, rotor power, and rotor torque. On that account, the implemented control concept does not need to be modified further for offshore system.

6.3.5 FATIGUE LOADS

Fatigue loads are relatively lower than static loads. They are mainly caused by the variation of loads. During power production, load variations due to wind turbulence can substantially affect the fatigue life of the wind turbine. Fatigue loads are often expressed in terms of damage equivalent loads (DELs). The present study considers fatigue loads from power production in normal turbulence wind DLC 1.2. Load time series from DLC 1.2 were post-processed using NREL MCrunch to compute simplified fatigue DELs. MCrunch uses a rain-flow counting algorithm to derive fatigue load cycle amplitudes and mean values from time series. Generally, a fatigue damage equivalent load about a fixed mean is solved using the following equation:

$$DEL_{eq} = \left(\frac{\sum n_i (L_i^{RF})^m}{n_{eq}} \right)^{1/m} \quad 6-1$$

Where, L_i^{RF} is the cycle's load range about a fixed load-mean value at time series i , n_i is cycle count and n_{eq} is the equivalent count for the time series. Typically, Wöhler's exponent m is taken to be 3 for steel and 10 for composite materials. In the present study, the lifetime fatigue DELs account for the design life of the turbine which is 20 years. The probabilities from the Rayleigh distribution were taken into account to weigh wind speed distributions. For that, the average mean wind speed was taken to be 10 m/s according to IEC 61400-3.

Fatigue DELs have been examined on the following main components where the change in structural geometry plays a critical role for fatigue strength checks:

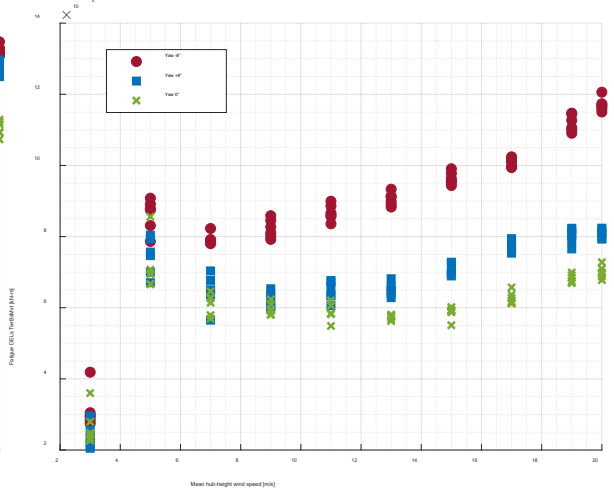
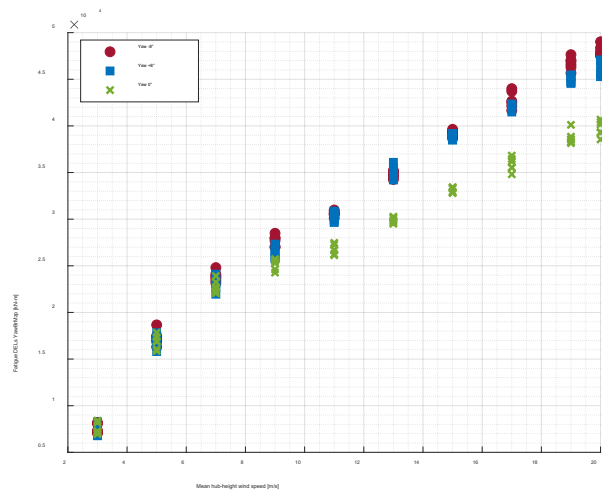
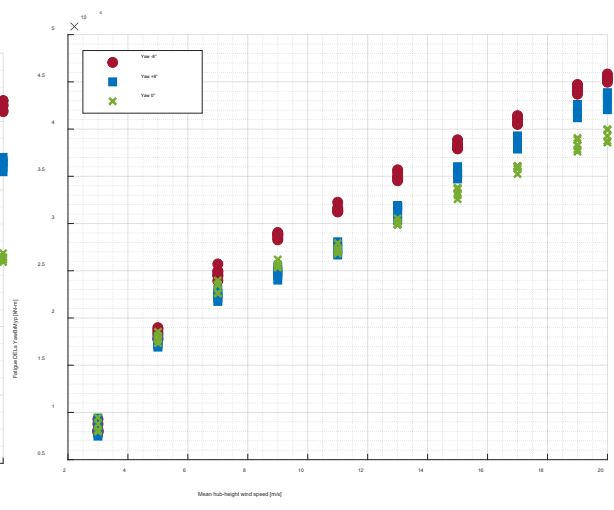
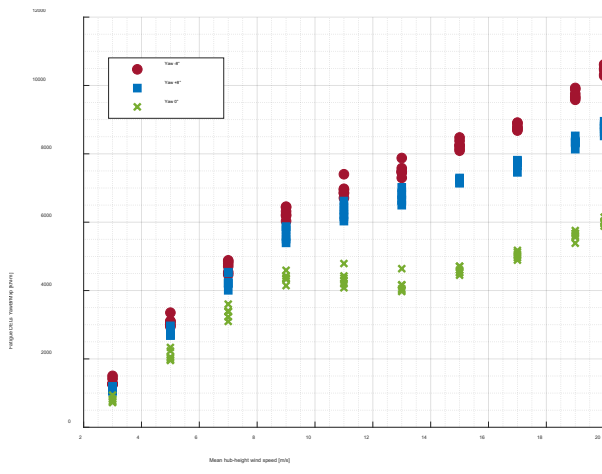
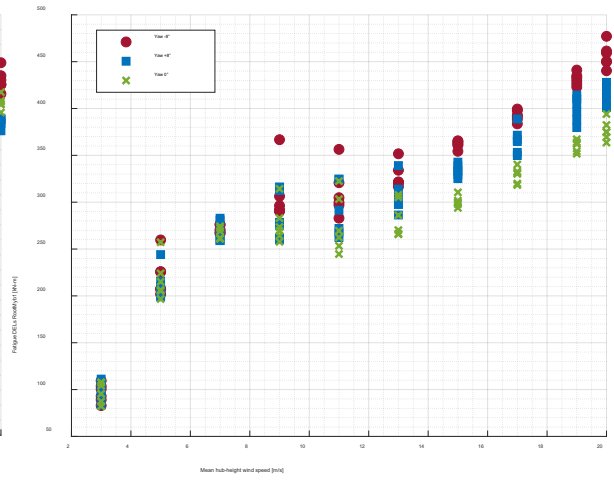
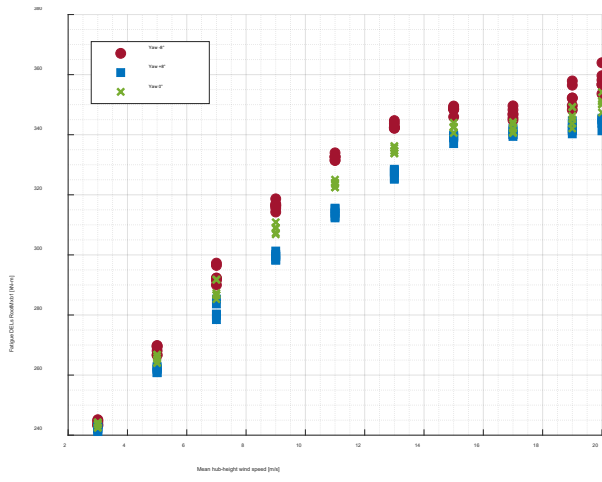
- Blade root in-plane bending moment denoted by "RootMxc1"
- Blade root out-of-plane bending moment denoted by "RootMyc1"
- Pitching moment at the blade root denoted by "RootMzc1"
- Edgewise moment at the blade root denoted by "RootMxb1"
- Flapwise moment at the blade root denoted by "RootMyb1"
- Tower-top roll moment denoted by "YawBrMxt"
- Tower-top pitch moment denoted by "YawBrMyt"
- Tower top yaw moment denoted by "YawBrMzt"
- Tower bottom side-to-side moment denoted by "TwrBsMxt"
- Tower bottom fore-aft moment denoted by "TwrBsMyt"
- Tower bottom torsional moment denoted by "TwrBsMzt"

While writing this thesis, the CART wind turbine has not been analysed at component level yet. Consequently, the ultimate strength of CART's components is not available. As a rule of thumb, it is assumed that the ultimate strength of the component can be obtained by multiplying

the extreme loads resulted from the normal operating conditions DLC 1.1, DLC 1.3, and DLC 1.4 with an ultimate load factor (ULF). Fundamentally, fatigue strength depends on utilized material properties. At first, the commonly used value of 3 for steel and 10 for the composite was taken into account. The following discussion will cover the effects of yaw misalignment on fatigue DELs, effects of material strengths on fatigue DELs, and effects of ULF on fatigue DELs.

Effects of yaw misalignment on fatigue DELs

As aforementioned in section 6.3, simulations in DLC 1.2 were performed under consideration of a yaw misalignment of $\pm 8^\circ$. It needs to be mentioned that the yaw misalignment largely changes the calculated DELs mainly due to the change in thrust force. This could be a case for floating offshore wind turbines since the platform pitch motion additionally causes the change in thrust force. Figure 54 shows how the fatigue damage equivalent loads change with the increase in wind speeds at different yaw angles. For edgewise and flapwise bending moment at the blade root, a negative misaligned yaw, which corresponds to the clockwise direction when looking from above, leads to higher fatigue DELs whereas the opposite is true for a positive misaligned yaw. For tower top roll and pitch moment, it was observed that a positive misaligned yaw increases the fatigue DELs significantly in high wind speeds. For tower top yaw moment, fatigue DELs resulted from positive and negative misaligned yaw angles are close to each other. It is interesting to note that fatigue DELs of all investigated parameters are nearly the same in low wind speeds whereas the change in DELs is remarkable for high wind speeds. As expected, this is due to the nature of stall-regulated wind turbine, in which the rotor thrust tends to get larger with the increase in wind speed. As a result of the platform pitch motion, the direction of the rotor thrust force changes ultimately leading to higher DELs in tower top and tower bottom load components. In addition to this, it is needed to mention again that the turbine was designed with a high rotor tip speed ratio. This means that the aerodynamic loads vary with the change in angle of attack. For yawed conditions, the angle of attack tends to vary differently from the aligned condition. Moreover, the gyroscopic blade moment can be quite large during yawed conditions. As a result, fatigue DELs become larger for yawed conditions.



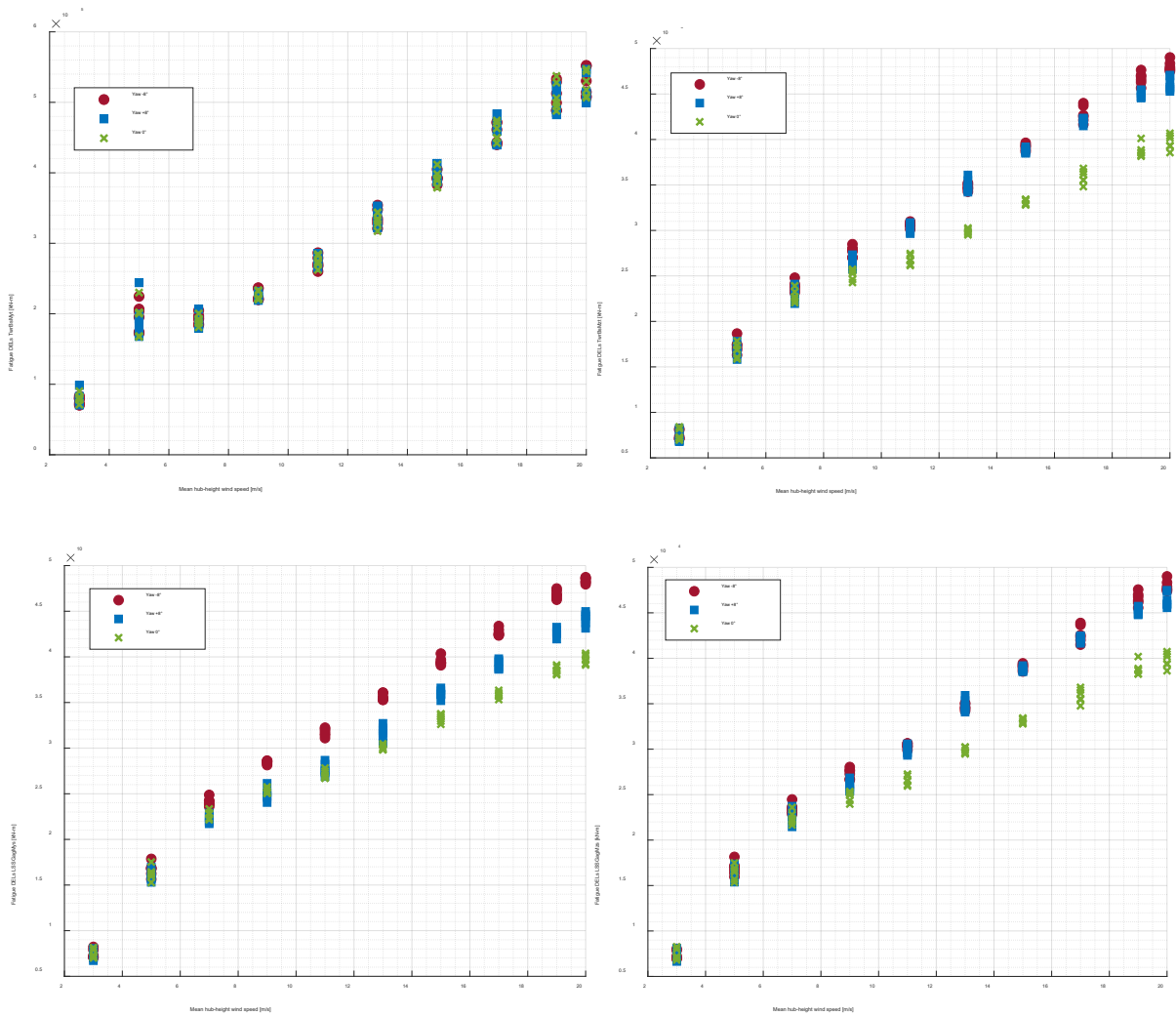


FIGURE 54: VARIATION OF FATIGUE DELS AS A FUNCTION OF MEAN HUB-HEIGHT WIND SPEED AT DIFFERENT YAW ANGLE FOR OFFSHORE CART SYSTEM (THE ABBREVIATIONS ARE EXPLAINED IN SECTION 6.3.5)

Effects of material strength on fatigue DELs

Another three different experiments were carried out to investigate the change in fatigue equivalent loads depending on the Wöhler's exponent. The Wöhler's exponent m was varied 3,4,5 for the steel components and 8,10,12 for the composite blades.

Figure 55 presents the fatigue DELs pitching moment at the blade root, tower bottom torsional moment, tower top yaw moment, and shaft bending moment about y axis as a function of mean hub-height wind speed. This result is based on sixty 10-minute simulations for each wind speed in DLC 1.2 and it does not account for yaw misalignment. Since wind seeds are not the same for all simulations, load time series are also different in DLC 1.2. The fatigue DELs of the above-described parameters seem to be affected by the controller. Since the power regulation in the partial load region and full load region is different, the response of the system can be different as well. Figure 56 explains which frequencies are excited with blade root flapwise bending moment as an example. The largest excitation occurs at the rotational frequency (1P)

of the turbine. The peak in 1P is primarily due to gravity and blade twist angle. The wave peak frequency is also visible. The blade passing frequencies 2P and 4P excitation seem to have less energy. The remaining peak between 2P and 4P corresponds to the eigenfrequency of the tower. It is not surprising that fatigue DELs for all load components have greater contribution in higher winds. However, it is worth mentioning that the probability of occurrence of very high wind is quite low in reality. By examining the different Wöhler's exponents, it was found that the fatigue DELs for the blade computed with a lower material exponent is higher than that with a higher material exponent. The same applies to the steel components as well.

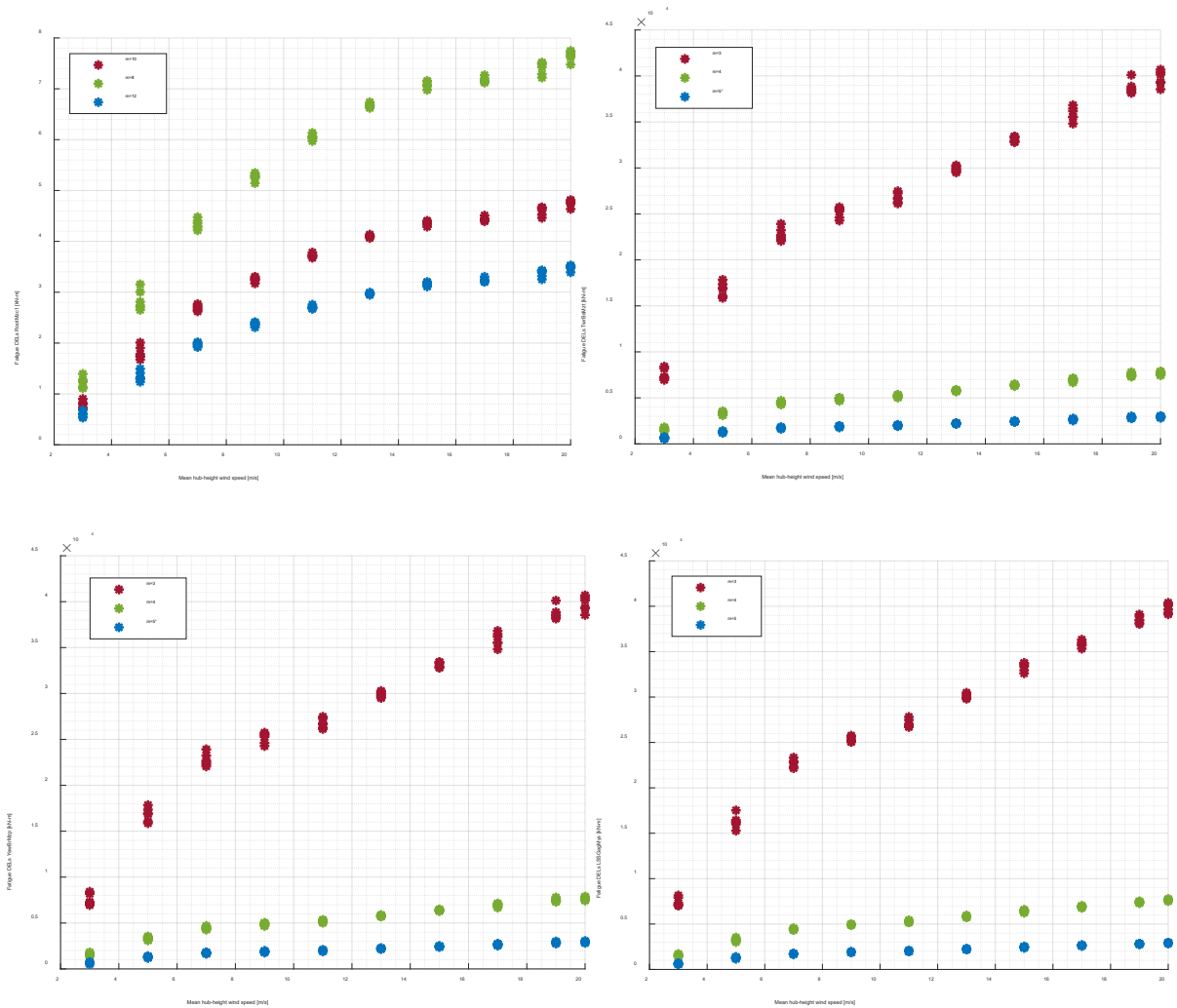


FIGURE 55: VARIATION OF DAMAGE EQUIVALENT LOADS (DELs) AS A FUNCTION OF MEAN HUB-HEIGHT WIND SPEED FOR OFFSHORE CART SYSTEM (THE ABBREVIATIONS ARE EXPLAINED IN SECTION 6.3.5)

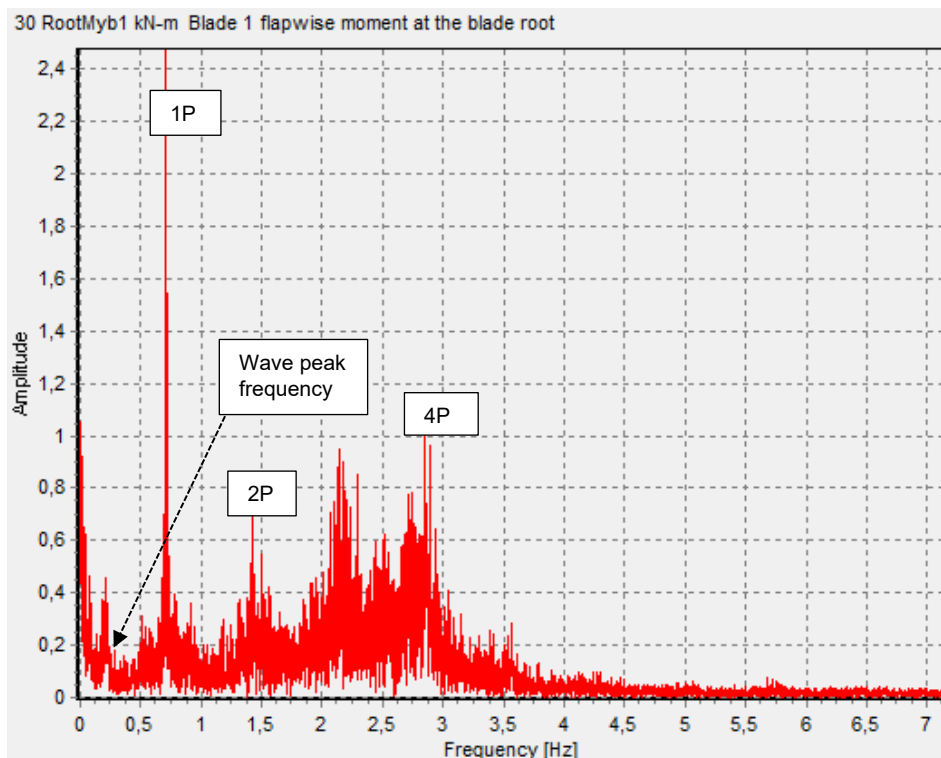


FIGURE 56: FFT OF BLADE ROOT FLAPWISE BENDING MOMENT AT RATED WIND SPEED

Effects of ULF on fatigue DELs

As mentioned above, the ultimate strength of load components was obtained by multiplying the extreme loads resulted from DLC 1.1, 1.3, and 1.4 with an ultimate factor. Here, a brief experiment was carried out to investigate the variations in fatigue DELs depending on the variation in ultimate load factor and Wöhler's exponent. The ultimate load factors considered are 1.25, 2.5, 5, 10, 20 respectively. Figure 57 shows how the fatigue DELs of tower bottom torsional moment changes with the variation in ULF for both onshore and offshore CART system. Fatigue DELs of tower bottom torsional moment for the offshore CART system are indicated by star whereas that of the onshore system are indicated by square. It is obvious that fatigue DELs of tower bottom torsional moment are lower for the offshore wind turbine than that for the onshore wind turbine. This means that the lifetime of offshore system is longer than that of the onshore system. It is especially true when the Wöhler's exponent is small. Nevertheless, there is no significant difference in fatigue DELs between onshore and offshore CART system when the Wöhler's exponent is large, for instance $m = 3$. Moreover, it seems that the lower ULF overestimates the fatigue DELs, for example, $ULF = 1.25$. It is interesting to note that the higher Wöhler's exponent leads to a greater difference in fatigue DELs between the onshore and offshore wind turbines.

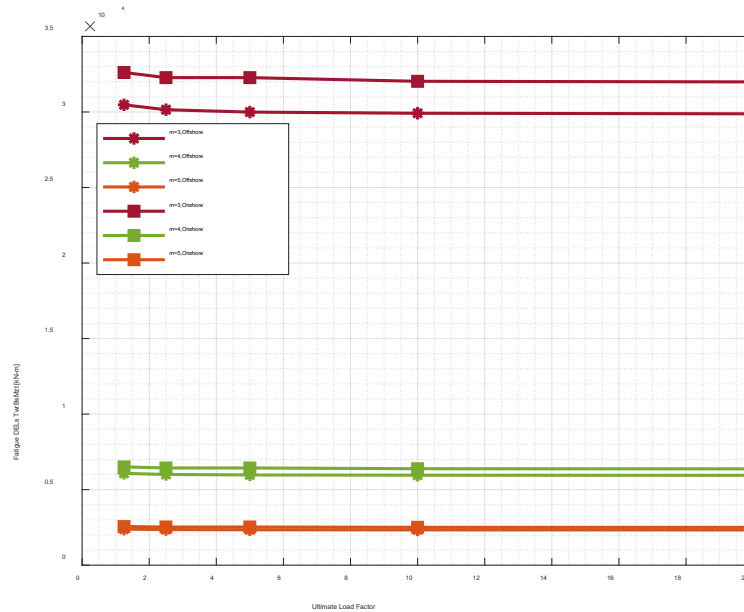


FIGURE 57: VARIATIONS IN FATIGUE DELS DEPENDING ON THE VARIATION IN ULF AND WÖHLER'S EXPONENT

6.4 EXTREME CONDITIONS WITH FAULTS

Having discussed dynamic responses and design driving load cases in normal operation in the previous section 6.3, load analyses for the extreme situation with faults during power production in severe sea state, power production with faults and parked with faults were examined in this section. It includes DLC 1.6, DLC 2.3, and DLC 6.1.

DLC 1.6 deals with power production in normal turbulence wind but severe sea state (SSS). The sea state was modelled with a significant wave height, $H_s = H_{s,SSS}[V_{hub}]$ as described in section 5.6. Currents are taken into account and the wind and wave directionality are considered to be unidirectional. Simulations were carried out at NWLR. A misaligned yaw between the direction of average inflow wind and the direction of rotor axis was taken to be $\pm 8^\circ$. Similar to DLC 1.1, a wind speed interval of 2 m/s was considered. For each environmental condition, simulations were performed for 10 min with six different wind and wave seeds.

DLC 2.3 simulates grid failures during power production in the extreme operating gust condition (EOG) and normal sea state (NSS). A deterministic EOG wind model was generated by NREL IECWind. The gust transient event starts at 77 s and duration wind gust is 10.5 s. Yaw misalignment was not taken into account. The vertical inflow was considered to be inclined $\pm 8^\circ$ according to IEC 61400-3. Normal current model was taken into account and wave is considered to be co-directional with the wind.

DLC 6.1a aims to investigate the dynamic behaviour of the turbine when it is subjected to extreme wind and wave conditions with a recurrence of 50 years. Extreme current model (ECM) was assigned as described in section 5.6. Simulations were performed at extreme water

level (EWLR). A misaligned yaw between the direction of average inflow wind and the direction of rotor axis was considered to be $\pm 8^\circ$.

6.4.1 DESIGN DRIVING LOAD CASES

By examining the response of the extreme events mentioned above for offshore wind turbine, it was found that DLC 2.3 contributes only a few parameters namely blade tip deflections, in-plane moment at the blade root, edgewise bending moment at the blade root, tower top yaw moment, and tower base axial force. On the other hand, DLC 6.1, which simulates storm condition and extreme sea states characterized by extreme wave heights, greatly influence the platform motions. It also contributes most parameters namely blade root bending moments, flapwise bending moment at the blade root, rotor thrust force, tower top side-to-side displacement, tower top bending moment, tower bottom fore-aft and side-to-side moments, and tower bottom torsional moment. It is quite common for a wind turbine with stall regulation that the highest rotor thrust force occurs in this load case. Figure 58 compares the maximum platform motion response of the offshore wind turbine between normal conditions and extreme events with faults. It is not surprising that faults-induced responses of several parameters are much higher than those in normal conditions. Nevertheless, it is worth mentioning again that fault-induced loads are resulted from situations that cause transient and short-term responses or involve extreme wind and wave conditions.

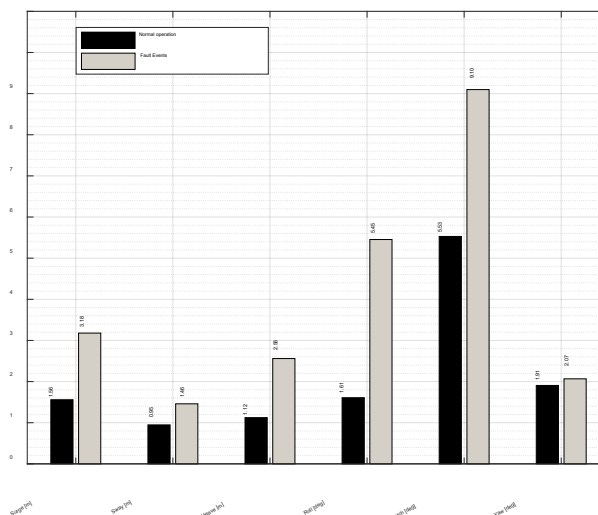


FIGURE 58: COMPARISON OF PLATFORM MOTION BETWEEN NORMAL OPERATIONS AND EXTREME EVENTS WITH FAULTS

6.4.2 COMPARISON OF OFFSHORE AND ONSHORE CART SYSTEM

Again, the extreme loads of several parameters were compared between the onshore and offshore CART system to investigate the effect of floating support structure on the dynamic behaviour of the turbine during extreme events with faults. The bar charts in Figure 59 give information about the ratio of the extreme loads resulted from offshore to onshore CART system.

By examining the response of the control system, it was found that the absolute maximum extreme load in rotor speed has increased by 43% for offshore CART system. For both the onshore and offshore CART system, the extreme rotor speed was triggered by DLC 2.3. In this particular case for the offshore wind turbine, the transient event starts at 77 s after simulation and maximum gust speed is reached at 82.25 s. As already mentioned, the grid was disconnected at 82 s and the mechanical brake is engaged at 82.5 s to capture the worst possible extreme load. As a result, the rotor speed goes up to 49.08 rpm, which is about 14 % of its nominal rotor speed. Nevertheless, it decays to zero quite quickly after the brake was engaged. There is also a significant increase in generator torque and generator power for the offshore wind turbine. As expected, the turbine is sensitive to cut-out wind speed. The increase in generator torque and generator power occur in a situation which simulates normal turbulence winds with a mean hub-height wind speed of 20 m/s and severe sea state conditions. This is particularly related to increased load excursion of pitch motions due to an increase in rotor thrust force in high winds. As a result, there is also an increase in generator torque and generator power. For the onshore wind turbine, the extreme load in generator torque and generator power was driven by DLC 2.3. Therefore, the difference in generator torque and generator power between the onshore and offshore CART system is so large. On the other hand, only a slight difference in rotor thrust force was observed between offshore and onshore wind turbine. It is clear that the thrust force is highest in storm conditions for both wind turbines. It is also interesting to note that the extreme thrust force for both onshore and offshore wind turbine seems to be driven by yaw misalignment of -8° , to be specific, simulation number 10 in DLC 6.1.

Based on the findings, nearly 138 % of blade in-plane tip deflection and 26% of blade out-of-plane deflection have increased for offshore wind turbine. This might be due to the fact that the tip deflections are affected by transient event DLC 2.3 for the offshore CART system whereas they are affected by storm conditions for onshore CART system. Tower top side-to-side displacement has reduced by about 6 % for offshore wind turbine whereas tower top fore-aft displacement has increased by about 6 %. On the other hand, the tower top pitch moment has increased by approximately 23 % for offshore wind turbine and tower top roll moment has reduced by about 66 %. The tower bottom fore-aft bending moment, side-to-side bending moment, and torsional moment have increased by about 59 %, 10% and 13 % respectively for offshore wind turbine. It is quite remarkable that shaft shear force along the y-axis and bending moment about the y-axis have increased as much as around 41 % and 82 % respectively.

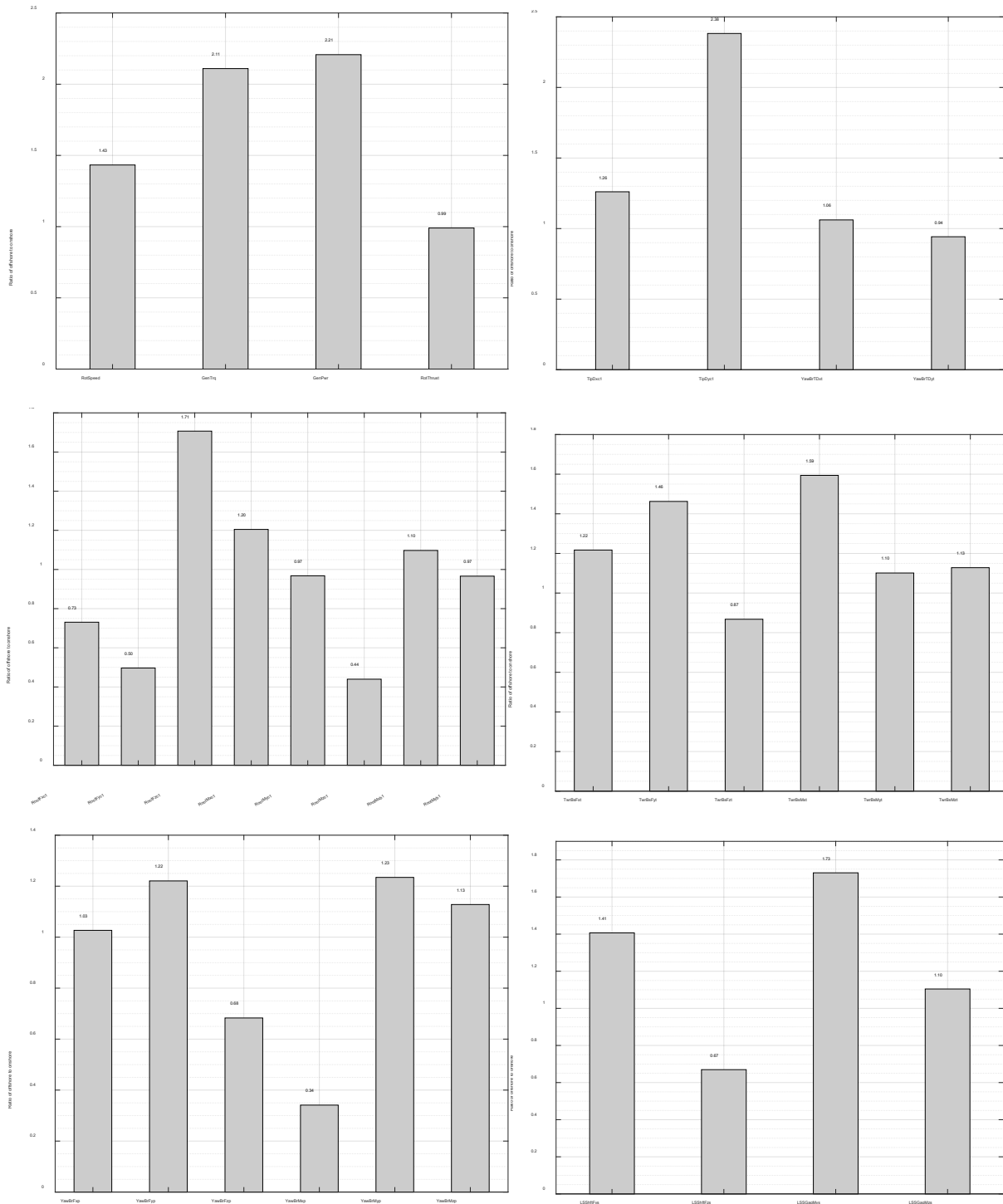


FIGURE 59: RATIO OF OFFSHORE TO ONSHORE CART SYSTEM FOR EXTREME EVENTS WITH FAULTS

6.4.3 TOWER TOP SIDE-TO-SIDE DISPLACEMENT FOR ONSHORE WIND TURBINE

By examining the response of the onshore wind turbine in extreme conditions with faults, it was observed that maximum tower side-to-side displacement was triggered by grid failure during extreme operating gust conditions. In the simulations of DLC 2.3 for the offshore CART system, the extreme tower top side-to-side displacement seems to be triggered by a yaw misalignment of 8° at cut-out wind speed. The maximum gust speed is 6.18 m/s. The extreme

gust starts 77 seconds after the simulation and the transient event lasts over 10.5 s. To capture the worst possible response of the turbine, loss in generator torque was implemented at 82 s, at which the maximum gust wind speed is reached. Figure 60 depicts the time history of wind speed, thrust force, edgewise and flapwise moment at the blade root, tower top side-to-side displacement, tower bottom side-to-side bending moment, and shaft brake torque. The extreme tower top side-to-side displacement was discovered in simulation number 6. It occurs at cut-out wind speed, to be more specific, 1.86 s after the grid failure. As a result of tower top side-to-side oscillations, there is also ringing oscillations in the mean value of tower bottom side-to-side bending moment. This ringing oscillation is also visible in edgewise and flapwise bending moment at the blade root and it decays afterward due to the fact that the turbine is no more in operating mode and the shaft brake is applied. It seems that the control system is working well to keep the reasonable amount of torque during peak wind gust. Based on the results, the braking torque drops sharply to around -17.53 kN-m which is visible as ringing oscillation, and afterward it dissipates quite quickly to zero. Upon taking a closer look at the FFT diagram depicted in Figure 61, it was found that the largest excitation occurs at the blade passing frequency of the rotor (2P). In figure, the excitation with the natural frequency of 1st tower side-to-side bending mode and harmonic frequencies of the rotor (4P,6P) are also visible.

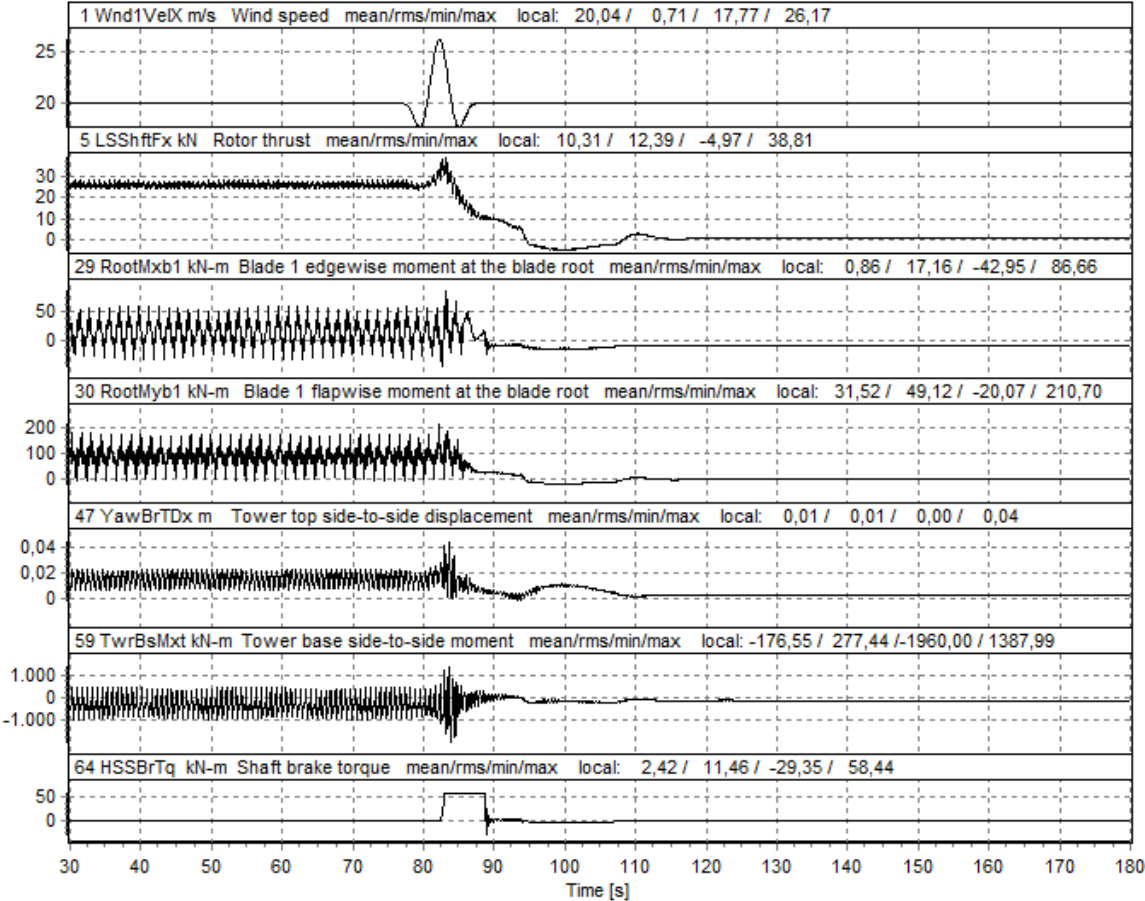


FIGURE 60: TIME HISTORY OF EXTREME TOWER TOP SIDE-TO-SIDE DISPLACEMENT FOR ONSHORE WIND TURBINE

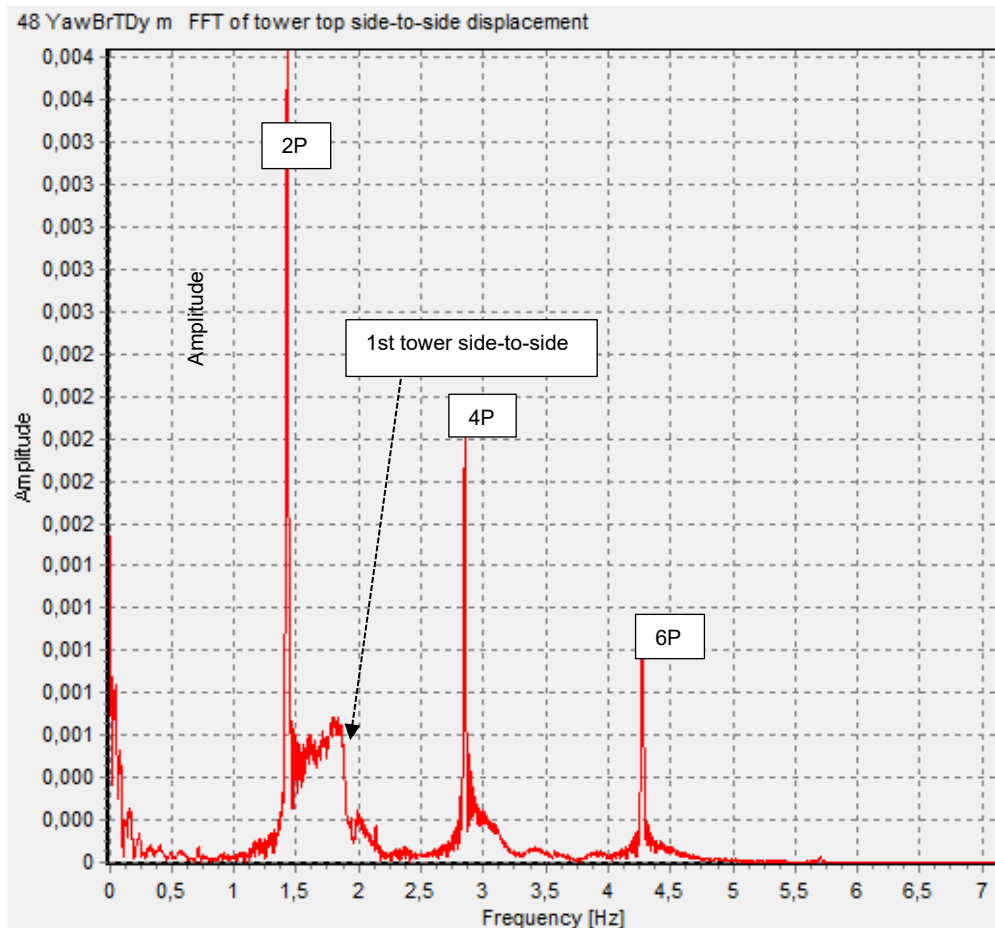


FIGURE 61: FFT OF TOWER TOP SIDE-TO-SIDE FOR ONSHORE WIND TURBINE

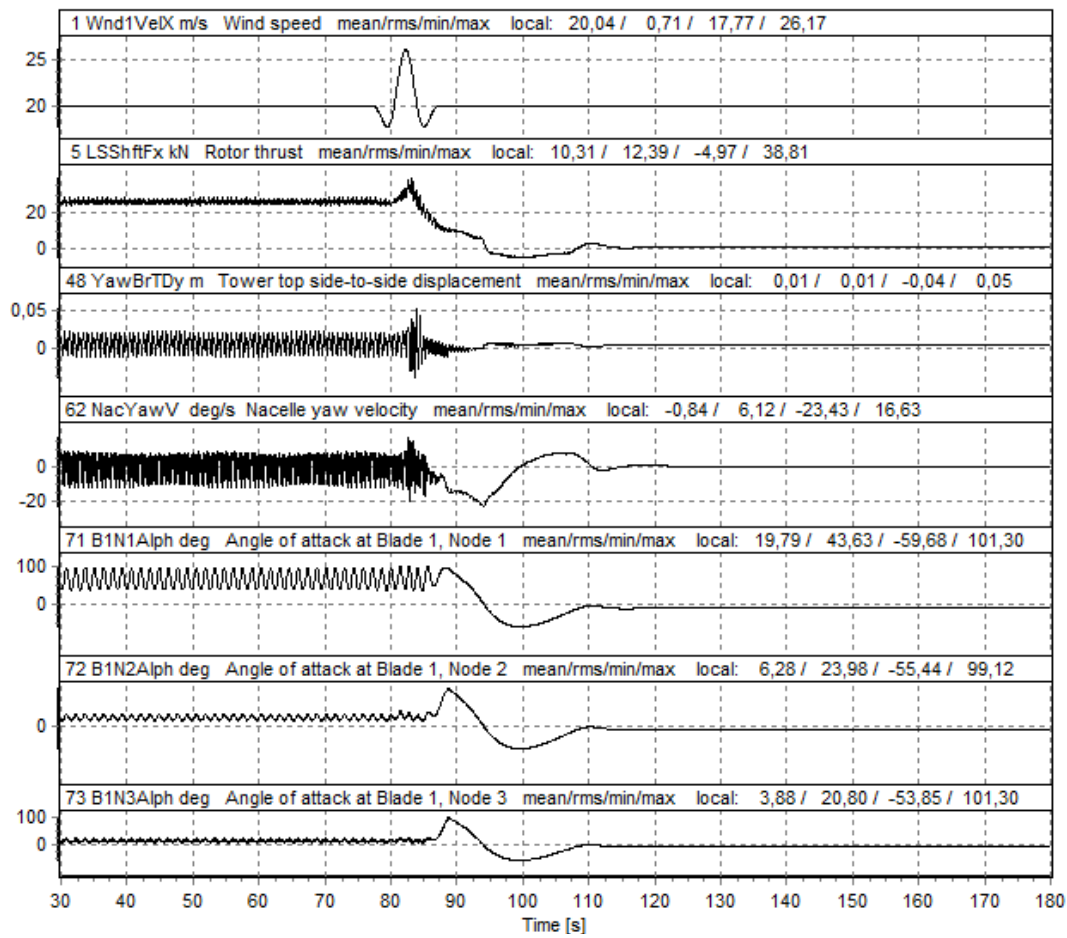


FIGURE 62: TIME HISTORY OF NACELLE YAW ANGULAR VELOCITY AND ANGLE OF ATTACK FOR ONSHORE WIND TURBINE

Figure 62 illustrates time history of wind speed, thrust force, tower top side-to-side displacement, nacelle yaw velocity, angles of attack on the blades for this transient event. It seems that the ringing oscillation in response of tower motions might be attributed to the sudden change in the rotor thrust force due to grid failure followed by shaft brake. Due to transient events posed by wind gusts, the thrust force is gradually increased and decreased. On top of that, it is interesting to observe that there are significant oscillations in angles of attack on the blades and nacelle yaw angular velocity before it decays to zero. All in all, the implemented control system and the mechanical brake is working well since it manages to bring the turbine to a complete standstill within a reasonable time.

6.4.4 EXTREME SURGE MOTION IN EXTREME WIND AND WAVE CONDITIONS

The maximum surge motion was observed in simulation number 29 of DLC 6.1. As mentioned in section 6.4, DLC 6.1 simulates the situation when the turbine is parked in storm conditions and an extreme sea state with a 50-year return period. The maximum surge motion of 3.19 m was driven by the particular simulation, in which no yaw misalignment was taken into account, but wind and wave misalignment of 30° was considered. The maximum surge motion occurs at a wind speed 53.27 m/s. This is visible at simulation time 568.19 s in Figure 63 which illustrates a close-up of the time history of platform surge motion. Mooring line 3 corresponds

to the upwind mooring line and tension at fairlead of the mooring line is denoted by T_3 . As it is evident in response of the platform in static equilibrium condition, the platform pitch and surge motion are coupled even in the absence of wind and wave forces. In this particular case, peak surge motion originates from the change in rotor thrust force which is caused by the platform pitch motion. It is interesting to note that peak surge motion occurs when the rotor thrust abruptly decreases and the rotor thrust force increases again when the surge motion reaches its maximum value. What we can see more in figure is that peak surge motion is also correlated to the tensions in the mooring lines which, in turn, is dominated by wind turbulence. When the platform is being pushed downward, the mooring line in the upwind side is being pulled upwards and large surge motion occurs. In order to get a better understanding of the correlation among wind, tension in mooring line upwind, and peak surge motion, FFT of wave elevation, wind, tension at fairlead of the mooring line 3, and surge motion are depicted in Figure 64.

Many studies have showed that the second-order wave loads influence on the platform motions especially for floating platforms like semisubmersibles. Figure 65 compares platform motion resulted from first-order hydrodynamic loads depicted in the red line and first-plus second-order hydrodynamic loads depicted in the blue line. Based on the results, the maximum surge motion was slightly lower and minimum surge motion was slightly higher when only first-order hydrodynamic loads are considered.

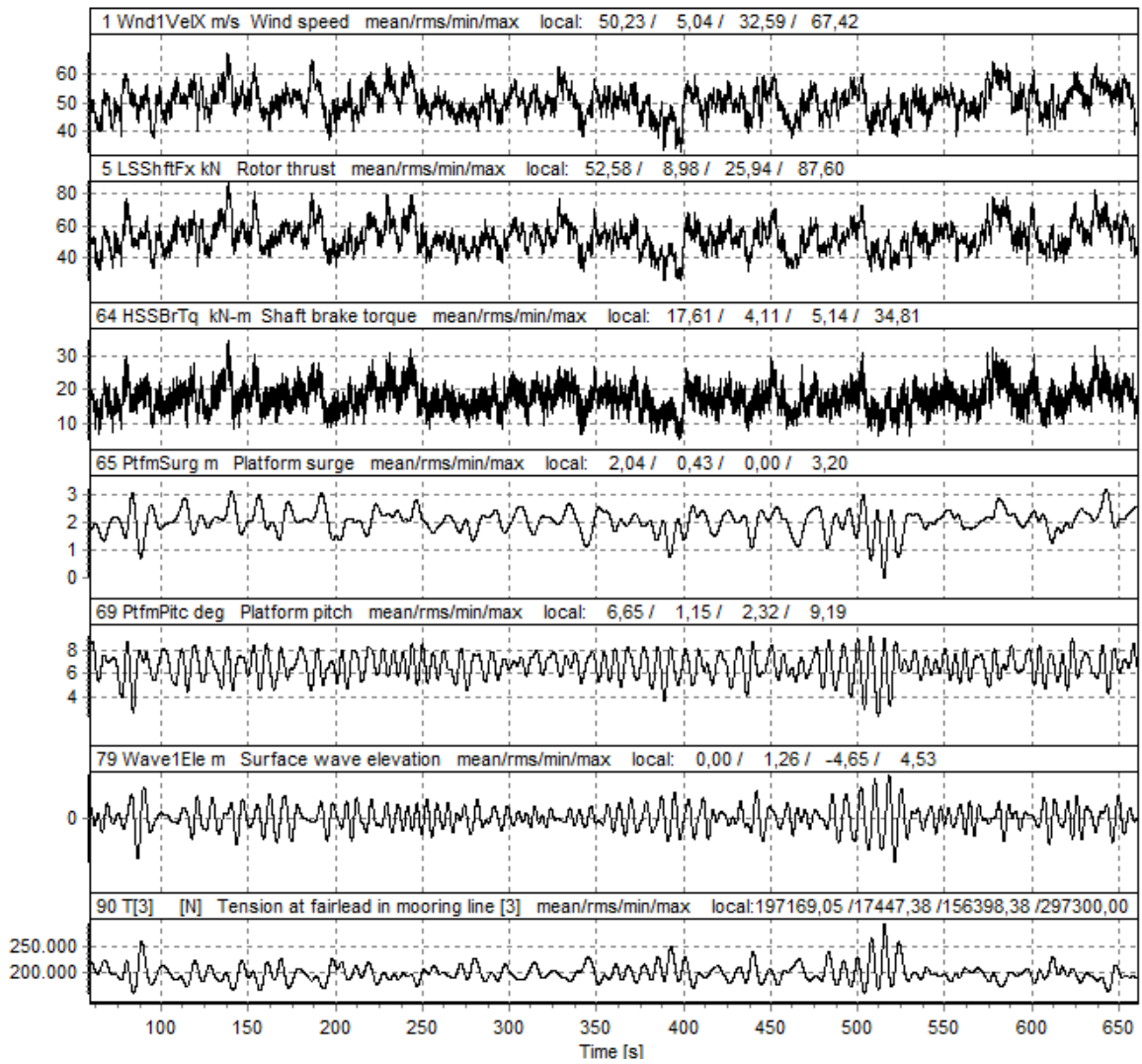
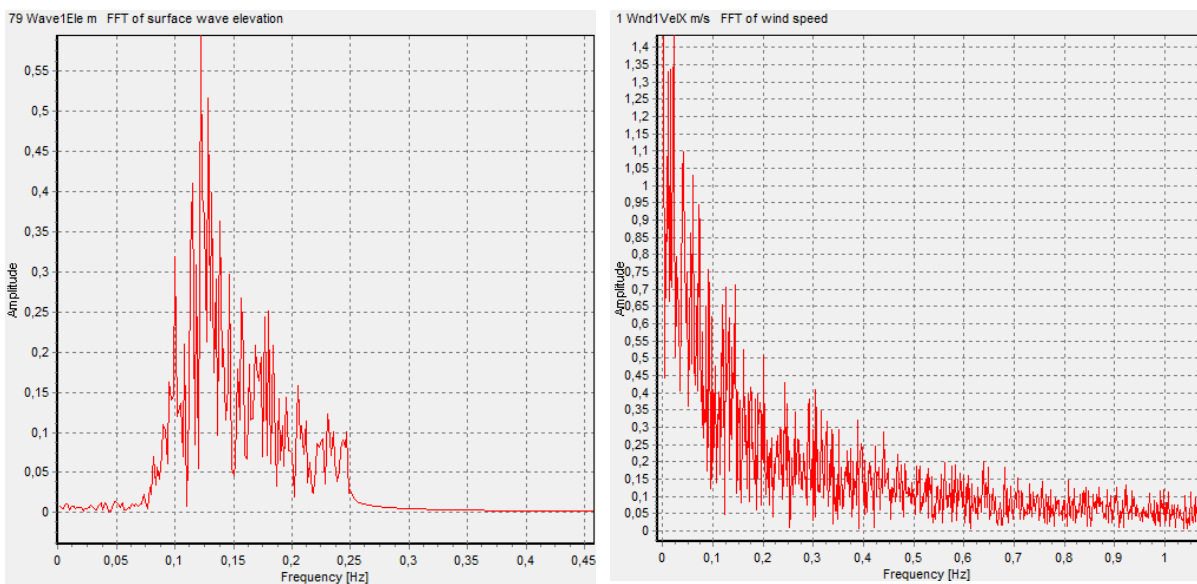


FIGURE 63: TIME HISTORY OF MAXIMUM SURGE MOTION, SIMULATION NUMBER 3 OF DLC 6.1



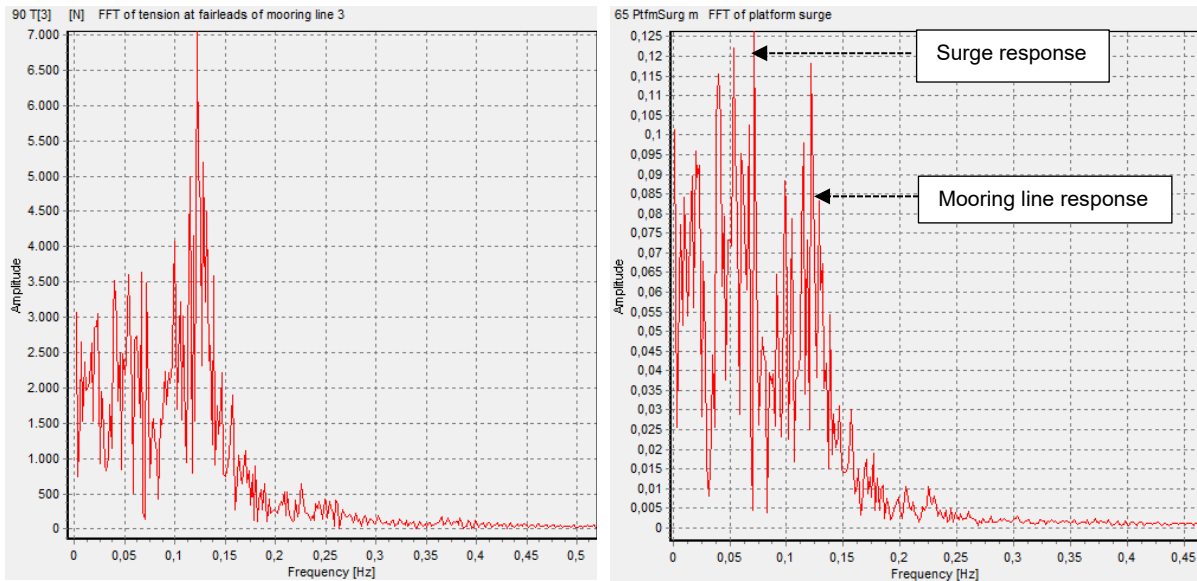


FIGURE 64: FFT OF WAVE SURFACE ELEVATION, WIND SPEED, MOORING LINE TENSION AND SURGE MOTION

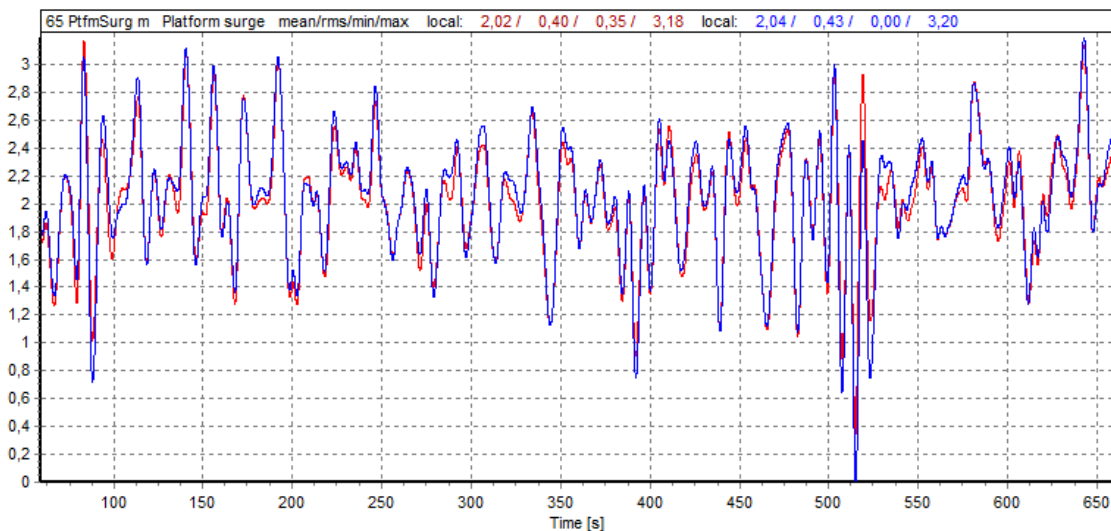


FIGURE 65: COMPARISON OF PLATFORM SURGE MOTION BETWEEN WAVE LOADS WITH AND WITHOUT SECOND-ORDER IMPLEMENTATION

6.4.5 EXTREME PITCH MOTION IN EXTREME WIND AND WAVE CONDITIONS

As mentioned above, the examined semisubmersible platform is quite sensitive to large amplitude platform motions especially when it is subjected to large incident waves during severe sea states. The mechanical shaft brake is engaged when the turbine is parked. Extreme platform pitch motion was observed in simulation number 18 of DLC 6.1. This particular case was simulated under consideration of a yaw misalignment of 8° and the directionality of wind and wave being colinear. Extreme pitch motion occurs at a wind speed of 55.78 m/s and time 531.37 s. It appears that the sudden change in rotor thrust leads to large pitch motion as the pitch restoring stiffness is usually low for semisubmersible platforms. This results in a pitch angle of 9.10° in storm conditions, which is just below the static inclination of 12° for survival conditions prescribed by DNV-GL-OS-C301 (2020). It was observed that the platform operates

with a mean pitch angle of 6.62° with a standard deviation of 1.04° in this situation. Since the shaft brake is applied, the rotor is not in operational mode, and thus no generator torque and subsequently no power is produced. The small oscillation in rotor speed reflects the motion of surface wave. As we can clearly see in the time history of pitch motion in Figure 66 and Figure 67, the platform keeps moving with the surface wave. Applying shaft brake stops only the rotor from spinning. To reduce the platform motion in such conditions, it is desirable to integrate structural control systems like tuned mass damper.

To gain more insight into the dynamic response of the platform, FFT diagrams of wave and pitch motion are depicted in Figure 68, capturing the important peaks. As it is evident in figure, the largest peak in the FFT diagram of pitch motion represents the structural natural frequency in pitch direction of 0.12 Hz which is already described in section 4.5.5. As it can be clearly seen in FFT of wave elevation, the wave peak frequency ranges between 0.12 Hz-0.24 Hz. It means that the wave frequency coincides with the structural frequency of the platform in pitch direction. To shift the natural frequency of pitch platform motion away from wave frequency, one way is to increase the structural stiffness in pitch direction. The other way is to incorporate a structural control system between the tower and the platform as mentioned above. Low peak before the largest peak represents the response in the wind energy range.

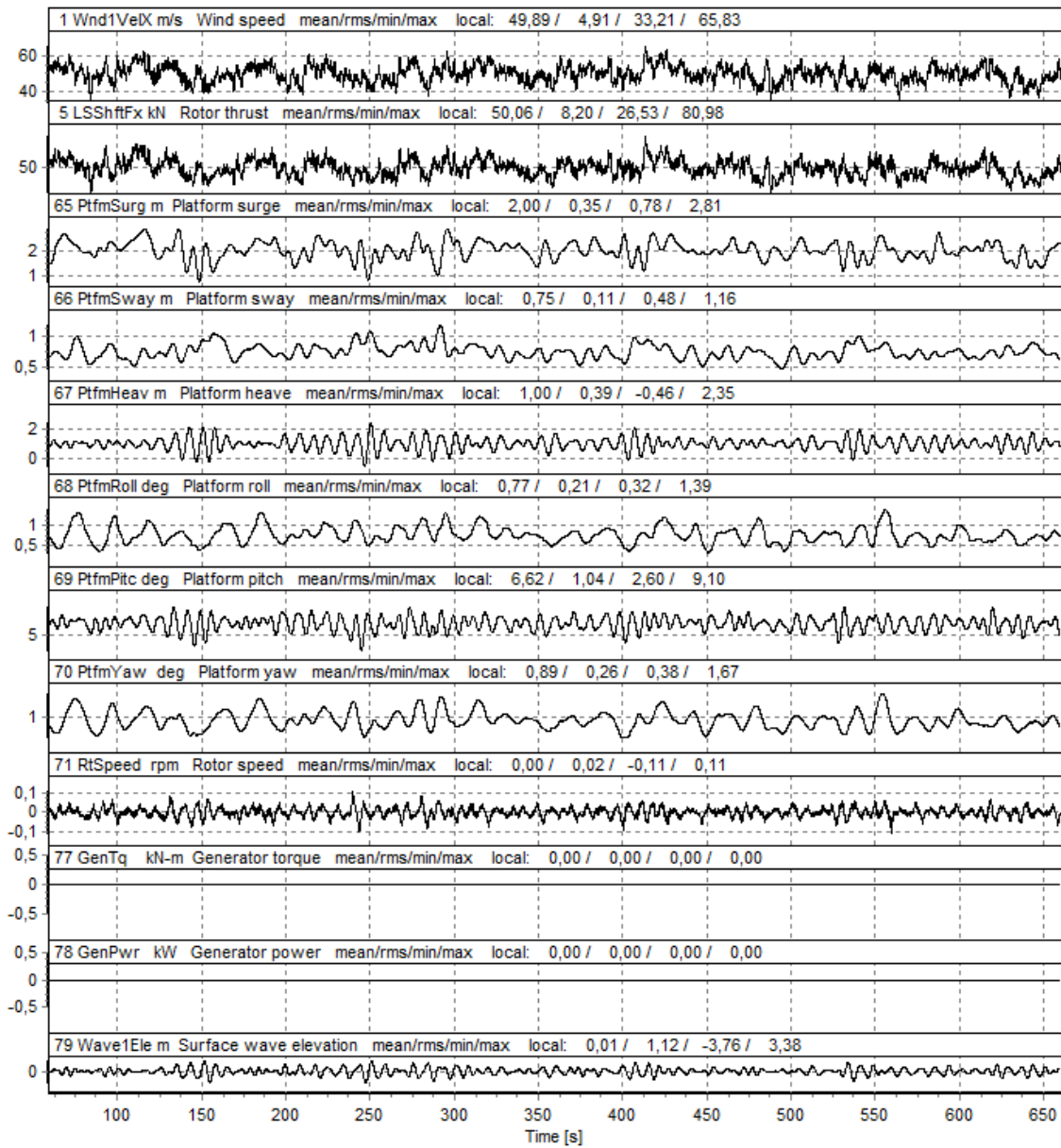


FIGURE 66: TIME HISTORY OF EXTREME PITCH MOTION IN SIMULATION NUMBER 18 OF DLC 6.1

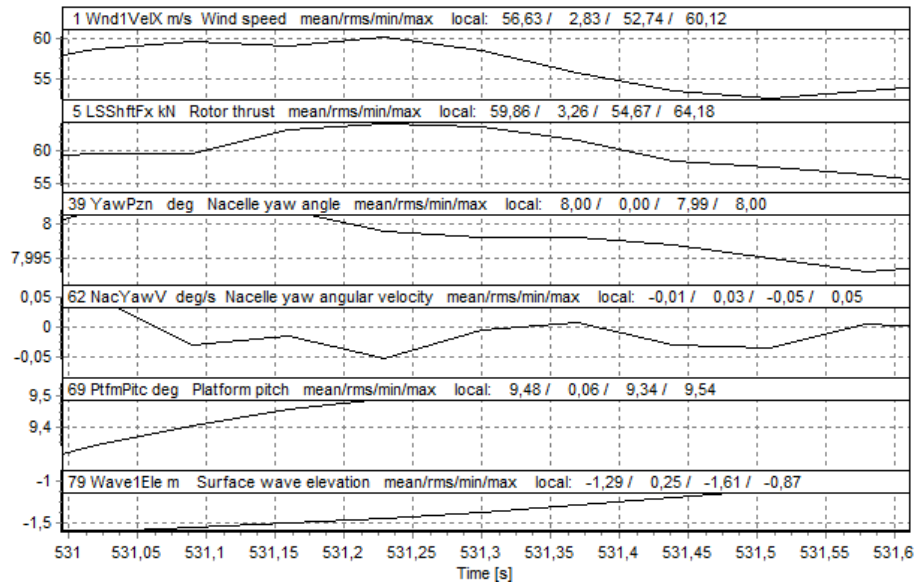


FIGURE 67: CLOSE-UP OF TIME HISTORY FROM SIMULATION NUMBER 18

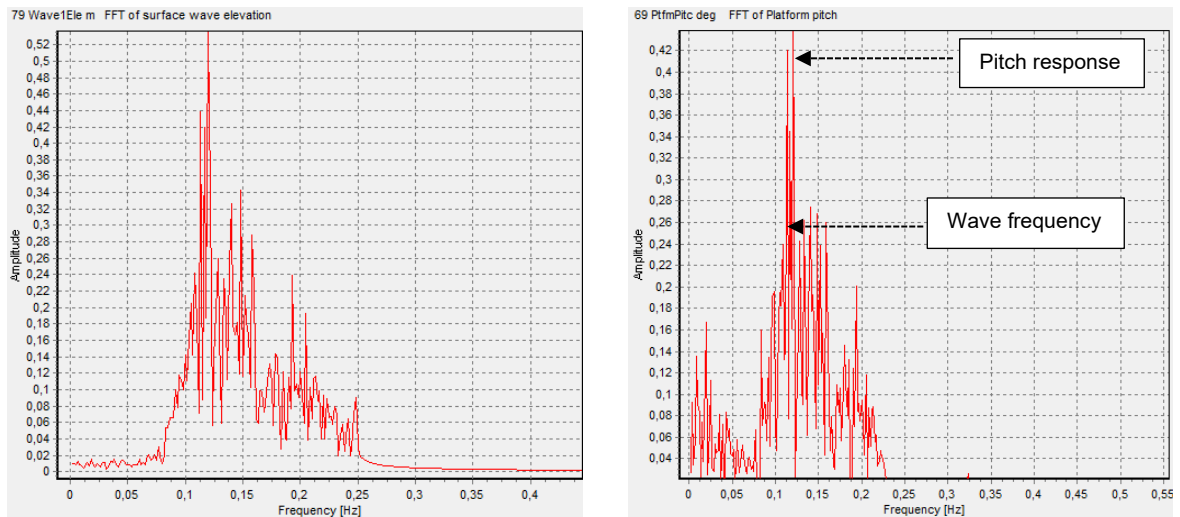


FIGURE 68: FFT OF WAVE SURFACE ELEVATION (LEFT) AND PITCH MOTION (RIGHT)

6.5 EXTREME CONDITIONS WITH FAULTS AND WORST CONSEQUENCES

In this section, the dynamic response of the remaining DLCs defining extreme conditions with faults and worst consequences was further analyzed. This encompasses DLC 2.1, DLC 2.2, DLC 6.2a, DLC 6.3, DLC 7.1a, and DLC 7.2 respectively.

DLC 2.1 simulates the transient event in which the turbine loses the electric grid connection during normal turbulence wind and normal sea state. Yaw misalignment was not taken into account. For each environmental condition, simulations were performed with 10 min mean wind speed containing six different wind seeds and a stochastic irregular wave model containing six different wave seeds. Wind and wave direction were considered to be unidirectional. This results in a total of 60 simulations for DLC 2.1. DLC 2.2 deals with faults in the yaw system during normal wind condition and normal sea state. Faults in the yaw system

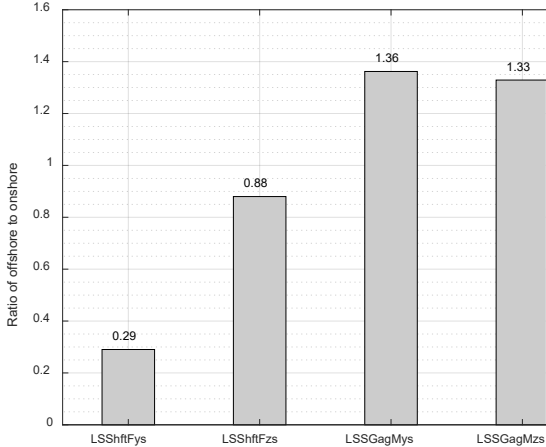
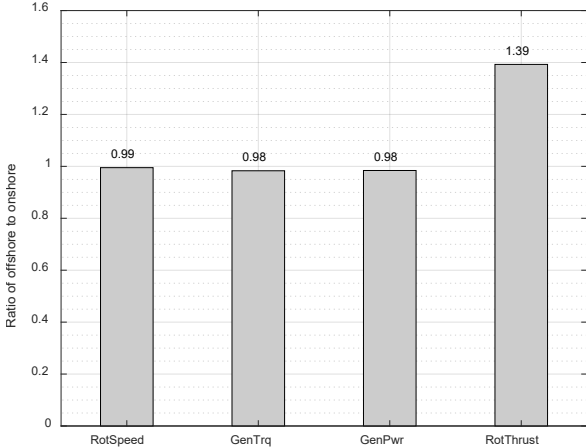
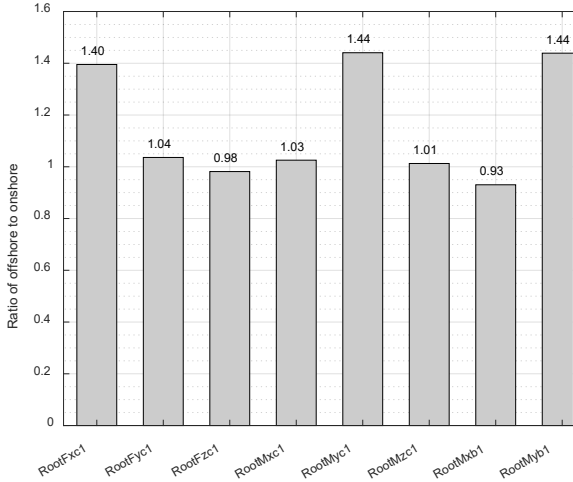
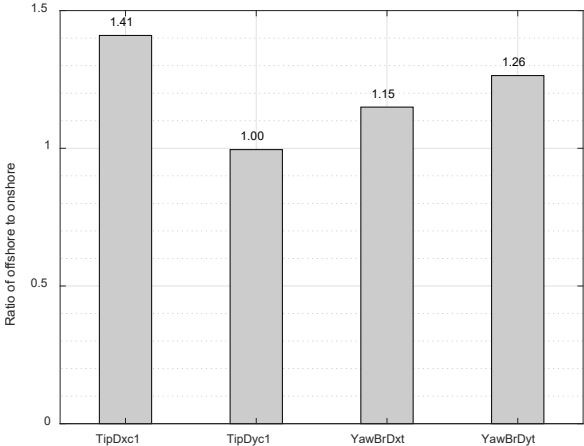
are implemented by taking into account a yaw misalignment ranging between -180° and 180° with an interval of 10° . DLC 6.2a covers the situation in which the turbine is parked in extreme wind and wave conditions. Similar to DLC 2.2, fault in the yaw system was implemented by taking into account a misaligned yaw ranging between -180° and 180° . As mentioned in section 6.4, the aerodynamic forces acting on the aerofoils are computed using steady model due to the fact that very high post-stall angles of attack are likely to be experienced in parked conditions. The dynamic stall model is only applicable to operational conditions. Wind and wave conditions of 50-year return period were considered. Current speed and water level variation in extreme condition is assigned as defined in section 5.6. DLC 6.3 simulates the turbine being parked in extreme wind and wave conditions when wind and wave are misaligned with an angle of $\pm 30^\circ$. In this load case, wind and wave conditions of 1-year recurrence were considered. Extreme current speed was modelled, but the normal water level variation was taken into account. A misaligned yaw of $\pm 20^\circ$ was taken into account. DLC 7.1a simulates the fault condition in which yaw system error occurs while parked in extreme wind and wave conditions. A misaligned yaw angle ranging between -180° and 180° with an interval of 10° was taken into account. Similar to DLC 6.3, wind and wave were misaligned with an angle of $\pm 30^\circ$, and wind and wave conditions of 1-year recurrence were assumed. Different from DLC 7.1a, DLC 7.2 simulates the fault condition in which yaw system error occurs while parked in normal wind and wave conditions. No current model was taken into account. Simulations were performed at normal water level as defined in section 5.6.

6.5.1 COMPARISON OF OFFSHORE AND ONSHORE WIND TURBINE

Aiming to investigate how the dynamic response of the system changes in the presence of the floating substructure in extreme conditions with the worst consequences, the load responses between offshore and onshore CART systems were compared. The bar charts in Figure 69 compare the resulted extreme loads in terms of the ratio of offshore to onshore CART system. As we can clearly see in figure, extreme loads of most parameters have significantly increased in the presence of floating substructure. Blade 1 out-of-plane tip deflection, blade 1 out-of-plane shear force and bending moment at the blade root, flapwise bending moment at the blade root have increased as much as approximately 41 %, 40 %, 44 % and 44% respectively. What is more, is that the response of the control system is barely affected by the presence of the floating substructure. It in turn indicates that the developed control concept is working quite well. However, rotor thrust has increased about 39 % for offshore CART system. Similarly, tower-top fore-aft shear force, tower-top side-to-side shear force and tower-top yaw moment have increased as much as 46 %, 11% and 32 % respectively. It is also quite remarkable that tower bottom fore-aft shear force, tower bottom side-to-side shear force, tower bottom side-to-side moment, tower bottom fore-aft moment and tower bottom torsional moment have significantly increased as much as about 60 %, 71 %, 41 %, 46 % and 32 % respectively. Shaft

bending moment about y-and z-axis have also increased by approximately 36 % and 33 % in the presence of floating substructure.

Based on the findings, the extreme tower bottom loads for the offshore CART system were driven by DLC 6.3 which simulates the turbine being parked in extreme wind and wave conditions when wind and wave are misaligned with an angle of $\pm 30^\circ$ and 1-year recurrence were assumed. On the other hand, the extreme tower bottom loads for the onshore CART system were driven by DLC 6.2 and DLC 2.2. The former simulates the turbine being parked in extreme wind condition with 50-year recurrence and the latter deals with faults in the yaw system during normal wind conditions.



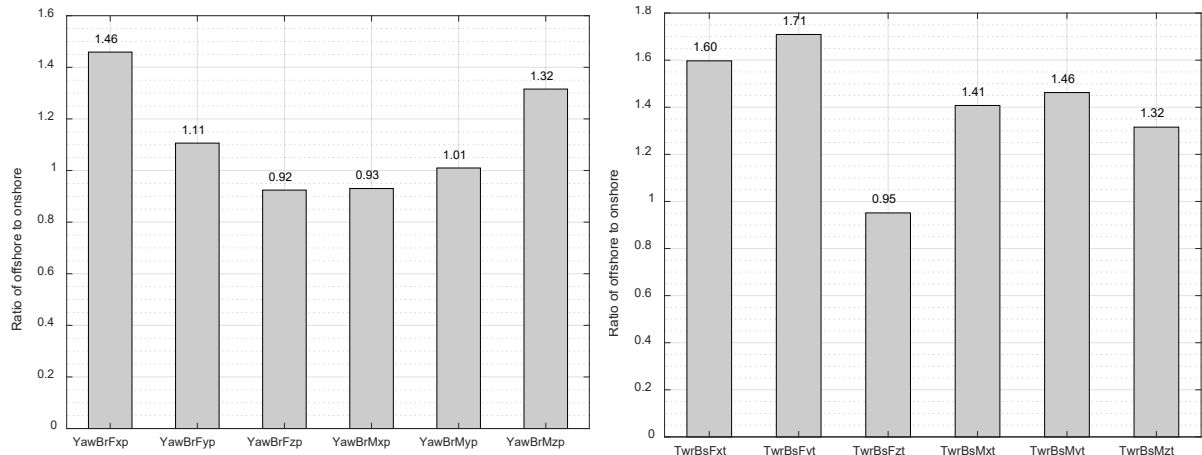
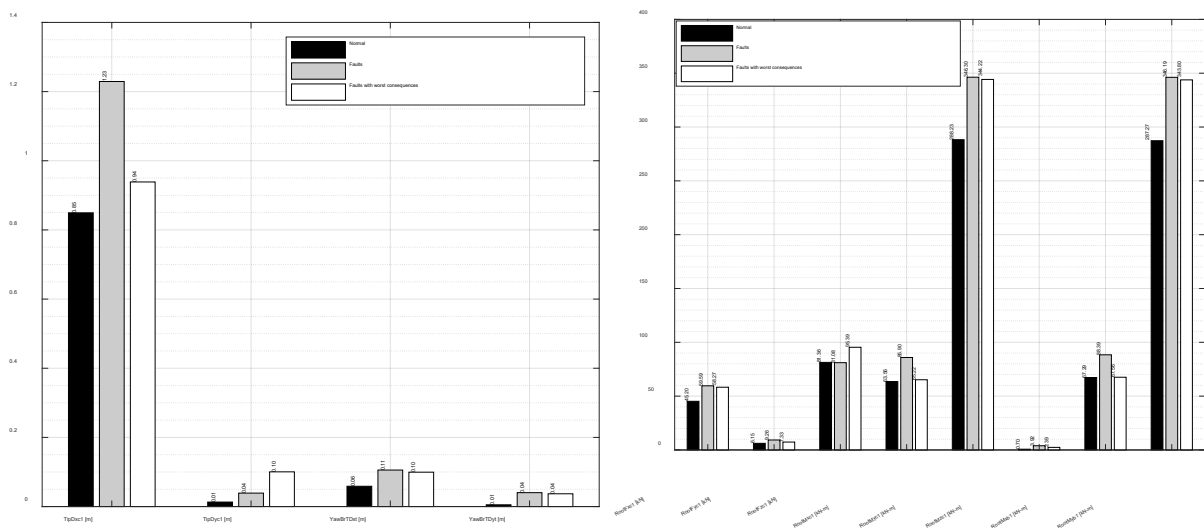


FIGURE 69: RATIO OF OFFSHORE TO ONSHORE CART SYSTEM FOR EXTREME FAULTS EVENTS WITH WORST CONSEQUENCES

6.5.2 RESPONSES IN NORMAL OPERATION, EXTREME EVENTS WITH FAULTS, AND FAULTS EVENTS WITH WORST CONSEQUENCES FOR OFFSHORE CART SYSTEM

To draw a conclusion on which load case drives which load component for offshore CART system, the extreme loads from normal operation, extreme events with faults, and faults events with worst consequences were compared in Figure 70. Based on the results, extreme loads of most parameters are triggered by extreme events with faults and extreme events with worst consequences. On the other hand, tower-top pitch moment and tower-top yaw moment are driven by normal operation, to be more specific, by wind gusts. Bending moments at the blade root in normal operation are slightly lower than those experienced in extreme events with faults and extreme events with worst consequences.



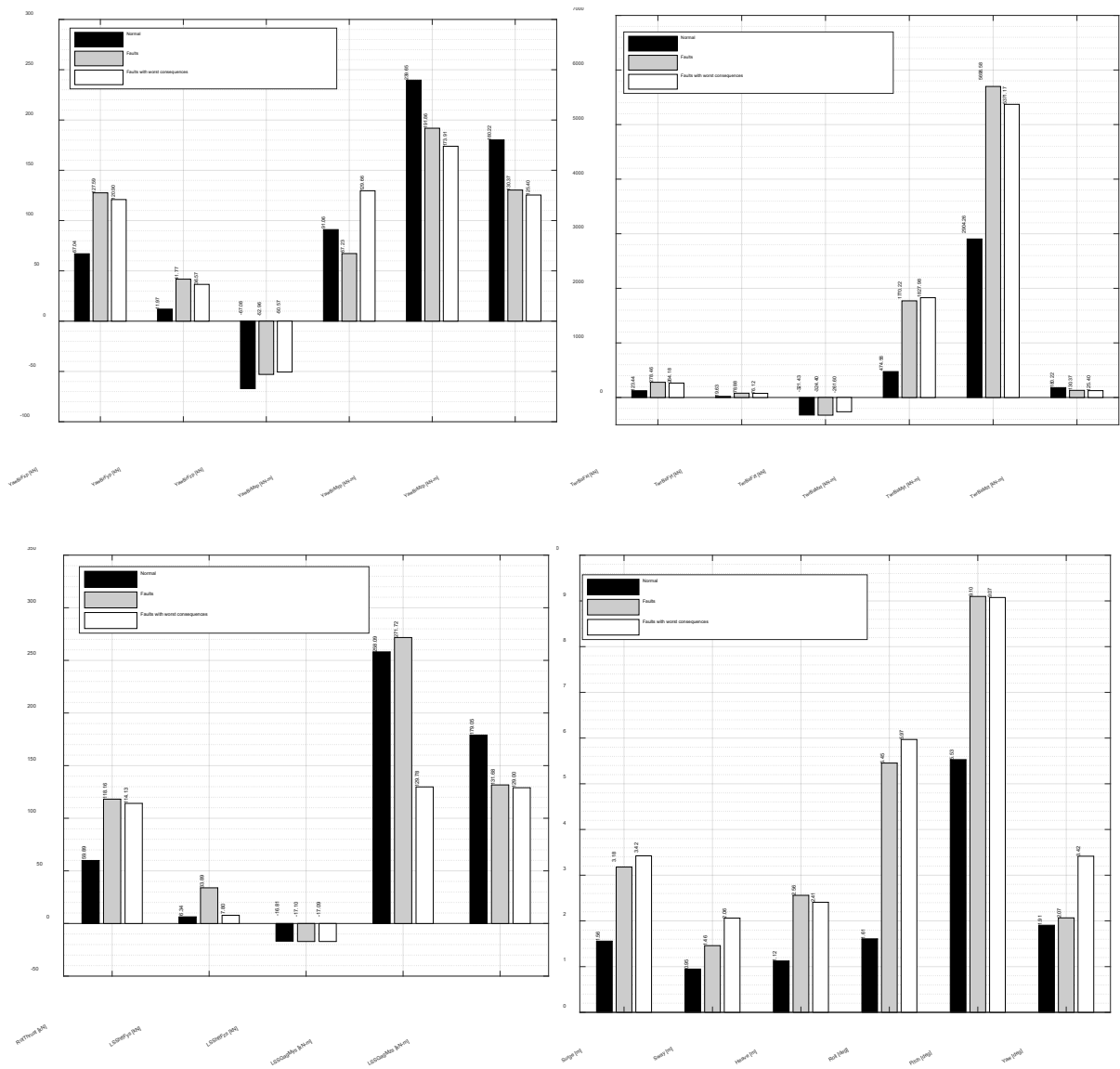


FIGURE 70: COMPARISON OF EXTREME LOADS FROM DIFFERENT LOAD CASES

The comparison of platform motions for different load cases indicates that platform heave and pitch motions were greatly affected by parking when the turbine is subjected to extreme wind and wave conditions with a recurrence of 50 years. For both cases, it was found that wind and wave were assumed to propagate in the same direction. Platform surge, sway, roll, and yaw motions were greatly affected by 50-year and 1-year wave conditions when the turbine is parked. The extreme surge motion of 3.42° appears in simulation 41 of DLC 6.3 which simulates the parked turbine in extreme wind and wave conditions with 1-year recurrence. In this particular case, wind and wave are misaligned with an angle of -30° . The extreme sway motion of 2.06° , roll motion of 5.97° , yaw motion of 3.42° appear in simulation number 4, 101 and 73 of DLC 6.2 which simulates the parked turbine in extreme wind and wave conditions with 50-year recurrence. Simulation number 4 was run under assumption of yaw misalignment of -140° , and wind and wave propagation of 0° . Simulation number 101 was run under assumption of a yaw misalignment of 110° , and wind and wave propagation -30° whereas

simulation number 73 was run under the assumption of a yaw misalignment of -170, wind and wave are misaligned -30°. Figure 71 depicts an exemplary of wind, wave and current direction distributions.

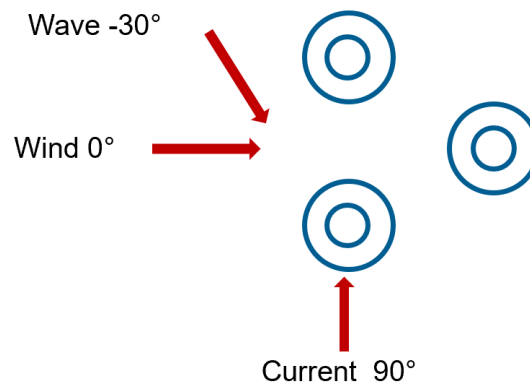


FIGURE 71: WIND, WAVE AND CURRENT MISALIGNMENT

6.5.3 INFLUENCE OF WIND-WAVE MISALIGNMENT ON PLATFORM MOTIONS

To examine the influence of wind-wave misalignment on platform motions, Figure 72 compares time history of simulation number 73 shown in blue and simulation number 1 shown in red of DLC 6.2, where the latter was run without wind and wave misalignment but keeping other boundary conditions the same. Besides faults in the yaw system, it was observed that wind-wave misalignment leads to extreme platform yaw motion in parked condition. The nacelle acceleration in the y-direction has significantly increased when the wind and wave are misaligned in -30°. It was observed that the platform sway, roll, and yaw motions have significantly increased whereas the platform surge and pitch motions have slightly decreased. As a result of the change in wind-wave misalignment, tensions in the mooring lines have changed. Consequently, platform sway, roll, and yaw motions have changed significantly. The mean platform yaw motion and standard deviation for the case with wind-wave misalignment are about 1.12 times and 1.64 times larger than that for the case in which wind and wave misalignment is not considered. The mean platform sway motion and standard deviation for the case with wind-wave misalignment are about 1.1 times and 2.07 times larger than that for the case in which wind and wave misalignment is not considered. Similarly, the mean platform roll motion and standard deviation for the case with wind-wave misalignment are about 1.14

times and 7.08 times larger than that for the case in which wind and wave misalignment is not considered.

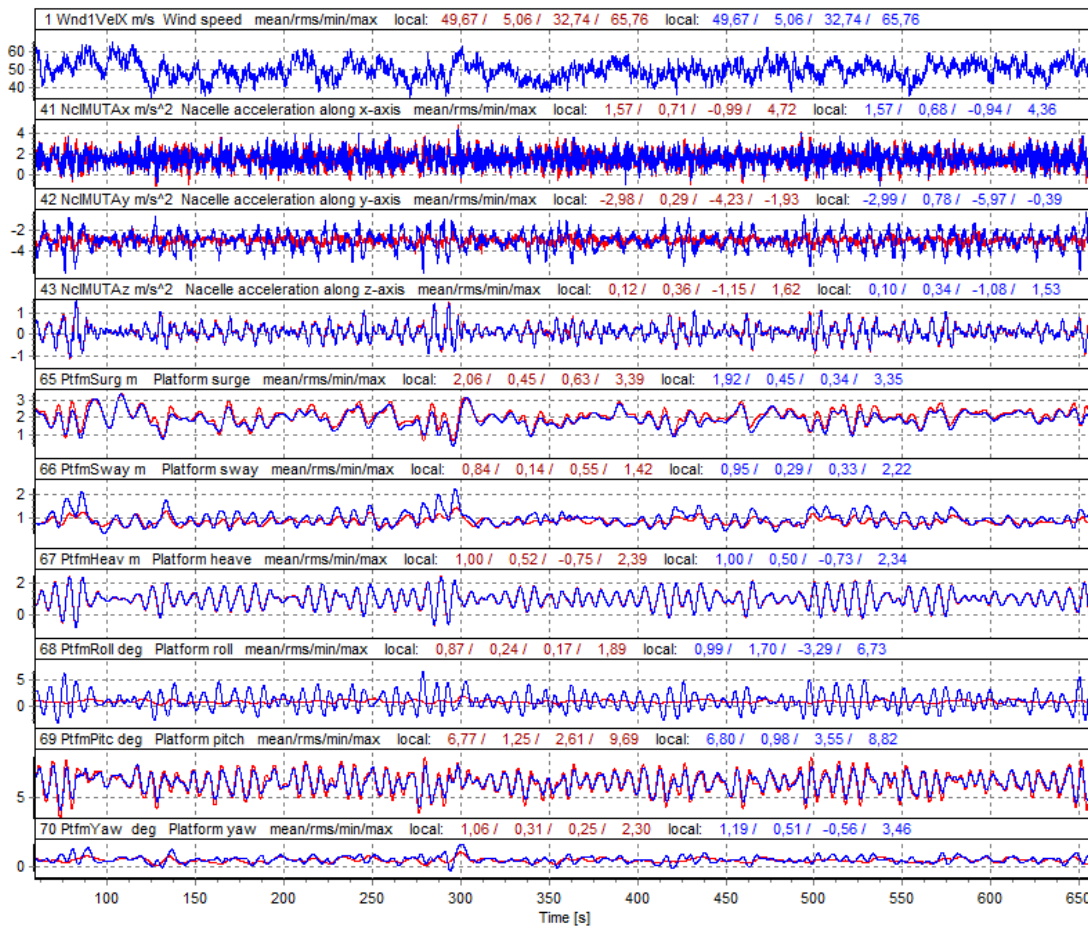


FIGURE 72: TIME HISTORIES OF PLATFORM MOTIONS AND NACELLE ACCELERATION FROM SIMULATION NUMBER 1 OF DLC 6.2 (SHOWN IN RED) AND SIMULATION NUMBER 73 OF DLC 6.2 (SHOWN IN BLUE)

6.5.4 INFLUENCE OF CURRENT LOADS ON PLATFORM MOTIONS

To examine the influence of current loads on the platform motions, simulation number 1 of DLC 6.2 was rerun by disregarding the current loads. Figure 73 compares time history of the platform motions and nacelle accelerations between the load case with current loads shown in blue and without current loads shown in red. As already mentioned, simulation number 1 was run under assumption of a yaw misalignment of 110°, no wind and wave misalignment and 90° of current direction.

Similar to wind-wave misalignment, it was observed that current loads and direction can change tension in the mooring lines. As a result, there is a significant increase in the platform sway, roll, and yaw motions but a slight decrease in platform surge and pitch motions. The mean platform sway motion for the case with current loads is about 2.5 times larger than that for the case without current loads. Similarly, the mean platform roll motion for the case with current loads is about 1.83 times larger than that for the case without current loads whereas the standard deviation for the case with current loads is about 8.94 times larger than that for

the case without current loads. The mean platform yaw motion and standard deviation for the case with current loads has increased as much as about 1.4 times and 2 times larger than that for the case without current loads.

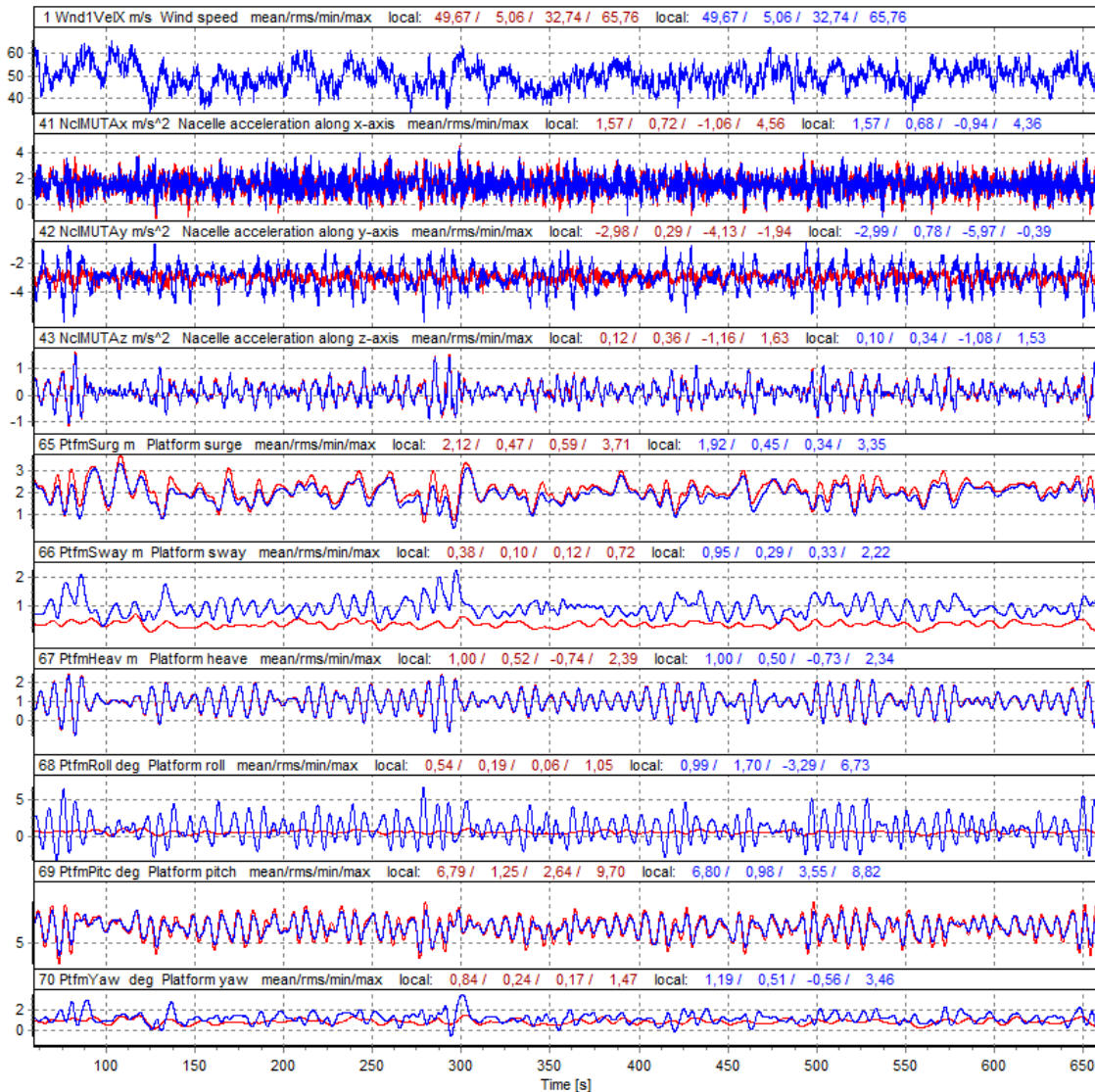


FIGURE 73: TIME HISTORY OF PLATFORM MOTIONS AND NACELLE ACCELERATION FROM SIMULATION NUMBER 1 OF DLC 6.2 WITHOUT CURRENT LOADS IN RED AND WITH CURRENT LOADS IN BLUE

6.5.5 EXTREME EDGEWISE BENDING MOMENT AT THE BLADE ROOT FOR THE ONSHORE CART SYSTEM

After comparing all extreme loads resulted from different load cases, the extreme edgewise bending moment at the blade root was identified for the onshore CART system during the grid failure followed by shut down. The shaft brake is engaged to bring the rotor to a complete standstill. The extreme edgewise bending moment occurs in simulation 40 of DLC 2.1 which was run under normal turbulence wind without considering yaw misalignment. To be more specific, it appears at wind speed 25.80 m/s and time 101.85 s. As expected, the turbine is quite sensitive to high wind speeds due to its stall regulation. Loss in generator torque was implemented at 100 s and the shaft brake is engaged at 100.5 s assuming that the control

system can detect the grid failure and react immediately. Figure 74 and Figure 75 depict the time history and close-up of edgewise bending moment at the blade root of blade 1 and its FFT diagram was depicted in Figure 76. As we can clearly see in the FFT diagram, the edgewise bending moment at the blade root was mainly caused by the rotational speed of the rotor. By observing its response in time history, the edgewise bending moment are cyclic between compression and tension when the rotor rotates. Intuitively it is because edgewise bending moment is contributed by the tension and compression forces at the leading and trailing edges of the blade. When the grid is lost, there is a small amount of overshoot in rotor speed. After engaging the shaft brake, the rotor speed deaccelerates to zero within a fairly reasonable time. Apparently, a combination of this fault and shutdown conditions, and wind turbulence pose transient loads on the turbine. Due to this transient effect, there is a large load variation at the blade root because the gravitational loads tend to increase from the blade tip to the blade root. According to the results, the edgewise bending moment has a mean value of 12.47 kN-m and a standard deviation of 11.80 kN-m. During the transient event, the bending moment jumps up to 48.24 kN which is almost 4 times greater than its mean value. Although this transient load is short-term, it can greatly influence the fatigue strength of the turbine.

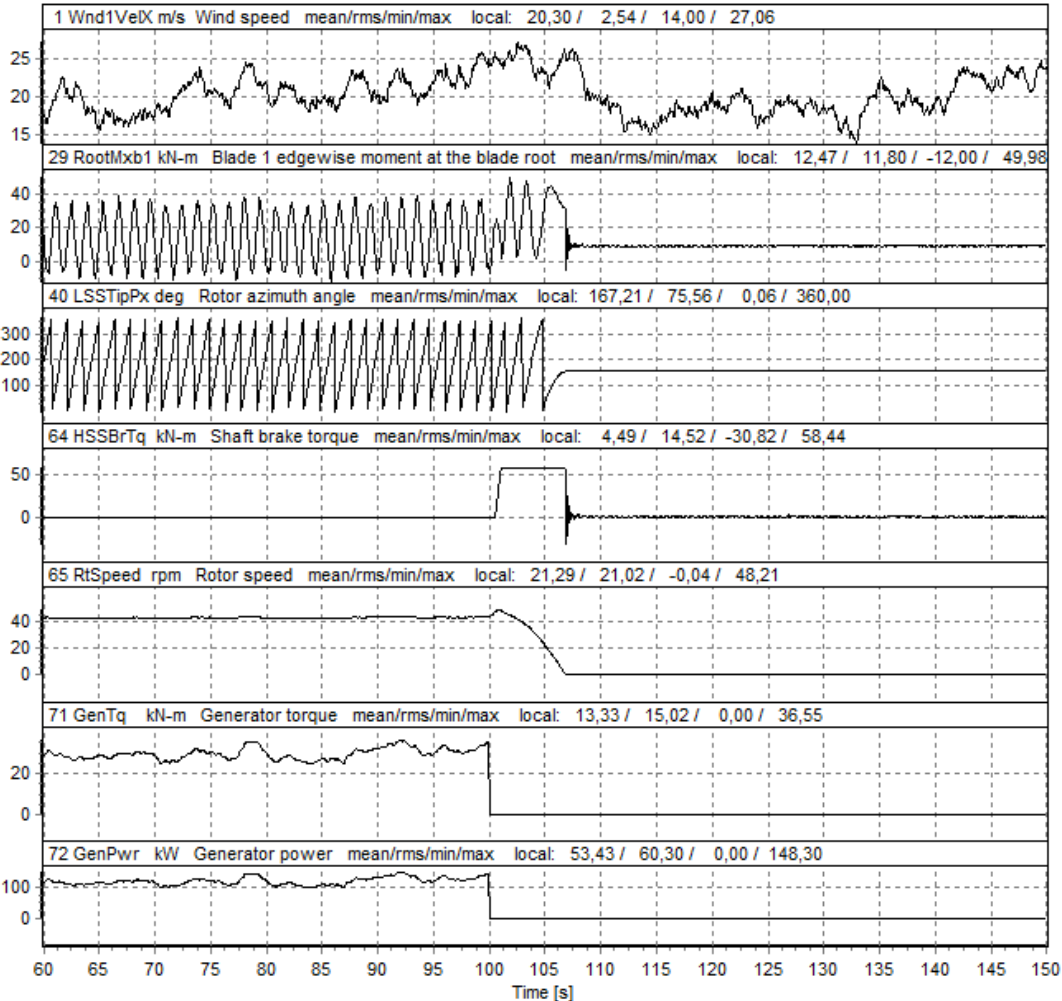


FIGURE 74: TIME HISTORY OF EXTREME EDGEWISE BENDING MOMENT AT THE BLADE ROOT (SIMULATION 40 IN DLC 2.1)

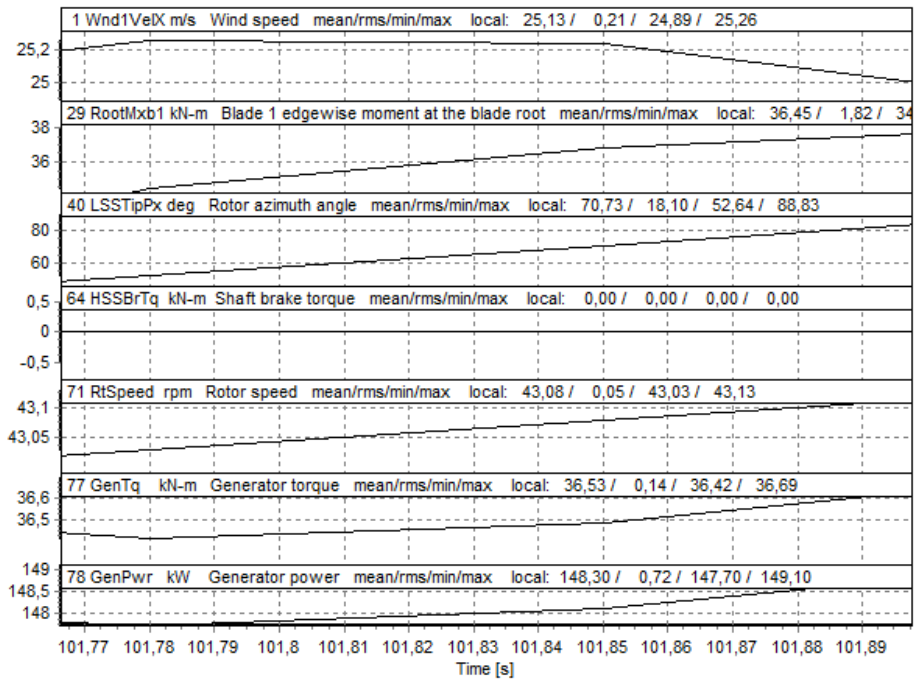


FIGURE 75: CLOSE-UP OF TIME HISTORY FROM SIMULATION NUMBER 40

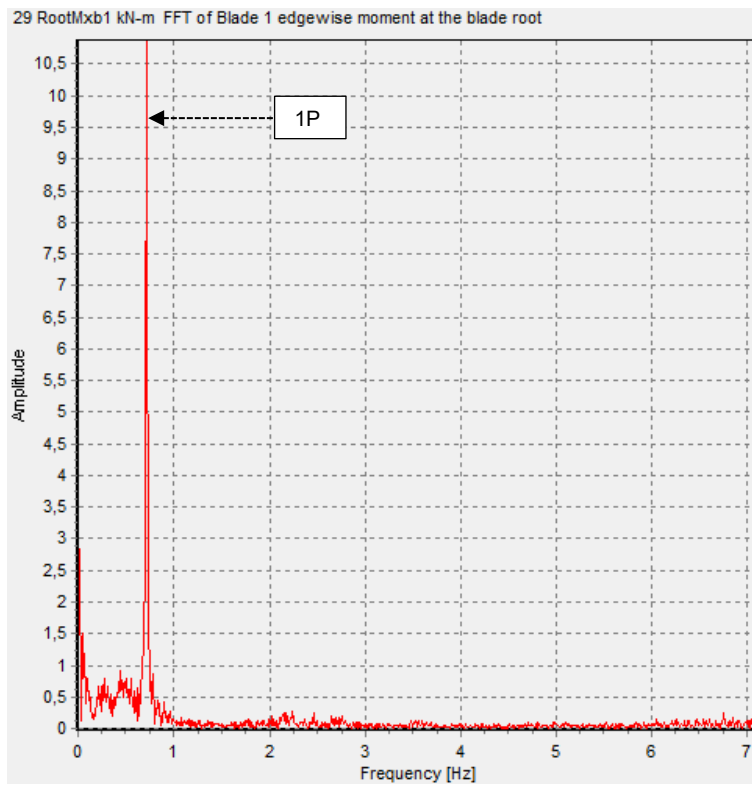


FIGURE 76: FFT OF EDGEWISE BENDING MOMENT AT THE BLADE ROOT

7 DISCUSSION, CONCLUSIONS AND OUTLOOK

7.1 DISCUSSION AND CONCLUSIONS

The overall objective of this study was to develop a control concept for a two-bladed medium-sized wind turbine and carry out fully integrated load analyses of the newly developed concept designed for an off-grid solution. This study began with the development of a stall control concept. Different control strategies for stall-regulated wind turbines were thoroughly reviewed and a simple control concept was proposed to maximize the power output in the partial load region and to limit the power output in the full load region. The variable-speed generator torque control algorithm was implemented by interfacing ServoDyn module with an external dynamic-link-library (DLL). The maximum allowable generator torque was set to 35 % above its nominal torque at a rated power of 144 kW in the control algorithm. This value should be multiplied by conversion efficiency to obtain the generated power. In the partial load region, the generator torque was set directly to $K\Omega^2$ defined by Leithead and Connor (2000), which is a well-known torque control law commonly applied in most variable speed wind turbines. The objective of the generator torque control in this region was to keep TSR at an optimum level by changing the rotor speed. In this way, the maximum power output can be achieved in the partial load region. In the full load region, the generator torque was varied to limit the rotor speed not to exceed its maximum allowable speed, which is nominal rotor speed in our case. Similar to the partial load region, the generator as a function of rotor speed was implemented. Once the rotor speed reaches its maximum speed in partial load region, the torque controller requests the greater torque to limit the rotor speed within a safe limit. This is done by tracking $C_{p,max}$ curve continuously and adding part of the generator torque found at $C_{p,max}$ to it. The amount of additional torque is obtained by multiplying the generator torque found at maximum $C_{p,max}$ by a variable slope G . The value of slope G was varied until the desired power output for the given wind speed is achieved. The best performance was found at $G= 1.86$, whereby the maximum allowable rotor speed for partial load region was set to 5 % below its nominal rotational speed of 43 rpm. The feasibility of the developed control concept was evaluated by simulating the turbine under steady wind conditions. Based on the resulted mean value, standard deviation, and maximum values of the response of the control system, the implemented torque control concept seems to be stable for the given control parameters. CART machine utilizes no active control system like blade tip brake to reduce the rotor speed in very high winds. Instead, it uses a mechanical brake to bring the turbine to a standstill in very high winds. It was assumed that it takes 0.3 s to activate the shaft brake, and 0.5 s of time lag for the brake to reach its maximum brake torque. It was assumed that a brake torque of 55 kN-m is achieved in its fully deployed state for an emergency or a fault condition, parking in storm condition, and overspeed protection. The torque controller does not contain start-up and shutdown logic. Therefore, the

feasibility of shaft brake was evaluated rather by simulating grid loss followed by the shaft brake. It was observed that the transient response in all parameters dissipated within quite reasonable time. The overshooting due to this transient event seem reasonable for the given wind speed.

As second part of this study, fully integrated coupled simulations were carried out for both onshore and offshore CART system according to the guideline prescribed by IEC wind turbine design standards. To conduct a comparative study on the performance between the onshore and offshore CART system, the wind turbine specification, rotor-nacelle-assembly, tower, and the turbulent intensity are kept the same for both systems. The reduced set of design load cases were investigated following the recommended practice by DNVGL (DNVGL-RP-0286, 2019) and the work of GL (2015) and Jonkman (2007) to focus only a subset of critical design load cases. The global dynamic behaviour of the coupled model was thoroughly investigated by evaluating the statistical distribution of each load component: minimum, mean, maximum, standard deviation, skewness, and range. Because stall-regulated wind turbines have no active aerodynamic control system to reduce the rotor thrust force in high winds, it was observed that the load responses to be more specific mean values of most parameters increase with the increase in wind speed in normal operations. The same applies to the load excursions of several parameters. On top of this, platform pitch motion contributes large fluctuations in power output and generator torque in high winds. Furthermore, large load excursions in tower-top fore-aft displacement and tower bottom fore-aft moment of offshore CART system might be related to an inverted pendulum effect which is mainly contributed from inertial forces due to tower deflection or platform motions. Regarding platform motions in normal operations, the extreme sway, heave, roll, pitch, and yaw motion appear at simulations in DLC 1.4 whereas the surge motion seems to be triggered by the extreme turbulence in DLC 1.3. Based on the findings, it was correlated to the fact that the tensions in the upwind mooring line are greatly influenced by wind turbulence. This phenomenon was amplified by the nature of stall-regulated wind turbines, whose sustained rotor thrust tends to increase with the wind speed. As a result, the platform is being pushed downward and the upwind mooring line is being pulled upwards. By comparing the nacelle acceleration at cut-out wind speed, it is observed that the acceleration of the nacelle in the y-direction has significantly decreased for offshore CART system. However, the acceleration of the nacelle in the z-direction was found to be significantly larger for offshore system. This might be related to the coupling between platform pitch and heave motion. As a result, tower bottom fore-aft and torsional moment has significantly increased for offshore system.

The present study considered fatigue loads from power production in normal turbulence wind DLC 1.2. According to the results, fatigue DELs were observed to be larger for high wind

conditions, which is quite common in stall-regulated wind turbines. In addition to this, yawed conditions showed less influence on fatigue DELs in low winds whereas they have a significant influence on fatigue DELs in high wind conditions. This might be related to the fact that the CART wind turbine was designed with a high tip speed ratio and the aerodynamic loads vary with the change in angle of attack. Especially in the stall region, the angle of attack for yaw conditions tend to vary differently from the aligned condition. By examining the different Wöhler's exponents, it was found that the fatigue DELs for the blade computed with a lower material exponent is higher than that with a higher material exponent. The same applies to the steel components as well.

Load analyses for extreme situations with faults showed that DLC 6.1 defining storm conditions and extreme sea states characterized by high wave heights greatly influence the platform motions. The extreme surge motion of 3.19 m was found to be driven by a particular case, in which no yaw misalignment was taken into account, but wind and wave misalignment of 30° was considered. The extreme pitch motion of 9.10° was observed in simulation which considers a misaligned yaw of 8° and wind-wave being colinear. Nevertheless, the pitch motion is still below the static inclination of 12° for survival conditions prescribed by DNVGL (DNV-GL-OS-C301, 2020). It was recommended to integrate a structural control system like a tuned mass damper to reduce the platform motions in storm conditions. For the onshore CART system, tower top side-to-side displacement was driven by the transient event posed by grid loss and shut down mode during EOG.

By examining on the load response in extreme condition with worst consequences, it was observed that extreme loads of most parameters were significantly increased in the presence of floating substructure. Upon comparing the resulted extreme loads among normal operation, fault events, and fault events with worst consequences, it was found that the extreme loads of most parameters were triggered by extreme events with faults. The comparison of different load cases confirmed that the heave, pitch, and roll motions are greatly affected by wave-induced motions whereas surge, sway, and yaw motions are affected by motions in the mooring system which in turn is dominated by wind turbulence. Moreover, wind, wave and current misalignment leads to a significant increase in platform sway, roll and yaw motions whereas it leads to a slight decrease in platform surge and yaw motions. Similar to wind-wave misalignment, it was observed that current loads and direction can change tension in the mooring lines. As a result, there is a significant increase in the platform sway, roll, and yaw motions but a slight decrease in platform surge and pitch motions.

By comparing the rotor thrust and tower bottom bending moment assumed during substructure design with those resulted from the present load simulations, it was found that the thrust force and tower bottom overturning moment resulted from current study is 2.5 times and 4.4 times

larger than the assumed value during the substructure design. While designing substructure, the rotor thrust and tower bottom overturning moment were calculated at wind speed in survival condition of 51.5 m/s. In the present study, the extreme rotor thrust force and tower bottom bending moment was found at wind speed of 61 m/s and 65 m/s respectively. Therefore, it is recommended to carry out structural analyses of substructure based on the design loads resulted from the present study.

Taken altogether, the findings from this study appear to be useful inputs to optimize the substructure design. It has highlighted the important dynamic system responses of the newly developed concept and delivered the preliminary estimates of critical design loads. To come to a technically and economically viable concept, there is still a lot to be done, which will be briefly explained in the next section.

7.2 OUTLOOK

This study forms the basic input to further assess the technical and economic feasibility of the CART system, especially for offshore deployment. To begin with, the implemented control concept was a simple generator torque control concept which lacks important functions like logic for start-up and shutdown events. It should be clear that the control system must ensure the fully automatic operation of the wind turbine with the change in environmental conditions in practice. Regarding modelling of environmental loads (wind, waves, and current), several assumptions have been made in the present study. It is desirable that the environmental loads should be modelled with more specific details, for example, wind-wave misalignment could have been more than $\pm 30^\circ$ in reality. Especially for fatigue loads, wind-wave misalignment could be an important factor contributing to the tower bottom bending moment. Although second-order wave loads such as mean drift, slow drift, and sum-frequency terms have been taken into account in the present study, one could also model fully nonlinear waves to accurately compute the hydrodynamic loads acting on the substructure. Also, it could surely be advantageous to run simulations with MoorDyn module which considers the structural dynamic and hydrodynamic forces acting on the mooring lines.

As clearly shown by the results of parking in storm conditions, the platform motion particularly platform pitch motion is quite large. It is recommended that the substructure structural design should be enhanced so that platform motions are reduced to a certain degree in storm conditions. This could be done by modifying the geometry of the platform or by integrating the structural control system like tuned mass damper. In the next steps, a complete set of load analyses should be rerun. Thereby, the scope of the load analyses could also be extended depending on the available information about envisioned site conditions and the improved control concept. Hence, it is also recommended to optimize the structural components of the tower and the substructure by means of finite element analysis.

8 REFERENCES

1. Adam, F., Schroeter, M., Manh, V. V., & Dierken, P. (2019). CART—a compact and robust wind turbine design for south Asia.
2. AG, G. L. (2012). Guidelines for the Certification of Wind Turbines. Germanischer Lloyd.
3. Andersen, M. T., Wendt, F. F., Robertson, A. N., Jonkman, J. M., & Hall, M. (2016, June). Verification and validation of multisegmented mooring capabilities in FAST v8. In The 26th International Ocean and Polar Engineering Conference. International Society of Offshore and Polar Engineers.
4. Atcheson, M., Garrad, A., Cradden, L., Henderson, A., Matha, D., Nichols, J., ... & Sandberg, J. (2016). Floating Offshore Wind Energy. Springer.
5. Bachynski, E. E., Etemaddar, M., Kvittem, M. I., Luan, C., & Moan, T. (2013). Dynamic analysis of floating wind turbines during pitch actuator fault, grid loss, and shutdown. *Energy Procedia*, 35, 210-222.
6. Bastick, N., 2009. Blue H - The World's First Floating Wind Turbine. The First Dutch Offshore Wind Energy Conference, "Essential Innovations", February 12th and 13th 2009, Den Helder, The Netherlands. (Presentation)
7. Berberich, J. F. (2015). Einfluss aktueller Technologietrends auf die Stromgestehungskosten bei Windenergieanlagen
8. Bianchi, F. D., De Battista, H., & Mantz, R. J. (2006). Wind turbine control systems: principles, modelling and gain scheduling design. Springer Science & Business Media.
9. Bianchi, F. D., Mantz, R. J., & Christiansen, C. F. (2005). Gain scheduling control of variable-speed wind energy conversion systems using quasi-LPV models. *Control engineering practice*, 13(2), 247-255.
10. BiMEP and IH Cantabria, "Metocean Analysis of BiMEP for Offshore Design," 2017
11. Bir, G. (2005). User's Guide to BModes (Software for Computing Rotating Beam-Coupled Modes) (No. NREL/TP-500-39133). National Renewable Energy Lab.(NREL), Golden, CO (United States).
12. Bossanyi, E. A. (2000). The design of closed loop controllers for wind turbines. *Wind energy: An International Journal for Progress and Applications in Wind Power Conversion Technology*, 3(3), 149-163.
13. Bourlis, D. (2011). Control Algorithms and Implementation for Variable Speed Stall Regulated Wind Turbines (Doctoral dissertation, University of Leicester).
14. Bratland, S., 2009. Hywind - The World First Full-scale Floating Wind turbine. Seminar and B2B meetings "Powering the Future – Marine Energy Opportunities", 5 November 2009, Lisbon, Portugal. (Presentation)

15. Buhl, M. L. (2008). MCrunch user's guide for version 1.00. Golden, Colorado, USA: National Renewable Energy Laboratory.
16. Burton, T., Jenkins, N., Sharpe, D., & Bossanyi, E. (2011). Wind energy handbook. John Wiley & Sons.
17. Butterfield, S., Musial, W., Jonkman, J., & Sclavounos, P. (2007). Engineering challenges for floating offshore wind turbines (No. NREL/CP-500-38776). National Renewable Energy Lab.(NREL), Golden, CO (United States).
18. Carbon Trust. (2015). Floating Offshore Wind: Market and Technology Review. The Scottish Government.
19. Cordle, A., & Jonkman, J. (2011, January). State of the art in floating wind turbine design tools. In The twenty-first international offshore and polar engineering conference. International Society of Offshore and Polar Engineers.
20. DNV, G. (2017). Recommended practice DNVGL-RP-C205 environmental conditions and environmental loads. Høvik: DNV GL AS.
21. DNVGL. DNVGL-CG-0130. Wave loads. Edition January 2018.
22. DNVGL. DNV-GL-OS-C301. Stability and Watertight Integrity. Edition July 2020.
23. DNVGL. DNVGL-RP-0286. Coupled analysis of floating wind turbines. Edition May 2019.
24. DTU Wind Energy - HAWC2 (Horizontal Axis Wind turbine simulation Code 2nd generation, viewed on 01 January 2021, [https://www.hawc2.dk/hawc2-info#:~:text=HAWC2%20\(Horizontal%20Axis%20Wind%20turbine,DTU%20Ris%C3%20Campus%20in%20Denmark](https://www.hawc2.dk/hawc2-info#:~:text=HAWC2%20(Horizontal%20Axis%20Wind%20turbine,DTU%20Ris%C3%20Campus%20in%20Denmark)).
25. Ekelund, T. (1994, August). Speed control of wind turbines in the stall region. In Proceedings of the third IEEE conference on control applications (Vol. 1, pp. 227-232).
26. Equinor, Hywind Tampen: the world's first renewable power for offshore oil and gas, viewed 05 June 2021, <https://www.equinor.com/en/what-we-do/hywind-tampen.html>
27. GL, L. B. D. (2015). Qualification of innovative floating substructures for 10MW wind turbines and water depths greater than 50m.
28. Hall, M. (2015). MoorDyn user's guide. Orono, ME: Department of Mechanical Engineering, University of Maine.
29. Hall, M. (2020, September). MoorDyn V2: New Capabilities in Mooring System Components and Load Cases. In ASME 2020 39th International Conference on Ocean, Offshore and Arctic Engineering. American Society of Mechanical Engineers Digital Collection.
30. Hasselmann, K. F., Barnett, T. P., Bouws, E., Carlson, H., Cartwright, D. E., Eake, K., ... & Walden, H. (1973). Measurements of wind-wave growth and swell decay during

- the Joint North Sea Wave Project (JONSWAP). Ergänzungsheft zur Deutschen Hydrographischen Zeitschrift, Reihe A.
31. Hayman, G. J. (2015). MExtemes Manual Version 1.00. National Renewable Energy Laboratory, Golden, CO (United States).
 32. Hoffmann, R. (2002). A comparison of control concepts for wind turbines in terms of energy capture (Doctoral dissertation, Technische Universität).
 33. Huijs, F., Mikx, J., Savenije, F., & de Ridder, E. J. (2013). Integrated design of floater, mooring and control system for a semi-submersible floating wind turbine. Proceedings of the EWEA Offshore, Frankfurt, Germany, 19, 21.
 34. International Electrotechnical Commission. (2019). Wind energy generation systems- Part 3-1: Design requirements for fixed offshore wind turbines. International standard IEC, 61400-3.
 35. International Electrotechnical Commission. (2019). Wind energy generation systems- part 3-2: design requirements for floating offshore wind turbines. Geneva, Switzerland: IEC TS, 61400-3.
 36. International Energy Agency. (2020). Global energy review 2020. OECD Publishing. [Accessed: 2020-09-10].
 37. Ishihara, T., Phuc, P. V., & Sukegawa, H. (2007, December). A numerical study on the dynamic response of a floating offshore wind turbine system due to resonance and nonlinear wave. In European Offshore Wind Conference & Exhibition.
 38. Ishihara, T., Phuc, P. V., Sukegawa, H., Shimada, K., & Ohyama, T. (2007, July). A study on the dynamic response of a semi-submersible floating offshore wind turbine system Part 1: A water tank test. In Proceedings of the 12th International Conference on (pp. 2511-2518).
 39. Ishihara, T., Waris, M. B., & Sukegawa, H. (2009, September). A study on influence of heave plate on dynamic response of floating offshore wind turbine system. In Proc. of European Offshore Wind Conference & Exhibition.
 40. Jirka, G. H. Einführung in die Hydromechanik (Universitätsverlag Karlsruhe, Karlsruhe, 2007).
 41. Jonkman, B. J., & Buhl Jr, M. L. (2006). *TurbSim user's guide* (No. NREL/TP-500-39797). National Renewable Energy Lab.(NREL), Golden, CO (United States).
 42. Jonkman, J. M. (2007). Dynamics modeling and loads analysis of an offshore floating wind turbine (No. NREL/TP-500-41958). National Renewable Energy Lab.(NREL), Golden, CO (United States).
 43. Jonkman, J. M., & Buhl Jr, M. L. (2005). FAST user's guide. Golden, CO: National Renewable Energy Laboratory, 365, 366.

44. Jonkman, J. M., Hayman, G. J., Jonkman, B. J., Damiani, R. R., & Murray, R. E. (2015). AeroDyn v15 user's guide and theory manual. NREL Draft Report.
45. Jonkman, J. M., Robertson, A. N., & Hayman, G. J. (2014). HydroDyn user's guide and theory manual. National Renewable Energy Laboratory.
46. Jonkman, J., Butterfield, S., Musial, W., & Scott, G. (2009). Definition of a 5-MW reference wind turbine for offshore system development (No. NREL/TP-500-38060). National Renewable Energy Lab.(NREL), Golden, CO (United States).
47. Journée, J. M., & Pinkster, J. A. (1997). Offshore hydromechanics. TUDelft, Faculty of Marine Technology, Ship Hydromechanics Laboratory, Report No. 1112-K, Lecture Notes.
48. Karimirad, M., & Michailides, C. (2015). Dynamic analysis of a braceless semisubmersible offshore wind turbine in operational conditions. *Energy Procedia*, 80, 21-29.
49. Karimirad, M., & Michailides, C. (2015). V-shaped semisubmersible offshore wind turbine: An alternative concept for offshore wind technology. *Renewable Energy*, 83, 126-143.
50. Kühn, M. J. (2001). Dynamics and design optimisation of offshore wind energy conversion systems. DUWIND, Delft University Wind Energy Research Institute.
51. Leith, D. J., & Leithead, W. E. (1997). Implementation of wind turbine controllers. *International Journal of Control*, 66(3), 349-380.
52. Leithead, W. E., & Connor, B. (2000). Control of variable speed wind turbines: design task. *International Journal of Control*, 73(13), 1189-1212.
53. Leithead, W. E., & Connor, B. (2000). Control of variable speed wind turbines: dynamic models. *International Journal of Control*, 73(13), 1173-1188.
54. Lemmer, F., Yu, W., Müller, K., & Cheng, P. W. (2020). Semi-submersible wind turbine hull shape design for a favorable system response behavior. *Marine Structures*, 71, 102725.
55. Luan, C., Chabaud, V., Bachynski, E. E., Gao, Z., & Moan, T. (2017). Experimental validation of a time-domain approach for determining sectional loads in a floating wind turbine hull subjected to moderate waves. *Energy Procedia*, 137, 366-381.
56. Luan, C., Gao, Z., & Moan, T. (2016, June). Design and analysis of a braceless steel 5-mw semi-submersible wind turbine. In *International Conference on Offshore Mechanics and Arctic Engineering* (Vol. 49972, p. V006T09A052). American Society of Mechanical Engineers.
57. Masciola, M. (2016). Map++ Documentation Release 1.15. Technical report, National Renewable Energy Laboratory-NREL.

58. Muljadi, E., Butterfield, C. P., & Buhl Jr, M. L. (1997). Effects of turbulence on power generation for variable-speed turbines. In 1997 ASME Wind Energy Symposium.
59. Muljadi, E., Forsyth, T., & Butterfield, C. P. (1998). Soft-stall control versus furling control for small wind turbine power regulation (No. NREL/CP-500-25100; CONF-980437-). National Renewable Energy Lab., Golden, CO (United States).
60. Muljadi, E., Pierce, K., & Migliore, P. (1998, June). Control strategy for variable-speed, stall-regulated wind turbines. In Proceedings of the American control conference (Vol. 3, pp. 1710-1714). AMERICAN AUTOMATIC CONTROL COUNCIL.
61. Muljadi, E., Pierce, K., & Migliore, P. (2000). Soft-stall control for variable-speed stall-regulated wind turbines. *Journal of Wind Engineering and Industrial Aerodynamics*, 85(3), 277-291.
62. Muljadi, E., Pierce, K., & Migliore, P. (2000, January). A conservative control strategy for variable-speed stall-regulated wind turbines. In 2000 ASME Wind Energy Symposium (p. 31).
63. OpenFAST, viewed on 01 January 2021, <https://openfast.readthedocs.io/en/dev/source/user/aerodyn-olaf/Introduction.html>
64. Parlak, C. Ö. (2017). Parameterstudie für die Rotorblätter bei WEA mit der Stallregulierung. (Unpublished Student Reserach Project). University of Rostock, Rostock, Germany.
65. Peregrine, D. H., & Jonsson, I. G. (1983). Interaction of waves and currents. BRISTOL UNIV (ENGLAND).
66. Pierce, K., & Migliore, P. (2000). Maximizing energy capture of fixed-pitch variable-speed wind turbines. In 2000 ASME Wind Energy Symposium (p. 32).
67. Pierson Jr, W. J., & Moskowitz, L. (1964). A proposed spectral form for fully developed wind seas based on the similarity theory of SA Kitaigorodskii. *Journal of geophysical research*, 69(24), 5181-5190.
68. Popko, W., Robertson, A., Jonkman, J., Wendt, F., Thomas, P., Müller, K., ... & Harries, R. (2021). Validation of numerical models of the offshore wind turbine from the alpha ventus wind farm against full-scale measurements within OC5 Phase III. *Journal of Offshore Mechanics and Arctic Engineering*, 143(1), 012002.
69. Principle Power, Entering a new era for floating wind, Principle Power unveils dynamic logo and brand identity, viewed on 03 February 2020, <https://www.principlepowerinc.com/en/news-press/press-archive/2020/02/03/entering-a-new-era-for-floating-wind-principle-power-unveils-dynamic-logo-and-brand-identity>
70. Principle Power, WindFloat Atlantic project starts supplying clean energy in Portugal, viewed on 02 January 2020, <https://www.principlepowerinc.com/en/news-press/press->

archive/2020/01/02/windfloat-atlantic-project-starts-supplying-clean-energy-in-portugal

71. Principle Power, WindFloat Atlantic, viewed on 06 June 2021, <https://www.principlepowerinc.com/en/windfloat>
72. Robertson, A. N., Wendt, F., Jonkman, J. M., Popko, W., Dagher, H., Gueydon, S., ... & Debruyne, Y. (2017). OC5 project phase II: validation of global loads of the DeepCwind floating semisubmersible wind turbine. *Energy Procedia*, 137, 38-57.
73. Robertson, A., Jonkman, J., Masciola, M., Song, H., Goupee, A., Coulling, A., & Luan, C. (2014). Definition of the semisubmersible floating system for phase II of OC4 (No. NREL/TP-5000-60601). National Renewable Energy Lab.(NREL), Golden, CO (United States).
74. Roddier, D., Cermelli, C., & Weinstein, A. (2009, January). WindFloat: A floating foundation for offshore wind turbines—Part I: design basis and qualification process. In *International Conference on Offshore Mechanics and Arctic Engineering* (Vol. 43444, pp. 845-853).
75. Roddier, D., Cermelli, C., Aubault, A., & Weinstein, A. (2010). WindFloat: A floating foundation for offshore wind turbines. *Journal of renewable and sustainable energy*, 2(3), 033104.
76. Rosmin, N. (2015). Internal Model Control (IMC) design for a stall-regulated variable-speed wind turbine system (Doctoral dissertation, Loughborough University).
77. Sarpkaya, T. (1981). Morison's Equation and the Wave Forces on Offshore Structures. SARP KAYA (TURGUT) CARMEL CA.
78. SBM Offshore, Renewable Energy, viewed on viewed 05 June 2021, <https://www.sbmoffshore.com/what-we-do/our-products/renewables/>
79. Schröter, M. (2018). Basis Design und Konstruktionsplanung einer schwimmenden Unterstruktur für eine Windenergieanlage mittlerer Größe für den südasiatischen Raum. (Unpublished Master thesis). University of Rostock, Rostock, Germany.
80. Sintef, Sima software, viewed on 05 June 2021, <https://www.sintef.no/en/software/sima/>
81. Stewart, G. M., Lackner, M. A., Robertson, A., Jonkman, J., & Goupee, A. J. (2012, January). Calibration and validation of a FAST floating wind turbine model of the DeepCwind scaled tension-leg platform. In *The Twenty-second International Offshore and Polar Engineering Conference*. International Society of Offshore and Polar Engineers.
82. Tao, L., & Dray, D. (2008). Hydrodynamic performance of solid and porous heave plates. *Ocean engineering*, 35(10), 1006-1014.

83. Windpower engineering and developments 2014, How vortex generators improve wind turbine performance, viewed on 01 January 2021, <https://www.windpowerengineering.com/vortex-generators-improve-wind-turbine-performance/>
84. X1 Wind, X1 Wind prepares PivotBuoy floating wind platform for Canaries deployment, viewed 05 June 2021, <https://www.x1wind.com/news/x1-wind-prepares-pivotbuoy-floating-wind-platform-for-canaries-deployment/>

LIST OF FIGURES

| | |
|---|----|
| Figure 1: Air flow pattern on wind turbine blade (Windpower engineering and developments, 2014) | 18 |
| Figure 2: Control strategy of a fixed speed stall regulated wind turbine (Bianchi et al., 2006) | 19 |
| Figure 3: Control strategy of a variable speed stall regulated wind turbine (Bianchi et al., 2006) | 20 |
| Figure 4: Comparison of active control and soft stall control strategy on stall regulation (Pierce and Migliore, 2000) | 22 |
| Figure 5: Rigid body motion of a ship (a) (DNVGL-CG-0130, 2018), Floating bodies in stable conditions (b,c) and unstable condition (d) (Jirka, 2007)..... | 25 |
| Figure 6: Floating offshore wind turbine substructure concepts (Graphic by Josh Bauer, NREL)..... | 26 |
| Figure 7: CART system (left) and impression of its logistic concept (right) (Adam et al., 2019) | 36 |
| Figure 8: 3D impression (left) and Plan (right) of the CART floater (left) (Schröter, 2018)..... | 40 |
| Figure 9: Schematic of coupled aero-hydro-servo-elastic modules (OpenFAST, 2021) | 42 |
| Figure 10: Aerodynamic characteristics of airfoil section at 75% R (a), chord (b) and blade twist (c) distribution of blade for CART wind turbine | 46 |
| Figure 11: Rotor power as a function of rotor speed at various wind speeds | 48 |
| Figure 12: Cp- λ curve of CART wind turbine..... | 48 |
| Figure 13: Rotor torque as a function of rotor speed at various wind speed | 49 |
| Figure 14: Torque speed curve with different efficiency ratios at various wind speeds | 50 |
| Figure 15: Time history of Rotor speed, generator torque and generator power under steady wind 8 m/s and 9 m/s | 55 |
| Figure 16: Time history of Rotor speed, generator torque and generator power under steady wind 13 m/s and 14 m/s | 56 |
| Figure 17: Time history of Rotor speed, generator torque and generator power under steady wind 15 m/s and 16 m/s | 57 |
| Figure 18: Time history of Rotor speed, generator torque and generator power under steady wind 19 m/s and 20 m/s | 58 |
| Figure 19: Time history of Rotor speed, generator torque and generator power under uniform step winds | 59 |
| Figure 20: Grid loss and Shutdown case | 60 |
| Figure 21: Tower mode Campbell diagram of land-based CART system and sea-based CART system | 61 |
| Figure 22: Time history (left) and FFT diagram (right) of Surge Motion | 63 |

| | |
|--|-----|
| Figure 23: Time history (left) and FFT diagram (right) of Sway Motion | 64 |
| Figure 24: Time history (left) and FFT diagram (right) of Heave Motion | 64 |
| Figure 25: Time history (left) and FFT diagram (right) of Roll Motion | 64 |
| Figure 26: Time history (left) and FFT diagram (right) of Pitch Motion..... | 65 |
| Figure 27: Time history (left) and FFT diagram (right) of Yaw Motion..... | 65 |
| Figure 28: Response of power coefficient (a), rotor thrust (b), generator power (c) as a function of wind speed, and torque-speed curve of CART system (d) | 67 |
| Figure 29: Mean offset of Surge (left) and Pitch (right) motion as a function of wind speeds | 68 |
| Figure 30: Typical environmental loads acting on a floating offshore wind turbine | 69 |
| Figure 31: Wind energy spectrum according to Van der Hoven (Kühn, 2001)..... | 70 |
| Figure 32: Example of 3D turbulent wind field generated by NREL TurbSim | 71 |
| Figure 33: Example of an extreme coherent gust with direction change (AG, 2012). | 72 |
| Figure 34: Example of Weibull's distribution for different k at constant mean wind speed (Burton et al., 2011)..... | 73 |
| Figure 35: Sea levels (DNVGL-RP-C205, 2017)..... | 75 |
| Figure 36: Wave particles movement in different water depth (DNVGL-RP-C205, 2017) | 76 |
| Figure 37: Definition of wave propagation (DNVGL-RP-C205, 2017) | 76 |
| Figure 38: Wheeler's stretching method (DNVGL-RP-C205, 2017)..... | 77 |
| Figure 39: Lateral drag coefficient as a function of RE number (a) (Robertson et al., 2014) and axial drag coefficient as a function of KC (b) (Tao and Dray, 2008)..... | 78 |
| Figure 40: Geometry of mooring line (Jonkman, 2007)..... | 80 |
| Figure 41: Statistics values of response of CART system as a function of wind speed for each simulation in DLC 1.1 | 94 |
| Figure 42: Time histories from DLC 1.4 simulation number 6 shown in red and 431 shown in blue for offshore CART system (a)..... | 97 |
| Figure 43: Time histories from DLC 1.4 simulation number 6 shown in red and 431 shown in blue for offshore CART system (b)..... | 98 |
| Figure 44: Close-up time history from simulation number 431 | 98 |
| Figure 45: Close-up of time history from simulation number 6..... | 99 |
| Figure 46: Time history from simulation which yields extreme surge motion | 100 |
| Figure 47: Extreme platform motions from normal operating condition: maximum (left) and minimum (right) | 100 |
| Figure 48: Time history of simulation 269 in DLC 1.4 | 102 |
| Figure 49: Close-up of time history from simulation number 269 | 102 |
| Figure 50: FFT of wind speed (upper left), surface wave elevation (upper right), tension at fairlead of mooring line (lower left), and platform yaw motion (Lower right)..... | 103 |
| Figure 51: Ratio of offshore to onshore CART system for normal operations..... | 105 |

| | |
|--|-----|
| Figure 52: Comparison of time histories from DLC 1.1 simulation number 29 between offshore (shown in blue) and onshore (shown in red) wind turbine | 107 |
| Figure 53: Comparison of FFT of nacelle acceleration along y axis and z axis between onshore (shown in red) and offshore (shown in blue) CART system | 107 |
| Figure 54: Variation of fatigue DELs as a function of mean hub-height wind speed at different yaw angle for offshore CART system (the abbreviations are explained in section 6.3.5) ... | 111 |
| Figure 55: Variation of Damage Equivalent Loads (DELs) as a function of mean hub-height wind speed for offshore CART system (the abbreviations are explained in section 6.3.5) . | 112 |
| Figure 56: FFT of blade root flapwise bending moment at rated wind speed | 113 |
| Figure 57: Variations in fatigue DELs depending on the variation in ULF and Wöhler's exponent..... | 114 |
| Figure 58: Comparison of platform motion between normal operations and extreme events with faults | 115 |
| Figure 59: Ratio of offshore to onshore CART system for extreme events with faults..... | 117 |
| Figure 60: Time history of extreme tower top side-to-side displacement for onshore wind turbine | 118 |
| Figure 61: FFT of tower top side-to-side for onshore wind turbine..... | 119 |
| Figure 62: Time history of nacelle yaw angular velocity and angle of attack for onshore wind turbine | 120 |
| Figure 63: Time history of maximum surge motion, simulation number 3 of DLC 6.1 | 122 |
| Figure 64: FFT of wave surface elevation (upper left), wind speed (upper right), mooring line tension (lower left) and surge motion (lower right) | 123 |
| Figure 65: Comparison of platform surge motion between wave loads with and without second-order implementation..... | 123 |
| Figure 66: Time history of extreme pitch motion in simulation number 18 of DLC 6.1 | 125 |
| Figure 67: Close-up of time history from simulation number 18..... | 126 |
| Figure 68: FFT of wave surface elevation (left) and pitch motion (right) | 126 |
| Figure 69: Ratio of offshore to onshore CART system for extreme faults events with worst consequences | 129 |
| Figure 70: Comparison of extreme loads from different load cases..... | 130 |
| Figure 71: Wind, wave and current misalignment | 131 |
| Figure 72: Time histories of platform motions and nacelle acceleration from simulation number 1 of DLC 6.2 shown in red and simulation number 73 of DLC 6.2 shown in blue ... | 132 |
| Figure 73: Time history of platform motions and nacelle acceleration from simulation number 1 of DLC 6.2 without current loads in red and with current loads in blue | 133 |
| Figure 74: Time history of extreme edgewise bending moment at the blade root (Simulation 40 in DLC 2.1)..... | 134 |

Figure 75: Close-up of time history from simulation number 40..... 135
Figure 76: FFT of edgewise bending moment at the blade root..... 135

LIST OF TABLES

| | |
|---|----|
| Table 1: Distributed Tower Properties..... | 37 |
| Table 2: Undistributed Tower Properties..... | 37 |
| Table 3: Drivetrain properties..... | 38 |
| Table 4: Nacelle and Hub Properties..... | 38 |
| Table 5: Geometric properties of the floater..... | 40 |
| Table 6: Structural properties of the floater..... | 41 |
| Table 7: Mooring system properties..... | 41 |
| Table 8: Control system properties..... | 45 |
| Table 9: Distributed blade aerodynamic properties..... | 46 |
| Table 10: Control algorithm of CART machine..... | 52 |
| Table 11: Properties of mechanical brake..... | 53 |
| Table 12: Natural frequency and natural period of platform motions..... | 65 |
| Table 13: Platform motion and response of controller as a function of wind speed..... | 66 |
| Table 14: Sea states..... | 81 |
| Table 15: Measured Load components..... | 83 |
| Table 16: Selected Design Load Cases..... | 87 |
| Table 17: Extreme Events for the blade 1 root moments- Onshore..... | 95 |
| Table 18: Extreme Events for the blade 2 root moments- Offshore..... | 95 |
| Table 19: Extreme Events for tower bottom bending moment – Onshore..... | 95 |
| Table 20: Extreme Events for tower bottom bending moment - Offshore..... | 95 |

DECLARATION

I declare that this dissertation for the degree of Doctor of Philosophy in Engineering, Chair of Wind Energy Technology, Faculty of Mechanical Engineering and Ship Technology at University of Rostock hereby submitted has not been submitted by me or anyone else for a degree at this or any other university. This is my own work and the materials consulted have been properly acknowledged.

City, Date: Rostock, 25.07.2022

Signature:

A handwritten signature in black ink, appearing to be 'Aye', written over a dotted line.

WISSENSCHAFTLICHER LEBENS LAUF

| | |
|-------------------|---|
| 10/2017-dato | Doktorandin am Lehrstuhl für Windenergietechnik an der Universität Rostock |
| 10/2017-10/2020 | Wissenschaftliche Mitarbeiterin am Lehrstuhl für Windenergietechnik an der Universität Rostock |
| 04/2013 - 11/2016 | Leibniz Universität Hannover, Konstruktiver Ingenieurbau Schwerpunkt: Stahlbau Abschluss: Master of Science (M.Sc.) |
| 12/2007 – 11/2011 | Mandalay Technological University, Bauingenieurwesen Schwerpunkt: Konstruktiver Ingenieurbau Abschluss: Bachelor of Technology (B.Tech) (Qualified) |